TECHNOLOGY DRIVEN. WARFIGHTER FOCUSED.

PROCEEDINGS OF THE EDGEWOOD CHEMICAL BIOLOGICAL CENTER

IN-HOUSE LABORATORY INDEPENDENT RESEARCH AND SURFACE SCIENCE INITIATIVE PROGRAMS FY14

U.S. ARMY RDECOM®

MESSAGE from the IN-HOUSE LABORATORY INDEPENDENT RESEARCH PROGRAM MANAGER

It is my pleasure to present the 2014 edition of the Proceedings of the Edgewood Chemical Biological Center's (ECBC) In-House Laboratory Independent Research (ILIR) and Surface Science Initiative (SSI) Programs. The ECBC ILIR program funds innovative basic research projects that are high-risk with high potential for fulfilling future Army capability needs. Specifically designed to foster increased innovation, the ILIR program also aims to mentor junior investigators in the art and practice of initiating technological innovations and pursuing phenomenology at the boundaries of chemistry, biology, mathematics, or physics to gain insight and advances in support of Chemical, Biological, Radiological, Nuclear & High-Yield Explosive (CBRNE) defense missions.

The ECBC ILIR program funds innovative basic research projects that are high-risk with high potential for fulfilling future Army capability needs.

In addition to an overview of ECBC's Strategic Mission and Vision, this report includes a description of the ILIR program's rigorous project selection and evaluation process. This process is centered on external reviews by senior scientists across the government. These external reviews ensure that we fund projects with the greatest potential for fulfilling Army needs, and that each project's progress is assessed at the end of the fiscal year. These reviews also provide us with an honest and unbiased assessment of our research efforts to hone the entire organization, strengthening the Basic Research program year after year.

This year, we added a new section to this report detailing key programmatic successes of the Basic Research Program. These successes include highlights from the 2014 annual Technical Advisory Board (TAB) Review, peer review publications, technical reports, presentations, and awards honoring key contributions of the Research & Technology (R&T) Directorate's Workforce.

Finally, the report concludes with a technical manuscript from each of the 12 funded ILIR and SSI projects in fiscal year 2014. The ECBC ILIR program funded seven projects in FY14, and the SSI Program funded five projects. Together, the ILIR and SSI projects covered areas of interest across the chemical, biological, and physical sciences, including: rational molecular and nano-system design, synthetic biology, nano-scale CB sensing and signaling, aerosol sciences, panomics and molecular toxicology, materials science, algorithm design and development, and surface science.

If you have questions about the ILIR Program or this report, please do not hesitate to contact me or my Scientific and Technical Assistant (SETA) directly. I can be reached by telephone at (410) 436-0683, DSN 584-0683, or by email at augustus.w.fountain.civ@mail.mil. My SETA, Ms. Rebecca Braun, can be reached at (410) 297-5979 or by email at rebecca.m.braun.ctr@mail.mil.

Sincerely,

Augustus W. Fountain III, Ph.D.
Acting Director, Research and Technology Directorate
Senior Research Scientist (ST), Chemistry

STRATEGIC MISSION and VISION

The U.S. Army Edgewood Chemical Biological Center (ECBC) is the nation's principal research, development, and engineering resource for non-medical chemical and biological (CB) defense applications. ECBC's mission is to be ***the nation's provider of innovative solutions to counter WMD threats.*** This mission recognizes that ECBC's range of influence, while it is rooted in chemical and biological defense, influences all weapons of mass destruction. ECBC's vision of ***working toward a world free of WMD*** highlights that ECBC understands the comprehensive threat to the world, and provides the scientific knowledge, technology, and materiel required to protect and enable the warfighter to effectively operate and implement strategic decisions while in the presence of CB contamination.

ECBC's mission and vision are supported by the Center's three Directorates of Research and Technology (R&T), Engineering, and Program Integration. The R&T Directorate provides integrated science and technology solutions that address CB defense knowledge gaps and vulnerabilities. Basic science research at ECBC contributes valuable information to the fundamental science knowledgebase, enabling the development of technologies that directly benefit the warfighter and further strengthen the Army's Science and Technology (S&T) mission. ECBC's unique set of core research and technology capabilities position it to be the Army's fundamental source of research in chemistry and biology.

U.S. Soldiers prepare to enter and clear a building of opposing forces during a simulated chemical attack in an annual combat support training exercise. (U.S. Army photo by Spc. Robert Farrell/Released)

ILIR PROJECT SELECTION and EVALUATION PROCESS

The purpose of the In-House Laboratory Independent Research (ILIR) program is to fund innovative basic research projects that are high risk and have high potential payoff for fulfilling future Army capability needs. The Department of Defense (DoD) defines basic research as "the systematic study directed toward greater knowledge or understanding of the fundamental aspects of phenomena and of observable facts without specific applications toward processes or products in mind." The ILIR program is specifically designed to foster increased innovation within the ECBC Basic Research portfolio. ECBC views the program as a critical part of its efforts at ensuring a high level of basic science, to foster innovation in the areas of chemistry and biology, and to mentor junior investigators in the art and practice of new technological innovations and new phenomenology at the boundaries of chemistry, biology, mathematics, or physics that will gain additional insight and advances in support of CBRNE defense missions.

The ILIR program solicits innovative proposals from the center's principal investigators that correspond to areas of interest across the chemical, biological, and physical sciences, including: rational molecular and nano-system design, synthetic biology, nano-scale CB sensing and signaling, aerosol sciences, panomics and molecular toxicology, materials science, algorithm design and development, and surface science.Proposals are first reviewed internally by the Branch and Division Chiefs for their technical innovation, alignment to Army/ECBC S&T topic areas, and programmatic completeness. The proposals are then reviewed and critiqued by a panel comprised of resident and external Department of the Army Senior Technologists (ST), Senior Scientists from other DoD organizations, and civilian and military faculty members at the U.S. Military Academy.

The review panel evaluates each proposal on its scientific objective, the scientific methods proposed, the qualifications of the investigator, and the budget, with the scientific objective and methods weighted as the most important criteria. The proposals are then ranked according to merit. Only proposals deemed by the panel as basic research are considered for funding. Quality comments from the reviewers are compiled and used, with the numerical score, as a critical assessment of the proposal. This written feedback is essential for ECBC's mentoring of researchers and for justifying the elimination of research programs that are not competitive.

Quarterly reviews of project performance provide guidance to the program's participants, ensuring projects meet significant milestones, and substantive new knowledge is being produced and transferred to the ECBC and broader scientific community. An external Technical Advisory Board (TAB), comprised of senior research scientists from across academia and government organizations, convenes annually in the fourth quarter of the program to assess the year-to-date performance of the funded basic science research projects. Comments and feedback from the TAB Review Panel are used as a guide for shaping the overall mission of the ILIR program and to improve the overall quality of ECBC's basic science research projects into subsequent years.

This cyclical review and assessment process was used to select and monitor the progress of two new ILIR projects and five projects already in existence. Internal funds were also used to support five directed basic research projects under the Surface Science Initiative (SSI) program. This Proceedings Report contains the technical reports from all twelve ECBC-produced ILIR and SSI-funded projects.

FY14 ILIR and SSI PROGRAM HIGHLIGHTS

ECBC R&T hosted its annual TAB Review of select R&T basic science programs on August 5 and 6, 2014. The TAB Review gives ECBC the opportunity to obtain an unbiased, external assessment of the content, quality, innovation, accomplishments, and relevance of select research programs from a panel of distinguished personnel.

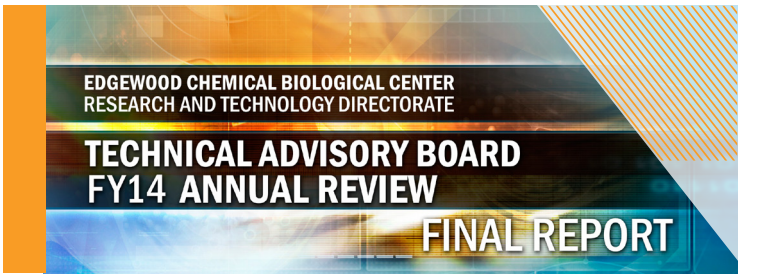

This year, the TAB evaluated 12 projects from the FY14 ILIR and SSI programs and 8 FY14 Section 219 Innovative Proposal Projects over two days. On the first day, principal investigators from the ILIR and SSI projects each made 30 minute presentations to the TAB on a variety of topics, ranging from "Secretome biomarkers for the identification and differentiation of enterohemorrhagic and enteropathogenic *Escherichia coli* strains," to "Plasmon-exciton coupling in multilayered nanoparticles." Section 219 Projects were evaluated in a separate poster session on the second day of the review.

The review concluded with the TAB formally presenting their assessment of the projects to the ECBC Director and ECBC R&T Director. The projects were evaluated against four criteria: scientific objectives, opportunity and significance, research methodology, its connections to the broader community, and overall capabilities and metrics. The TAB also provided recommendations on how best to refine each project for success. Several projects were noted as particularly strong, with highly novel ideas, well-organized and executed plans, and extremely knowledgeable PIs. The TAB's feedback on the projects will help to shape the overall quality and mission of ECBC's basic science research programs.

This year, the TAB consisted of experts from both the DoD and National Academies of Science and Engineering:

- Dr. Ronald Hann, Director, Defense Threat Reduction Agency, Chemical and Biological Technologies Department
- LTC John Burpo, Deputy Head of the Department of Chemistry and Life Sciences, United States Military Academy
- Dr. Jennifer Becker, Division Chief, Chemical Sciences Division, Army Research Office
- Dr. Kate Ong, Senior Scientist, Joint Program Executive Office for Chemical and Biological Defense
- Dr. John Russell, Head, Surface Chemistry Branch, Naval Research Laboratory
- Dr. Naomi Halas, Stanley C. Moore Professor in Electrical and Computer Engineering, Professor of Biomedical Engineering, Chemistry, Physics & Astronomy, and Director, Laboratory for Nanophotonics, Rice University
- Dr. Tim Swager, John D. MacArthur Professor, Massachusetts Institute of Technology,
- Dr. John Yates, Professor of Chemistry, University of Virginia

Overall, the TAB concluded that the projects were all aligned with the DoD's priorities and although there was limited funding, there was still a good return on investment.

Awards

The U.S. Army Research and Development Award (RDA) is only awarded to slightly more than one percent of the Army's Scientists and Engineers. This year, multiple ECBC personnel recipients were awarded RDAs.

As a result of 6.1 ILIR Basic Research efforts:

- Rabih Jabbour, Ph.D, ECBC Detection Spectrometry Branch, Outstanding Technical Achievement Award for Biological Detection Using Mass Spectrometry-based Proteomics

The following individuals received RDA awards in FY14 for their work in support of the Army 6.2 Explosives Program. The Explosives Program was evaluated during the FY13 TAB Review.

- Jason Guicheteau, Ph.D, ECBC Spectroscopy Branch, Outstanding Technical Achievement Award, Raman Chemical Imaging of Explosive-Contaminated Fingerprints for Forensic Attribution
- Steven Christesen, Ph.D, ECBC Spectroscopy Branch, Outstanding Technical Achievement Award for Raman Chemical Imaging of Explosive-Contaminated Fingerprints for Forensic Attribution
- Phillip Wilcox, ECBC Spectroscopy Branch, Outstanding Technical Achievement Award for Raman Chemical Imaging of Explosive-Contaminated Fingerprints for Forensic Attribution
- Augustus W. Fountain III, Ph.D, ECBC Acting R&T Director, Outstanding Technical Achievement Award for Raman Chemical Imaging of Explosive-Contaminated Fingerprints for Forensic Attribution

Peer Reviewed Publications

- Alam, R.; Lightcap, I.V.; Karwacki, C.J.; and Kamat, P.V., "Sense and shoot: simultaneous detection and degradation of low-level contaminants using graphene-based smart material assembly", *ACS Nano*. JUL 2014. 8(7), p7272-7278. DOI: 10.1021/nn502336x ISSN: 1936-0851 eISSN: 1936-086X
- Behler, K.D.; Pesce-Rodriguez, R.; Cabalo, J.; and Sausa, R., "Infrared spectroscopy and Density Functional Theory of crystalline beta-2,4,6,8,10,12-hexanitrohexaaziosowurtzitane (beta CL-20) in the region of its C-H stretching vibrations", *Spectrochimica Acta Part A Molecular and Biomolecular Spectroscopy*. OCT 2013. 114, p708-712. DOI: 10.1016/j.saa.2013.05.075 ISSN: 1386-1425
- Caretti, D.M. and Barker, D.J., "Effects of respirator ambient air cooling on thermophysiological responses and comfort sensations", J*ournal of Occupational and Environmental Hygiene*. MAY 2014. 11(5), p269-281. DOI: 10.1080/15459624.2013.858819 ISSN: 1545-9624 eISSN: 1545-9632
- DeLacy, B.G.; Lacey, S.; Zhang, D.J.; Valdes, E.; and Hoang, K., "Controlling the morphology of indium tin oxide using PEG-assisted hydrothermal synthesis", *Materials Letters*. FEB 2014. 117, p108-111. DOI: 10.1016/j.matlet.2013.11.114 ISSN: 0167-577X eISSN: 1873-4979
- Hsu, C.W.; DeLacy, B.G.; Johnson, S.G.; Joannopoulos, J.D.; and Soljacic, M., "Theoretical criteria for scattering dark states in vanostructured particles", *Nano Letters*. MAY 2014. 14(5), p2783-2788. DOI: 10.1021/nl500340n ISSN: 1530-6984 eISSN: 1530-6992

continues on next page

Peer Reviewed Publications continued

- Hsu, C.W.; Zhen, B.; Qiu, W.J.; Shapira, O.; DeLacy, B.G.; Joannopoulos, J.D.; and Soljacic, M., "Transparent displays enabled by resonant nanoparticle scattering", *Nature Communications*. JAN 2014. 5, Article #3152. DOI: 10.1038/ncomms4152 ISSN: 2041-1723

- Jabbour, R.E. and Synder A.P., "Mass spectrometry-based proteomics techniques for biological identification", *Biological Identification: DNA Amplification and Sequencing, Optical Sensing, Lab-On-Chip and Portable Systems*, 1st Edition. R. Schaudies, Editor. Elsevier, UK. 2014. p370-430. DOI: 10.1533/9780857099167.4.370

- Jabbour, R.E.; Deshpande, S.V.; McCubbin, P.E.; Wright, J.D.; Wade, M.M.; and Snyder, A.P., "Extracellular protein biomarkers for the characterization of enterohemorrhagic and enteroaggregative Escherichia coli strains", *Journal of Microbiological Methods*. MAR 2014. 98, p76-83. DOI: 10.1016/j.mimet.2013.12.017 ISSN: 0167-7012 eISSN: 1872-8359

- Klinger, D.; Wang, C.X.; Connal, L.A.; Audus, D.J.; Jang, S.G.; Kraemer, S.; Killops, K.L.; Fredrickson, G.H.; Kramer, E.J.; and Hawker, C.J., "A facile synthesis of dynamic, shape-changing polymer particles", *Angewandte Chemie International Edition*. JUL 2014. 53(27), p7018-7022. DOI: 10.1002/anie.201400183 ISSN: 1433 7851 eISSN: 1521 3773

- Miller, O.D.; Hsu, C.W.; Reid, M.T.H.; Qiu, W.; DeLacy, B.G.; Joannopoulos, J.D.; Soljacic, M.; and Johnson, S.G., "Fundamental limits to extinction by metallic nanoparticles", *Physical Review Letters*. MAR 2014. 112(12), Article #123903. DOI: 10.1103/PhysRevLett.112.123903 ISSN: 0031-9007 eISSN: 1079 7114

- Mogilevsky, G.; Hartman, O.; Emmons, E.D.; Balboa, A.; DeCoste, J.B.; Schindler, B.J.; Iordanov, I.; and Karwacki, C.J., "Bottom-up synthesis of anatase nanoparticles with graphene domains", *ACS Applied Materials & Interfaces*. JUL 2014. 6(13), p10638-10648. DOI: 10.1021/am502322y ISSN: 1944-8244

- Tripathi, A.; Emmons, E.D.; Christesen, S.D.; Fountain, A.W.; and Guicheteau, J.A., "Kinetics and reaction mechanisms of thiophenol adsorption on gold studied by surface-enhanced Raman spectroscopy", *Journal of Physical Chemistry C*. NOV 2013. 117(44), p22834-22842. DOI: 10.1021/jp407105v ISSN: 1932-7447

Technical Reports

- Bevilacqua, V.L.H.; Jabbour, R.E.; Wade, M.M.; Deshpande, S.V.; and McCubbin, P.E. "Effect of genetic database comprehensiveness on fractional proteomics of Escherichia coli O157:H7". *ECBC-TR-1154.* JAN 2014

- Killops, K.L.; Rodriguez, C.; and Lynd, N.A., "Platform approach to produce polymer nanoparticles with modular functionality from amphiphilic block copolymer stabilizers". *ECBC-TR-1231.* APR 2014.

- Madren-Whalley, J.S.; Sekowski, J.W.; Palmer, J.A.; Donley, E.L.R.; West, P.; and Conard, K. "Metabolomic analysis of the secretome of human embryonic stem cells following methyl parathion and methyl paraoxon exposure, phase III: LC-MS-MS structural confirmation". *ECBC-TR-1161.* JAN 2014.

- Madren-Whalley, J.S.; Sekowski, J.W.; West, P.R.; Donley, E.L.R.; and Burrier, R.E. "Metabolomic analysis of the secretome of human embryonic stem cells following methyl parathion and methyl paraoxon exposure, phase II: metabolite downselection for structural confirmation". *ECBC-TR-1178.* DEC 2013.

- Sekowski, J.W.; Bevilacqua, V. L.H.; Madren-Whalley, J.S.; Palmer, J.A.; Donley, E.L.R.; and Burrier, R.E. "Metabolomic analysis of the secretome of human embryonic stem cells following methyl parathion and methyl paraoxon exposure, phase I: initial nontargeted LC-MS". *ECBC-TR-1177.* JAN 2014.

Presentations and Proceedings

- Cabalo, J. and Emmons, E., "Ultraviolet resonance Raman spectroscopy and surface-enhanced Raman spectroscopy of model peptide chains", *SciX (FACSS)*. SEP-OCT 2014. Reno, NV.

- Emmons, E. and Cabalo, J., "Solvent effects in aqueous resonance Raman measurements of short peptides", *SciX (FACSS)*. SEP-OCT 2014. Reno, NV.

- Gonella, G.; Xu, B.; DeLacy, B.; and Dai, H.L., "Characterization of the surface of colloidal Ag NPs by second harmonic light scattering", *Bulletin of the American Physical Society, APS Meeting 59(1)*. MAR 2014. Denver, CO.

- Gonella, G.; Xu, B.; DeLacy, B.; and Dai, H.L., "Molecular layers on Ag nanoparticles characterized by second harmonic light scattering", *ACS Colloids & Surfaces Symposium*. JUN 2014. Philadelphia, PA.

- Jabbour, R., "Keynote-I mass spectroscopy applications", *Onsite-Analysis - HomeLand Security*. JAN 2014. Arlington, VA.

- Jabbour, R.E.; Nirujogi, R.S.; Deshpande, S.V.; Wade, M.M.; Snyder, A.P.; and Pandey, A.S., "Global phosphoproteome profiling for the characterization of Escherichia coli strains" (Poster), *ASMS Conference on Mass Spectrometry and Allied Topics*. JUN 2014. Baltimore, MD.

- Snyder, A.P.; Jabbour, R.E.; and Deshpande, S.V., "Identification of bacteria in complex double-blind microorganism mixtures by LC-ESI-MS/MS", *Pittcon*. MAR 2014. Chicago, IL.

- Tripathi, A.; Emmons, E.; Christesen, S.; Fountain, A.; and Guicheteau, J., "Effect of ionization of thiophenol on the mechanism of heterogeneous adsorption on gold substrates by surface-enhanced Raman spectroscopy." *SciX (FACSS)*. SEP-OCT 2014. Reno, NV.

TABLE OF CONTENTS

In-House Laboratory Independent Research Projects

Surface Science Initiative Projects


ECBC
ILIR
PROJECTS

Secretome biomarkers for the identification and differentiation of enterohemorrhagic and enteropathogenic *Escherichia coli* (EHEC and EPEC) strains

Rabih E. Jabbour[a], Samir V. Deshpande[b], Patrick E. McCubbin[c], James D. Wright[a], Mary Margaret Wade[a]

[a]U.S. Army Edgewood Chemical Biological Center, Research & Technology Directorate, 5183 Blackhawk Rd, Aberdeen Proving Ground, MD 21010

[b]Science and Technology Corporation, 500 Edgewood Rd, Edgewood, MD 21040

[c]Optimetrics, Inc., 100 Walter Ward Blvd, Abingdon, MD 21009

ABSTRACT

The secreted proteins of enterohemorrhagic *Escherichia coli* (EHEC) can cause hemorrhagic colitis which may cause life threatening hemolytic-uremic syndrome, while those of enteropathogenic and enteroaggregative *E. coli* (EPEC and EAEC) can clump to intestinal membranes. Liquid chromatography-electrospray ionization-tandem mass spectrometry-based proteomics is used to evaluate a preliminary study on the secreted and whole cell protein extracts associated with *E. coli* strain pathogenicity. Quantitative proteomics analyses for non-O157 Shiga toxin *E. coli* strains identified a number of secreted proteins that provided differentiation among the studied *E. coli* strains. The analyses also provided a method to compare the relative expression of potential protein biomarkers in different strains, and most identified proteins with large expression count were associated with the secretion portion of the pathogenic strains. Secretome analysis compared to whole cell processing entails few steps and convenient experimental extraction procedures. Bacterial characterization results are promising in exploring the impact of environmental conditions on *E. coli* secreted biomarker proteins with a few relatively straightforward protein extraction steps.

Keywords: Electrospray, liquid chromatography-tandem mass spectrometry, proteomics, enteropathogenic, enterohemorrhagic *E. coli*, non-O157 Shiga toxin *E. coli*

1. INTRODUCTION

The United States (U.S.) Government has initiated efforts for the detection and identification of biological threats in the Defense Advanced Research Projects Agency programs that explore the "detect-to-protect" and "detect-to-treat" paradigms.[1,2] These initiatives cover areas of general health risk, bioterrorism utility, Homeland Security, agricultural monitoring, food safety, and biological warfare agents in battlefield situations.[2] Some of the health concerns include food contamination outbreaks that affect military and civilian populations and also the transmission from abroad to the U.S. An example of the latter is the fatal enteroaggregative *E. coli* (EAEC) O104:H4 outbreak that occurred in Germany in 2011, which infected citizens from sixteen different nations including the U.S.[3-5]

Non-O157 Shiga toxin *E. coli* strains are emerging as the major cause of *E. coli* outbreaks; it is estimated that these strains are responsible for more than 85 percent of the total *E. coli* outbreaks in the U.S. and Europe. The six non-O157 Shiga toxin *E. coli* (STEC) strains are O26, O45, O103, O111, O121, and O145. These strains cause hemolytic uremic syndrome (HUS), hemorrhagic colitis, and death if not treated. The infection is mainly caused by Shiga toxin encoded by two Shiga toxin genes, *stx1* and *stx2*.

The virulent nature of EHEC and EPEC, coupled with their sporadic occurrence, require countermeasures that are effective in providing a rapid and reliable response in a non-restrictive approach. Currently, conventional genomic fingerprinting analysis takes 1-4 days,[1] in contrast, the metaproteomics approach has the potential to provide an effective and reliable diagnosis within a few hours. However, to develop such an approach, basic research studies are needed to isolate, identify, and characterize the biomolecules involved in the pathogenicity of the mentioned *E. coli* strains. Once the key virulence biomolecules and proteins are identified and their characterizations established, the results can be utilized to develop assays for rapid identification and differentiation of the EHEC and EPEC strains. It is widely agreed upon that the virulence proteins are mostly present in the secreted systems of the bacteria.[4] Direct isolation and characterization of these proteins has not been reported in the literature, but rather inferred based on other genomic and transcriptomic studies.[4] It is imperative to utilize the metaproteomics approach to evaluate the extraction approach and to validate the presence of virulence proteins in the secreted system of the non-O157 STEC strains. Also, characterization of the virulence proteins

APPROVED FOR PUBLIC RELEASE

and classification of the bacterial strains using these unique virulence factors could serve as an effective and reliable alternative to genomic classification. These secreted virulence proteins could prove to be excellent model biomarkers for strain differentiation among EHEC and EPEC strains.

This study sought to determine whether mass spectrometry (MS)-based proteomics could be used to distinguish between non-O157 STEC strains and differentiate the EHEC strains from EPEC ones using their secreted and whole cell protein compositions. Therefore, the objective of this study is to establish the sequence-based identity of secreted proteins isolated from the aforementioned *E. coli* strains. To achieve this goal, a high-throughput proteomic analytical system was utilized to provide a rapid means of characterizing virulence proteins and producing amino acid sequence information to be used as differentiation biomarkers of EHEC and EPEC strains in various biological matrices.

2. METHODS

2.1 EHEC, EPEC, and EAEC strain preparation

In the present study, the pathogenic *E. coli* strains are O26, O45, O103, O111, O121, and O145. The cultures were prepared by streaking cells from cryopreserved stocks onto minimal media and incubated at 37 °C with shaking at 180 rpm overnight until a stationary growth phase was observed. After incubation, cells were harvested and the colony counts were performed using optical density measurements. Three biological replicates for each strain were cultivated as mentioned above.

2.2 Isolation of the secreted proteins

The harvested cells were pelleted by centrifugation at 2,300 relative centrifugal force (RCF) for 30 minutes and the supernatant was immediately separated into 30 mL aliquots. The supernatants were filtered using 0.22 µm hollow fiber dialysis filters to ensure no large particulates or cellular debris were present in the samples. Pelleted and supernatant samples were frozen at -70 °C until further processing.

2.3 Cell lysis, protein digestion, and tandem mass tag (TMT) labeling

The secretome from each *E. coli* strain was lysed with lysis buffer (2% sodium dodecyl sulfate (SDS), 50 mM triethylammonium bicarbonate buffer (TEABC), 5 mM sodium fluoride, 1 mM sodium orthovanadate, and 1 mM β-glycerophosphate), sonicated, and centrifuged at 16,000 × g at 15 °C for 20 minutes. The supernatant protein concentration was determined using a bicinchoninic acid (BCA) assay (Pierce, Waltham, MA). An equal amount of protein, 100 µg, from each condition was reduced using dithiothreitol (DTT) at a final concentration of 5 mM at 60 °C for 20 minutes and alkylated using 10 mM iodoacetamide for 10 minutes at room temperature in the dark. The samples were then subjected to the filter aided sample preparation (FASP) protocol as described earlier. TMT labeling was carried out as per the manufacturer instructions with minor modifications. The digested peptides were mixed with TMT reagent and incubated at room temperature for 1 hour.

2.4 Basic reversed-phase liquid chromatography (bRPLC) and TiO_2-based phosphopeptide enrichment

Peptides were fractionated by bRPLC as described earlier.[20] Briefly, TMT-labeled and lyophilized peptide mixtures were resuspended and fractionated by bRPLC on an Agilent 1100 liquid chromatography (LC) system. Twelve fractions were subjected to TiO_2-based phosphopeptide enrichment. Eluted peptides were vacuum dried and resuspended in 30 µL of 0.1% trifluoroacetic acid (TFA) and desalted using C18 Stage Tips. The eluted peptides were subjected to liquid chromatography-tandem mass spectrometry (LC-MS/MS) analysis.

2.5 LC-MS/MS analysis of enriched peptides

A total of 12 bRPLC fractions were analyzed on an LTQ-Orbitrap Elite mass spectrometer (Thermo Electron, Bremen, Germany) interfaced with an Easy-nLC II nanoflow LC system (Thermo Scientific, Odense, Denmark). The peptide digests were reconstituted in 0.1% formic acid and loaded onto a trap column (75 µm x 2 cm) packed in-house with Magic C18 AQ (Michrom Bioresources, Inc., Auburn, CA, USA). Peptides were resolved on an analytical column (75 µm x 50 cm) at a flow rate of 300 nL/minute using a linear gradient of 10-35% solvent B (0.1% formic acid in 95% acetonitrile) over 85 minutes. The total run time including sample loading and column reconditioning was 120 minutes. Data dependent acquisition with full scans in the 350-1700 mass-to-charge ratio (m/z) range was carried out using an Orbitrap mass analyzer at a mass resolution of 120,000 at 400 m/z. The fifteen most intense precursor ions from a survey scan were selected for tandem mass spectrometry (MS/MS) fragmentation using higher energy collisional dissociation (HCD) fragmentation with 37% normalized collision energy and detected at a mass resolution of 30,000 at 400 m/z. Dynamic exclusion was set for 30 seconds with a 10 ppm mass window. Internal calibration was carried out using the lock mass option (m/z 445.1200025) from ambient air.

APPROVED FOR PUBLIC RELEASE

2.6 Mass spectrometry data analysis

The MS-derived data were searched using Mascot (Version 2.2.0) and SEQUEST search algorithms against an *E. coli* Reference Sequence (RefSeq) database using Proteome Discoverer 1.4 (Version 1.4.0.288) (Thermo Fisher Scientific, Bremen, Germany). The search parameters for both algorithms included carbamidomethylation of cysteine residues (57.02 Da), peptide N-terminal of TMT sixplex (229.16 Da), and lysine side chain of TMT sixplex (229.16 Da) as a fixed modification and oxidation of methionine (15.99 Da) as variable modifications. MS/MS spectra were searched with a precursor mass tolerance of 20 ppm and fragment mass tolerance of 0.1 Da. Trypsin was specified as protease and a maximum of two missed cleavages were allowed. The data were searched against target decoy database and the false discovery rate was set to 1% at the peptide level. The TMT ratio for each phosphopeptide-spectrum match was calculated by the quantitation node. Peptides with ratios greater than two-fold were considered for further analysis.

2.7 Protein database and database search engine

A protein database was constructed in a FASTA format using the annotated bacterial proteome sequences derived from fully sequenced chromosomes of all available *E. coli* strains. There were 57 documented strains as of August 2014 with 42 EHEC, 10 EPEC, and 5 EAEC strains. A Perl program (http://www.activestate.com/ActivePerl; accessed August 2014) was written to download these sequences automatically from the National Institutes of Health National Center for Biotechnology (NCBI) site (http://www.ncbi.nlm.nih.gov; accessed August 2014). Of the six STEC strains investigated, O26, O45, and O145 did not have their corresponding genome sequenced. Each database protein sequence was supplemented with information about a source organism and a genomic position of the respective open reading frame (ORF) embedded into a header line. The database of the *E. coli* bacterial proteome was constructed by translating putative protein-coding genes and consists of a few million amino acid sequences of potential tryptic peptides obtained by the in-silico digestion of all proteins (allowing up to two missed cleavages).

The experimental MS/MS spectral database of bacterial peptides was searched using the SEQUEST algorithm against a constructed proteome database of microorganisms. The SEQUEST thresholds for searching the product ion mass spectra of peptides were Xcorr, deltaCn, Sp, RSp, and deltaMpep. The top peptide hits generated by SEQUEST were filtered with a relative correlation score $\Delta Cn > 0.1$ and the filtered hits were accepted as peptide identifications when their correlation scores (Xcorr) were higher than the thresholds that allowed generating a desired false discovery rate value.[9] The peptide validation was performed using the PeptideProphet algorithm[10] to provide probability scores on the peptide assignment to the MS/MS spectra. Peptide sequences with a probability score of 95% and higher were retained in the dataset and used to generate a binary matrix of sequence-to-bacterium (STB) assignments. The binary matrix assignment was populated by matching the peptides with corresponding proteins in the database and assigning a score of 1. A score of 0 was assigned for a non-match. The column in the binary matrix represents the proteome of a given *E. coli* strain, and each row represents a tryptic peptide sequence from the LC-MS/MS analysis. A protein is identified as present when it is found in two or more of the three biological replicates that were analyzed for each *E. coli* strain. Analyzed samples were matched with the *E. coli* strains based on the number of unique peptides that remained after further filtering of degenerate peptides from the binary matrix. Verification of the classification and identification of candidate microorganisms was performed through hierarchical clustering analysis and taxonomic classification.

The in-house developed software ABOid™[11,12] transformed the results of searching the product ion mass spectra of peptide ions against a custom protein database, which was downloaded from NCBI with the commercial software SEQUEST into a taxonomically meaningful and easy to interpret output. It calculated probabilities that peptide sequence assignment to a product ion mass spectrum was correct and used accepted spectrum–to-sequence matches to generate an STB binary matrix of assignments. Validated peptide sequences, differentially present or absent in various strains (STB matrices), were visualized as assignment bitmaps and analyzed by ABOID™ that used phylogenetic relationships among *E. coli* strains as part of the decision tree process. The ABOID™ bacterial classification and identification algorithm uses assignments of organisms to taxonomic groups (phylogenetic classification) based on an organized scheme that begins at the phylum level and follows through classes, orders, families, and genus down to the strain level. ABOID™ was developed in-house using Perl, MATLAB, and Microsoft Visual Basic.

3. RESULTS AND DISCUSSION

3.1 Determination of common proteins in secretome lysates for non-O157 STEC strains

O26, O45, O103, O111, O121, O145, and K12:B2 strains were analyzed by MS proteomics to determine the proteins from their secretomes' lysate, respectively. Figure 1 shows the result of replicate analysis of the secretome lysate of the combined samples that contains the mentioned non-O157 STEC strains. The Mascot and Sequest alignment algorithms were used to determine the number of proteins in the pooled secretome of the six non-O157 STEC strains. The total number of proteins identified, using at least two peptides that match to the same protein, was on average 1006 proteins. The

common proteins among the three replicate analyses of the secretome lysates of the non-O157 STEC strains were on average 632 proteins. A closer look at those proteins showed that the proteins with the highest number of peptides identified by the reaching algorithm were related to the pathogenicity and extracellular functions in the STEC strains.

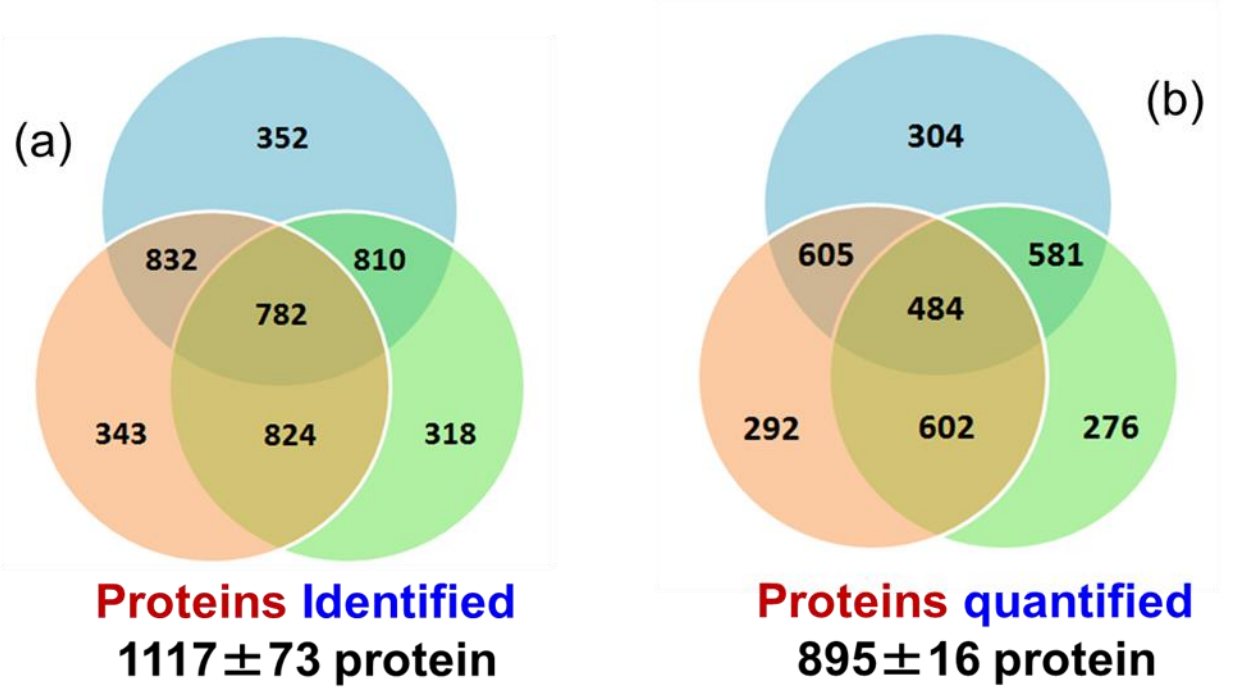

Figure 1. Venn diagram for the biological replicates of six non-O157 STEC strains. (a) first technical triplicate analyses on the first biological sample of the pooled six strain, (b) second technical triplicate analyses on the second biological sample of the pooled six strain. Proteins were identified with the presence of two or more peptides at a 95% confidence level.

We observed that the Stx1 and Stx2 proteins were found in different degrees of abundance across the STEC strains. For example, Table 1 shows the TMT result of the relevant peptides that have pathogenicity functions and the distribution ratio of those peptides in different STEC strains as compared to *E. coli* K12. The relatively high number of proteins in the secretome milieu is due to the presence of 30 percent of cytoplasmic proteins versus the rest which were associated with the extracellular milieu. These intracellular proteins in the secreted milieu could be due to cell death such as from lysate, autoproteolysis, and cell lysis. Xia et al.,[15] however, list 83 extracellular proteins from two *E. coli* strains of which the majority are known to be of intracellular origin. The experimental method included the usual protein extraction, purification, and isolation procedures.[15] It is noteworthy to mention that cytoplasmic proteins have the lowest scores among all identified proteins which could indicate their low abundance in the secreted lysates of the non-O157 STEC strains.

Table 1. Quantitative distribution of proteins in the secreted portion of the six non-O157 STEC strains. Functionality of the listed proteins is mostly associated with pathogenicity islands and extracellular

functions. Blue colored values represent the highest level of expression for the given protein in the analyzed strains.

Protein Description	Fold Change Value						Function
	O111: H8/K12	O145/ K12	O26:H11/ K12	O103: H11/K12	O45:H2/K 12	O121: H19/K12	
Secreted protein EspA	1.0	31.5	0.3	0.1	0.8	0.4	EspA is a core member of the type III secretion system. This protein is essential for attaching and effacing lesion formation.
Secreted protein B	0.6	0.8	3.0	9.3	21.0	0.8	This protein is known to be involved in EPEC pathogenesis.
Secretion system effector C family protein	1.0	1.0	1.9	3.3	8.0	1.0	A member of the type III secretion system and plays a role in the injection of effector proteins into host cells.
Type III secretion system translocator, LEE associated protein	64.5	0.1	4.1	0.3	0.6	0.9	One of the core members of the pathogenic island T3SS system and is essential for bacterial virulence and pathogenesis.
EspP	0.4	1.2	4.8	4.9	0.7	7.4	A member of the type IV secretion system and an autotransporter domain containing protein.
Translocated intimin receptor (Tir)	0.3	0.5	1.6	1.4	27.3	1.8	Tir proteins are known as bacterial proteins that mediate adhesion between mammalian cells and attaching and effacing (A/E) pathogens.
Universal stress protein UP 12	0.02	0.4	0.05	0.04	0.05	0.03	A member of the UspA family of universal stress proteins and has been shown to be overexpressed during growth inhibitory conditions induced by heat shock.
Hypothetical protein	3.4	7.1	7.1	2.4	14.3	6.0	This uncharacterized protein contains Imelysin peptidase domain.

3.2 Effect of cellular fraction on the differentiation of non-O157 STEC strains

The pooled secreted fractions from the non-O157 STEC strains were analyzed by LC-MS/MS followed by ABOID™ data processing. The database contained all sequenced strains of *E. coli* and the laboratory's contaminants. This constructed proteome database did not contain the proteome for O45, O121, and O145 STEC strains due to the lack of their genomic sequencing data in public consortium. A nearest neighbor analysis, using the Euclidean distance single linkage approach, showed 100 percent similarity (linkage distance) between the analyzed secretome (Figure 2a) and nearest neighbor in the database. There was approximately 78 percent similarity of the mixture sample containing the six non-O157 STEC strains with O26, O103, and O111 strains in the database. There was approximately 50 percent dissimilarity between the same mixture and that of O157 strains.

APPROVED FOR PUBLIC RELEASE

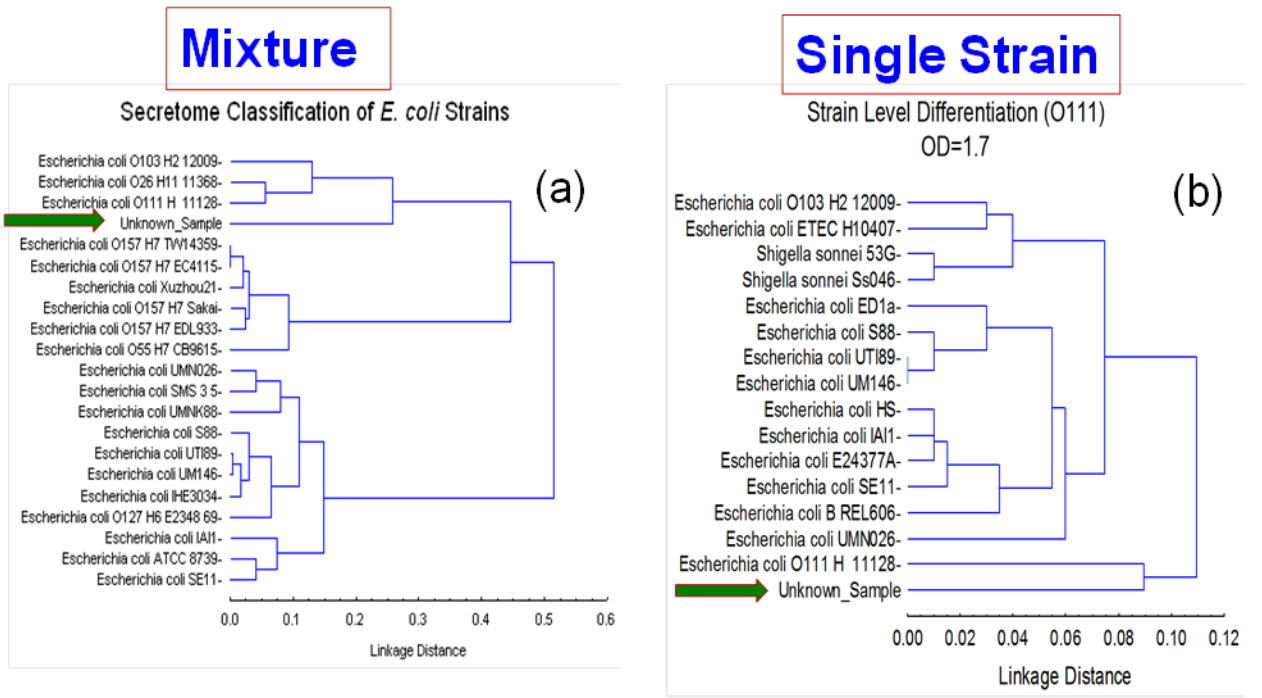

Figure 2. Euclidean distance single linkage dendrograms for the nearest neighbor classification of a mixture (a) and a single strain (b) from the six non-O157 STEC strains.

These near-neighbor comparisons showed that we can correctly identify a mixture of non-O157 strains to the strains that are actually present in the sample, and this was evident by the high percentage similarity of the sample with that of the non-O157 strains as compared to that of O157. The reason O45, O121, and O145 do not show up is due to their absence from the proteome database as stated above. Moreover, Figure 2b shows the Euclidean distance result of the single linkage of the secretome lysate from a non-O157 STEC strain, namely O111. The result shows more than 90 percent similarity with O111 in the database and strain level identification can be inferred. This classification indicates that this approach is capable of providing a simple and relatively rapid experimental method which is capable of enhancing characterization information with respect to the secreted protein extract procedure. Although the proteomics classification showed strain level classification, each strain did not show close relation to the others. This observation is important to support the findings reported in genomic studies that those strains are different in their protein expression.[16,17]

3.3 Identification of potential biomarkers for six non-O157 STEC strains

Secretome protein fractions from six non-O157 STEC and non-pathogenic K12 strains were pooled and TMTs were added to the pooled samples. The result from those pooled samples provided a distribution ratio of various proteins in the six non-O157 strains as compared to the non-pathogenic *E. coli* K12 strain. Figure 3 shows the distribution of potential protein biomarkers with respect to the mentioned strains. Figure 3 reveals that for each studied strain there are potential biomarkers that can be identified. For example, Figure 3 shows that colicin and colicin immunity proteins are highly expressed in O111. Autonomous glycyl radical cofactor A (GrcA) and EspB, a virulence factor of EHEC that is known to be dependent on a type III secretion system (T3SS) and the multifunctional effector with 312 amino acid residues, are both highly expressed in O145. Cystine transporter subunit and hypothetical proteins are highly expressed in O26; EaeB protein, a triggering protein in host cell signal transduction, is highly expressed in O103; a translocated intimin receptor is highly expressed in O45, and flagellum related proteins are highly expressed in O121 as compared to the other studied strains.

APPROVED FOR PUBLIC RELEASE

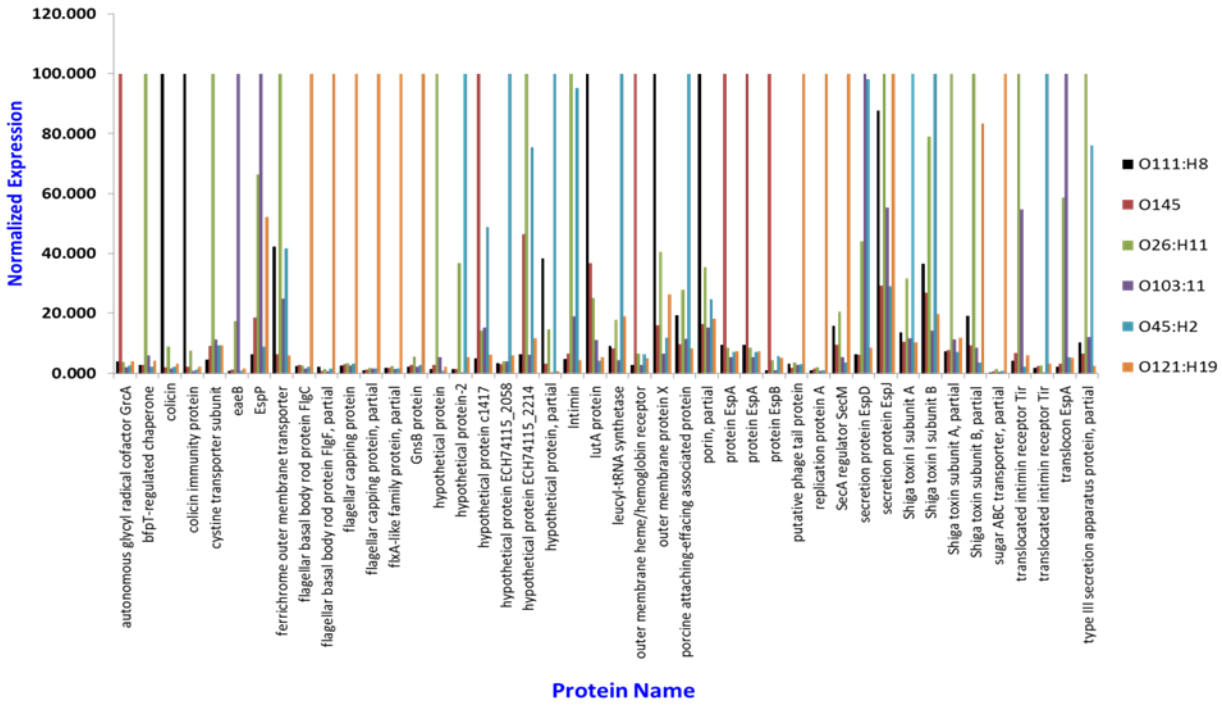

Figure 3. Comparative proteomics of secreted proteins among the six non-O157 STEC strains.

It should be mentioned that this study is the first one to address the relative proteomic quantitation among the common non-O157 STEC strains. Most of the determined potential protein biomarkers are commonly found in the extracellular portion and most of the potential protein biomarkers are associated with extracellular and pathogenicity functions. Also, we observed during the alignment searching process that some proteins have the same name but different accession numbers, as in the case with the translocated intimin receptor (Tir), which is an essential component in the adherence of the EPEC and EHEC to the cells lining the small intestine. The Tir protein with accession number WP_024228466 was highly expressed in O26 and the Tir protein with accession number WP_024233847 was highly expressed in O45. Homology analysis of those proteins showed that there was a 28 percent variation among them in their corresponding amino acid sequence, which could potentially indicate a difference in their respective cellular functions.

3.4 Diagnostic application of the quantitative proteomics approach for the non-O157 STEC strains

Figure 4 shows the result obtained from the ratio comparison of Stx2 to EaeB of the six non-O157 STEC strains. The ratio of Stx2/EaeB has been proposed to predict if a given EHEC or EPEC strain will cause HUS, a bloody diarrhea.[18] It can be observed that there is a variation in the abundance of Stx2 and EaeB in the studied STEC strains. While O103 and O45 showed much higher abundance of EaeB as compared to Stx2, the other four non-O157 STEC strains have equal distribution and thus could be predicted to cause HUS. This observation is in agreement with reported literature that addressed this subject.[18]

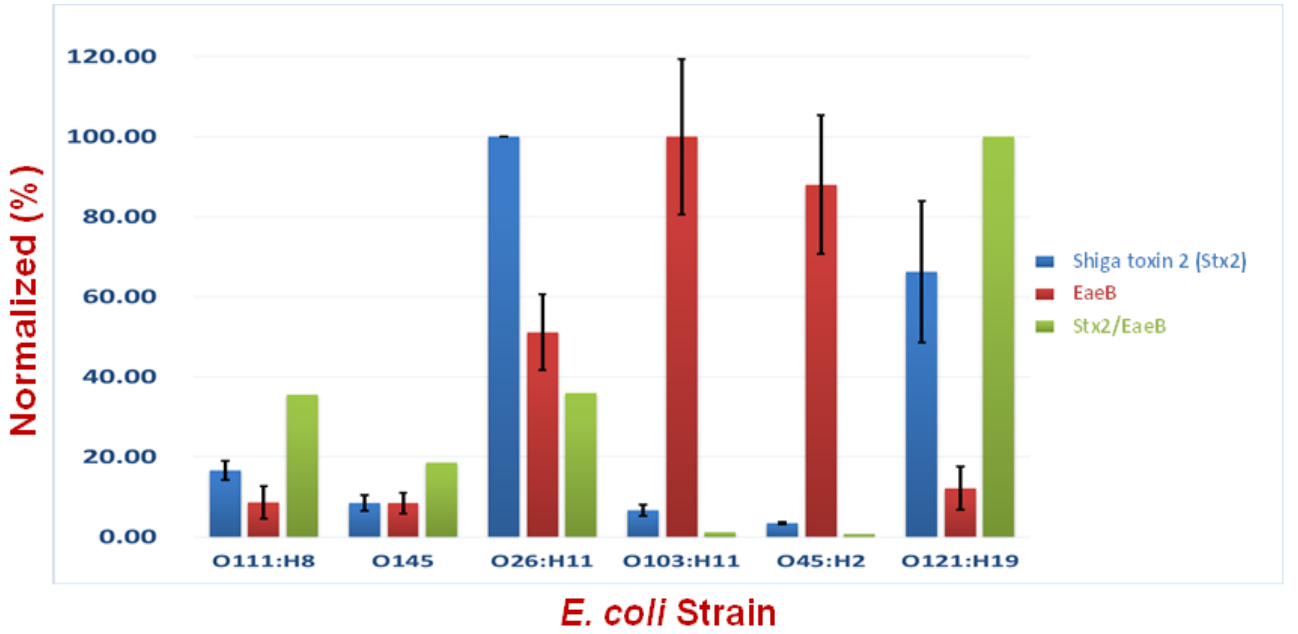

Figure 4. Predictive model of HUS in the six non-O157 STEC strains. A distribution ratio comparing the abundance of Stx2 to EaeB proteins in each studied strain.

While diagnostic studies are beyond this reported work, it is noteworthy to mention the potential of using such an approach of quantitative proteomics to predict some diagnostic indicator. It is also important to indicate that the strain differentiation reported in this work using secreted proteins in combination with quantitative proteomic approaches can be a useful method to predict some diagnostic parameters in case of an outbreak of non-O157 STEC strains.

4. CONCLUSIONS

The utility of secretome proteins as biomarkers for characterization of EPEC and EHEC strains is useful, practical, and uses few and efficient experimental procedures. Moreover, quantitative proteomics is a useful technique to aid in discovering potential protein biomarkers for strain differentiation and the development of effective medical countermeasures. This study presents a pioneer discovery on the semi quantitative distribution of secreted proteins for the six most common non-O157 STEC strains. We were able to show that taxonomic classification is a vital method to determine if the non-O157 STEC strains are present in a given sample as a mixture of bacteria or as an individual one. Although some of the strains studied were not included in the constructed proteome database due to lack of their sequencing genome, there was strong agreement between the differentiated strains and the ones actually present in a given sample. Using secretome proteins provide a unique source of cellular variability that was not observed when compared to whole cell lysates as previously reported.[19]

MS/MS-based proteomics and bioinformatics were shown to have utility in the comparative proteomics study for the differentiation of EHEC and EPEC strains. This resulted in different degrees of separation between the correctly determined database organism and the next nearest neighbor organism(s). Classification and identification of an organism that is not in the genome database and not using a genome sequencing technique is possible as with the case of O103:H2, O26:H11, and O111:H8 compared to the absent ones of O121:H19, O45:H2, and O145 strains. Also, the fact that the mixture of those strains was totally separated from O157 serovars during the taxonomic classification is in agreement with genomic sequencing and classification studies that support our findings on the proteomic level.[20] Such properties will allow the utilization of this MS-based proteomics approach to infer taxonomic classification based on the depth of available genomic sequencing information. The secretome MS-proteomics approach has the potential to characterize emerging and unknown microbes and aid in genomic sequencing analyses.

ACKNOWLEDGEMENTS

The authors wish to thank the U.S. Army Edgewood Chemical Biological Center In-House Laboratory Initiative Research (ILIR) program for funding this work, and Dr. Augustus W. Fountain, III for his guidance and oversight of the program.

APPROVED FOR PUBLIC RELEASE

REFERENCES

[1] Demirev, P.A.; Feldman, A.B.; and Lin, J.S., "Chemical and biological weapons: current concepts for future defenses", *Johns Hopkins APL Technical Digest*. **2005**. 26(4), p321-333.

[2] Demirev, P.A. and Fenselau, C., "Mass spectrometry for rapid characterization of microorganisms", *Annual Review of Analytical Chemistry*. **2008**. 1, p71-93.

[3] European Centre for Disease Prevention and Control and European Food Safety Authority. "Shiga toxin/verotoxin-producing Escherichia coli in humans, food and animals in the EU/EEA, with special reference to the German outbreak strain STEC O104", *Joint EFSA/ECDC Technical Report*. **2011**. Available from: http://www.efsa.europa.eu/en/supporting/doc/166e.pdf.

[4] Perna, N.T., *et al.*, "Genome sequence of enterohaemorrhagic Escherichia coli O157 H7", *Nature*. **2001**. 409(6819), p529-533.

[5] Mellmann, A., *et al.*, "Prospective genomic characterization of the German enterohemorrhagic Escherichia coli O104:H4 outbreak by rapid next generation sequencing technology", *PLOS ONE*. **2011**. 6(7): e22751.

[6] Frankel, G., *et al.*, "Enteropathogenic and enterohaemorrhagic Escherichia coli: more subversive elements", *Molecular Microbiology*. **1998**. 30(5), p911-921.

[7] Deng, W., *et al.*, "Quantitative proteomic analysis of type III secretome of enteropathogenic Escherichia coli reveals an expanded effector repertoire for attaching/effacing bacterial pathogens", *Molecular & Cellular Proteomics*. **2012**. 11(9), p692-709.

[8] Jabbour, R.E., *et al.*, "Double blind characterization with non-genome sequenced bacteria by mass spectrometry-based proteomics", *Applied Environmental Microbiology*. **2010**. 76(11), p3637-3644.

[9] Peng. J., *et al.*, "Evaluation of multidimensional chromatography coupled with tandem mass spectrometry (LC-MS/MS) for large-scale protein analysis: the yeast proteome", *Journal of Proteome Research*. **2003**. 2(1), p43–50.

[10] Keller, A., *et al.*, "Empirical statistical model to estimate the accuracy of peptide identifications made by MS/MS and database search", *Analytical Chemistry*. **2002**. 74(20), p5383-5392.

[11] Jabbour, R.E., *et al.*, "Identification of Yersinia pestis and Escherichia coli strains by whole cell and outer membrane protein extracts with mass spectrometry-based proteomics", *Journal of Proteome Research*. **2010**. 9(7), p3647-3655.

[12] Deshpande, S.V., *et al.*, "A software for automated identification and Phyloproteomics classification of tandem mass spectrometry data", *Journal of Chromatography & Separation Techniques*. **2011**. S5:001.

[13] Wang, N., *et al.*, "Development of mass spectrometry-based shotgun method for proteome analysis of 500 to 5000 cancer cells", *Analytical Chemistry*. **2010**. 82(6), p2262-2272.

[14] Dworzanski, J.P., *et al.*, "Mass spectrometry-based proteomics combined with bioinformatic tools for bacterial classification", *Journal of Proteome Research*. **2006**. 5(1), p76-87.

[15] Xia, X.X., *et al.*, "Comparison of the extracellular proteomes of Escherichia coli B and K-12 strains during high cell density cultivation", *Proteomics*. **2008**. 8(10), p2089-2013.

[16] Kupferschmidt, K., "Scientists rush to study genome of lethal E. coli.", *Science*. **2011**. 332(6035), p1249-1250.

[17] Al Safadi, R., *et al.*, "Correlation between in vivo biofilm formation and virulence gene expression in Escherichia coli O104:H4". *PLOS ONE*. **2012**. 7(7), e41628.

[18] Ethelberg, S., *et al.*, "Virulence factors for hemolytic uremic syndrome, Denmark", *Emerging Infectious Diseases*. **2004**. 10(5), p842-847.

[19] Bugarel, M. *et al.*, "Virulence gene profiling of enterohemorrhagic (EHEC) and enteropathogenic (EPEC) Escherichia coli strains: a basis for molecular risk assessment of typical and atypical EPEC strains", *BMC Microbiology*. **2011**. 11, p142.

[20] Jabbour, R.E. *et al.*, "Extracellular protein biomarkers for the characterization of enterohemorrhagic and enteroaggregative Escherichia coli strains", *Journal of Microbiological Methods*. **2014**. 98, p76–83.

Examination of the mechanism for translocation of BotNT *in vivo*, and its use in neutralization of the toxin

Edward R. Hofmann[a], James M. Myslinski[a], Edward J. Emm[b], Patricia E. Buckley*[c]
[a]Excet, Inc., 8001 Braddock Rd, Suite 303, Springfield, VA 22151
[b]Leidos, Inc., 11951 Freedom Dr, Reston, VA 20190
[c]U.S. Army Edgewood Chemical Biological Center, Research & Technology Directorate, 5183 Blackhawk Rd, Aberdeen Proving Ground, MD 21010

ABSTRACT

Botulinum neurotoxin (BotNT) remains one of the deadliest substances known to man, yet few methods for neutralizing the BotNT toxin exist today, and side effects associated with these antidotes are often debilitating and less than efficacious. Previously, we were able to employ an *in vitro* model, BE(2)-M17 neuroblastoma cells, to use as a primary screen for blocking the cleavage of synaptosomal-associated protein 25 (SNAP-25), the primary target for BotNT activity. Currently, methods for developing treatments for exposure or efficient models for identifying BotNT inhibitors continue to rely heavily on lethal animal testing. An intermediate *in vivo* model that "bridges the gap" between *in vitro* testing and full-fledged animal studies would serve as an invaluable tool. In this new study, we propose the use of the model organism *Caenorhabditis elegans* as an intermediate model to the mouse lethality assay in order to determine whether previous *in vitro* results can be repeated in an *in vivo* model that is not only scalable, but also reproducible and automatable. This effort investigates the ability of BotNT to cleave *C. elegans* homologous proteins in an *in vivo* system, without the use of mice as the model organism.

Keywords: *C. elegans*, botulinum neurotoxin exposure, SNAP-25, VAMP2, SNB-1, RIC 4B, protein cleavage

1. INTRODUCTION

There are many bacteria that are known to cause disease in humans, but there are few that produce as deadly an effect as *Clostridium botulinum*. The neurotoxins that are produced by *C. botulinum*, and some strains of *C. butyricum* and *C. baratii*, have been declared Category A agents on the scale for "Critical biological agent categories for public health preparedness".[1] The category A agents on this list have the greatest potential for adverse public health impact, and have a moderate to high potential for large-scale dissemination, or the ability to invoke mass fear in the general population due to their heightened recognition to cause death.[1]

Botulinum neurotoxin (BotNT), as one of the deadliest substances known to man and a Category A threat agent, has the potential to be used in a terrorist event,[2,3] yet its paralyzing effects have been exploited for the treatment of neurological diseases[4,5] and cosmetic therapy.[6] The current method for neutralizing BotNT toxin is to inject human[7] or equine antisera into the affected individual.[8] The side effects associated with these antidotes are often debilitating, and less than therapeutically desired.[7] Thus, there is an increased demand for finding better treatment methods to treat exposure and to find efficient models for measuring and identifying BotNT inhibitors.[9,10] The goal of this effort is to investigate the practicality of using the nematode *C. elegans* as an *in vivo* model for mediating the translocation of BotNT across the cell membrane using antibodies that prevent the subsequent intracellular catalytic cascade; thus neutralizing BotNT. We hypothesize that the intrinsic biology of *C. elegans* can be used as an *in vivo* model for predicting BotNT toxicity and, consequently, can be developed as a new method for screening/testing therapeutic interventions for BotNT poisoning.

There are seven serotypes of toxin (BotNT A-G) produced by these bacteria, categorized based upon their immunological properties and amino acid variations.[11] Out of these seven serotypes, there are four toxin types known to cause outbreaks in humans: A, B, E, and F.[2,12-15] All seven of the Botulinum neurotoxins are zinc metalloproteases that inactivate specific cellular proteins.[13] They are produced as 150 kDa single chain proteins comprised of three functional domains: *N*-terminal catalytic domain (light chain (LC)), an internal translocation domain (heavy chain translocation (HCT)), and a *C*-terminal receptor binding domain (heavy chain receptor, (HCR)).[16] The HCR can then be further subdivided into *N*-terminal (HCR_N) and *C*-terminal (HCR_C) domains.[16] The LC targets the soluble N-ethylmaleimide-sensitive factor attachment protein receptor. Specifically, the LC of BotNTA, /C, and /E cleave nine amino acids from the *C*-terminal peptide of the synaptosomal-associated protein SNAP-25;[13,16-18] whereas, the LC of BotNTB, /D, /F, and /G all cleave vesicle-associated membrane protein 2 (VAMP2).[13,14,19,20] The HCR is responsible for the binding and translocation of the toxin *in vivo*.[16,20] Both chains, bound by a single interchain disulfide bond, are required for toxicity[15] (Figure 1).

APPROVED FOR PUBLIC RELEASE

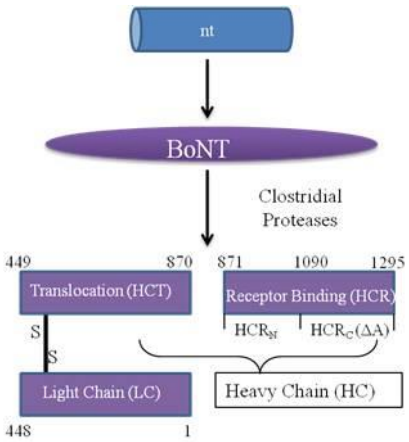

Figure 1. Model of BotNT (adapted from Baldwin[16]). The neurotoxin gene (nt) produces BotNT; which is cleaved by clostridial proteases into a dichain toxin, whose light (LC) and heavy (HC) chains are linked by a disulfide bond. The N-terminal LC is a zinc protease. The *C*-terminal HC includes a translocation domain (HCT), and a *C*-terminal receptor binding domain which can be subdivided into an *N*-terminal (HCR_N) and *C*-terminal domain [$HCR_C(\Delta A)$].

Previous studies have shown that exposing the nematode *C. elegans* to various drugs produces electrophysiologically comparable results to vertebrate neurons.[21] Furthermore, a number of human stress responses are conserved in *C. elegans*.[21] *C. elegans* is well-established as a model system to elucidate molecular mechanisms involved in toxicological responses relevant to human intoxication.[21-23] The nematode model system has a neuromuscular junction with similar proteins of interest that, when disrupted, exhibit the same phenotypical results as human BotNT intoxication;[24,25] therefore, the animal activity, before and after BotNT exposure, is predictive of the activity or inhibition of the toxin. Both SNAP-25 (Ric4B homologue) and synaptobrevin 2 (VAMP2; SNB-1 homologue), the substrates of BotNT cleavage (Figure 2), are conserved in many lower organisms including the nematode *C. elegans*. These orthologues function in neurotransmitter secretion in *C. elegans* and mutant animals demonstrate various dysfunctional neurotransmitter phenotypes from arrested development to paralysis depending on the nature of the mutation.[25] Sequence alignment of the orthologues to these proteins in *C. elegans* suggests the cleavage sites of these proteins are conserved and therefore should be sensitive to proteolytic cleavage by BotNT.

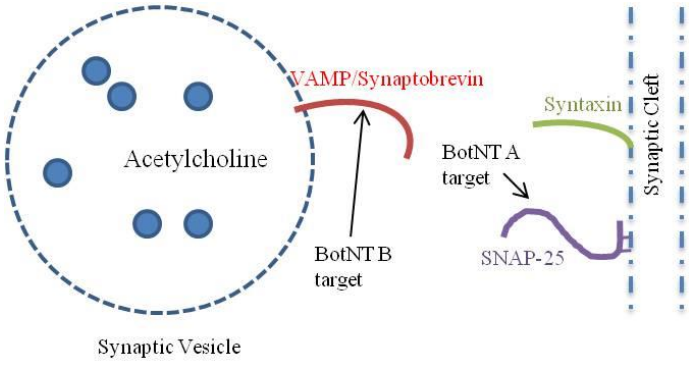

Figure 2. Model of action of BotNT activity (adapted from Barr[13]). BotNT blocks the cholinergic transmission from the synaptic vesicle to the synaptic cleft. BotNT A degrades SNAP-25 and BotNT B degrades VAMP, which prevents the vesicle from being bound to the membrane. This leads to flaccid muscles paralysis and nerve destruction, followed by difficulties in breathing and swallowing, leading to death.

2. MATERIALS AND METHODS

2.1 Reagents

BotNT A and B complexes were purchased from Metabiologics (Madison, WI). Plasmids containing the *ric4B* or *snb-1* genes from *C. elegans*, homologues to SNAP-25 and VAMP2 respectively, with *C*-terminal His tags were purchased from DNA 2.0 (Menlo, CA). All chemicals were purchased from Sigma unless otherwise noted. Trisialoganglioside GT_{1b} was purchased from Matreya (Pleasant Gap, PA) and reconstituted with sterile media. Luria-Bertani (LB) Broth and

Terrific Broth (TB) Overnight Express™ media were prepared according to the manufacturer's instructions and contained kanamycin (30 µg/mL).

2.2 *C. elegans* strains for *in vivo* exposure studies

All *C. elegans* strains were purchased from the Caenorhabditis Genetics Center at the University of Missouri. Strains used in this study include Wild-type (N2), *snb-1* mutants (NM467 and NM833), *ric-4* mutants (RM965), and the *snb-1::gfp* transgenic strain CZ333. Strains were grown on nematode growth media (NGM) plates according to methods described in Wormbook, Maintenance of *C. elegans*.[26] For synchronizing the worms, mature adults were placed in a standard hypochlorite solution to release the eggs, and after three washes the eggs were placed on unseeded NGM plates to hatch as described in Wormbook, Maintenace of *C. elegans*.[26]

2.3 Optimizing protein production

To select the highest protein-producing colonies, protocols were adapted from Li et al.[27] First, an appropriate plasmid was transformed into chemically competent DH5α cells by incubating the cells (100 µL) with the plasmid (1 µL, 50.1 ng/µL) for 30 minutes at 0 °C, followed by 30 seconds at 42 °C, whereupon the cells were rescued with 250 µL super optimal broth with catabolite repression (SOC) media in a 37 °C shaking incubator (200 rpm) for 1 hour. LB plates were spread with two volumes (50 µL and 150 µL) of the rescued media, and incubated at 37 °C overnight. Three colonies were then selected and used to inoculate 2 mL LB cultures, which were grown in a shaking incubator at 37 °C overnight. To evaluate the expression, the cultures (1 mL) were used to inoculate three 300 mL Erlenmeyer flasks containing TB Overnight Express™ media (50 mL), which were incubated at 37 °C in a shaking incubator (200 rpm) overnight. A glycerol stock was prepared from each culture, and the rest was centrifuged at 4,000 x g for 15 minutes, the supernatant was discarded and the pellet was resuspended in SDS lysis buffer, and incubated at 95 °C for 10 minutes. The lysed solutions were analyzed by sodium dodecyl sulfate-polyacrylamide gel electrophoresis (SDS-PAGE) (Bio-Rad Criterion XT 4-12%) to evaluate the expression, and the culture that appeared to have the highest expression was carried forward, repeating the above process to select for the highest expressing culture.

In order to determine the optimum incubation time for expression, a culture was grown in TB Overnight Express™ media (50 mL) at 30 °C in a shaking incubator (200 rpm) and aliquots (1 mL) were taken at approximately 2 hour intervals, according to the manufacturer's directions (QIAgen, Valencia, CA). A fresh LB plate was streaked and incubated at 37 °C overnight. A LB culture (2 mL) was inoculated with a single colony and incubated at 37 °C for 8 hours in a shaking incubator (200 rpm); whereupon additional LB (50 mL) was added, and incubation continued for 17 hours. Each of four baffled Erlenmeyer flasks containing TB Overnight Express™ media (500 mL) were inoculated with 2 mL of the aforementioned 50 mL culture, and incubated at 30 °C for 24 hours in a shaking incubator (200 rpm); which was determined to be the optimal expression protocol.

2.4 Expressed protein purification

The cultures expressing protein were centrifuged at 4,000 x g for 15 minutes, the supernatant was discarded, and the pellet was resuspended in His-Tag wash buffer. This resuspended pellet was then lysed using a microfluidizer, and the cell debris was removed by centrifugation (14,000 rpm) and filtration (22 µm). The resulting solution was purified on an AKTAexpress FPLC system (GE Healthcare) using a HisTrap HP 1 mL column and a gradient elution, where buffer A was 20 mM phosphate buffered saline (PBS) containing 20 mM imidazole and buffer B was 20 mM PBS containing 520 mM imidazole. Using the Experion Lab on a Chip system, samples of the protein were analyzed under nonreducing conditions in order to determine the molecular weight of the proteins, which represents the detection of degradation products as well as contaminants within the sample.

2.5 Optimizing *C. elegans* protein extraction

To select the method that produces the greatest quantity of proteins, two different methods of preparing *C. elegans* were evaluated. For both methods, starved worms were collected in M9 buffer and centrifuged (16,000 x g). Using the freeze thaw method required the worm pellet to be resuspended in 200 µL of M9 buffer and alternately snap frozen in liquid nitrogen (LN_2) and thawed at room temperature for 5 cycles. The lysed material was centrifuged (16,000 x g) for 5 minutes, the sample decanted to 25 µL, and 10 µL of 2X SDS gel loading buffer was added. The sample was then sonicated in a sonication bath (VWR Scientific, 50HT Aquasonic) for 2 minutes and immediately incubated at 95 °C for 5 minutes. The sample was then analyzed by SDS-PAGE (Bio-Rad Criterion XT 4-12%) using standard procedures. Alternatively, using the immersion sonication method, the supernatant was discarded and the worm pellet was resuspended in an isotonic 4-(2-hydroxyethyl)-1-piperazineethanesulfonic acid (HEPES) solution (360 mM sucrose and 12 mM HEPES). The worms were then sonicated on ice at maximum power using four 5 second pulses (Cole Parmer 4710 Series Ultrasonic Homogenizer). The lysed material was centrifuged (16,000 x g) for 5 minutes and the supernatant was analyzed by SDS-PAGE (Bio-Rad Criterion XT 4-12%) using standard procedures; which was determined to be the optimal extraction protocol.

2.6 *In vitro* toxin exposure

In order to determine if recombinant Ric4B *N*-His from *C. elegans* is susceptible to cleavage by BotNT A complex, purified protein was incubated with 66 nM BotNT A complex at 37 °C for 24 hours. Using the Experion Lab on a Chip system, samples of the protein were analyzed under nonreducing conditions in order to determine the molecular weight of the proteins, which represents the detection of degradation products as well as contaminants within the sample.

Also, in order to determine if recombinant SNB-1 *C*-His from *C. elegans* is susceptible to cleavage by BotNT A or B complex, the pooled fractions (circa 25 mL, 1.5 mg/mL) were dialyzed (2 x 500 mL, 12 hours, 3 hours) in the optimized sample buffer (0.2 mg/mL bovine serum albumin (BSA), 0.25 mM zinc chloride ($ZnCl_2$), 5 mM dithiothreitol (DTT), 50 mM HEPES, pH 7.4)[28] at 4 °C to give a final solution of SNB-1 *C*-His (25 mL, 1.1 mg/mL). The purified protein was incubated with 3 nM and 0.3 nM of each toxin at 37°C for 24 hours. Aliquots of each sample were combined with SDS-PAGE gel loading buffer, heated to 95 °C for 5 minutes, run on an 18% Criterion XGT (Bio-Rad) SDS PAGE gel, and electrophoretically transferred to a nitrocellulose filter for Western blotting using standard procedures. Blots were probed with Mouse anti-SNB-1 (DSHB, Ames, Iowa) in 1X milk diluent blocking buffer (KPL), washed and incubated with Goat anti-Mouse HRP (KPL). The blots were then developed using GE Amersham's Western Development Kit according to the manufacturer's instructions, and read on a Bio-Rad Gel Doc system.

2.7 *In vivo* toxin exposure

Synchronized *C. elegans* CZ333 worms were washed from their plates with liquid NGM and collected in a conical tube. The worms were then centrifuged at 1,300 x g for 1 minute, the majority of the liquid was removed and 80 µL of the remaining concentrated material was pipetted into a 96 well plate. After counting and diluting, roughly 20 to 40 worms were aliquoted into 5 wells and incubated with trisialoganglioside GT_{1b} for 5 hours. After incubation, the worms were exposed to BotNT A by adding 0.25 µM, 0.5 µM, 1 µM, and 2 µM concentrations of each toxin to a well containing the synchronized *C. elegans* CZ333. Each of these wells was surrounded by wells of water in order to prevent drying of the experimental wells, and incubated at 37 °C for 72 hours. Samples were then plated onto NGM plates containing 1 mM aldicarb and incubated at room temperature for 1 hour. Movement of worms was assessed by probing them with a platinum wire, using standard procedures.

3. RESULTS

3.1 Purified expressed proteins

Both of the recombinant homologous *C. elegans* proteins, Ric4B and SNB-1, were produced and purified for this study (Figure 3). There was sufficient protein in the soluble portion of the productions to allow for purification of these proteins. Each protein was analyzed with the Bio-Rad Experion, and Ric4B was found to be 90% pure (Figure 3A) and SNB-1 was 10% pure (Figure 3B).

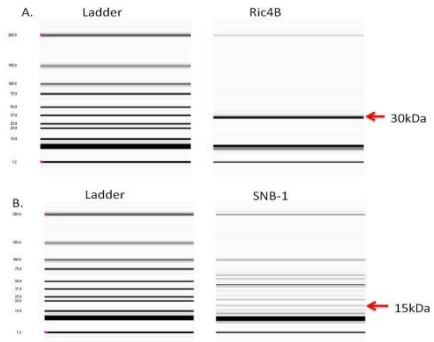

Figure 3. Experion gel of expressed and purified proteins. Purified Ric4B gel indicates that the defined band is at the expected molecular weight (MW) of 30 kDa (A), and that the band comprises 90% of the sample. Purified SNB-1 gel indicates there is a band at the expected MW of 15 kDa (B), but that it comprises 10% of the sample.

3.2 *In vitro* toxin exposure

Since the purified recombinant Ric4B was a relatively pure protein, it was selected for determination of cleavage by BotNT complex A. The MW of one of the proteins in the toxin complex is close to the MW of Ric4B; however, as seen in Figure 4, a shift in the band is visible; which indicates that cleavage of Ric4B does occur.

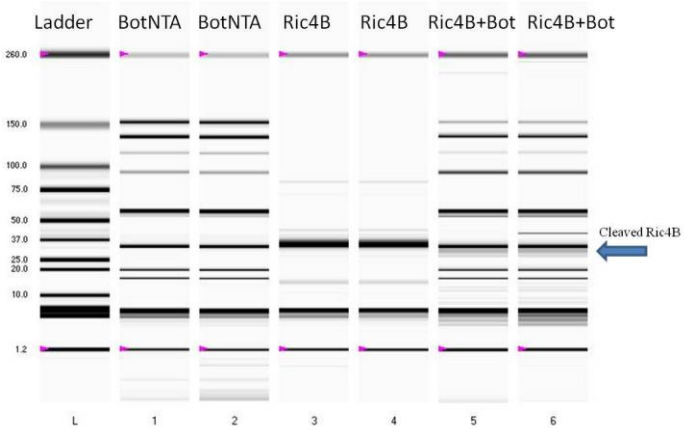

Figure 4. Experion gel of Ric4B exposed to BotNT complex A. Lane L contains the ladder, lanes 1-4 are the protein controls, and lanes 5 and 6 are the Ric4B incubated with BotNT complex A.

In order to test SNB-1 for cleavage, larger quantities of pure protein were produced (Figure 5).

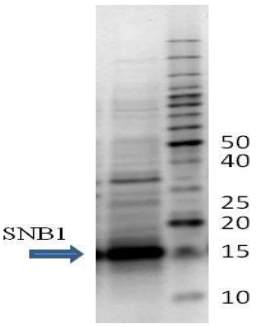

Figure 5. SDS-PAGE (4-12%) gel of FPLC (HisTrap, 1 mL column) purified SNB-1 *C*-His protein.

Testing has begun to determine cleavage of this protein (data not shown), and the results are currently inconclusive.

3.3 *In vivo* toxin exposure

Using *C. elegans*, probing for SNB-1 with the monoclonal antibody produced the brightest band when samples were extracted with immersion sonication (data not shown). Preliminary testing was performed to determine the effects of *C. elegans* exposure to BotNT. Observation of the worms after exposure produced inconclusive results.

4. CONCLUSION

This study was designed to determine the efficacy of using *C. elegans* as an *in vivo* model for studying BotNT exposure. Previous studies have shown that exposing the nematode *C. elegans* to various drugs produces electrophysiologically comparable results to vertebrate neurons.[21] There are a number of human stress responses that have been conserved in *C. elegans*,[21] and there have also been studies that indicate synaptobrevin (*snb-1*) is expressed in the *C. elegans* nervous system.[25] Furthermore, there is a large body of work supporting the measuring of SNAP-25 cleavage as an indicator of BotNT activity.[29-33] Although functional assays such as the neurotransmitter release assay could also be used, SNAP-25 cleavage is the most time efficient and sensitive assay for inhibitor screenings.[9] With the aim to utilize this cleavage, the present investigation was designed to determine if the homologous *C. elegans* proteins react similarly to SNAP-25 in the presence of BotNT. We have shown that BotNT does cleave the *C. elegans* Ric4B protein, and are working to determine if BotNT produces a measurable effect on the worms. Future studies are underway to determine optimal worm exposure parameters, such as ganglioside and toxin concentrations, incubation times and temperatures, and collection and scoring methods.

ACKNOWLEDGEMENTS

The authors would like to acknowledge U.S. Army funding provided through the Edgewood Chemical Biological Center's In-House Laboratory Independent Research and Surface Science Initiative programs.

REFERENCES

[1] Rotz, L.D., *et al.*, "Public health assessment of potential biological terrorism agents", *Emerging Infectious Diseases*. **2002**. 8(2), p225-230.

[2] Arnon, S.S., *et al.*, "Botulinum toxin as a biological weapon, medical and public health management", *The Journal of the American Medicical Association*. **2001**. 285(8), p1059-1070.

[3] Wein, L.M. and Liu, Y., "Analyzing a bioterror attack on the food supply, the case of botulinum toxin in milk", *Proceedings of the National Academy of Science U S A*. **2005**. 102(28), p9984-9989.

[4] Arimitsu, H., *et al.*, "Purification of fully activated Clostridium botulinum serotype B toxin for treatment of patients with dystonia", *Infection and Immunity*. **2003**. 71(3), p1599-1603.

[5] Atassi, M.Z., *et al.*, "Molecular recognition of botulinum neurotoxin B heavy chain by human antibodies from cervical dystonia patients that develop immunoresistance to toxin treatment", *Molecular Immunology*. **2008**. 45(15), p3878-3888.

[6] Brin, M.F., "Basic and clinical aspects of BOTOX", *Toxicon*. **2009**. 54(5), p676-682.

[7] Arnon, S.S., *et al.*, "Human botulism immune globulin for the treatment of infant botulism", *New England Journal of Medicine*. **2006**. 354(5), p462-471.

[8] Black, R.E. and Gunn, R.A., "Hypersensitivity reactions associated with botulinal antitoxin", *American Journal of Medicine*. **1980**. 69(4), p567-570.

[9] Kiris, E., *et al.*, "Embryonic stem cell-derived motoneurons provide a highly sensitive cell culture model for botulinum neurotoxin studies, with implications for high-throughput drug discovery", *Stem Cell Research*. **2011**. 6(3), p195-205.

[10] Lee Jhong-O, J.R.; Tzipori, S.; and Park, J-B., "M17 human neuroblastoma cell as a cell model for investigation of Botulinum Neurotoxin A activity and evaluation of BotNT/A specific antibody", *The Botulinum Journal*. **2008**. 1(1), p135-152.

[11] Smith, T.J., *et al.*, "Analysis of the neurotoxin complex genes in Clostridium botulinum A1-A4 and B1 strains, BoNT/A3, /Ba4 and /B1 clusters are located within plasmids", *PLOS ONE*. **2007**. 2(12), e1271.

[12] Baldwin, M.R., *et al.*, "Subunit vaccine against the seven serotypes of botulism", *Infection and Immunity*. **2008**. 76(3), p1314-1318.

[13] Barr, J.R., *et al.*, "Botulinum neurotoxin detection and differentiation by mass spectrometry", *Emerging Infectious Diseases*. **2005**. 11(10), p1578-1583.

[14] Evans, E.R.; Skipper, P.J.; and Shone, C.C., "An assay for botulinum toxin types A, B and F that requires both functional binding and catalytic activities within the neurotoxin", *Journal of Applied Microbiology*. **2009**. 107(4), p1384-1391.

[15] Montecucco, C. and Schiavo, G., "Mechanism of action of tetanus and botulinum neurotoxins", *Molecular Microbiology*. **1994**. 13(1), p1-8.

[16] Baldwin, M.R., *et al.*, "Characterization of the antibody response to the receptor binding domain of botulinum neurotoxin serotypes A and E", *Infection and Immunity*. **2005**. 73(10), p6998-7005.

[17] Adekar, S.P., *et al.*, "Neutralization of botulinum neurotoxin by a human monoclonal antibody specific for the catalytic light chain", *PLOS ONE*. **2008**. 3(8), e3023.

[18] Schiavo, G., *et al.*, "Botulinum neurotoxins serotypes A and E cleave SNAP-25 at distinct COOH-terminal peptide bonds. *FEBS Letters*. **1993**. 335(1), p99-103.

[19] Cheng, L.W., *et al.*, "Antibody protection against botulinum neurotoxin intoxication in mice", *Infection and Immunity*. **2009**. 77(10), p4305-4313.

[20] Kalb, S.R., *et al.*, "Extraction and inhibition of enzymatic activity of botulinum neurotoxins/A1, /A2, and /A3 by a panel of monoclonal anti-BoNT/A antibodies", *PLOS ONE*. **2009**. 4(4), e5355.

[21] Leung, M.C., *et al.*, "Caenorhabditis elegans, an emerging model in biomedical and environmental toxicology", *Toxicological Sciences*. **2008**. 106(1), p5-28.

[22] Nass, R. and Hamza, I., "The nematode C. elegans as an animal model to explore toxicology in vivo, solid and axenic growth culture conditions and compound exposure parameters", *Current Protocols in Toxicology*. **2007**. Chapter 1, Unit1.9.

[23] Kaletta, T. and Hengartner, M.O., "Finding function in novel targets, C. elegans as a model organism", *Nature Reviews Drug Discovery*. **2006**. 5(5), p387-398.

[24] Saifee, O.; Wei, L.; and Nonet, M.L., "The Caenorhabditis elegans unc-64 locus encodes a syntaxin that interacts genetically with synaptobrevin", *Molecular Biology of the Cell*. **1998**. 9(6), p1235-1252.

[25] Nonet, M.L., *et al.*, "Synaptic transmission deficits in Caenorhabditis elegans synaptobrevin mutants", *The Journal of Neuroscience*. **1998**. 18(1), p70-80.

[26] Eisenmann, D.M. WormBook. The *C. elegans* Research Community WormBook. **2005**; Available from, www.wormbook.org.[Accessed 3 March 2013].

[27] Sivashanmugam, A., *et al.*, "Practical protocols for production of very high yields of recombinant proteins using Escherichia coli", *Protein Science*. **2009**. 18(5), p936-948.
[28] Mizanur, R.M.; Stafford, R.G.; and Ahmed, S.A., "Cleavage of SNAP25 and its shorter versions by the protease domain of serotype A botulinum neurotoxin", *PLOS ONE*. **2014**. 9(4), e95188.
[29] Apland, J.P.; Adler, M.; and Oyler, G.A., "Inhibition of neurotransmitter release by peptides that mimic the N-terminal domain of SNAP-25", *Journal of Protein Chemistry*. **2003**. 22(2), p147-153.
[30] Apland, J.P., *et al.*, "Peptides that mimic the carboxy-terminal domain of SNAP-25 block acetylcholine release at an Aplysia synapse", *Journal of Applied Toxicology*. **1999**. 19(Suppl 1), pS23-S26.
[31] Ferrer-Montiel, A.V., *et al.*, "The 26-mer peptide released from SNAP-25 cleavage by botulinum neurotoxin E inhibits vesicle docking", *FEBS Letters*. **1998**. 435(1), p84-88.
[32] Binz, T., *et al.*, "Proteolysis of SNAP-25 by types E and A botulinal neurotoxins", *The Journal of Biological Chemistry*. **1994**. 269(3), p1617-1620.
[33] Blasi, J., *et al.*, "Botulinum neurotoxin A selectively cleaves the synaptic protein SNAP-25", *Nature*. **1993**. 365(6442), p160-163.

APPROVED FOR PUBLIC RELEASE

The persistence of microbial memory: an exploration of the potential of bacteria as an information storage medium

Matthew W. Lux*[a], Sarah Katoski[a], Michael Kim[a], Frank J. Kragl[a], James Myslinski[a]
[a]U.S. Army Edgewood Chemical Biological Center, Research & Technology Directorate,
5183 Blackhawk Rd, Aberdeen Proving Ground, MD 21010

ABSTRACT

The ability of deoxyribonucleic acid (DNA) to store immense amounts of information in a tiny space is remarkable; meanwhile, the cost to read and write DNA is plummeting. As such, the notion of DNA as a viable data storage material has recently emerged. Existing efforts have focused on *in vitro* DNA for storage; here, we investigate storing data in living bacteria cells. In addition to demonstrating data storage in bacteria, we use the system to assess two fundamental scientific questions regarding "non-functional" DNA: (a) the relative mutation rate of non-functional data-storing DNA versus genomic DNA, and (b) the stability of a mixed population of functionally identical but genetically different strains. We first implement an encoding strategy robust to the types of errors expected in living cells, namely mutations, insertions, deletions, and recombinations. We use this algorithm to encode into DNA a 3D-printable model of the Death Star. We also perform preliminary work to assess our experimental system for accumulating mutations in a population in a continuous flow environment. Future work will assess our ability to recover the data in the face of actual mutation accumulation by testing data-containing strains in our experimental system, the relative error rates, and stability of mixed populations.

Keywords: DNA storage, synthetic biology, mutation rates

1. INTRODUCTION

1.1 DNA as a storage medium

With the recent costs of synthesis and sequencing of DNA plummeting, the notion of storing data in DNA has become of interest and was demonstrated by two studies storing a significant amount of digital data in *in vitro* DNA.[1,2] The incredible density of information per volume and the natural stability of DNA offer a potential solution to the enormity of today's data storage needs. The obvious shortfalls are very slow read/write times and destructive reads, which target the emerging technology toward archival storage applications. Indeed, at the current stage of development and price-point, it is estimated that DNA can already compete with existing technology in the most extreme cases where access is roughly once per 10 years.[1]

In this work, we investigate the use of bacteria as a host to store DNA encoded with digital information. Working *in vivo* offers several advantages and disadvantages. In practical archival storage applications, storing in bacteria offers the ability to rapidly reproduce data for redundancy or to circumvent destructive read issues, but at the cost of higher storage demands, higher error rates, and lower density. Beyond archival storage, storage in bacteria allows the data to survive in natural environments. Applications include covert transmission of information and embedding source information into engineered or biothreat organisms for attribution of potential downstream releases.

1.2 Mutation rate of non-functional DNA

Computing the *in vivo* mutation rate of organisms has long been an area of research.[3-6] One of the complicating factors in studying mutation rates is the inherent functional bias, whereby impacts on the fitness resulting from a mutation influence the prevalence of that mutation in a population. As it is impossible to assess the impact on function of an individual base pair *a priori*, genomes are far too large to test exhaustively, and many "functions" may only present themselves under certain conditions, it is impossible to label any individual base pair as "non-functional". Moreover, the definition of "function" is hotly contested.[7] The insertion of large amounts of synthetic data-storing DNA into bacteria offers an opportunity to address this issue from a different angle by making the assumption that this data-storing DNA will be "random" and have no function. Of course, function can occur by chance, thereby undermining the assumption; however, the odds of significant function occurring by chance are low and can be made lower by scanning the DNA bioinformatically for predicted function. At the least, assessing the mutation rate of data-storing DNA should provide a reasonable estimate for *in vivo* DNA replication errors that is less influenced by functional bias than is genomic DNA. This baseline estimate of *in vivo* rates has uses in understanding natural evolution, predicting the stability of information encoded into living organisms, and as a baseline rate for mutation of functional DNA.

APPROVED FOR PUBLIC RELEASE

1.3 Competition between functionally identical strains

The roles of microbial communities in health and environmental concerns have been rapidly emerging.[8-10] Understanding how the genetic makeup of these populations and their interactions impact outcomes is a daunting task. Complex competition and cooperation between species and subspecies, in both time and space, makes the work especially challenging. Indeed, even isogenic strains have been shown to produce variable population structures.[11] Here, by splitting data among multiple strains and growing them together, we are naturally able to ask questions about the stability of mixed populations of functionally equivalent but genetically diverse strains over time.

2. METHODS

2.1 Software and 3D-printing

All described software is written in Matlab (The MathWorks, Inc.). Reed-Solomon (RS) encoding/decoding used built-in Matlab functions. *In silico* simulations leveraged infrastructure housed at the U.S. Army Research Laboratory as part of the Department of Defense Supercomputing Resource Center. Multi-file compression is performed by the unix zip utility. Hex-dumps are performed by the unix xxd utility.

We created the 3D model using ZEdit software and saved the file in .zpr format. The model was printed using ZPrint software and a Solidworks 3D-printer. File compression was done with the open-source utility 7-zip, set to the highest compression setting.

2.2 DNA synthesis, assembly, and cloning

DNA blocks are manufactured as gBlocks from IDT, and all primers are produced by IDT. The Gibson Assembly Kit is provided by NEB. Polymerase chain reaction (PCR) amplification is performed using GQ5 High-fidelity PCR Master Mix (NEB).

Primers are automatically generated using custom software written in Matlab (The MathWorks, Inc.). With a user-defined target melting temperature and maximum primer length, the software generates primer sets for each block such that all amplifications can be performed simultaneously. The software also allows the user to flag blocks that were modified to pass repetitiveness scans (see above) such that the additional sequences are ignored.

The BAC vector used is CopyRight v2.0 pEZ BAC (Lucigen). Hosts are DH5α, CopyRight-optimized competent cells (Lucigen) and XL-1 Red mutator cells (Agilent Technologies).

2.3 Batch and continuous flow cultures

Batch culture experiments are in a 20 L reactor containing Luria-Bertani (LB) medium and appropriate antibiotics. Continuous flow experiments are also performed in a 20 L reactor with a flow rate that adjusted by experiment. For the 20 L batch culture, cells were grown overnight, added to the reactor, and samples taken at t=0 and t=6.7 hours after inoculation. For the 250 mL flask culture, cells were grown overnight in 50 mL conical tubes, 1 mL of each mixed into 50 mL of fresh LB, and grown overnight.

3. RESULTS

3.1 Encoding/decoding strategy

3.1.1 Encoding

The first step in using bacteria as a data storage medium is to encode the information into a string of virtual DNA base pairs. In contrast to *in vitro* efforts[1,2] where synthesis and sequencing errors are the only significant source of errors, challenges to information stability are potentially very high in cells and error correcting methods are crucial. Error handling is a field rich in digital design and communications, providing many tools ripe for adaptation. A noticeable difference, however, is that unlike digital applications where the runtime of the encoder/decoder is typically of critical importance, we are effectively unconstrained by runtime because the time spent in the bacteria is the rate-limiting step of the communication channel. We use a modular, multilayer approach to maximize our chances of recovering the data. Our architecture is designed such that by adjusting input parameters for the encoding algorithm, the system can be tuned to be robust to different error rates for different error types, such as point mutations, insertions, etc. We use *in silico* simulations based on our experimental set up to select values that should be robust to expected *in vivo* error rates.

APPROVED FOR PUBLIC RELEASE

3.1.1.1 Data blocks

The primary functional unit in our strategy is designated as a "block" of length *b* and is divided into three subsections: the address (length *a*), the data (length *d*), and the error-correcting code (ECC) (length *e*). The address determines the location of the data contained in the block in relation to all other blocks. The ECC enables recovery of both the data and address subsections in the face of mutations anywhere in the block. The ECC uses Reed-Solomon (RS) encoding, which breaks up a message sequence into *k* symbols of *m* bits and adds additional symbols to create a codeword of length *n* symbols such that a corresponding decoder is capable of correcting *t* symbols and detecting *2*t* symbol errors. Here, we set *b=m*n* such that each block is one codeword. RS encoders are constrained by two inequalities:

$$t \leq \frac{n-k}{2} \tag{1}$$

and

$$n \leq 2^m - 1 \tag{2}$$

By choosing values for *b*, *m*, and *t*, these constraints result in an ECC length of *e=2t*m*. By additionally choosing a value of *a*, the data length can be computed as *d=b-a-2t*m.* See Table 2 for the values selected in this work.

To encode a set of arbitrary data, the algorithm is pointed to a folder, which it compresses into a single file. The resulting file is then hex-dumped, and the hex sequence converted to binary. Using the value of *d* an arbitrary binary sequence can be divided into appropriate sized blocks. Incrementally increasing binary addresses are then appended to the front of each block, and the address plus data sequence is passed through an RS encoder to create a full block with ECC appended to the end. Since the total amount of data is unlikely to be divisible by *d*, the leftover data is padded by a single 1 followed by enough 0's to make a full-sized block. These blocks of binary sequence are then converted to a DNA sequence as shown in Table 1.

Table 1. Conversion table between binary and base pairs.

Binary	00	01	10	11
Base Pair	A	T	C	G

3.1.1.2 Data drives and RAID

Blocks are subsequently arranged into larger units called "drives". Each drive represents an individual bacterial strain containing encoded data. Each drive contains a sequence of blocks separated by stop codons. The stop codons serve two purposes: (1) to provide a marker for the decoding algorithm to separate blocks, and (2) to help reduce the probability of random functionality arising from the encoded DNA. The blocks are arranged across drives by striping in a RAID 6 implementation. The outcome of this RAID 6 approach is that two additional drives are added to the pool, the blocks are spread amongst the drives, and the overall system becomes tolerant to the complete or partial loss of up to two full drives. This approach protects against the situation where one or two strains lose large chunks of data through recombination or otherwise, or disappear from the population entirely.

Generation of the RAID drives uses the same RS theory described above. Here, however, the message sequence is the symbol from each data drive in a given position, and thus has length $D=k_{RAID}$ equal to the number of data drives. Unlike in the ECC case, when data is missing during RAID recovery the position of missing data is known. In this special case, RS decoders can recover these "erasures" at double the rate of the case where the position is unknown, allowing recovery of up to $T=t_{RAID}$ symbols, where $t_{RAID}=n_{RAID}-k_{RAID}$, $n_{RAID}=D+R$, and *R* is the total number of RAID drives. See Table 2 for our choice of these parameters in this work.

Table 2. Values used for various encoding parameters.

Block Parameters			*Drive Parameters*		
Total Block Size	*b*	2000 bits	# of Data Drives	*D*	8 drives
Address Size	*a*	10 bits	# of RAID Drives	*R*	2 drives
ECC Symbol Length	*m*	10 bits	RAID Codeword Length	*M*	10 bits
Correctable Symbols per Codeword	*t*	4 symbols	Correctable Drives per Stripe	*T*	2 symbols

To generate RAID drives, data drives are first divided such that the block in each position across drives is in the same group, called a stripe. For each symbol position of each stripe, a RAID RS encoder is used to generate symbols to recover from errors within stripes. However, this process is only applied for address and data symbol positions. For the ECC positions, the ECC RS is applied to the generated RAID data to complete the RAID block. This approach allows for recovery from point mutations before applying RAID. At this stage, the data is fully encoded into DNA blocks and assembled into drives.

3.1.2 Synthesis keys

An additional consideration in encoding the data into DNA is the ability to actually synthesize the DNA. *In vitro* efforts have used large pools of DNA oligos, which simplifies synthesis significantly compared to the much larger assembled DNA molecules required here. For oligo synthesis, the only barrier to high fidelity synthesis is that error rates increase significantly with length for homopolymer runs. Thus, previous efforts have used encoding strategies that preclude homopolyer runs completely. In this work, we use newly available commercial services to order DNA in one kilobase pair (kbp) chunks, exactly the size of the data blocks. These chunks are produced commercially by synthesizing overlapping oligos that can be assembled directly into the desired chunk. However, this process enforces rules on the sequence of the chunk to prevent complications in the assembly process, most notably rules limiting receptiveness. By encoding the DNA to preclude homopolymer repeats, the odds of a block passing the repetition screens drops dramatically. Therefore, in this work we do not enforce any homopolymer restrictions.

Even without homopolymer restrictions, blocks can be rejected for repetition. This repetition can occur by random chance or because the actual binary data is low complexity; indeed, the use of padding of the final block can introduce long stretches of low complexity. To avoid this issue, we use an encryption key to perturb the sequence in a reversible way. The encryption breaks the sequence into W words of size w base pairs, then perturbs each word by a randomly generated key value, k, where $0<k<4^w$. The perturbation occurs by converting the word back to binary (see Table 1) and adding the binary of the current key value (disregarding any carry) to create a new word. The same set of K key values, where $K=W/w$, is applied to all blocks. In this way, by passing the key along to the decoder, the process can be reversed and the original block sequence recovered. Here, we use w=4.

The encryption key method does not, however, guarantee that a block will pass the repetition screen because even randomly generated sequences will fail with some probability. For the special case of repetitive sequences occurring on the block ends, two randomly generated eight base pair (bp) sequences that do not occur in the block in forward or reverse can be generated and appended to each end. Such blocks are noted for special processing later. Otherwise, if a set of drives contains blocks that still fail the repetition screens after encryption, a new random encryption key can be generated and applied and the blocks rescreened. Thus, by looping until a successful key is found, the repetition screens can be passed without modifying the encoding process.

3.1.3 Simulated passaging

In order to assess the efficacy of our encoding strategy *in silico* beforehand, we created software that simulates cells evolving in a continuous-flow environment. In a continuous-flow reactor, cells flow out of the reactor at a rate equal to their growth rate. Though in reality the population is asynchronous, this can be modeled by taking a population, duplicating it, and then randomly removing half of the individuals from the new double-sized population. By introducing errors in the duplication process based on literature values, we can assess the likely mutation accumulation in a population based on realistic experimental conditions. The values in Table 2 were informed by this analysis.

3.1.4 Encoded contents

We used the above described algorithm to encode a 3D-printable model file of a “Death Star” (see Methods). The model file was compressed to the smallest size possible and then zipped together with a readme file. This file was then used as input to the encoding algorithm, resulting in 364 blocks spread across 10 drives totaling 364,000 base pairs. The final file

APPROVED FOR PUBLIC RELEASE

size was 63 kB, yielding ~1.4 bits/bp or ~70% encoding efficiency. The encoding efficiency is highly dependent on the choice of encoding parameters.

3.1.5 Decoding

The decoding algorithm is essentially the inverse of the encoding procedure. Assembled contigs from sequencing data are treated as drives and scanned for stop codons spaced by the size of the blocks. In cases where an expected stop codon is not found, the scan looks +/- 5 bps from the expected location and also checks for single base pair mutations from the expected stop codon. Based on these stop codons, potential blocks are passed through the ECC Reed-Solomon decoder to check for errors. Blocks that have too many errors for correction are flagged; blocks that are successfully decoded are arranged by their respective address value. Based on which blocks are present or absent, RAID is applied to recover any missing blocks as necessary. For example, if only a RAID block is missing from a stripe, that block is not recovered as the data for that stripe is already present. If any data blocks cannot be recovered by RAID, the algorithm reports a failure. Otherwise, the algorithm assembles the data blocks into a single sequence, converts the sequence to a file, and unzips the file.

3.2 Drive synthesis

3.2.1 Assembling blocks into drives

The individual blocks are assembled by PCR-amplifying each block with specially designed primers that contain overhangs complementary to the sequence of the neighboring block (see Methods). These products can then be rapidly assembled using Gibson Assembly[12] (see Methods). We are currently awaiting delivery of the first set of these blocks.

3.2.2 Barcodes

The use of multiple data drives allows us to ask fundamental questions about functionally equivalent but genetically different strains. While the mutation rates will be assessed by next-generation sequencing of samples of growing cultures, this data is only roughly able to approximate the relative quantities of the DNA in a sample. A more quantitative approach is the use of quantitative real-time polymerase chain reaction (qPCR), which with properly designed assays is capable of giving relatively accurate estimates of the number of copies of a specific DNA sequence present in a sample. Rather than designing new assays for each drive, we repurposed computationally designed and experimentally verified genetic barcode sequences that can be added to the drive (data not yet published). Using these barcodes, we can quickly assess the relative abundance of each drive in a growing population.

3.2.3 Inserting data into cells

The assembled blocks are inserted into a bacterial artificial chromosome (BAC) using Gibson Assembly, and transformed into *Escherichia coli*. Three strains are used: the commonly used DH5α, a BAC-optimized strain called CopyRight, and a mutator strain deficient in a proof-reading enzyme called XL-Red. See Methods for more detail.

3.3 Passaging of strains

3.3.1 Mutation accumulation experiments

In order to test the ability of the algorithm to recover data in the face of *in vivo* mutations and analyze the mutation rates of non-functional DNA, experimental accumulation of mutations is necessary. To accomplish this, we are processing mixed cultures of cells in a continuous-flow reactor. Over time, samples are collected for next-generation sequencing and mutational analysis. More frequently, samples are taken for qPCR analysis to assess the stability of the population.

We have established growth rates of control strains in fermentor conditions to inform continuous-flow reactor settings. Trial runs of the continuous-flow set up are in progress.

3.3.2 Preliminary stability assessment of mixed cultures

We have tested mixed populations of cells containing 10 different genetic barcodes. The tests were performed under two experimental conditions: a 20 L batch culture and a 250 mL flask (see Methods). Table 3 summarizes the results. Interestingly, the relative proportions of each barcode were not particularly stable. These results suggest that either (a) the barcode sequence confers some unexpected impact on fitness, or (b) that competition between phenotypically identical cells is significantly impacted by noise. Further tests to assess the reproducibility of the success or lack thereof of each barcode in this experimental design, as well as testing a strain containing no barcode, should resolve the source of the change in relative proportion; additionally, these experiments will inform the predicted stability of our encoded data and address the fundamental question of the stability of phenotypically identical but genetically diverse populations.

APPROVED FOR PUBLIC RELEASE

Table 3. Stability of mixed population.

	% of Total Population			
	20 L Batch Culture, not normalized		250 mL Flask Culture, normalized	
Barcode	**0 hours**	**6.7 hours**	**0 hours**	**16 hours**
1	7.07%	17.87%	10%	9.86%
2	6.69%	4.89%	10%	6.06%
3	9.38%	6.22%	10%	7.63%
4	nd*	nd*	nd*	nd*
5	14.60%	9.99%	10%	13.46%
6	n/a**	n/a**	n/a**	n/a**
7	20.33%	31.50%	10%	17.69%
8	n/a**	n/a**	n/a**	n/a**
9	10.83%	7.94%	10%	11.38%
10	9.51%	5.61%	10%	8.88%
11	11.24%	8.46%	10%	15.12%
12	10.35%	7.52%	10%	9.93%

*Barcode 4 assays failed for unknown reason, returning no data.
**Barcodes 6 and 8 from the original set of 12 were not used here for poor performance reasons.

3.4 Mutation rate analysis

Samples will be sequenced using next-generation sequencing to achieve high read coverage. Mutation rates will be assessed using a Bayesian approximation method that leverages the distribution of read coverage at each individual base pair. This approach will allow estimation of overall mutation rates and comparison of rates for non-functional and genomic DNA, and leverages the information present in read-variability that is typically lost by building consensus sequences.[13]

4. DISCUSSION

At this stage, results are too preliminary to justify significant discussion. A custom encoding strategy has been developed and rigorously tested *in silico* and experimental validation is underway. Preliminary tests of mixed cultures of phenotypically identical strains some instability, but it remains unclear if that instability is due to fitness consequences of genetic tags, stochastic competition, or an artifact resulting from sampling or assay error. Further, it remains unclear if the instability will exist in continuous flow culture or for strains carrying large amounts of encoded DNA. These questions, along with questions involving mutation rates and data recovery capacity, remain to be explored with further work.

5. CONCLUSIONS

The preliminary nature of this work precludes significant conclusions. Impending results will begin to shed light on the key questions explored by this project.

ACKNOWLEDGEMENTS

The authors would like to acknowledge U.S. Army funding provided through the Edgewood Chemical Biological Center's In-House Laboratory Independent Research and Surface Science Initiative programs.

REFERENCES

[1] Goldman, N., *et al.*, "Towards practical, high-capacity, low-maintenance information storage in synthesized DNA", *Nature*. **2013**. 494(7435), p77-80.

[2] Church, G.M., *et al.*, "Next-Generation digital information storage in DNA", *Science*. **2012**. 337(6102), p1628.
[3] Lee, H., *et al.*, "Rate and molecular spectrum of spontaneous mutations in the bacterium Escherichia coli as determined by whole-genome sequencing", *Proceedings of the National Academy of Science*. **2012**. 109(41), pE2774-E27783.
[4] Drake, J., "Contrasting mutation rates from specific-locus and long-term mutation-accumulation procedures", *Genes Genomes Genetics.* **2012**. 2(4), p483-485.
[5] Ochman, H., "Neutral mutations and neutral substitutions in bacterial genomes", *Molecular Biology and Evolution*. **2003**. 20(12), p2091-2096.
[6] Wielgoss, S., *et al.*, "Mutation rate inferred from synonymous substitutions in a long-term evolution experiment with Escherichia coli", *Genes Genomes Genetics.* **2011**. 1(3), p183-186.
[7] Graur, D., *et al.*, "On the immortality of television sets: "function" in the human genome according to the evolution-free gospel of ENCODE", *Genome Biology and Evolution*. **2013**. 5. p578-590.
[8] Joscelyn, J. and Kasper, L., "Digesting the emerging role for the gut microbiome in central nervous system demyelination", *Multiple Sclerosis Journal*. **2014**. 20(12). p1553-1559.
[9] Bultman, S., "Emerging roles of the microbiome in cancer", *Carcinogenesis.* **2014**. 23(2), p249-255.
[10] Sandek, A., *et al.* "The emerging role of the gut in chronic heart failure", *Current Opinion in Clinical Nutrition and Metabolic Care*. **2008**. 11(5), p632-639.
[11] Coward, C., *et al.*, "Competing isogenic Campylobacter strains exhibit variable population structures in vivo", *Applied Environmental Microbiology*. **2014**. 80(21), p3857-3867.
[12] Gibson, D., *et al*, "Enzymatic assembly of DNA molecules up to several hundred kilobases", *Nature Methods*. **2009**. 6(5), p343-345.
[13] Schuh, A., *et al,* "Monitoring chronic lymphocytic leukemia progression by whole genome sequencing reveals heterogeneous clonal evolution patterns", *Blood.* **2012**. 120(20), p4191-4196.

Microbial wargaming: modeling the contributions to fitness of bacteria encoding deployable genetic weaponry

Aleksandr Miklos[a,b], Matthew Lux[a], Vanessa Funk[a], Steven Yee[a,c], Henry S. Gibbons[a]
[a]U.S. Army Edgewood Chemical Biological Center, Research and Technology Directorate, 5183 Blackhawk Rd, Aberdeen Proving Ground, MD 21010
[b]Excet, Inc., 8001 Braddock Rd, Suite 303, Springfield, VA 22151
[c]Defense Threat Reduction Agency, 8725 John J. Kingman Rd, Fort Belvoir, VA 22060

ABSTRACT

Basic biological research seeks to understand the workings of observable biological phenomena, and to recapitulate those phenomena under controlled conditions in which variables can be individually tested to understand the underlying rules of behavior. While this reductionist, experimentally driven approach can easily be applied to single organisms, the application of such approaches to complex behaviors of social organisms, such as warfare or terrorism in human societies, is not possible. Recent advancement in synthetic biology tools has enabled the modeling of simple *in vitro* systems of complex community dynamics. Here, we develop a simple *in vitro* model system for inter-community warfare using bacterial strains equipped with antibacterial colicin and/or phage weapons, and test carriage to determine how deployment of weapons affects strain fitness in model ecosystems. The use of the concepts of synthetic biology, namely the treatment of genes, promoters, and regulatory systems as interchangeable parts, will facilitate the construction of defined strains containing cryptic weapons systems that can be developed and employed with a range of experimentally tunable frequencies of development or deployment. We will therefore be able to test defined hypotheses regarding the emergence of warfare in a simple and infinitely permutable model system.

Keywords: Colicin, competition, evolution, synthetic biology, niche maintenance, competitive exclusion

1. BACKGROUND

To date it has not been possible to test in a controlled manner what factors lead to the evolution of intraspecies aggression, nor have the effects of such abilities on the development or maintenance of communities been thoroughly explored. We propose a novel approach to studying the emergence of warfare in large populations – a petri-plate based wargaming system in which opposing bacterial communities are equipped with weapons existing in either a fully evolved state or in a cryptic, resting state awaiting development or deployment. Using this simple modeling system with defined and interchangeable genetic components, we hope to quantify the contribution to fitness of bacterial communities of model weapon systems.

1.1 Bacteria as models of social behavior

Recent research has revealed that bacteria, despite their relatively simple unicellular structure and small size, engage in a number of striking collective behaviors, including altruism, cooperation, restricted growth, and self-policing.[1-4] While bacterial communities can be observed to follow paths in which the whole community benefits from the actions of its individual parts, on the level of individual bacterial cells this is not always the case, and bacteria have been observed cheating,[5-7] that is to exploit the activity of the community without contributing to a common good, polluting,[7] and performing other individual deviant behaviors. Likewise, cooperative communities have been shown to evolve strategies to suppress cheater populations.[8] Together, these represent both collective survival strategies combined with bet-hedging strategies on the level that, in spite of the divergent and antisocial behavior of a small minority, benefits the species by ensuring maximal likelihood of survival should growth conditions rapidly become unfavorable.

1.2 Bacterial communities employ both offensive weaponry and defensive measures to take and hold territory

Bacteria have been engaging in competitive behaviors for billions of years, and have evolved highly diversified strategies to achieve superiority within a niche relative to their interspecies and intraspecies rivals. These include strategies that are analogous to human wartime behaviors, and include offensive, defensive, counteroffensive, intelligence, and counterintelligence strategies. Offensive strategies include the synthesis of antibacterial compounds (antibiotics, bacteriocins); defensive measures include modifications to cell walls and the acquisition of resistance cassettes or degradative enzymes; intelligence strategies include utilizing quorum-sensing signals from opposing communities to “read the enemy's mail,” and so forth. The diversity of methods employed in the microbial world suggests that these simple

APPROVED FOR PUBLIC RELEASE

organisms might serve as model systems for complex social human behaviors such as warfare (Table 1). Bacteriocins in particular have been shown to play roles in competitive exclusion ("taking and holding territory") against invading strains.[9]

1.3 A body of knowledge is readily exploitable to develop synthetic model systems

The signals driving communal behaviors are becoming better understood and are being employed as interchangeable tools for engineering complex social behaviors among microbial communities.[10,11] Communal behavior is driven by quorum-sensing mechanisms, which rely on secreted diffusible small molecules to monitor bacterial population density. Offensive weapons are often driven by population density, proximity (antibiotics can themselves be considered quorum sensing molecules), or contact with the enemy,[9] while defensive measures can be either pre-emptive (regulated based on the ambient environmental conditions rather than direct encounter), or triggered by encounter with an enemy's offensive weapons, or both.[12] The effector molecules and regulatory systems are well-characterized and can serve as model systems to study the deployment of tactical and strategic weaponry including weapons of mass destruction by individuals or states (Table 1). Interestingly, as with defense budgets for human societies, deployment of colicins and defensive measures incurs a significant energetic cost that must be carefully balanced with the evolutionary gains lest it become a fitness disadvantage.[13]

Table 1. Bacterial components as models for human weapons classes.

Class	Characteristics	Weapon	Model system	Costs to produce	Defense	Costs to defend
Strategic	Transmissible, mass casualty	Plague, smallpox	Cryptic lytic bacteriophage	Metabolic burden, host cell lysis	Target modification	Nutrient loss due to target function changes
Tactical	Non-contagious, diffusible	Anthrax, Chemicals, Artillery	**Bacteriocins (e.g., colicins), antibiotics**	Metabolic costs of production, efflux,	Outer membrane modification; target modification; degradation; immunity	Decreased permeability to nutrients; efflux effort
Individual	Single-victim, contact	Ricin	Contact-dependent inhibition toxins[14]		Target modification	Nutrient loss due to target function changes

Colicin protein toxins offer ideal platforms for the development of simple *in vitro* competition systems for Gram-negative bacteria. Broadly, colicins belong to a wide family of bacteriocidal proteins that are produced and secreted by bacteria. Cidal activities of bacteriocins can either exhibit broad or narrow host ranges depending on the nature of the toxin and can even in some cases suppress the growth of competitive eukaryota. Specifically, colicins are secreted by Enterobacteriaceae, notably *Escherichia coli* for which they are named. Most wild-type isolates of *E. coli* and almost all pathogenic *E. coli* strains encode at least one colicin module, suggesting prominent roles for these genetic elements in establishing and maintaining the presence of a given strain within an ecological niche.

In general, colicins target a specific protein localized in the outer membrane which facilitates entry and uptake into the host cell by means of one or more ABC transporters. Colicins are generally internalized by this process and then exhibit a toxic behavior toward the target strain.[15] Different colicins have different enzymatic or inhibitory functions, such as nuclease activity, the ability to depolarize membranes, or inhibition of peptidoglycan synthesis. Colicins are typically encoded as three-gene modules containing the colicin itself, an immunity protein, and a lysis protein. The immunity protein protects the host strain from the effects of the colicin while the lysis protein functions to break open expressing cells to discharge the colicin payload into the environment (Figure 1).

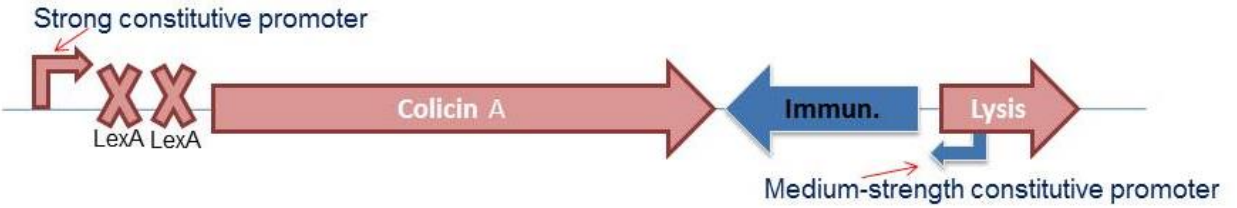

Figure 1. Colicin A locus showing colicin A, immunity, and lysis protein genes, LexA repressor binding sites, and promoters. The colicin itself is the toxic secreted product, the immunity protein protects the host population, while the lysis protein causes a sub subpopulation of the host strain to lyse, liberating the colicin proteins into the culture medium.

2. METHODS

2.1 Bacterial strains

E. coli W3110 (ATCC 27325), *E. coli* (ATCC 14763), *Pseudomonas aeruginosa* (ATCC 25360), and *P. aeruginosa* (ATCC 25360) were acquired from American Type Culture Collection (Manassas, VA). Colicin-producing *E. coli* strains BZB 1011, BZB 1030, BZB 1191, BZB 2101, BZB 2102, BZB 2103, BZB 2104, BZB 2125, BZB 2149, PAP 308, and PAP 702 (Table 1) were obtained from Institute Pasteur (Paris, France).

2.2 Strain fitness assay

Luria-Bertani (LB) broth (Sigma-Aldrich, St. Louis, MO) and Tryptic Soy (TS) broth (EMD Chemicals, Inc., Gibbstown, NJ) were prepared according to manufacturer's instructions. Non-swarming agar plates were prepared using either 1.5% bacto-agar (Sigma-Aldrich) in LB or TS broth. Swarming agar plates were prepared using 0.75% or 0.5% bacto agar, or 0.5% Eiken agar (Eiken Chemical Co., Ltd., Tokyo, Japan) in either LB or TS broth. Cultures were grown overnight from glycerol stocks in either LB or TS broth at 37 °C with shaking at 180 rpm (Innova 4200 Incubator Shaker; New Brunswick Scientific, Edison, NJ). Inocula were normalized to $OD_{600} < 0.1$ (Spectronic 21 Spectrophotometer; Milton Roy Company, Ivyland, PA) and plated on (swarming or non-swarming) agar plates using a sterile toothpick in a 1-to-1 competition style of some combination of pyocin-susceptible or pyocin-producer *P. aeruginosa* and/or colicin-susceptible or colicin-producer *E. coli.* These competition-style plates were quartered with the upper quadrants reserved for controls and the bottom quadrants reserved for a single inocula susceptible or producer strain surrounded by three inoculums of susceptible or producer strains. Plates were incubated at 37 °C in a humidified Innova 4200 for up to 21 days. Colony growth photographs were taken at various times using a Colony Q Count Automatic Colony Counter with Color Count (version 2.3) software (Spiral Biotech, Inc., Norwood, MA). Alternatively, time-lapse images were collated from plates incubated at 37 °C in an Innova 4330 (New Brunswick Scientific, Edison, NJ) and scanned hourly using an Epson Perfection V600 Photo Scanner (Seiko Epson; Longbeach, CA) with Rap-ID Software (Specific Technologies).

2.3 Colicin induction

Following normalization, inocula were heated in a water bath (Isotemp 215; Fisher Scientific International, Inc., Hampton, NH) at 37 °C for up to 1 hour and then plated on swarming agar plates and incubated as above.

2.4 Synthetic green fluorescent protein (GFP)-reporter construct

A sequence based on the Colicin A operon (Figure 1) was designed in which the *sfGFP* gene replaced the *colA* gene and was placed under a tetracycline-inducible promoter and synthesized (DNA2.0, Menlo Park, CA) in a low-copy expression vector. The plasmid was introduced into *E. coli* W3110 by standard transformation methods. Expression of *sfGFP* was monitored by fluorescence on agar plates (Figure 2).

We began development of a simple *in vitro* competition assay using a number of colicin-expressing strains obtained from the Institut Pasteur (Table 2). These strains, initially described by Pugsley and co-workers,[16] express a variety of colicins and are resistant to a number of colicins produced by other strains within the collection, making these an ideal set of initial tester strains for the development of simple competition scenarios.

APPROVED FOR PUBLIC RELEASE

Table 2. Colicin-producing strains utilized in this study.

CIP idx	Strain	PRODUCES	RESISTS	Mechanism	Receptor	Translocation
105643	BZB2101	colA	colA	Pore Forming	BtuB	OmpF/TolQRAB
105642	BZB2102	colB	colB	Pore Forming	FepA	?/TonB, ExbBD
105641	BZB2103	colD	colD	tRNase	FepA	?/TonB, ExbBD
105640	BZB2104	colE1	colE1	Pore Forming	BtuB	OmpF/TolQRAB
105644	BZB2125	colE2	colE2	DNase	BtuB	OmpF/TolQRAB
105646	BZB2149	colE3	colE3	16s rRNase	BtuB	OmpF/TolQRAB
105664	BZB1011	--	--			
105637	BZB1191	--	--			
105665	BZB1030	--	(A),(E1),E2,E3			
105669	PAP308	--	A,E2-8 tol.			
105671	PAP702	--	--			

2.5 *In vitro* competition assay

For this study, 0.5% agar plates were inoculated with spot cultures of each strain using a toothpick or inoculation loop such that a single colony of a "target" strain would be surrounded by three colonies of the producer strain.

3. RESULTS

To demonstrate that we could visualize colicin-mediated growth inhibition, we developed a simple growth assay on low-concentration agar plates that allow greater strain mobility on the plate surface. Colicin strains were plated in a spatial scheme noted in Figure 2 that was modified such that only two surrounding colonies were utilized instead of three. In this assay system, colicin-mediated growth inhibition manifests itself as the formation of smaller colonies at the centers of the triangular arrangements, or as distorted colony shapes in the colonies at the apices.

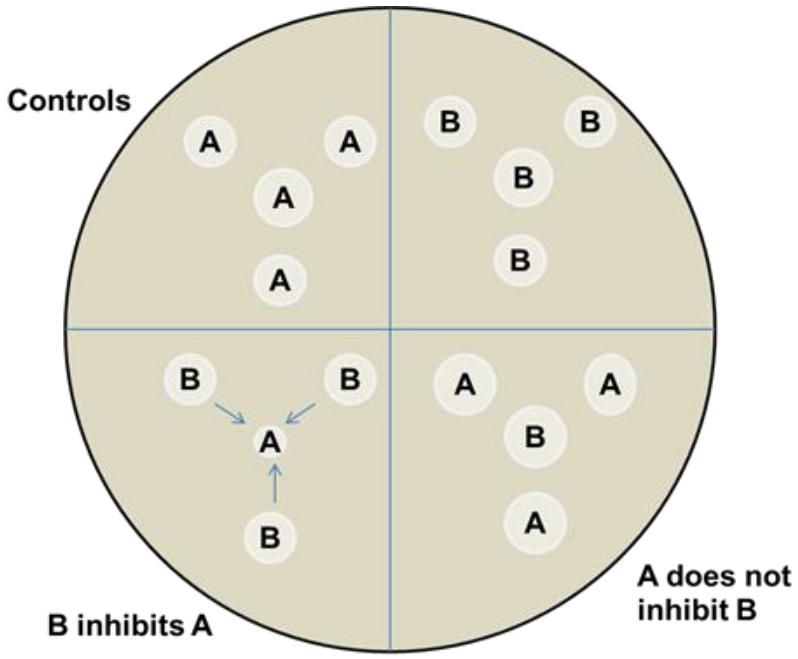

Figure 2. Colicin plate inhibition assay. Two strains A and B are plated in arrangements to allow the comparison of colony size. Growth inhibition manifests as a decrease in size of the central colony in one or both of the lower quadrants relative to the same strain in the upper quadrants. The top quadrants represent controls to insure that colony size difference of the middle colony are not due to autoinhibition.

We demonstrated growth inhibition at interfaces between colicin-producing and non-producing organisms (Figure 3). In this system, a tetracycline inducible promoter governs the expression of GFP in the non-producing strain, whereas the

colicin immunity gene remains under the control of the colony growth of the non-producing strain (green or partially green colonies), is inhibited by the producing strain, and appears as if the colony itself were being driven away by the producing strain. In addition, the colonies of the non-producing strain were not consistently labeled with GFP, which should be produced consistently given the presence of the inducer (anhydrotetracycline) in the medium. However, non-producing strains consistently produced high levels of GFP expression when plated next to or in between colonies of colicin A-expressing strains (Figure 3).

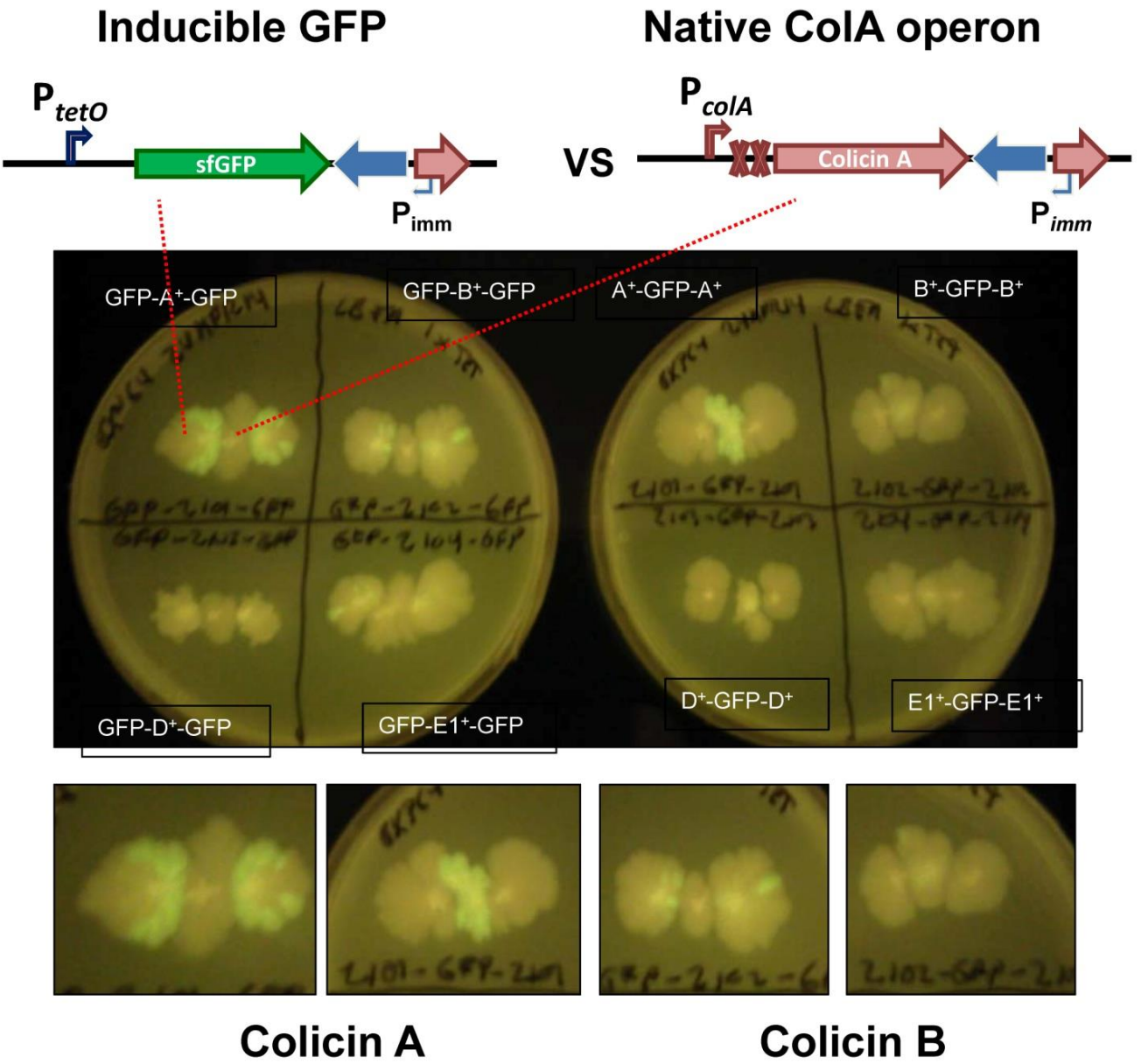

Figure 3. Forced maintenance of GFP reporter plasmid indicates colicin-mediated selection of strains expressing ColA immunity protein. Producer strains expressing native colicin operon and non-producer strains were inoculated between colonies of the other strain and were allowed to grow on Eiken agar for several days.

We believe this to represent preliminary evidence of colicin-mediated selection, as non-producing strains that harbor the immunity protein to colicin A would be predicted to have a growth advantage in the presence of colicin A secreted by the producing strains; this would not be the case against strains that produce other colicins (e.g., colicin B). Non-producing colonies formed sectored colonies when plated next to producers of other colicins, indicating instability of the plasmid that would result either from metabolic burdens conferred by GFP expression or by the expression of the lysis protein from the colicin A operon, which is retained in this expression construct.

We wished to obtain more quantitative readouts of the colony growth and to be able distinguish fluorescent from non-fluorescent colonies over time. We therefore constructed an imaging system that synchronizes the operation of a transilluminator with a camera outfitted with filters for assessment of GFP expression (Figure 4). In this system, a standard microbiological incubator is configured with a blue-light transilluminator, a camera, and appropriate emission filters to register the GFP fluorescence (Figure 4A). Bleaching of fluorescence due to constant illumination is avoided by synchronizing the transilluminator output with the camera, which is actuated on a timer switch (Figure 4B). The final configuration of the system is shown in Figure 4C.

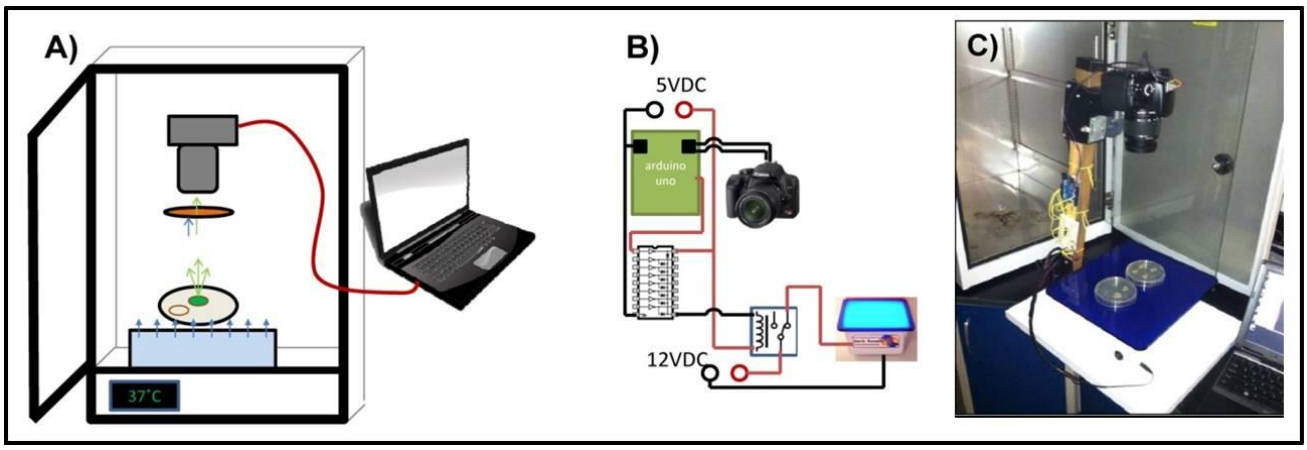

Figure 4. A device for time-lapse imaging of colony growths. A) Schematic showing a bacterial incubator configured with a transilluminator, fluorescence filter, camera, and computer controller for imaging of colonies. B) Process control of time-lapse imaging. When camera is signaled (by PC) to take a picture, the shutter-release signal is read by the Arduino microcontroller. Upon this signal, the Arduino sets an output pin high to (via a darlington transistor bridge) close a relay, switching on the light box. The microcontroller holds the pin high for 2 seconds after initial signal to ensure the light is on long enough for a full exposure, then the system resets (with the light box off) until the next photo is taken. C) Imaging system removed from the incubator compartment.

Using this imaging technique, we generated time-lapse images of growing colonies on plates and utilized this to show the fluorescence of non-producing strains grown in the presence of colicin-producing strains (Figure 5). As in our previous result, in the presence of a colicin A-producing strain, the non-producing strain maintained its fluorescence across the entire colony throughout the time-lapse series, which indicates that the plasmid expressing the modified colicin operon is under selection. This would make sense given that the strain maintains the expression of the native immunity protein to colicin A. This provides unambiguous evidence of colicin-mediated antagonism in this system, and sets the stage for the ongoing work that will utilize synthetic colicin operons in isogenic strain backgrounds, currently under construction in the laboratory.

We attempted to visualize the antagonism directly by utilizing a DNA-reactive fluorophore (SYBR Safe stain) that was incorporated into the plates. Our reasoning was that microbial death resulting from colicin-mediated lysis would manifest as zones of more intense fluorescence across the plates; however high backgrounds, presumably due to constitutive strain lysis even in the non-expressing strains, have prevented any interpretable data from emerging from these studies (not shown).

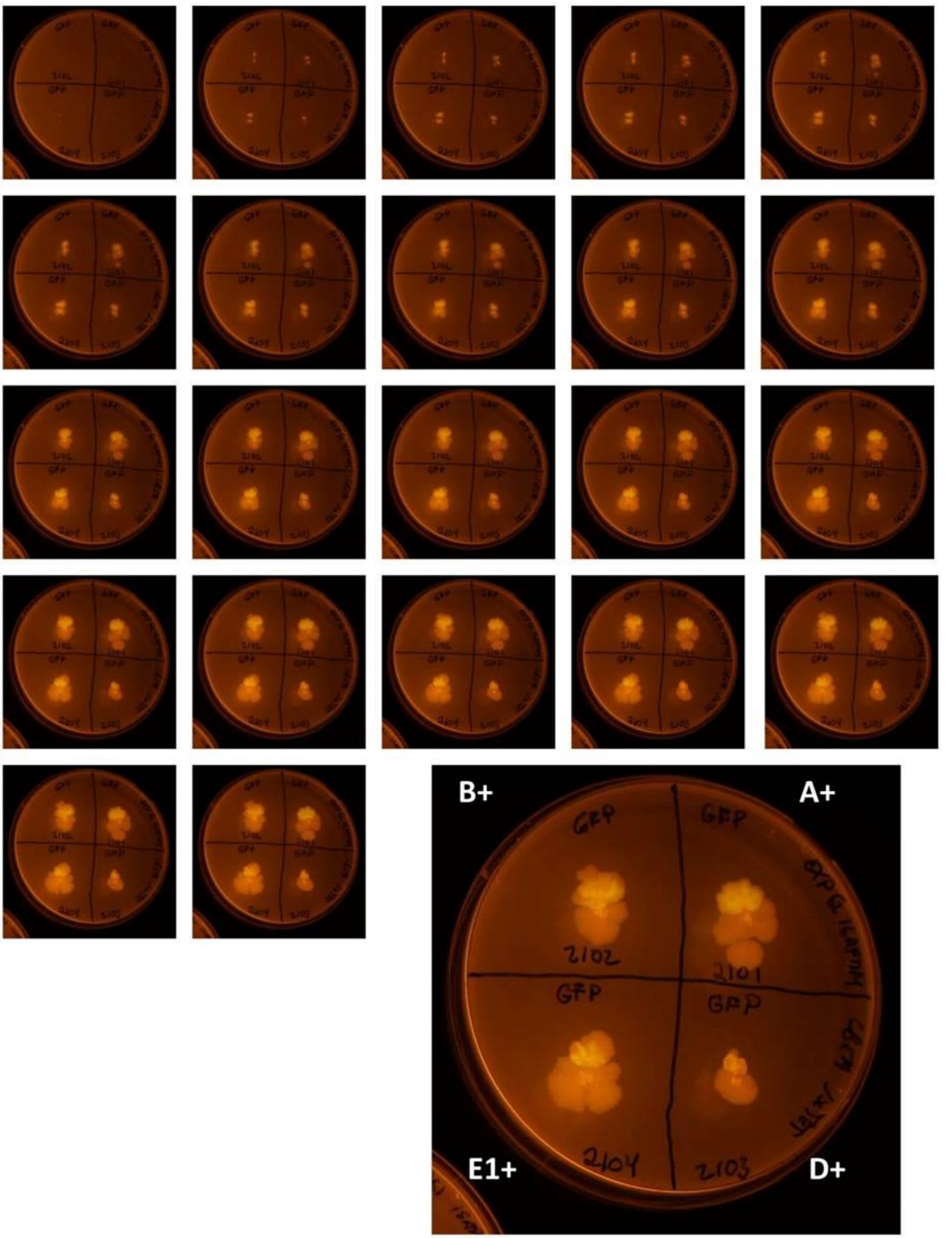

Figure 5. Time lapse of *E. coli* colony-level antagonism mediated by colicin expression. Strains from (16) expressing the indicated colicin protein were competed against W3110 transformed with a plasmid expressing GFP. Plates were photographed every 30 minutes for time-lapse movies. Static images spaced 2.5 hours apart are shown here.

4. CONCLUSIONS AND FUTURE WORK

As of the preparation of this report, we are currently working to re-engineer several of the colicin A and colicin E expression constructs into identical vector backbones. This is necessary to ensure that all strains are in similar vector backbones so that they can be placed into isogenic strain backgrounds to normalize for promoter strength, plasmid copy number, and host strain heterogeneity, which would complicate any direct comparison of the competition assays.

At this stage, several of the constructs are nearing completion which is expected early in the first quarter of fiscal year 2015. Once isogenic plasmid backbones are constructed, competition assays in Eiken and broth cultures will be possible.

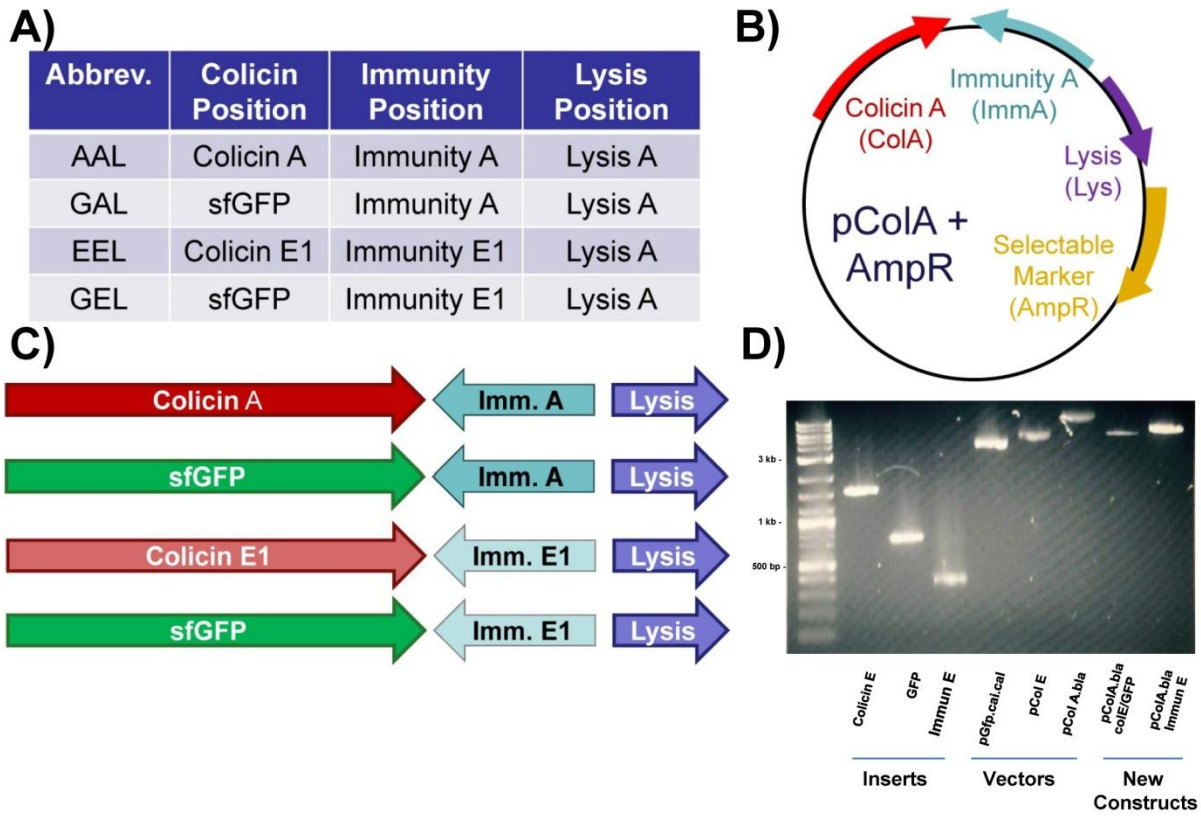

Abbrev.	Colicin Position	Immunity Position	Lysis Position
AAL	Colicin A	Immunity A	Lysis A
GAL	sfGFP	Immunity A	Lysis A
EEL	Colicin E1	Immunity E1	Lysis A
GEL	sfGFP	Immunity E1	Lysis A

Figure 6. Redesign and isogenization of colicin expression constructs. All colicin expression constructs are being re-cloned into a single expression background with cognate immunity proteins but with identical lysis proteins to control for efficiency of host cell lysis, as well as for the efficiency of the immunity gene promoters, which resides in the lysis gene. A) Nomenclature table, B) plasmid schematic, C) organization of redesigned operons, and D) gel electrophoresis of new constructs showing integration of immunity and GFP genes into pColA.bla (AmpR).

ACKNOWLEDGEMENTS

The authors would like to acknowledge U.S. Army funding provided through the Edgewood Chemical Biological Center's In-House Laboratory Independent Research and Surface Science Initiative programs.

REFERENCES

[1] Wintermute, E.H. and Silver, P.A., "Emergent cooperation in microbial metabolism", *Molecular Systems Biology*. **2010**. 6(1), p407.
[2] Hosoda, K. *et al.*, "Cooperative adaptation to establishment of a synthetic bacterial mutualism", *PLOS ONE*. **2011**. 6(2), p1.
[3] Tan, C. *et al.*, "Emergent bistability by a growth-modulating positive feedback circuit", *Nature Chemical Biology*. **2009**. 5(11), p842-848.
[4] Xavier, J.B., "Social interaction in synthetic and natural microbial communities", *Molecular Systems Biology*. **2011**. 7, p483.

[5] Fiegna, F. and Velicer, G.J., "Competitive fates of bacterial social parasites: persistence and self-induced extinction of Myxococcus xanthus cheaters", *Proceedings of the Royal Society B: Biological Sciences*. **2003**. 270(1523), p1527-1534.
[6] Sandoz, K.M. *et al*., "Social cheating in Pseudomonas aeruginosa quorum sensing", *Proceedings of the National Academy of Sciences of the United States of America*. **2007**. 104(40), p15876-15881.
[7] Maharjan, R.P. *et al*., "Divergence and redundancy of transport and metabolic rate-yield strategies in a single Escherichia coli population", *Journal of Bacteriology*. **2007**. 189(6), p2350-2358.
[8] Manhes, P. and Velicer, G.J., "Experimental evolution of selfish policing in social bacteria", *Proceedings of the National Academy of Sciences of the United States of America*. **2011**. 108(20), p8357-8362.
[9] Majeed, H. *et al*., "Competitive interactions in Escherichia coli populations: the role of bacteriocins", *ISME Journal*. **2011**. 5(1), p71-81.
[10] Li, C.H. *et al*, "Potential landscape and probabilistic flux of a predator prey network", *PLOS ONE*. **2011**. 6(3), e17888.
[11] Prindle, A. *et al*., "A sensing array of radically coupled genetic 'biopixels'", *Nature*. **2012**. 481(7379), p39-44.
[12] Prost, L.R. and Miller, S.I., "The Salmonellae PhoQ sensor: mechanisms of detection of phagosome signals", Ce*ll Microbiology*. **2008**. 10(3), p576-582.
[13] Chao, L. and Levin, B.R., "Structured habitats and the evolution of anticompetitor toxins in bacteria", *Proceedings of the National Academy of Sciences of the United States of America*. **1981**. 78(10), p6324-6328.
[14] Aoki, S.K. *et al*., "Contact-dependent inhibition of growth in Escherichia coli", *Science*. **2005**. 309(5738), p1245-1248.
[15] Cascales, E. *et al*., "Colicin biology", *Microbiology and Molecular Biology Reviews*. **2007**. 71(1), p158-229.
[16] Pugsley, A.P., "Escherichia coli K12 strains for use in the identification and characterization of colicins", *Journal of General Microbiology*. **1985**. 131(2), p369-376.

Role of acetylcholinesterase in the regulation of mesenchymal stem cell proliferation and differentiation

Amber M. Prugh[a], Stephanie D. Cole[b], Daniel J. Angelini[b]
[a]U.S. Army Edgewood Chemical Biological Center, Research & Technology Directorate,
5183 Blackhawk Rd, Aberdeen Proving Ground, MD 21010
[b]Excet, Inc., 8001 Braddock Rd, Suite 303, Springfield, VA 22151

ABSTRACT

Mesenchymal stem cells (MSC) are multipotent cells located in various adult tissues including bone marrow. These cells play a significant role in tissue maintenance and repair. Recently, it has been reported that bone marrow-derived MSCs express active acetylcholinesterase (AChE) and that disruption of this activity by organophosphate chemicals affects the ability of MSCs to differentiate into osteoblasts. It is currently unknown what role AChE plays in MSC proliferation and differentiation. In this study, we tested the hypothesis that organophosphates affect AChE activity in MSCs and this modification reduces the proliferation and/or differentiation potential of these cells. We established MSC toxicity profiles of the cholinesterase reactivator pralidoxime (pyridine-2-aldoxime methochloride or "2-PAM") and the efficacy of 2-PAM in recovery of cellular viability following exposure to the organophosphate chemicals parathion and paraoxon. Also, we used the previously determined optimal inhibitory parathion/paraoxon doses for AChE inhibition during MSC differentiation into osteoblasts and adipocytes and quantified the effects over several time points. Finally, to prove a role for AChE in these processes, we are currently developing a small interfering (si)RNA-based strategy to knockdown AChE expression in human MSCs. Understanding the pathways associated with MSC proliferation and differentiation could lead to the development of future MSC-based tissue repair therapies.

Keywords: acetylcholinesterase, differentiation, mesenchymal stem cells, organophosphates, paraoxon, parathion, tissue repair, siRNA

1. INTRODUCTION

Mesenchymal stem cells (MSC) can be isolated from various adult tissues and play a significant role in tissue maintenance and repair. *In vitro*, these cells are capable of self-renewal and, under the appropriate culture conditions, can be differentiated into bone, cartilage, and fat.[1,2] More recent studies have demonstrated that MSCs are capable of differentiating into other cell types including: alveolar epithelium, hepatocytes, myocytes, and neurons.[2] The mechanisms of MSC differentiation are poorly understood, but recent studies have demonstrated that MSCs derived from bone marrow express acetylcholinesterase (AChE),[3,4] and AChE activity levels affect their ability to differentiate into osteoblasts.[4] Given that organophosphate chemicals block AChE activity, it is certainly possible that organophosphates could affect the ability of MSCs to differentiate and/or proliferate. This is significant to the Army's mission because service members in the field are exposed to or could be potentially exposed to a host of toxic chemicals, including organophosphates. Exposure to these chemicals could affect MSCs' ability to proliferate and/or differentiate, therefore, reducing the ability to recover from any injuries sustained during assignments. Also, tissue repair is essential to the long-term health of individuals exposed to chemical warfare agents. The previous experimental findings lead us to propose the hypotheses that organophosphates will affect AChE activity in MSCs, and this modification will reduce the proliferation and/or differentiation potential of these cells. Our long-term objective is to determine the signaling pathways associated with MSC proliferation and differentiation and how these pathways relate to MSC-mediated tissue repair.

2. BACKGROUND AND SIGNIFICANCE

2.1 Mesenchymal stem cells

MSCs, also known as marrow stromal cells, were initially described in 1968 by Friedenstein and colleagues.[5] In their studies, MSCs were isolated from bone marrow due to their characteristic ability to attach to tissue culture flasks. Once attached, these cells displayed a fibroblast-like morphology. Since their initial discovery in bone marrow, MSCs have been isolated from several other tissues including umbilical cord, Wharton's jelly of the umbilical cord, placenta, adipose tissue, dental pulp, as well as from the lungs of lung transplant patients.[2] MSCs are capable of self-renewal and can be maintained in a multipotent state *in vitro*.[6] Since no single marker is available to identify MSCs, the International Society for Cell Therapy has published a consensus statement regarding identification requirements.[1] According to this definition, MSCs

must display the following properties: 1) adherence to plastic under routine cell culture conditions; 2) expression of the cellular markers CD73, CD90, and CD105; 3) lack of expression of CD11b, CD14, CD19, CD34, CD45, CD79a, and human leukocyte antigen (HLA); and 4) the capacity for *in vitro* differentiation into osteoblasts, adipocytes, and chondroblasts.[1]

2.2 MSC proliferation pathways

It has been reported that MSC growth occurs in three distinct phases; these phases include a lag phase (three to five days in culture), a rapid proliferation phase, and a stationary phase.[2] It has been demonstrated that the Wnt signaling cascade plays a critical role in this process and it is likely that there are many other signaling pathways associated with MSC proliferation yet to be identified; it is possible that AChE may play a role in this process.

2.3 Current understanding of MSC differentiation

Even though MSCs have been traditionally thought of as multipotent progenitors for bone, cartilage, and adipose tissue, recent investigations have revealed that MSCs have the ability to differentiate into other cell types including astrocytes, neurons, alveolar epithelial cells, and hepatocytes.[2] Currently, only a few genes have been identified that play critical roles in MSC differentiation. These genes include, but are not limited to Wnt, Runt-related transcription factor 2 (Runx2), transforming growth factor-β (TGFβ), peroxisome proliferator-activated receptor γ (PPARγ), osterix, and brain-derived neurotrophic factor (BDNF).[2] For example, Runx2 acts as a master gene for the regulation of osteogenic differentiation. Up-regulation of this gene product promotes both osteogenic and chondrogenic differentiation, while inhibiting adipogenic differentiation.[2] Even though AChE has been shown to be expressed in MSCs, the exact role it plays in MSC differentiation is currently unknown.

3. MATERIALS AND METHODS

3.1 Human MSC culture

Primary human bone marrow-derived MSCs were obtained from Lonza (Walkersville, MD) and cultured in Mesenchymal Stem Cell Growth Medium (MSCGM) supplemented with Mesenchymal Stem Cell Growth Supplement (MSCGS), L-glutamine, gentamicin, and amphotericin-B (all supplements from Lonza) as described.[7,8] Only MSCs from passages four through eight were examined for the proposed studies.

3.2 Preparation of the organophosphate chemicals

Stock solutions of the organophosphate pesticide (OPP) parathion as well as its metabolite, paraoxon, (both from ULTRA Scientific; N. Kingstown, RI) were prepared in 100% ethanol (EtOH) and stored at 4 °C.

3.3 Preparation of reactivator

The cholinesterase reactivator pralidoxime (pyridine-2-aldoxime methochloride or "2-PAM") (Sigma-Aldrich; St. Louis, MO) was prepared in sterile deionized water to a 1 M stock solution. Working stocks of lower concentrations were prepared from this stock in sterile deionized water as needed. All stocks were stored at 4 °C.

3.4 MSC toxicity studies

To evaluate the toxicity of the cholinesterase reactivator (2-PAM) alone on these cells, we plated $1x10^4$ MSCs in the wells of 96-well tissue culture plates and allowed the cells to attach for 24 hours. Then, we exposed the MSCs to increasing concentrations (0.1 mM, 1 mM, and 10 mM) of 2-PAM for 24 hours and 48 hours. Cellular viability in the presence of this reactivator was determined by the MTT assay (Roche Applied Science; Indianapolis, IN).

3.5 MSC proliferation studies

To evaluate the effects of 2-PAM alone on MSC proliferation, we plated $1x10^3$ cells per well in 96-well plates and allowed the cells to attach for 24 hours. Then, we exposed the MSCs to increasing concentrations (0.1 mM, 1 mM, and 10 mM) of 2-PAM for 24 hours and 48 hours. MSC proliferation in the presence of this reactivator was determined by the 5-bromo-2-deoxyuridine (BrdU) Cell Proliferation Assay (Roche Applied Science).

3.6 Evaluation of cholinesterase reactivator in the presence of OPPs

Based on the results from 3.4 and 3.5, we chose reactivator concentration(s) with no significant effects on cellular viability or proliferation over 48 hours for our experiments with parathion and paraoxon. To evaluate the role of cholinesterase reactivation, we performed the stated viability and proliferation assays in the presence or absence of media alone, vehicle (EtOH), 2-PAM (100 µM, 250 µM), OPP [parathion/paraoxon (1000 µM, 3000 µM, 10000 µM)], or OPP with 2-PAM (100 µM, 250 µM).

3.7 MSC differentiation studies

3.7.1 Adipogenic differentiation

For these studies, MSCs were plated in 96-well tissue culture plates at $5x10^3$ cells per well and allowed to grow to confluence in the presence of MSCGM. Once the cells reached confluence, the media was replaced with Human MSC Adipogenic Induction Medium (Lonza) and Adipogenic Maintenance Medium (Lonza) with or without vehicle (EtOH) or OPP in cycles in accordance with the manufacturer's recommended protocol. The cells were cultured for 7 days, 14 days, or 21 days. At the end of each differentiation period, the cells were stained using the AdipoRed Assay Reagent (Lonza) protocol and measured using a microplate fluorescence spectrophotometer.

3.7.2 Osteogenic differentiation

For osteogenic differentiation, MSCs were plated in 96-well tissue culture plates at $1\text{-}4x10^3$ cells per well. After attachment but prior to confluence (24-72 hours), the media was replaced with Osteogenic Differentiation Medium (Lonza) with or without vehicle (EtOH) or OPP. This medium was replaced every 3-4 days for 7 days, 14 days, or 21 days. At the end of each differentiation period cells were fixed with absolute EtOH or 4% paraformaldehyde (PFA) for 20 minutes then stained using the OsteoImage Mineralization Assay (Lonza) protocol and measured using a microplate fluorescence spectrophotometer.

3.8 Human MSC small interfering (si)RNA studies

3.8.1 Efficiency of siRNA transfection

To evaluate the efficiency of siRNA transfection, we used siRNA directed against the housekeeping gene GAPDH (siGENOME GAPD Control siRNA, human; GE Healthcare Dharmacon; Pittsburgh, PA). Both lyophilized non-targeting (siGENOME Non-Targeting siRNA Pool #1) and GAPD control siRNA (GE Healthcare Dharmacon) were resuspended in 1X siRNA buffer to a 5 µM stock concentration. For these experiments, MSCs ($2.5\text{-}3x10^4$) were plated in 6-well plates and allowed to grow to near confluence. The cells were then transfected with increasing concentrations of GAPDH-directed siRNA (25 nM, 33 nM, 42 nM, 50 nM, and 100 nM) or equivalent concentrations of scrambled siRNA in the presence of DharmaFECT transfection reagent (GE Healthcare Dharmacon). At 48 hours, 72 hours, 96 hours, 120 hours, or 144 hours after transfection, MSCs were lysed and collected in 1X RIPA buffer (Cell Signaling Technology, Inc.; Danvers, MA), centrifuged, and the supernatants assayed for protein concentration with the Pierce 660 nm Protein Assay (Thermo Fisher Scientific; Waltham, MA). The samples were resolved using the 4-12% gradient Bolt™ Bis-Tris Plus Gel according to the manufacturer's instructions (Life Technologies; Grand Island, NY) and transferred onto nitrocellulose membranes/PVDF (Life Technologies) using the iBlot® 7-Minute Blotting System (Life Technologies). The membranes were blocked, incubated with mouse anti-GAPDH monoclonal antibodies (Santa Cruz Biotechnology; Dallas, TX), and incubated with anti-mouse IgG antibodies conjugated to alkaline phosphatase using the iBlot® Western Blot System (Life Technologies) according to the manufacturer's instructions. Finally, the membranes were developed using the iBlot® Western Detection, Chromogenic Kit (Life Technologies).

3.8.2 Optimization of siRNA transfection conditions

siRNAs labeled with fluorescent transfection indicators were used to optimize transfection conditions. Lyophilized Silencer® Cy3-labeled negative control siRNA #1 (GE Healthcare Dharmacon) was resuspended in RNAse free water to a 5 µM stock concentration. Using this siRNA, three different transfection reagent protocols were evaluated: Lipofectamine RNAiMAX (Life Technologies), DharmaFECT, and TransMessenger (Qiagen; Germantown, MD). MSCs were plated at a density of $2\text{-}2.5x10^4$ cells per well in 6-well plates. Once confluent, spent medium was removed and cells were washed with HEPES buffered saline solution (Lonza). After washing, transfection complexes were prepared and incubated with the cells in accordance with the manufacturer's instructions. After 4 hours, transfection medium was removed from wells and replaced with MSCGM. Plates were incubated for an additional 24 hours, 48 hours, 72 hours, or 96 hours then fixed with 4% PFA for 20 minutes and counterstained with Hoechst 33342 (1 µL/mL solution) (Life Technologies). High content analysis (HCA) was used to analyze transfection efficiency. After analysis, Lyophilized Silencer® Cy3-labeled GAPDH siRNA (Life Technologies) was resuspended in RNAse-free water to a 5 µM stock concentration and transfection was repeated under the same conditions using Lipofectamine RNAiMAX only, with fixation and nuclear counterstaining after 24 hours and 48 hours. HCA was used to analyze transfection efficiency.

3.8.3 Inhibition of AChE using siRNA

Several different siRNA approaches were used in this part of the study. Initially, SMARTPool siRNA duplex products designed to target human AChE (Thermo Fisher Scientific) and the appropriate non-targeting siRNA duplexes were used to knockdown AChE protein expression. MSCs were plated at a density of $4\text{-}9x10^4$ and allowed to grow to near confluence. The AChE and control siRNAs were incubated with transfection complexes which contained starting siRNA

concentrations recommended by the manufacturer's protocols [Lipofectamine RNAiMAX (15 nM), DharmaFECT (25 nM), and TransMessenger (33 nM)]. Transfections were performed for 4 hours in serum-free media. In follow-up experiments, we used Lipofectamine RNAiMAX (15 nM siRNA) with transfection times of 4 hours, 7 hours, and 18 hours in the absence of serum. We also performed reverse transfection experiments. These were completed by preparing transfection complexes (10-11 nM siRNA concentration) and adding MSCs in serum-free media at a density of $1.5x10^5$ cells/well in 6-well plates with an 18 hour transfection time. To determine the effectiveness of all AChE-directed siRNA transfection, MSCs were lysed (72 hours post-transfection) and processed for immunoblotting with rabbit anti-AChE polyclonal antibodies (Abcam; Cambridge, MA), and incubated with anti-rabbit IgG antibodies conjugated to alkaline phosphatase anti-AChE antibodies as described above (3.8.1).

3.9 Intracellular localization of AChE in MSCs

To detect the presence and location of AChE in the cell using immunofluorescence microscopy, $1x10^4$ MSCs were grown on 4-well chamber slides and allowed to attach/proliferate for 48 hours. The cells were then treated with parathion (30 µM or 100 µM), paraoxon (30 µM or 100 µM), equivalent amounts of vehicle (EtOH), or media alone for 24 hours. The cells were washed with ice-cold phosphate buffered saline (PBS), fixed with cold 4% PFA, and then permeabilized with 0.5% Triton X-100 in PBS. The MSCs were then blocked with 5% normal donkey serum in a 1% bovine serum albumin (BSA)/PBS solution for 30 minutes at room temperature, incubated in rabbit anti-AChE polyclonal antibodies (Abcam) for 90 minutes, washed with PBS, and then incubated for 30 minutes with AlexFlour 488-conjugated donkey anti-rabbit IgG. Finally, the slides were washed three times with PBS, coverslipped using VECTASHIELD® Mounting Media with DAPI (Vector Laboratories; Burlingame, CA), and visualized using a fluorescence microscope.

3.10 Determination of potential AChE binding partners in MSCs

For these studies, we used the Pierce™ Pull-Down PolyHis Protein:Protein Interaction Kit (Thermo Scientific) and proceeded according to the manufacturer's recommended protocol. Briefly, previously prepared His-tagged AChE protein was incubated with MSC lysates for 1 hour at room temperature. These mixtures were placed on filter columns, washed, and protein eluted (column flow-through was kept from each step for analysis). The eluted protein and the initial flow-through were then prepared for SDS-PAGE and bands visualized using SimplyBlue™ Safe Stain (Life Technologies).

3.11 Statistical analysis

A Student's t-test was used to compare mean responses between individual, experimental, and control groups. Analysis of variance (ANOVA) was used to compare the mean responses among experimental and control groups in experiments with multiple groups. Tukey's test was used to determine between which groups significant differences existed. A p-value < 0.05 was considered significant for all experiments.

4. RESULTS

4.1 Human bone marrow-derived MSC culture

Human bone marrow-derived MSCs were grown on tissue culture-treated plastic in MSCGM. MSCs attach to tissue culture-treated plastic and display a fibroblast-like morphology. Figure 1 is a phase contrast photomicrograph of passage 5 MSCs.

Figure 1. Cultured MSCs. A representative phase contrast image of undifferentiated human MSCs. Bar = 100 µm.

4.2 Human MSC siRNA transfection efficiency studies

In the subsequent figures, we demonstrate several different ways of potentially knocking down AChE in MSCs.

4.2.1 Evaluation using Western Blot analysis

To evaluate the efficiency of siRNA transfection, we used siRNA directed against the housekeeping gene GAPDH. For these experiments, MSCs ($2.5\text{-}3x10^4$) were plated in 6-well plates and allowed to grow to near confluence. The cells were then transfected with increasing concentrations of GAPDH-directed siRNA (25 nM, 33 nM, 42 nM, 50 nM, and 100 nM) or equivalent concentrations of scrambled siRNA in the presence of DharmaFECT transfection reagent. At 72 hours, 96 hours, 120 hours, or 144 hours after transfection, MSCs were processed for immunoblotting with anti-GAPDH antibodies as described in Section 3.8.1 (Figure 2). Transfection of the scrambled (non-targeting) siRNA sequence had no effect on the protein expression levels of GAPDH when compared to media controls, which suggests the lack of off-target effects. There was an observable reduction in GAPDH expression following the transfection of GAPDH-directed siRNA especially at 96 hours and 120 hours post-transfection, but this reduction was not complete.

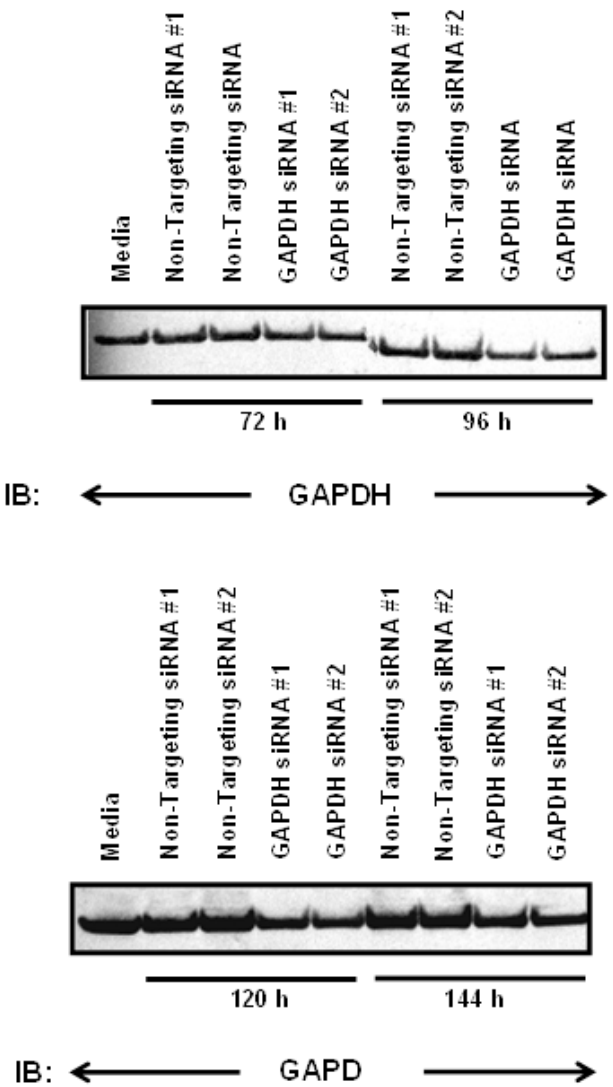

Figure 2. GADPH-directed siRNA partially knocks down GAPDH expression in MSCs. Representative Western blots from 72 hours, 96 hours, 120 hours, and 144 hours following GAPDH-directed or non-targeting siRNA transfection using DharmaFECT transfection reagent.

4.2.2 HCA evaluation with siRNA conjugated to Cy3

To visually evaluate the efficiency of siRNA transfection into MSCs, we used non-targeting siRNA conjugated to Cy3 in combination with Lipofectamine RNAiMAX, DharmaFECT, or TransMessenger transfection reagents (Figure 3). This transfection was followed by HCA evaluation at 24 hours, 48 hours, or 72 hours post-transfection. Inspection of the collected images revealed the greatest increase in fluorescence intensity was at 72 hours post-transfection with either Lipofectamine or DharmaFECT. Some fluorescence signal was observed using TransMessenger at 72 hours, but it was much less compared to the other two reagents. At 24 hours and 48 hours, there was a minimal fluorescence signal from the siRNA transfected with either Lipofectamine or DharmaFECT. Little to no signal was seen using TransMessenger at either of these time points.

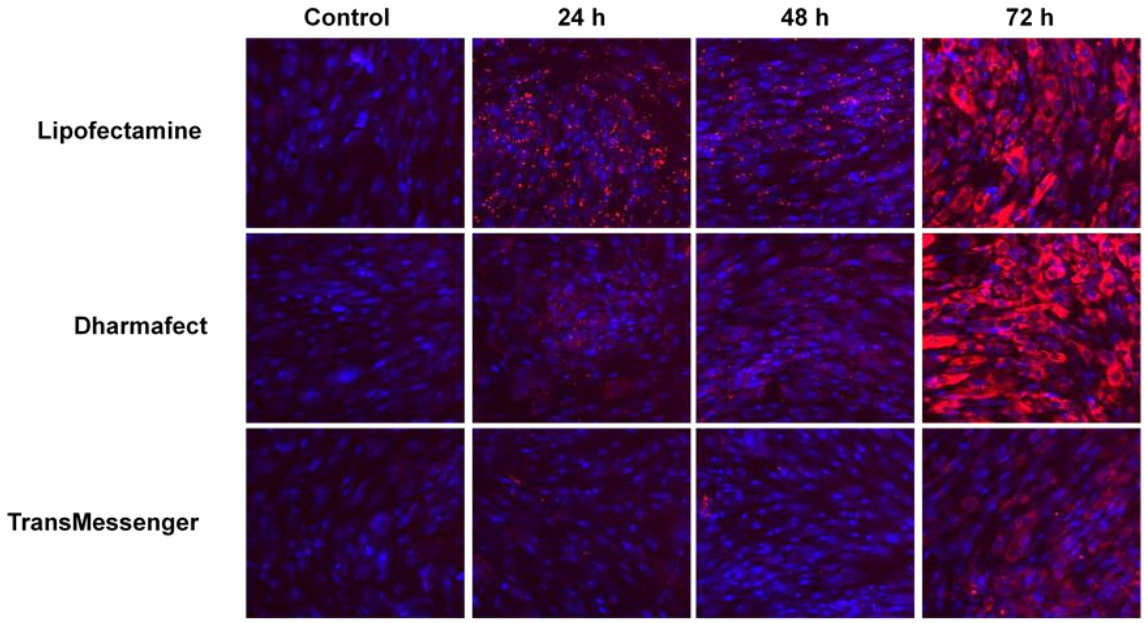

Figure 3. HCA of siRNA transfection using three different transfection reagents. Representative HCA images from 24 hours, 48 hours, and 72 hours following MSC transfection with non-targeting siRNA conjugated to Cy3. The MSCs were counterstained with Hoechst 33342 to allow for the HCA identification of individual cells.

4.2.3 HCA evaluation of siRNA transfection using three different transfection reagents

We used non-targeting siRNA conjugated to Cy3 in combination with Lipofectamine, DharmaFECT, or TransMessenger transfection reagents to determine the optimal transfection protocol for these cells. The transfections were quantified using the HCA settings of Mean Total Intensity (total well fluorescence) (Figure 4) and the percentage of individual cells that have an increase in fluorescence signal compared to the baseline (% Responders) (Figure 5) at 24 hours, 48 hours, or 72 hours post-transfection. When evaluating Mean Total Intensity, the Lipofectamine produced the highest fluorescence intensity at 24 hours and 48 hours post-transfection compared to the other reagents (Figure 4A,B). At 72 hours, DharmaFECT appeared to have the highest fluorescence intensity, but it was not statistically different than Lipofectamine (Figure 4C). TransMessenger transfection reagent failed to produce significant increases in fluorescence intensity post-transfection. Evaluation of % Responders (Figure 5) produced similar results as the Mean Total Intensity results in Figure 4. By 72 hours, both Lipofectamine and DharmaFECT appeared to produce at least 40% of the MSCs to show positive for the siRNA transfection.

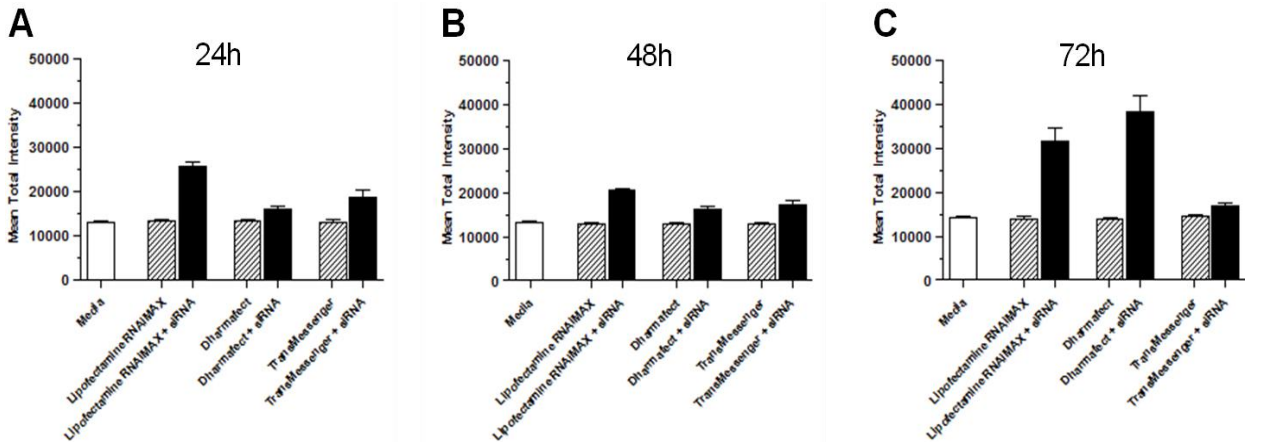

Figure 4. HCA evaluation of siRNA transfection efficiency through quantification of total well fluorescence. MSCs were plated at a density of 2-2.5x10^4 cells per well in 6-well plates and allowed to attach for 72 hours. The cells were then transfected with 5 µM non- targeting siRNA conjugated to Cy3 using Lipofectamine RNAiMAX, DharmaFECT, or TransMessenger transfection reagents. The plates were then read using the HCA instrument at (A) 24 hours, (B) 48 hours, or (C) 72 hours and Mean Total Intensity of fluorescence was measured. Open bars represent media alone; cross-hatched bars represent transfection agent alone; closed bars represent siRNA + transfection reagent. Mean total intensity is expressed as relative fluorescence units (RFU) and the results are reported as mean ± SEM of RFU.

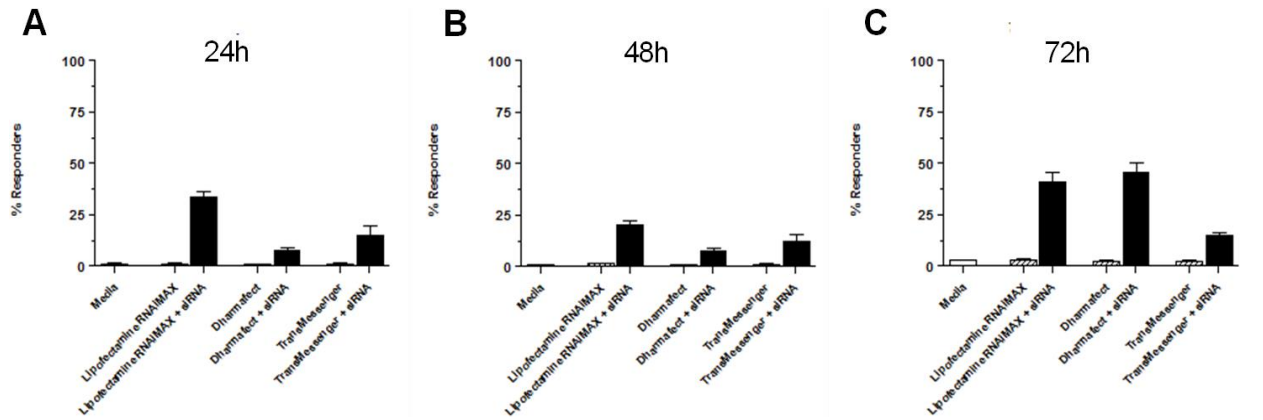

Figure 5. HCA evaluation of siRNA transfection efficiency through quantification of individual cellular responders. MSCs were plated at a density of 2-2.5x104 cells per well in 6-well plates and allowed to attach for 72 hours. The cells were then transfected with 5 µM non-targeting siRNA conjugated to Cy3 using Lipofectamine RNAiMAX, DharmaFECT, or TransMessenger transfection reagents. The plates were then read using the HCA instrument at (A) 24 hours, (B) 48 hours, or (C) 72 hours and % Responders were evaluated. The results are reported as mean ± SEM of % Responders. Open bars represent media alone; cross-hatched bars represent transfection agent alone; closed bars represent siRNA + transfection reagent.

4.3 Human MSC time course differentiation studies

4.3.1 Effect of OPPs on MSC adipogenic differentiation

MSCs were plated in 96-well tissue culture plates at a density of 5x10^3 cells per well and allowed to grow to confluence in the presence of MSCGM. Once the cells reached confluence, the media was replaced with Human MSC Adipogenic Differentiation Medium and Adipogenic Maintenance Medium with or without vehicle (EtOH) or OPP in cycles in accordance with the manufacturer's recommended protocol. The cells were cultured for 7 days (Figure 6A), 14 days (Figure 6B), or 21 days (Figure 6C). At the end of each differentiation period, the cells were stained using the AdipoRed Assay Reagent protocol and measured using microplate fluorescence spectrophotometer (Figure 6). There were slight, but statistically significant, increases in adipogenic differentiation following 7 days of induction (Figure 6A). At this time point, the OPPs had no observable effect on adipogenic differentiation. At both 14 days and 21 days of differentiation, both OPPs reduced the observable amount of adipogenesis compared to vehicle control (Figure 6B,C). These results indicate that these OPPs are altering the normal adipogenic differentiation pattern of MSCs. Further investigation is

required to determine if this change is due to the OPPs' inhibition of AChE activity or is a result of an undetermined secondary effect.

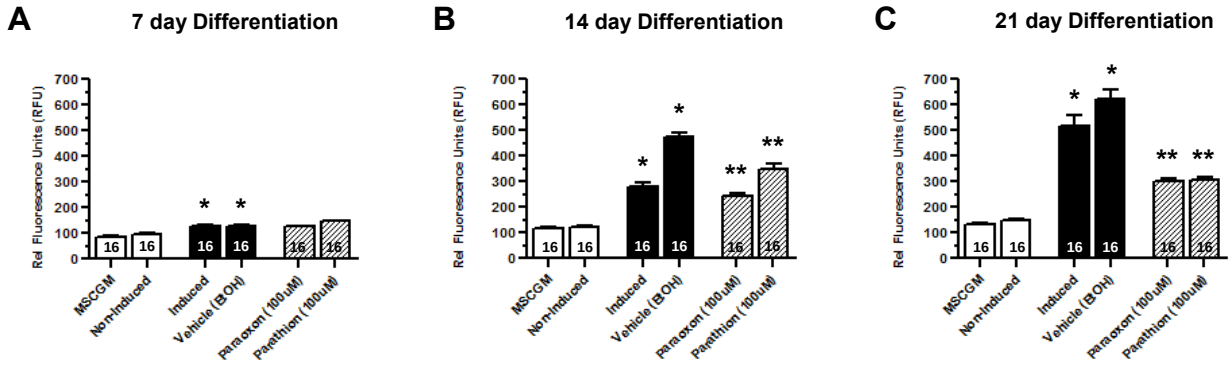

Figure 6. Evaluation of OPPs on MSC adipogenic differentiation. Quantitative graph of RFU for each adipogenic differentiation condition. MSCs were exposed to adipogenic differentiation media for (A) 7 days, (B) 14 days, or (C) 21 days and then evaluated for differentiation using the fluorescence-based AdipoRed Assay Reagent. The results are reported as mean ± SEM of RFU. Open bars represent negative control conditions; closed bars represent positive control conditions; cross-hatched bars represent experimental conditions. *n* for each condition is indicated within each bar. *$p < 0.05$ versus non-induced control; **$p < 0.05$ versus vehicle control.

4.3.2 Effect of OPPs on MSC osteogenic differentiation

MSCs were plated at a density of 1-4x10^3 cells per well in 96-well tissue culture plates in MSCGM. After 18-24 hours, the media was replaced with Osteogenic Differentiation Medium with or without vehicle (EtOH) or OPP. This medium was replaced every 3-4 days for 7 days (Figure 7A), 14 days (Figure 7B), or 21 days (Figure 7C). At the end of each differentiation period cells were fixed with absolute EtOH or 4% PFA then stained using the OsteoImage Mineralization Assay protocol and measured using a microplate fluorescence spectrophotometer. In these experiments, there were no significant changes in following 7 days or 14 days of osteogenic differentiation (Figure 7A, B). At 21 days of differentiation, there were significant increases in osteogenesis in both the positive and vehicle controls (Figure 7C). Treatment of the differentiating MSCs with parathion significantly reduced the formation of bone cells. There was also an observable reduction in bone formation associated with paraoxon exposure, but this change was not statistically significant at this point.

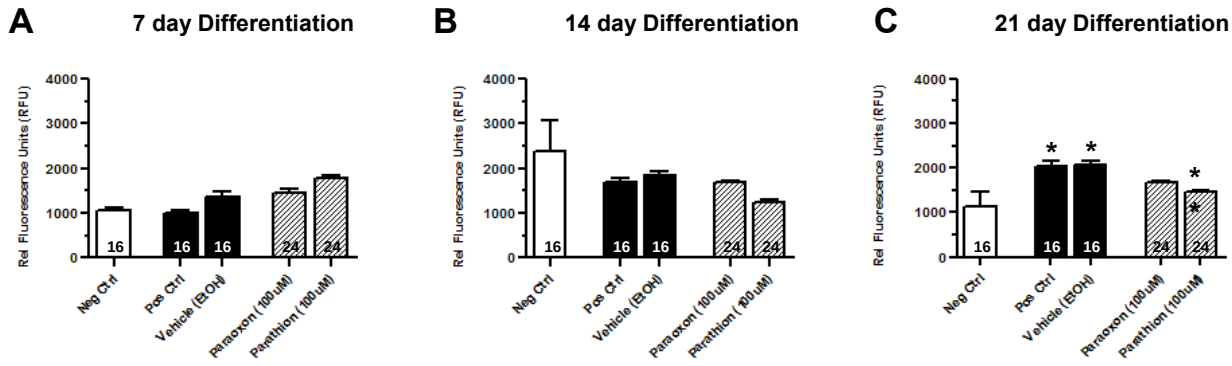

Figure 7. Evaluation of OPPs on MSC osteogenic differentiation. Quantitative graph of RFU for each osteogenic differentiation condition. MSCs were exposed to osteogenic differentiation media for (A) 7 days, (B) 14 days, or (C) 21 days and then evaluated using the OsteoImage Mineralization Assay. The results are reported as mean ± SEM of RFU. Open bars represent negative control conditions; closed bars represent positive control conditions; cross-hatched bars represent experimental conditions. *n* for each condition is indicated within each bar. *$p < 0.05$ versus negative control; **$p < 0.05$ versus vehicle control.

4.4 Evaluation of the cholinesterase reactivator 2-PAM

Prior to introducing 2-PAM into any of our viability, proliferation or differentiation studies, it was essential to determine the toxicity levels of 2-PAM in our MSC system. The following studies address these issues.

4.4.1 Effect of 2-PAM on MSC viability

MSCs were plated at a density of $1x10^4$ in the wells of 96-well tissue culture plates with 24 hour attachment. Once the cells have sufficiently attached, the MSCs were exposed to increasing concentrations of 2-PAM (0.1 mM, 1 mM, and 10 mM) for either 24 hours (Figure 8A) or 48 hours (Figure 8B). There was no change in MSC viability following a 24 hour or 48 hour exposure to either 0.1 mM or 1 mM 2-PAM. There was a slight, but significant, decrease in cellular viability following an exposure to 10 mM 2-PAM at both 24 hours and 48 hours. We therefore selected a 2-PAM concentration that is between 0.1 mM and 1 mM for future experiments.

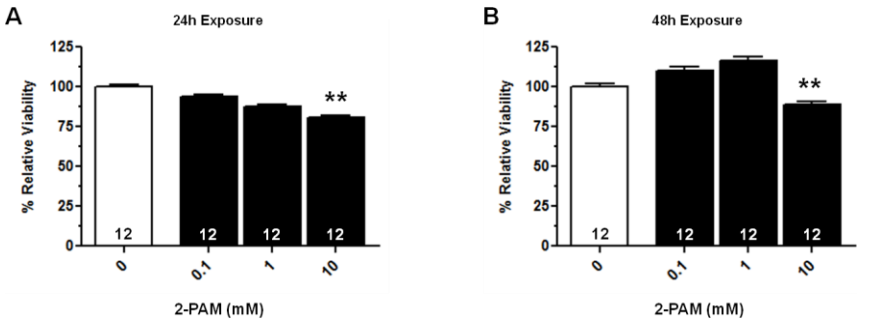

Figure 8. Effects of 2-PAM on the viability of cultured human MSCs. MSCs were exposed to increasing concentrations of 2-PAM (0.1 mM, 1 mM, or 10 mM) (closed bars) or media alone (open bars) for either (A) 24 hours or (B) 48 hours, after which they were assayed for viability using the MTT Cell Viability Assay. The results are reported as mean ± SEM of % Relative Viability; *n* = 12 (indicated in each bar) for each condition tested. **$p < 0.05$ versus media control.

4.4.2 Effect of 2-PAM on MSC proliferative ability

MSC proliferation in the presence of 2-PAM was determined by the BrdU Cell Proliferation Assay (Roche Applied Science). MSCs were plated at a density of $1x10^3$ cells per well in 96-well plates and allowed to attach for 24 hours. The MSCs were exposed to increasing concentrations of 2-PAM (0.1 mM, 1 mM, and 10 mM) for either 24 hours or 48 hours. At the end of the exposure, BrdU was added to the cells and incubated for an additional 2 hours. The culture media was then removed and the cells were fixed and washed. A peroxidase-labeled anti-BrdU antibody was added and developed. The plate was then read on a scanning multiwall spectrophotometer and the absorbance values recorded. These data indicate that exposure for 24-48 hours of 0.1-1 mM of 2-PAM have little to no effect on the proliferative ability of undifferentiated MSCs (Figure 9); however, we did observe a significant decrease in MSC proliferative ability when these same cells were exposed to 10 mM 2-PAM for 24-48 hours.

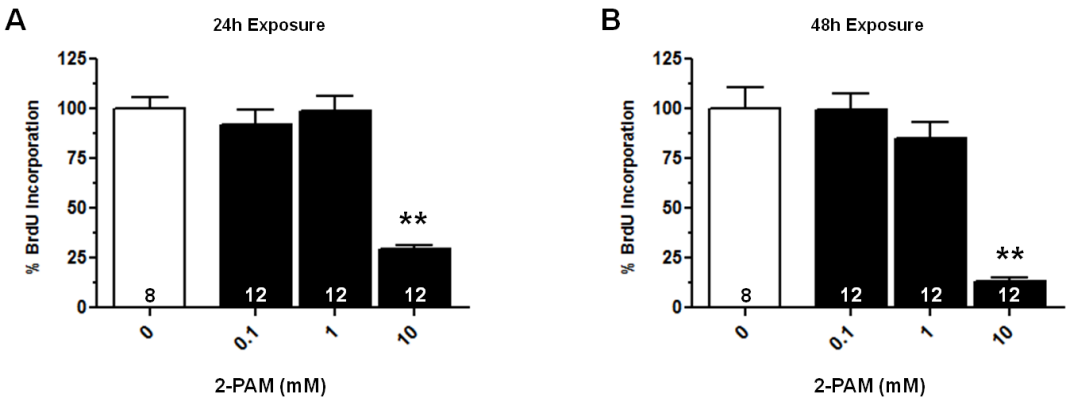

Figure 9. Effects of 2-PAM on the proliferative ability of cultured human MSCs. MSCs were exposed to increasing concentrations of 2-PAM (0.1 mM, 1 mM, or 10 mM) (closed bars) or media alone (open bars) for either (A) 24 hour or (B) 48 hour equivalent, after which they were assayed for proliferation using the BrdU Cell Proliferation Assay. The results are reported as mean ± SEM of % BrdU Incorporation; *n* is indicated within each bar. **$p < 0.05$ versus media control.

4.4.3 Effect of 2-PAM on MSC viability in the presence of OPPs

MSCs were plated at a density of $1x10^4$ in the wells of 96-well tissue culture plates and allowed to attach for 24 hours. The cells were then exposed to media alone, vehicle (EtOH), 2-PAM (250 µM), increasing concentrations of paraoxon (1000 µM, 3000 µM, or 10000 µM), or increasing concentrations of paraoxon (1000 µM, 3000 µM, or 10000 µM) in the

presence of 2-PAM (250 µM) for 24 hours, after which they were assayed for viability using the MTT Cell Viability Assay (Figure 10). In these experiments, paraoxon produced dose-dependent reduction in MSC viability after 24 hours of exposure. Co-incubation of the MSCs with 2-PAM reduced the amount of paraoxon-induced cellular death. The amount of protection garnered by AChE reactivation through 2-PAM was also dependent on the paraoxon dose. Cells dosed with 3,000 µM paraoxon, which induced approximately 60% cell death, were completely protected by the addition of 2-PAM. These data suggest that AChE plays a role, at least in part, to paraoxon-mediated cell death in MSCs. This experiment was repeated with parathion, but doses of 10,000 µM parathion alone were unable to induce cell death in our system (data not shown).

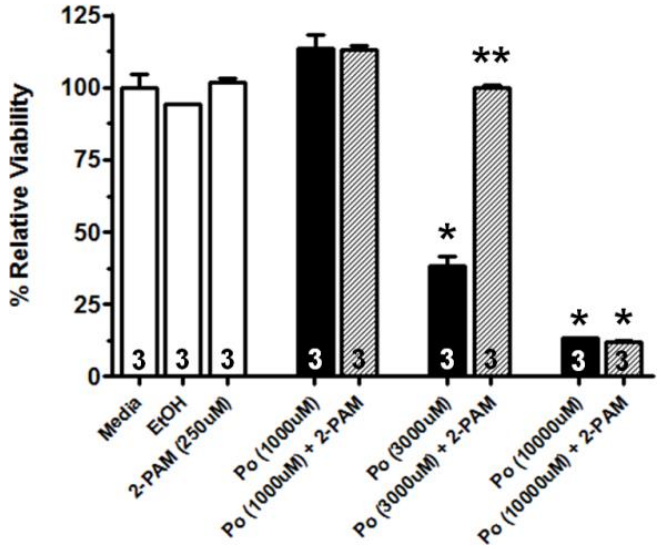

Figure 10. Effects of 2-PAM on MSCs cultured in the presence of paraoxon. MSCs were exposed to media alone, vehicle (EtOH), 2-PAM (250 µM), increasing concentrations of paraoxon (1,000 µM, 3,000 µM, or 10,000 µM), or increasing concentrations of paraoxon (1,000 µM, 3,000 µM, or 10,000 µM) in the presence of 2-PAM (250 µM) for 24 hours, after which they were assayed for viability using the MTT Cell Viability Assay. Open bars indicate negative controls; closed bars represent exposure to paraoxon; cross-hatched bars indicate exposure to paraoxon + 2-PAM. The results are reported as mean ± SEM of % Relative Viability; $n = 3$ for each condition tested. *$p < 0.05$ versus vehicle control; **$p < 0.05$ versus paraoxon.

4.5 Intracellular localization of AChE in MSCs

On control slides, AChE observed by fluorescence microscopy, was localized in the cytoplasm in a punctate pattern. These areas appeared to be associated with the cytoskeleton (data not shown). Following a 24 hour paraoxon exposure (100 µM), AChE appeared to be concentrated in the perinuclear region (data not shown). This suggests that paraoxon is altering the normal state of AChE in these cells. Further investigation will need to be performed to determine the exact nature of this change.

4.6 Determination of potential AChE binding partners in MSCs

During the second year of this project, we have begun to look for potential AChE binding partners in MSCs by performing His-tag pulldown assays (data not shown). In our initial studies, we used a His-tagged AChE protein that was previously generated at ECBC and untreated MSC lysates to determine potential binding partners. These initial pulldown studies produced gels that contained multiple bands and possible binding partners (data not shown). Further investigation and refinement of the assay will be required to identify these possible AChE binding partners.

5. CONCLUSIONS

During the first year of this project, our results indicated that OPPs affect the cellular viability, proliferative ability, and differentiation potential of MSCs. We demonstrated that the OPPs, parathion and paraoxon, reduced the cellular viability as well as the proliferative ability of MSCs in a dose-dependent manner. Also during year 1, we demonstrated the ability to differentiate MSCs into several different cell types in our laboratory including adipocytes, osteoblasts, and neurons (determined by morphology analysis). Prior treatment with either parathion or paraoxon significantly reduced the MSCs' ability to differentiate into adipocytes. Together, the year 1 results suggest that parathion and paraoxon are disrupting the normal pathways associated with AChE in MSCs; these altered pathways are inducing cellular death as well as altering the normal proliferative and differentiation functions of MSCs. Building on the data that was generated in year 1 of this

project, we examined the adipogenic and osteogenic differentiation using a more quantitative fluorescence-based approach in year 2. For adipogenic differentiation, we examined three time points (7 days, 14 days, and 21 days). There were significant increases in adipocyte formation as early as 7 days (~1.2-fold) which increased through 21 days (~5-6-fold) (Figure 6); this differentiation was significantly reduced when performed in the presence of either OPP. We also were able to quantify our osteogenic differentiation using a fluorescence-based assay during year 2. Like the adipogenic differentiation, we examined three time points (7 days, 14 days, and 21 days). We detected significant mineralization (indicating bone development) following a 21 day differentiation of ~2-fold compared to the control (Figure 7). Treatment of these MSCs with either paraoxon or parathion reduced osteogenic differentiation. To determine a possible role for AChE, we introduced the cholinesterase reactivator, 2-PAM, into our studies. First, we determined the appropriate concentrations of 2-PAM to use in both the MTT and BrdU assays; it was important to determine this concentration as to not disrupt the normal cell viability or proliferative potential. We determined that a dose of 0.1-1 mM of 2-PAM will not affect either of these pathways (Figures 8,9). Once this was determined, we introduced 2-PAM into our paraoxon/parathion toxicity studies. Co-incubation of MSCs with paraoxon and 2-PAM reduced paraoxon-induced cell death (Figure 10). In fact, when MSCs were treated with 3000 µM of paraoxon, 2-PAM prevented any losses in cellular viability. These results complement our year 1 findings that AChE is playing a key role in many of the signaling pathways associated with MSCs. To complement our 2-PAM studies, we are continuing to work on our AChE-directed siRNA studies (Figures 2-5); these studies are currently in progress.

ACKNOWLEDGEMENTS

The authors would like to thank Dr. Augustus Way Fountain, III, Ms. Rebecca Braun, and Dr. Nicole Rosenzweig for continued scientific and administrative support.

REFERENCES

[1] Dominici, M. *et al.*, "Minimal criteria for defining multipotent mesenchymal stromal cells. The International Society for Cellular Therapy position statement", *Cytotherapy.* **2006**. 8(4), p315-317.
[2] Rastegar, F. *et al*., "Mesenchymal stem cells: Molecular characteristics and clinical applications", *World Journal of Stem Cells.* **2010**. 2(4), p67-80.
[3] Hoogduijn, M.J.; Cheng, A.; and Genever, P.G., "Functional nicotinic and muscarinic receptors on mesenchymal stem cells", *Stem Cells and Development.* **2009**. 18(1), p103-112.
[4] Hoogduijn, M.J.; Rakonczay, Z.; and Genever, P.G., "The effects of anticholinergic insecticides on human mesenchymal stem cells", *Toxicoligical Sciences.* **2006**. 94(2), p342-350.
[5] Friedenstein, A.J. *et al.*, "Heterotopic of bone marrow. Analysis of precursor cells for osteogenic and hematopoietic tissues", *Transplantation.* **1968**. 6(2), p230-247.
[6] Pittenger, M.F. *et al.*, "Multilineage potential of adult human mesenchymal stem cells", *Science.* **1999**. 284(5411), p143-147.
[7] Angelini, D.J. *et al.*, "Hypoxia-induced mitogenic factor (HIMF/FIZZ1/RELM alpha) recruits bone marrow-derived cells to the murine pulmonary vasculature", *PLOS ONE.* **2010**. 5(6), p11251.
[8] Kolosova, I.A. *et al.*, "Resistin-like molecule alpha stimulates proliferation of mesenchymal stem cells while maintaining their multipotency", *Stem Cells and Development.* **2013**. 22(2), p239-247.

pH Stable cationic polymer nanoparticles via cyclopropenium-based monomers and block copolymers

Kato L. Killops*[a], Kourtney L. Rutkowski[b], Spencer D. Brucks[c], Erica R. Valdes[a], Jessica L. Freyer[c], Yivan Jiang[c], Luis M. Campos[c*]
[a]U.S. Army Edgewood Chemical Biological Center, Research and Technology Directorate, 5183 Blackhawk Rd, Aberdeen Proving Ground, MD 21010
[b]Oak Ridge Institute for Science and Education, 1299 Bethel Valley Rd, Oak Ridge, TN 37830
[c]Department of Chemistry, Columbia University, 3000 Broadway, New York, NY 10027

ABSTRACT

Particles bearing cationic charge were synthesized using either cyclopropenium-based (CP) monomers or block copolymers via surfactant-free emulsion polymerization. Hydrated particle diameters for most of the monomers studied were smaller than 100 nm. Particle size could be adjusted by altering the amount of CP monomer added. Since CP is a remarkably stable carbocation, the particles retained their cationic charge (as measured by zeta potential) over a large pH range. These cationic particles have a wide range of applications in gene delivery, interfacial additives, cosmetics, enzyme stabilization, and chromatography, among others.

Keywords: Nanoparticles, latex, cationic, block copolymers, emulsion

1. INTRODUCTION

Exploration of the use of polymeric colloidal systems for applications in therapeutics and drug delivery has witnessed a dramatic increase the last decade. The ability to precisely tune the size and peripheral functionality of high surface area particles, along with the ability to load the interior with a therapeutic moiety is very desirable. Particles possessing a positive surface charge are well-suited for biological applications due to the known interaction of cationic groups with the extracellular membrane and subsequent cellular uptake. Furthermore, cationic particles have been shown to complex negatively charged DNA[1] and RNA,[2] which has implications for gene-based therapies.[3]

Particles prepared by emulsion polymerization provide an attractive means of accomplishing aforementioned goals for a number of reasons. Emulsion particles can be synthesized in large batches using water as the solvent, making them easily scalable for industrial manufacturing. Many traditional methods to achieve polymers in the sub-100 nm range involve the use of surfactants,[4] which can leach from the particles post-synthesis or require extensive cleaning procedures.[5] Alternatively, polymerization-induced self-assembly yields small particles in the absence of surfactant.[6,7] Although well-defined nano-objects can be synthesized, this strategy relies on the previous synthesis of a macro chain-transfer agent. Synthesizing particles with diameters less than 100 nm by surfactant-free emulsion polymerization remains a challenge,[8,9] and this size regime shows the most promise for *in vitro* and *in vivo* applications.[10,11]

Cationic particles in the sub-200 nm size regime are synthesized via surfactant-free emulsion polymerization primarily through the copolymerization of cationic monomers with hydrophobic monomers and a radical initiator.[12] Traditionally, tertiary amine and quaternated ammonium functional groups have been employed to yield cationic particles. Where amino moieties are concerned, syntheses must typically be conducted in acidic pH in order to maintain the charge on the ammonium group.[13] In the latter case, particles with stable positive charge due to quaternated ammonium monomers have limited synthetic versatility. Additionally, cation-containing block copolymers (BCP) can be employed as emulsion stabilizers, although there are relatively fewer of these reports in contrast with the use of cationic monomers.[14,15]

As the smallest Hückel aromatic structure, cyclopropeniums are emerging as a versatile class of carbocations that exhibit remarkable stability.[16] Within this realm, aminocyclopropeniums benefit from inductive charge stabilization of the amino substituents,[17] yielding cationic groups with pK_{R+} values near 13.[18] Thus, the aminocyclopropenium cations exist in their charged state over a very wide pH range. Furthermore, cyclopropenium can be functionalized with a range of dialkylamine groups and synthesized efficiently in large batches, with their versatility making them attractive for modular synthetic protocols. Potential applications for cyclopropenium ions include ionic liquids,[16] organocatalysts,[19-21] polyelectrolytes, and transition-metal ligands.[22]

Herein, we describe the synthesis of cationic nanoparticles with diameters down to ca. 30 nm by utilizing novel cyclopropenium-containing (CPR) monomers and BCPs (Scheme 1). The modularity of this approach is exemplified by

APPROVED FOR PUBLIC RELEASE

the ability to alter the R groups on the cyclopropenium monomer to achieve a range of monomer polarities. The particle diameters can be tuned by changing the cationic monomer incorporation. Additionally, both the interior and exterior of the particles can be addressed through the use of hydrophobic or anionic dyes, respectively.

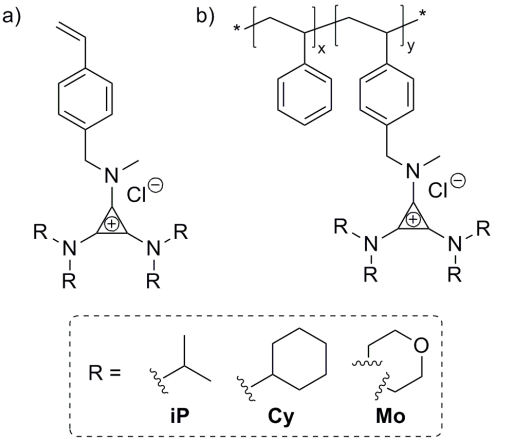

Scheme 1. Structures of (a) CPR monomers and (b) PS-*b*-P(CPR) diblock copolymers.

2. RESULTS AND DISCUSSION

Recently, a new class of polymerizable cyclopropenium molecules has been developed. The modularity of the cyclopropenium synthesis allows for tuning functional handle, and thus the resultant macromolecular physical properties.[18] Here, we investigate the use of isopropyl-, cyclohexyl-, and morpholine-functional CP moieties (**iPM, CyM,** and **MoM**, respectively) as comonomers to form stable cationic latexes with styrene. Particles were prepared in the absence of surfactant by standard emulsion polymerization with V-50 [2,2′-azobis(2-methylpropionamidine) hydrochloride] as the initiator. Table 1 summarizes the properties of the particles synthesized.

Table 1. Cationic latex particles prepared with different CP monomers.

Latex	D_h[a] (nm)	PD[a]	Zeta Potential (mV)	D_n[b] (nm)
0CP	337	0.44	16	214
1iPM	89	0.13	23	76
2.5iPM	70	0.16	35	58
5iPM	60	0.18	37	39
10iPM	45	0.22	46	36
20iPM	34	0.28	54	33
5CyM	61	0.25	44	53
10CyM	75	0.12	40	68
20CyM	62	0.36	33	53
5MoM	164	0.13	36	145

[a] Hydrodynamic diameter and polydispersity (PD determined by dynamic light scattering (DLS)).
[b] Particle diameter determined by scanning electron microscopy (SEM).

It has previously been difficult to achieve sub-100 nm emulsion particles without the addition of surfactant; however, the use of CP monomer enables the formation of particles with diameters down to circa 30 nm. To demonstrate control over particle size, we adjusted the amount of **iPM** incorporated into the monomer feed from 1 wt.% up to 20 wt.%. At just 1 wt.% **iPM** (denoted **1iPM**) relative to styrene (SI), the particle size and polydispersity (PD) were dramatically reduced, as compared with particles synthesized in the absence of SI, accompanied by an increase in zeta potential. In the absence of CP comonomer, the polystyrene (PS) latex is stabilized solely by the charges conferred from the V-50 initiator. This led to large particles with a bimodal size distribution and lower zeta potential, relative to the CP-stabilized particles. Figure 1

APPROVED FOR PUBLIC RELEASE

demonstrates the evolution of particle size and PD with the amount of iPM. With increasing CP incorporation, particle size is reduced, down to 34 nm in the case of 20iPM. The increase in CP corresponds to an increased coverage of the particle surface with cationic charges, allowing for smaller particles to be electrostatically stabilized. Full conversion of iPM was monitored by proton nuclear magnetic resonance (^{1}H NMR) spectroscopy, where the protons from unpolymerized monomer were absent from the region between circa 5.8 and 5.3 ppm, indicating that they are fully copolymerized with SI. Correspondingly, several broad peaks due to distinct protons from **iPM** are visible in the ^{1}H NMR spectrum between 5.0 ppm and 3.0 ppm.

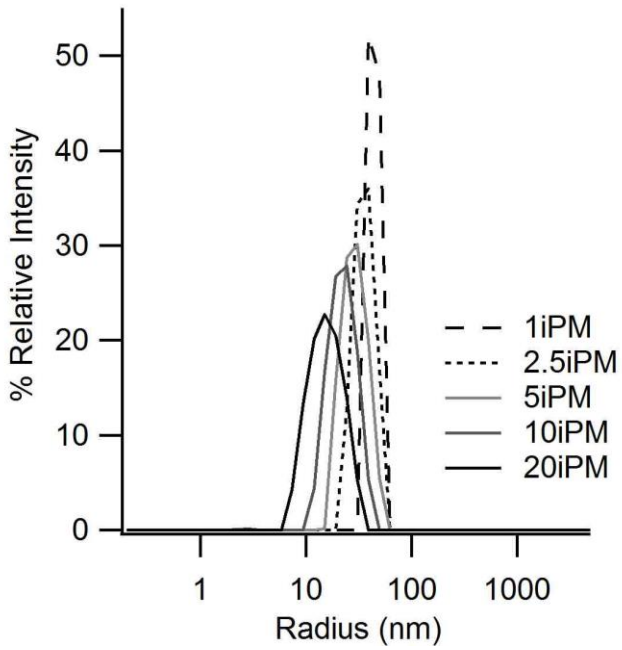

Figure 1. DLS particle size distributions with varied iPM incorporation.

Evolution of particle size was monitored over time for **10iPM** by removing aliquots of the polymerization solution and performing DLS. Figure 2 shows that within 5 minutes of starting the emulsion polymerization, the particles had reached 37 nm in diameter. The particle size continued to evolve over the course of the reaction, but changed little after the first hour, growing from 43 nm after 15 minutes to 45 nm after 24 hours. Light scattering of the reaction mixture prior to heating showed large particles and multimodal populations relative to the particle histograms collected after the start of the reaction (SI). The formation of small particles immediately after the application of heat and shear forces is indicative of stabilized monomer minidroplets,[13] where the charges on **iPM** decrease the surface tension of the styrene monomer and repel other particles against coalescence over the course of the polymerization.

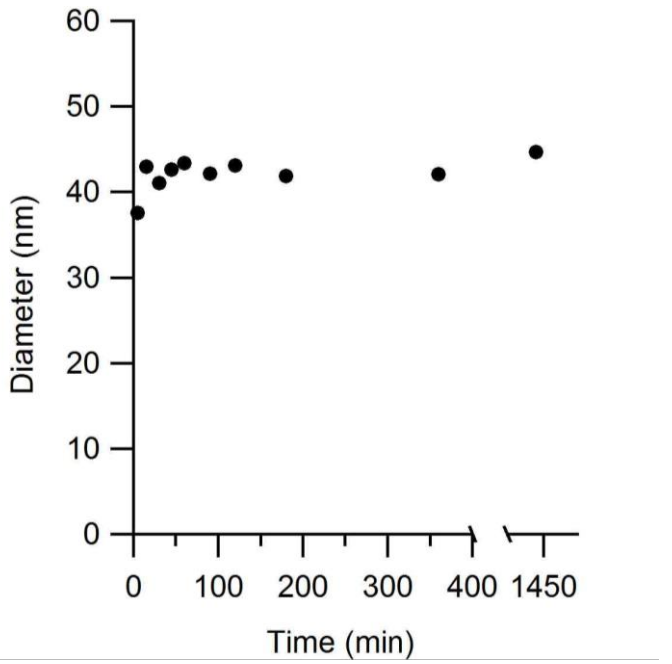

Figure 2. Growth in particle size of 10iPM over time as measured by DLS.

In an effort to tune the physical properties of the resultant particles, monomers encompassing cyclohexyl and morpholine functional groups were also investigated as emulsion stabilizers. In the case of **CyM**, the particles synthesized at 5 wt.% comonomer displayed a size (60 nm) similar to that of **5iPM**. Furthermore, in a smaller series of **CyM** particles, the same trend of decreasing particle size with increasing CP content was not observed. Because the **Cy** monomers are the most hydrophobic of the set, they may become entrapped within the growing particles more easily, decreasing their charge-stabilizing contribution to the particle overall. This hypothesis is supported by the gradual decrease in zeta potential with increasing **CyM** content. For **MoM**, the most hydrophilic monomer, particles synthesized with 5 wt.% feed had hydrated diameters of 164 nm. The increase in diameter may be attributed to the water solubility of the **MoM**, causing a significant amount of comonomer to be partitioned into the aqueous phase, leading to homopolymer formation.[23] There is no unpolymerized **MoM** present in the ^{1}H NMR spectrum, but it is difficult to distinguish homopolymer versus random copolymer formation in the spectra of these polydisperse macromolecules.

For applications requiring a persistent cationic charge, it is imperative that a cationic moiety remain positively charged over a wide pH range.[24,25] Cyclopropenium moieties have been shown to be remarkably stable, with pK_{R+} (the pH at which half of the CP groups are converted to the carbinol species) values greater than 10 for aminocyclopropenium ions.[17] To examine the stability of cationic charge on the cyclopropenium particles, zeta potential was measured as a function of pH for **5iPM**, as shown in Figure 3. The zeta potential of the particles remains above 30 mV for the entire pH range from pH 1.4 to 12.6. This stands in contrast to typical protonated amine cationic systems, which have an inflection point near the pK_a of the amine.[8] The particles appear stable over most of the pH range, as indicated by the constant hydrodynamic radius. However, at the highest and lowest pH values measured, an increase in the radius of the particles is observed suggesting the stability of the particles is compromised. Near the pK_{R+} at pH 12.6, a portion of the particles are converted to the carbinol, causing decreased repulsion and aggregation of the particles.

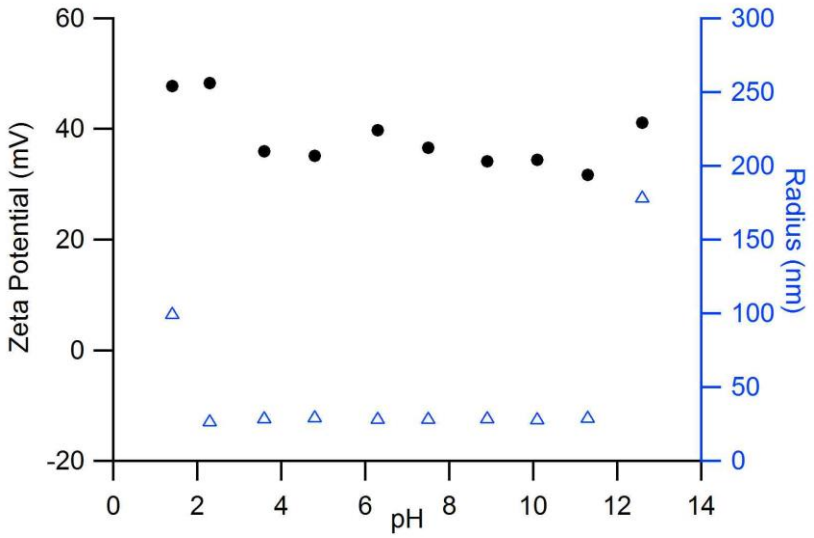

Figure 3. Zeta potential as a function of pH on 5iPM particles (black circles). Particle radii were measured simultaneously (blue triangles).

Amphiphilic CP BCPs were used as electrosteric particle stabilizers in the surfactant-free emulsion polymerization of styrene. Particles were synthesized with PS-*b*-P(CP) BCPs containing cyclohexyl-, isopropyl-, and morpholine-functional CP (**CyBCP**, **iPBCP**, and **MoBCP**, respectively). Each of the BCPs were synthesized to contain 30 mol% CP relative to PS. The data for the BCPs used can be found in Table 2. The BCPs were not directly soluble in water, so they were dissolved in the styrene before the addition of water to create the emulsion. The amphiphilic nature of this BCP causes the PS block to be anchored to the particle core[26] with the CP block extending into solution to stabilize the particle.

Table 2. CP BCP properties and cationic latex particles synthesized using CP BCPs.

CP BCP	MW[a] (kg/mol)	mol. % CP[a]	Latex	D_h[b] (nm)	PD[b]	Zeta Potential (mV)	D_n[c] (nm)
MoBCP	47	30	**5MoBCP**	194	0.29	45	146
CyBCP	50	30	**5CyBCP**	180	0.18	36	174
iPBCP	27	30	**5iPBCP**	94	0.15	39	72

[a] Determined by ^{1}H NMR.
[b] Hydrodynamic diameter and PD determined by DLS.
[c] Particle diameter determined by SEM.

The BCPs were added to the emulsion at 5 wt.% relative to styrene, which translates to less than 1 mol.% of CP. Even at this low incorporation of BCP, stable particles were formed. The particles were characterized by DLS, electrophoretic mobility, and SEM. Particles formed from **5MoBCP** had the largest diameter at 194 nm. These particles also exhibited the highest zeta potential at 45 mV. Since the **MoBCP** is the most hydrophilic of the CP BCPs, it is likely that the BCP chains are well-solvated and extend into the water phase, increasing the hydrodynamic radius of the particle. With the BCPs, decreasing polarity of the CP moiety corresponded with decreasing zeta potential. For the most hydrophobic **CyBCP** it is possible that some of the polymer chains became entrapped within the particle, leading to a decrease in surface charge and zeta potential. Further evidence of the BCP anchoring to the particles is provided by the existence of the polymer corona extending from the particle surface, exemplified by the significant difference between particle diameters measured by DLS and SEM.[27] Interestingly, the difference in particle diameters between DLS and SEM measurements also correlates with the hydrophilicity of the CPR group. The hydrated diameter of **MoBCP** particles includes the well-solvated chains extending from the particle surface and is 48 nm larger than SEM, where the BCP chains are collapsed. Particles synthesized with **iPBCP** having intermediate hydrophilicity, albeit with a lower overall MW, exhibit a difference of 12 nm. The most hydrophobic **CyBCP** particles display a difference of only 6 nm between the hydrated and collapsed diameters, indicating that the chains are minimally extended in solution, as expected. Overall, the particles formed through stabilization with CP BCPs are much larger than those formed by CP monomers. This can be understood by comparing the relative number of moles of CP present, where there are fewer molecules of BCP present to stabilize particles.

Conversely, a larger number CP monomer molecules can achieve better surface coverage, which more effectively stabilizes the droplet/particle interface, leading to smaller particles overall.

3. CONCLUSION

To summarize, we have synthesized cationic polymer nanoparticles by using novel cyclopropenium-based monomers and BCPs. The application of CP-containing molecules to stabilize the particle interface has negated the need for additional stabilizers, solvent mixtures, or multi-step protocols, while enabling the formation of sub-100 nm particles. The particles were found to have highly positive zeta potential values, which were maintained over a wide pH range. We expect that these nanoparticles have tremendous potential for a range of biological and industrial applications.

ACKNOWLEDGEMENTS

This research was funded by the Department of the Army Basic Research Program and sponsored by the Edgewood Chemical Biological Center. Financial support for Columbia University researchers was partially provided by the Army Research Office. K.R. thanks the Minority Undergraduate Summer Internship Program for the opportunity to conduct research at the U.S. Army Edgewood Chemical Biological Center.

REFERENCES

[1] Singh, M. *et al.*, "Cationic microparticles: A potent delivery system for DNA vaccines", *Proceedings of the National Academy of Sciences.* **2000**. 97(2), p811-816.
[2] Forbes, D. and Peppas, N., "Polycationic nanoparticles for siRNA delivery: Comparing ARGET ATRP and UV-initiated formulations", *ACS Nano.* **2014**. 8(3), p2908-2917.
[3] Guo, X. and Huang, L., "Recent advances in nonviral vectors for gene delivery", *Accounts of Chemical Research.* **2012**. 45(7), p971-979.
[4] Ramos, J. *et al.*, "Kinetics of the batch cationic emulsion polymerization of styrene: A comparative study with the anionic case", *Journal of Polymer Science Part A: Polymer Chemistry.* **2006**. 44(15), p4461-4478.
[5] Ramos, J. *et al.*, "Cationic polymer nanoparticles and nanogels: From synthesis to biotechnological applications", *Chemical Reviews.* **2014**. 114(1), p367-428.
[6] Charleux, B. *et al.*, "Polymerization-induced self-assembly: From soluble macromolecules to block copolymer nano-objects in one step", *Macromolecules.* **2012**. 45(17), p6753-6765.
[7] Zhang, X. *et al.*, "Well-defined amphiphilic block copolymers and nano-objects formed via RAFT-mediated aqueous emulsion polymerization", *Macromolecules.* **2011**. 44(11), p4149-4158.
[8] Voorn, D-J. *et al.*, "Control of charge densities for cationic latex particles", *Macromolecules.* **2005**. 38(9), p3653-3662.
[9] Liu, Z. *et al.*, "Emulsifier-free emulsion copolymerization of styrene with quaternary ammonium cationic monomers", *Journal of Applied Polymer Science.* **2000**. 76(7), p1129-1140.
[10] Elsabahy, M. and Wooley, K., "Design of polymeric nanoparticles for biomedical delivery applications", *Chemical Society Reviews.* **2012**. 41(7), p2545.
[11] Minigo, G. *et al.*, "Poly-l-lysine-coated nanoparticles: A potent delivery system to enhance DNA vaccine efficacy", *Vaccine.* **2007**. 25(7), p1316-1327.
[12] Liu, Q. *et al.*, "Research progress on the preparation and application of monodisperse cationic polymer latex particles", *Polymer International.* **2012**. 61(11), p1593-1602.
[13] Ni, H. *et al.*, "Mechanism of soap-Free emulsion polymerization of styrene and 4-vinylpyridine: Characteristics of reaction in the monomer phase, aqueous phase, and their interface", *Macromolecules.* **2001**. 34(19), p6577-6585.
[14] Amalvy, J. *et al.*, "Synthesis of sterically stabilized polystyrene latex particles using cationic block copolymers and macromonomers and their application as stimulus-responsive particulate emulsifiers for oil-in-water emulsions", *Langmuir.* **2004**. 20(11), p4345-4354.
[15] Save, M. *et al.*, "Synthesis by RAFT of amphiphilic block and comblike cationic copolymers and their use in emulsion polymerization for the electrosteric stabilization of latexes", *Macromolecules.* **2005**. 38(2), p280-289.
[16] Curnow, O. *et al.*, "Triaminocyclopropenium salts as ionic liquids", *Chemical Communications.* **2011**. 47(37), p10248.
[17] Kerber, R. and Hsu, C-M., "Substituent effects on cyclopropenium ions", *Journal of the American Chemical Society.* **1973**. 95(10), p3239-3245.
[18] Bandar, J. and Lambert, T. "Aminocyclopropenium ions: Synthesis, properties, and applications", *Synthesis.* **2013**. 45(18), p2485-2498.

[19] Bandar, J. and Lambert, T., "Enantioselective brønsted base catalysis with chiral cyclopropenimines", *Journal of the American Chemical Society.* **2012**. 134(12), p5552-5555.
[20] Bandar, J. and Lambert, T., "Cyclopropenimine-catalyzed enantioselective mannich reactions of -butyl glycinates with -boc-imines", *Journal of the American Chemical Society.* **2013**. 135(32), p11799-11802.
[21] Bandar, J. *et al.,* "Transition state analysis of enantioselective brønsted base catalysis by chiral cyclopropenimines", *Journal of the American Chemical Society.* **2014**. 136(30), p10700-10707.
[22] Bruns, H. *et al.,* "Synthesis and coordination properties of nitrogen(I)- based ligands", *Angewandte Chemie International Edition.* **2010**. 49(21), p3680-3683.
[23] Ramos, J. and Forcada, J., "The role of cationic monomers in emulsion polymerization", *European Polymer Journal.* **2010**. 46(5), p1106-1110.
[24] Wang, Y-J. *et al.,* "Alkaline polymer electrolyte membranes for fuel cell applications", *Chemical Society Reviews.* **2013**. 42(13), p5768.
[25] Zeng, Z. *et al.,* "Synthetic polymer nanoparticle–polysaccharide interactions: A systematic study", *Journal of the American Chemical Society.* **2012**. 134(5), p2681-2690.
[26] Burguière, C. *et al.,* "Block copolymers of poly(styrene) and poly(acrylic acid) of various molar masses, topologies, and compositions prepared via controlled/living radical polymerization. application as stabilizers in emulsion polymerization", *Macromolecules.* **2001**. 34(13), p4439-4450.
[27] Riess, G. and Labbe, C., "Block copolymers in emulsion and dispersion polymerization", *Macromolecular Rapid Communications.* **2004**. 25(2), p401-435.

On resonant Raman enhancement driven by nano-scale intermolecular interactions

Jerry B. Cabalo*[a], Erik B. Emmons[b], Craig K. Knox[b], Semion K. Saikin[c], Dmitrij Rappoport[c]
[a]U.S. Army Edgewood Chemical Biological Center, Research and Technology Directorate, 5183 Blackhawk Rd, Aberdeen Proving Ground, MD 21010
[b]Leidos, Inc., P.O. Box 68, Gunpowder Branch, Aberdeen Proving Ground, MD 21010
[c]Department of Chemistry and Chemical Biology, Harvard University, 12 Oxford St, Cambridge, MA 02138

ABSTRACT

The understanding of how intermolecular interactions affect resonance Raman spectroscopy is relevant to a number of Army missions, such as the sensing of hazardous materials. To investigate changes in the resonance Raman in response to intermolecular interactions we used an experimental and theoretical study of two series of peptides containing tyrosine and cysteine, and tyrosine and L-C-propargylglycine, in solution, and in contact with the surface of titania anatase nanoparticles. Four technical barriers were shown in the course of this study. The first barrier was the incorrect assumption that high-lying electronic states could be neglected. Our results show that for tyrosine, high-energy electronic states out of resonance with the excitation can influence the Raman response and that intermolecular interactions can act on the molecular polarizability through these states. Three of the technical barriers were not overcome: 1) correct preparation of amino acid or peptide samples in close contact with the nanoparticle surfaces where signal predominantly arises from molecules on the surface, 2) correct calculation of peptides in contact with a transition metal oxide including the excited electronic states, and 3) correct selection of test molecules that demonstrate change in response to the presence of a surface.

Keywords: resonance Raman, SERS, titania, anatase, tyrosine, sum of states

1. INTRODUCTION

Raman spectroscopy is a very important analytical tool because it has such a high degree of chemical specificity. This spectroscopic approach is highly applicable to a number of Army missions, including the sensing of hazardous materials such as explosives,[1] toxic chemicals,[2] and pathogenic organisms,[3] or obtaining an understanding of how these toxic materials affect biological systems, such as the binding of organophosphates to acetylcholinesterase. However, low sensitivity limits the utility of this powerful technique. In recent years, a number of methods for overcoming sensitivity limitations involving surface enhanced Raman spectroscopy (SERS) or resonance Raman spectroscopy (RRS) have been demonstrated. These methods, such as RRS, exploit the selectivity of Raman spectroscopy while taking advantage of the electronic structure of the target molecule to amplify the Raman signal.

RRS depends on resonance between the excitation laser and electronic states within the analyte molecule. Only normal mode vibrations involving the atoms within the chromophore experience enhancement.[4] While this selectivity towards vibrational modes within a chromophore is an advantage for some applications, it is also desirable to permit vibrational modes outside of the chromophore to experience resonant enhancement in a controlled manner. An understanding of how vibrational modes that do not directly involve the chromophore interact with the excited electronic states of that chromophore may permit controlled enhancement of these modes.

Within the sum-of-states framework,[5,6] the polarizability tensor elements depend on the electronic transition dipole moments and vibrational wavefunctions. More specifically, the symmetric part of the RRS enhancement depends on the probability of transition to the intermediate excited vibrational state and back down to the final vibrational state. These probabilities are proportional to the Franck-Condon (F-C) factors.[7] The non-symmetric vibrations are enhanced by the Herzberg-Teller (H-T) terms,[8] which are the overlap integrals of the nuclear wavefunctions and the normal mode coordinate. Also contributing to the non-symmetric portion of the enhancement are the gradients of the transition dipole moments between electronic states in the sum. Based on this, we expect anharmonicity within a molecule to allow for coupling between the excited vibronic states, thus permitting enhancement of normally dark vibrational modes.[9] We initially hypothesized *that intermolecular interaction induced anharmonicity will delocalize resonance enhancement from the absorbing chromophore due to greater than expected mixing between vibrational modes.* However, this hypothesis makes a number of assumptions. First, it assumes the most important perturbation to the target molecule comes from intermolecular interactions acting on the ground state potential energy surface or on the potential energy surface of the

APPROVED FOR PUBLIC RELEASE

excited state in resonance with the excitation. Second, it assumes the contribution to the resonance Raman signal can be neglected from high energy electronic states not in resonance with the excitation. We found these assumptions to be inadequate, and reformulated the hypothesis to focus on the modifications to the electronic structure. *We hypothesize that intermolecular interaction will delocalize resonance enhancement from the absorbing chromophore due to induced changes to the molecular electronic structure.* In other words, intermolecular interactions will either modify the energy spacings between the electronic states (as observed when the absorption spectrum of compounds shifts in wavelength depending on solvent), or will modify the curvature of the ground and excited state potential energy surfaces, that is, cause vibrational frequency shifts.

Understanding the connection between the electronic structure of the analyte molecule and the resonance Raman spectrum has been a focus of this program as a stepping stone to understanding how intermolecular interactions affect the resonance Raman signature. The impact of molecular electronic structure on the resonance Raman signature can be seen through the anti-resonance phenomenon, where the Raman intensity is much less than to be expected based on the optical absorption. Anti-resonances are thought to occur[10-14] when pre-resonance of a strongly allowed electronic transition destructively interferes with the resonance with a weakly allowed electronic transition. This is why the resonance Raman signal does not simply follow the curve of the absorption spectrum. Destructive interference between electronic states in the sum-over-states in tryptophan results in a "window" around 205 nm with reduced Raman return that enables studies of RRS of amide bonds with minimal interference.[12] Theoretical modeling is essential to understanding of anti-resonance phenomena in RRS spectra, which in turn is critical for understanding the impact of intermolecular interactions. While it is not experimentally possible to probe in detail the connection between the RRS and the electronic structure, e.g., detect electronic transitions deep in the vacuum UV or probe weakly allowed and unresolved transitions, it is possible to model the electronic structure in detail. The electronic structure of molecules can be simulated with experimentally-validated time-dependent density functional theory (TDDFT) models, and the influences of the individual electronic states on the RRS return can be studied in the model. Thus, the general approach is to first simulate a relevant molecule both in solution and on a surface and predict a quantity, such as a resonance Raman spectrum, that can be experimentally measured; then, validate the model by comparison to the experiment, and then use the model to deduce the impact of intermolecular interactions on the resonance Raman under the sum-over-states framework.

We use tyrosine, and peptides containing it in solution and on surfaces, in this study for three reasons. First, tyrosine is biologically very important, where it serves as a ligand for metal containing enzymes or even as part of the active site itself, as in the globins or acetylcholinesterase. Second, tyrosine possesses an aromatic side chain that enables it to experience resonance enhancement independently from most other amino acids, at readily accessible UV wavelengths. Third, this amino acid has been examined extensively with a number of experimental studies reported that can be used to validate modeling results. Therefore, a detailed theoretical analysis, combined with experimental studies, helps to shed additional light on the influence of dark or weakly allowed electronic states. To test the hypothesis, we utilize a set of peptides containing tyrosine and L-C-propargylglycine (PG). PG is not one of the standard twenty α-amino acids, but it is a naturally occurring toxin found in the *Aminita abrupta* mushroom. PG contains an acetylene side chain with a distinctive vibrational frequency around 2250 cm^{-1} that is easily separated from the rest of the vibrational spectrum. Furthermore, the C-C stretch is highly symmetric, so we expect this mode to receive significant RRS enhancement. The set of peptides uses different numbers of glycine "spacer" residues to control the molecular distance between PG and tyrosine. Thus, PG is expected to act as a "reporter" which we monitor as a function of distance from the tyrosine. We expect to see the impact of intermolecular interactions in how the PG signal changes whether it's in contact with a surface or in solution. For our test surfaces, we utilize nano-scale titania anatase particles. Titania anatase is known to allow charge transfer to occur when in the presence of UV light, and this substrate is expected to have a maximum impact on the electronic structure of the tyrosine-containing peptides.

2. EXPERIMENTAL APPROACH

2.1 Laboratory methods

Non-resonance Raman, RRS, and SERS measurements were performed both for solution and solid phase samples. The solution phase samples for the cross section measurements were prepared by dissolving the material of interest in ultrapure water. To mitigate the photodegradation of the tyrosine solutions, the samples were magnetically stirred in small glass cups during the measurements, so that the laser beam was continuously exposed to fresh sample. The cups were covered with UV-transparent quartz cover slips to prevent evaporation of the acetonitrile internal standard.

The UV RRS measurements were carried out with an in-house built spectrometer system. The UV laser light was generated with two different laser systems. A frequency-doubled argon-ion laser was used to generate 229 nm and 244 nm continuous wave excitation light. A frequency-quadrupled pulsed neodymium-doped yttrium lithium fluoride (Nd:YLF) laser was used to generate 262 nm radiation with a high-repetition rate (~3 kHz) and low pulse energies. In all cases the incident

laser power on the sample averaged ~10-50 mW. A backscattering configuration was used in which the laser beam was directed onto the sample by a right angle mirror attached to the central obscuration of the reflecting objective. A triple grating spectrometer was used to disperse the Raman scattered light. The light was detected using a thermoelectrically-cooled UV-enhanced charge-coupled device camera. The Raman shift was calibrated for each excitation wavelength by measuring known bands of acetonitrile and cyclohexane. Blank spectra were collected at each excitation wavelength and subtracted from the RRS spectra. Standard laboratory bench top Raman spectrometers were used to measure non-resonant Raman and SERS spectra at 532 nm and 785 nm. For SERS measurements, cysteine-containing peptides were added to silver colloid to examine the effect of chain length on the SERS response. This set of peptides contained tyrosine, cysteine with the thiol side chain, and an increasing number of glycine residues acting as spacers (TyrCys, TyrGlyCys, and TyrGlyGlyCys).

Ultraviolet-visible spectroscopy (UV-Vis) absorption measurements were performed to obtain the absorbance in the wavelength range from 190-800 nm. In addition to general guidance for the RRS measurements, the absorption measurements provide parameters necessary to correct for absorption effects on the Raman cross section values. High-performance liquid chromatography-grade acetonitrile was used as the cross section standard, where the cross section values for acetonitrile were obtained from the work of Asher et al.[15]

For measurements of solid samples as well as amino acid and peptide residues on titania anatase nano-particles, the same equipment as above was used. For the preparation of peptides deposited on nano-particle surfaces, 1 mL of the amino acid/peptide stock solution was taken, and a measured amount of the titania powder was added to the solution. The mass of the added powder was determined by the necessary surface area to nominally adsorb one monolayer of peptide. To determine the degree of pure amino-acid/peptide formation, scanning electron microscopy (SEM), powder X-ray diffraction (XRD), and UV microscopy were used to search for crystal formation. Solid samples were mounted on aluminized glass slides, and the RRS scattering was collected in the same system as described above.

2.2 Theoretical methods

2.2.1 Raman prediction methods

In order to validate theoretical models, UV-Vis absorption spectra, RRS spectra, and RRS excitation profiles were predicted and compared to experimental measurements. For UV-Vis absorption spectra, simple single point energy calculations within TDDFT were performed and compared to laboratory measurements. For the calculation of RRS and RRS excitation profiles, the sum-over-states approach was used. Excitation profiles are the RRS cross section of a given vibrational mode as a function of excitation energy. Within the simplified sum-over-states approach, the resonance Raman cross section is represented as a sum over excited electronic states and is obtained by straightforward differentiation of the sum-over-states expansion of the frequency-dependent polarizability with respect to a vibrational normal mode.[16] The differential Raman scattering cross section for a given normal mode Q can be written as

$$\left(\frac{\partial\sigma}{\partial\Omega}\right)_Q = \frac{(\omega-\omega_Q)^4}{2\omega_Q c^4}\left|\langle\boldsymbol{\sigma}_Q(\omega)\rangle\right|^2 \quad (1)$$

where w is the excitation frequency, w_Q is the vibrational frequency of mode Q, c is the speed of light, and $\langle\boldsymbol{\sigma}_Q(\omega)\rangle$ is the angle-averaged Raman scattering tensor. The Cartesian component mn of the Raman scattering tensor is computed as

$$\sigma_Q^{mn}(\omega) = \sum_k\left[-\mu_{0k}^m\mu_{0k}^n\left[\frac{(\Omega_k-\omega)^2-\gamma_k^2}{\left((\Omega_k-\omega)^2+\gamma_k^2\right)^2}+\frac{2i(\Omega_k-\omega)\gamma_k}{\left((\Omega_k-\omega)^2+\gamma_k^2\right)^2}\right]\frac{\partial\Omega_k}{\partial Q}+\left[\mu_{0k}^m\frac{\partial\mu_{0k}^n}{\partial Q}+\frac{\partial\mu_{0k}^m}{\partial Q}\mu_{0k}^n\right]\left[\frac{\Omega_k-\omega}{(\Omega_k-\omega)^2+\gamma_k^2}+\frac{i\gamma_k}{(\Omega_k-\omega)^2+\gamma_k^2}\right]\right] \quad (2)$$

where Ω_k is the electronic state excitation energy of the k^{th} electronic state, $\mu_{0k}{}^m$ and $\mu_{0k}{}^n$ are the m and n components of the $0\rightarrow k$ transition dipole moment, and γ_k is its linewidth. There are some key features in the above expression. First, the two terms in equation (2) are analogous to the Albrecht A and B terms.[5] As with the Albrecht A term, the first term in equation (2) has the derivative of the excitation energy Ω_k with respect to the normal coordinate Q which is only non-zero for symmetric vibrational modes. Second, as the excitation frequency ω approaches the excitation energy Ω_k, there is resonance with one of the excited electronic states and that state is expected to dominate the Raman intensity, which potentially allows us to restrict the summation to the excited states near or below the excitation frequency ω. The linewidth γ_k of the k^{th} excited electronic state cannot be computed from first principles. Thus, we approximated γ_k in resonance Raman spectra by the linewidth fitted from the experimental absorption spectrum.

We optimized the ground-state structures using density functional theory with Becke, three-parameter, Lee-Yang-Parr (B3LYP) hybrid functional[17] and triple-zeta basis TZVPP (triple-zeta valence plus polarization) sets.[18] The structure optimizations included the conductor-like solvation model (COSMO) with the effective dielectric constant for water.[19] Subsequently, vibrational modes, transition dipole derivatives, and excitation energy gradients were computed by

numerical differentiation of the ground-state energy gradients, transition dipoles,[20,21] and excitation energies,[22] respectively, including the effect of solvation, while the frequencies of electronic transitions and transition dipoles were computed analytically without COSMO. Most calculations were performed using the Turbomole suite of programs, version 6.0, although some calculations were performed using Gaussian 2009 Rev C.01.[24] In order to compare computed sum-over-states RRS with another approach, we calculated the RRS of neutral tyrosine using the time-dependent approach of Jensen et al.[25] as implemented in the Amsterdam Density Functional (ADF) code. Following the approach of Jensen and Schatz we utilized the BP86[26-28] functional and the TZP[29] (triple ζ plus polarization functions Slater type orbitals basis set). Spectra were calculated with the AORESPONSE[30,31] module as well as using the COSMO model to account for solvation in water.

The use of the sum-over-states approach is preferred for this study because it allows us to examine the influence of individual electronic states to the RRS excitation profile and see the influence of interference or anti-resonance enhancement, and it allows us to readily examine the influence of electronic state lifetime on RRS.

2.2.2 Modeling on surfaces

Models of the titania anatase surface were constructed from the bulk unit cell structure and cleaved on the (1 0 1) crystal plane. A three dimensional model was formed with periodic boundary conditions with a vacuum slab, making a 4 x 4 supercell, and optimizing the structure within the DFT code DMOL3. Up to 16 explicit water molecules were added to the surface of the model, and the surface was reoptimized to take into account hydration of the anatase surface. A model of the tyrosine and tyrosine containing peptides were then optimized on that surface. Because TDDFT is not currently implemented for periodic systems, calculation of the RRS necessitated removing the periodic boundary conditions and working with an atomic cluster model. The hydrated titania cluster model is then imported into either TURBOMOLE or GAUSSIAN, and treated as a frozen and only the amino acids are optimized. In the same way, models of the tyrosine and cysteine containing peptides on silver are treated as an interaction with a small metal cluster, although since the SERS experiments occur in solution, and the water is treated with a polarizable continuum model. To explore possible preferred orientations, molecular dynamics simulations were performed using LAMMPS and the CHARMM force field on replicates of a model of PG-Tyr interacting with an anatase surface in the presence of explicit water molecules. The force field parameters of titanium and oxygen atoms in the metal oxide were taken from gas phase DFT potential energy surface scans along the bond coordinates and partial charge data were taken from Kang, et al.[32] The simulations were used to determine the portion of the peptide that preferentially bound to the titania surface as well as the most likely orientation to the surface in terms of the cant angle, i.e. the angle between the normal to the surface and the vector between the ends of the peptide.

3. RESULTS AND DISCUSSION

3.1 Investigation of RRS, electronic structure, and anti-resonance enhancement

In order to improve the understanding of the connection between the excitation profiles and the electronic structure, we performed a detailed experimental and theoretical study of tyrosine and the tyrosinate anion in solution. The excitation profiles determine the relative intensities of the RRS spectrum at any given excitation wavelength. Although this system has been already extensively reported on in the literature, the existing literature values provide validation points for both modeling and experimental methods, as well as providing the simplest system as a starting point. To this end, we first establish the accuracy of the simplified sum-over-states approach for tyrosine and tyrosinate by comparing the theoretical predictions to experimental UV-Vis absorption spectra, RRS spectra measured with 229 nm and 244 nm excitation, and excitation profiles from this work and in the literature. In addition, a detailed understanding of tyrosine alone should help highlight differences in the RRS spectrum caused by its inclusion in a peptide chain.

3.1.1 Validation of TDDFT models

For a first validation point for the theoretical RRS, we compared the theoretical and experimental UV-Vis spectra of tyrosine and tyrosinate. For the neutral tyrosine, the form of the predicted curve generally follows the experimental measurement. Molar absorptivities were measured, which compare well with literature values.[33] The differences between the theoretical and experimental spectra are typical for TDDFT calculations. For the tyrosinate at pH 13 the agreement between theory and experiment is even better, where the experimental UV-Vis absorption spectrum replicates the red shift in the predicted electronic absorption curve.

The second validation point for the theoretical models of the two forms of tyrosine is the comparison of theoretical and experimental RRS spectra. Figure 1 shows the comparison of theoretical and experimental RRS spectra with 229 nm and 244 nm laser excitation. Excellent agreement in terms of relative intensities is obtained for neutral tyrosine with 229 nm excitation. Peaks are easily assigned to the 8a, 8b, ring-O stretch, ring-C stretch, 9a, and a ring breathing mode. Except for the excited-state linewidth γ, which was fitted to the experimental absorption spectrum, no empirical or scaling factors

were applied in the calculation of the RRS. Similarly, the theoretical spectrum for the 244 nm excitation matches the experimental spectrum very well. For tyrosinate with 244 nm excitation, similar agreement between theory and experiment is obtained. For this particular system, the sum-over-states result visually resembles the experimental spectrum more than the conventional finite-lifetime calculation.

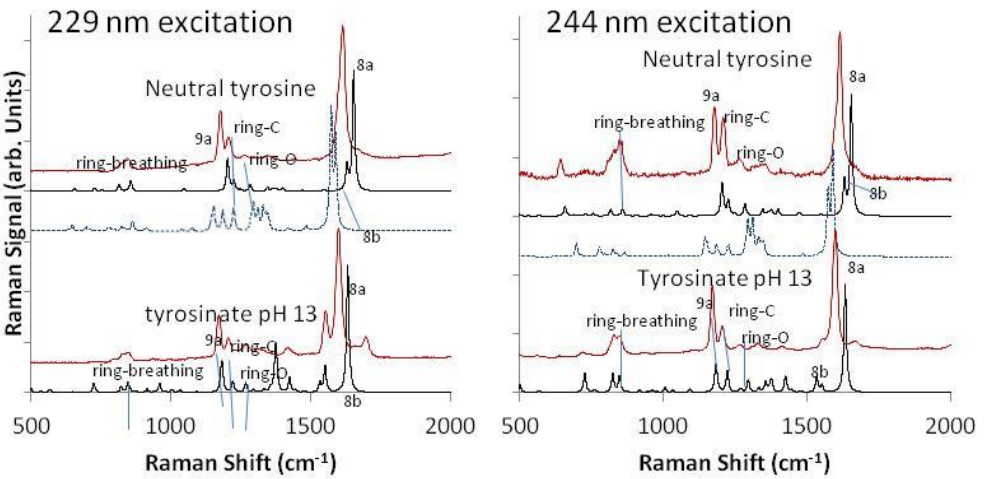

Figure 1. Comparison of theoretical and experimental RRS spectra with 229 nm and 244 nm laser excitation. Red traces represent experimental measurements, the black traces represent the results of the simplified sum-over-states calculations for 20 electronic states, and the blue dashed lines represent the results of the time-dependent approach as implemented in the ADF code for comparison.

We compared theoretical predictions for the absolute Raman cross sections to experimental measurements from this study and Fodor,[34] Ludwig,[35] and Asher.[36] The excitation profiles, that is, theoretical absolute Raman cross sections as a function of excitation wavelength, compare well to the experimental measurements for all modes considered.

3.1.2 Destructive interference

The crucial advantage of the simplified sum-over-states approach is that it allows investigation of the interference between contributions from different electronic states to the RRS excitation profiles. Figure 2 shows the comparison of the theoretical electronic absorption curve to the RRS excitation profiles predicted from the summation of 5, 10, 15, and 20 lowest-energy electronic states for the 8a mode. The summation over the five lowest lying electronic states includes the two transitions at 253 nm and 221 nm that we assigned to the L_a and L_b transitions in the TDDFT electronic excitation spectrum. In addition, the TDDFT calculations predict much weaker transitions between 190 nm and 205 nm, and the strongly absorbing $B_{a,b}$ transitions are predicted to fall within the 170-190 nm range. The effects of different electronic states on the total predicted RRS cross section are clearly visible for the investigated modes. As with Figure 1, three absorption features are apparent in the electronic absorption spectrum even in log scale.

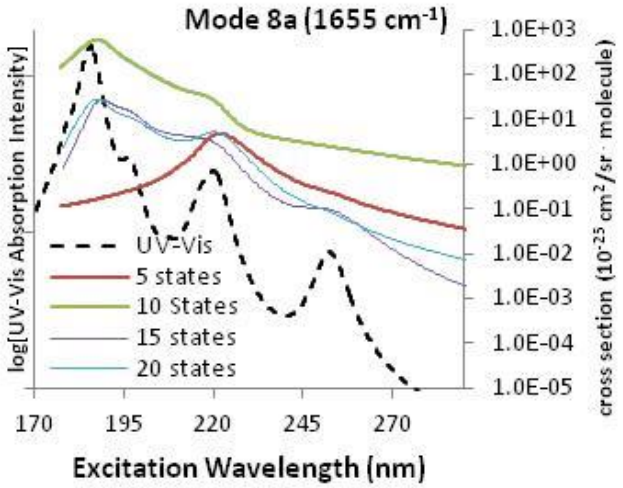

Figure 2. Comparison of the excitation profiles of the 9a, ring-C stretch, 8b, and 8a modes of neutral tyrosine for summations of 5, 10, 15, and 20 electronic states to the theoretical electronic absorption curve. All y-axes are on log scale.

As five next higher-lying electronic states are added to the sum-over-states, the excitation profile increases, so that the excitation profile generally matches the maximum absorption at approximately 185 nm, and the absorption feature at 220 nm is reflected as a shoulder in the excitation profile. However, when additional excited states deep in the UV are included in the sum for a total of 15 states in the summation, two interesting observations can be made. First, the excitation profile relative to that determined for the 10-state summation, is reduced across the entire excitation energy range considered. For excitation wavelengths close to the 220 nm feature we attribute to the L_a absorption, the absolute cross sections are reduced by nearly a factor of four. The reduction in cross section approaches two orders of magnitude for excitation wavelengths far from the 220 nm feature. This is a surprising result because high-energy electronic states that are far from resonance with the optical excitation can have such a strong influence, even when the optical excitation is in resonance with a lower energy transition. The contribution of high-energy electronic states should not be neglected, especially when the oscillator strengths are much greater than the lower energy transitions. The terms in the sum-over-states corresponding to higher energy transitions have a considerable effect on the calculated cross section. Without inclusion of at least 15 electronic states, the agreement between the experimental and theoretical excitation profiles is clearly unsatisfactory.

For additional electronic states, convergence seems to be reached with respect to the number of electronic states included in the sum since the excitation profile for 20 states is nearly identical to that obtained for 15 electronic states. Based on the dependence of the predicted excitation profile on the electronic states included in the sum-over-states, we conclude that the theoretical model is showing destructive interference between different transition dipole moments to different electronic states. While excitation can be in direct resonance with a given electronic state, interference from more strongly absorbing states deep in the UV can have a strong impact on the RRS cross section. Although it is possible that other states deeper in the UV may still have an effect, the summation over the 20 lowest electronic states including the L_a, L_b, and $B_{a,b}$ transitions captures the behavior of the RRS spectra and excitation profiles sufficiently well. We had similar findings for the tyrosinate anion. It should also be pointed out that the models give insight on the influence of very high-energy transitions that cannot be measured experimentally due to photoinduced degradation of the analyte molecule. The importance of destructive interference from electronic states above the excitation photon energy means that intermolecular interactions may also impact the RRS spectrum through these states as well.

3.1.3 Considerations of the effects of broadening of the electronic transitions on the RRS spectrum

It is necessary to consider the effect of electronic transition broadening on the sum-over-states model in order to use the latter to understand interference effects on the RRS spectrum. In using the experimental linewidth in the calculation of the RRS spectrum for the damping constant in the sum-over-states approach, we assume that the linewidth arises only from homogeneous broadening mechanisms, and neglect inhomogeneous broadening, such as solvent effects, or other mechanisms. As shown in equation (2), the simplified sum-over-states utilized in this study only accounts for the effect of homogeneous broadening to the electronic absorptions. If mechanisms other than homogeneous broadening make a significant contribution to the experimental linewidth, then the true homogeneous broadening factor would be smaller than

that used to calculate RRS spectra. In addition, inhomogeneous broadening also can change the lineshape of an electronic transition from a Lorentzian to a Gaussian or Voigt shape. Outside of the full width half max (FWHM), the Gaussian and Voigt lineshapes go more rapidly to zero than the Lorentzian lineshape. Thus, the effect of a significant contribution from an inhomogeneous broadening mechanism would be to reduce interference between electronic states in the sum-over-states. In addition to a reduction of interference between electronic transitions, a decrease in the homogeneous broadening damping factor would be to increase the predicted Raman cross section. It was noted above that the theoretical absolute Raman cross sections consistently underestimate the experimental values, and a smaller homogeneous damping factor may account for the consistent difference between theoretical prediction and experimental cross section values.

To demonstrate the effect of a smaller contribution of homogeneous broadening to the linewidth in the electronic spectrum on the sum-over-states model, and to provide a basis for comparison to experimental data, excitation profiles are calculated for a progression of damping constants. Figure 3 shows a comparison of calculated excitation profiles for the 8a, mode for the values 0.05 eV and 0.2 eV of homogeneous broadening. For the 0.2 eV and 0.3 eV linewidths, the excitation profiles are nearly identical, and the excitation profile values for the 0.1 eV linewidth fall midway between those for the 0.05 eV and 0.2 eV profiles. As expected, the result of the reduction of the linewidth is to reduce interference between contributions from individual electronic states to the Raman cross section.

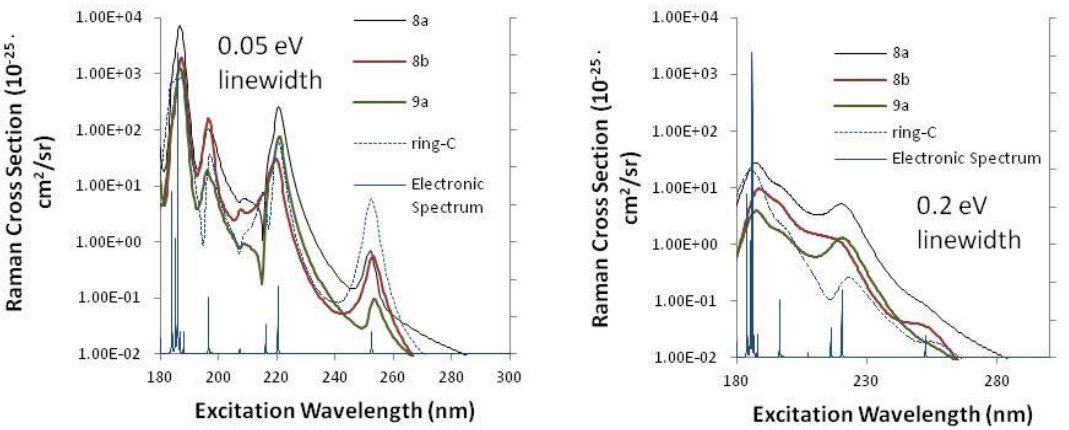

Figure 3. A comparison of the sum-over-states calculated excitation profiles for 0.05 eV and 0.2 eV linewidths for the 8a, 8b, 9a, and ring-C modes. The electronic spectrum calculated with TDDFT is included for comparison. The values for the excitation profiles for 0.1 eV linewidth are midway between the values for the 0.05 eV and 0.2 eV

The reduced interference shows itself in two ways. First, when the linewidth is reduced to 0.05 eV, the Raman cross section is enhanced by up to two orders of magnitude when in resonance with an electronic transition. Second, the excitation profile starts to follow the absorption spectrum more closely in that the L_b transition at 253 nm becomes significantly more apparent in the excitation profile. However, this will have a significant impact on the relative intensities between the ring-C, 8a, and 9a peaks that is not consistent with experimental data. For the narrow 0.05 eV linewidth, the ring-C mode receives significant enhancement in the vicinity of the L_b electronic transition so that on resonance it would be expected to dominate the 8a peak by an order of magnitude and have equal intensity at ~245 nm. For the same electronic linewidth our model also predicts the ring-C mode should dominate the 9a mode by nearly two orders of magnitude on resonance and should have equal intensity at 240 nm. However, experimental excitation profile data for neutral tyrosine shown in Figure 3 shows that both the 8a and 9a intensities consistently dominates the signal from the ring-C mode. The neutral tyrosine spectrum in Figure 2 from 244 nm excitation also shows the 9a still has slightly greater intensity than the ring-C mode. The relative peak intensities for the 8a, 9a, and ring-C modes predicted using a damping factor of 0.2 eV are more consistent with the experimental data than results obtained with damping factors of 0.05 eV or 0.1 eV. We conclude that the assumption of homogeneous broadening as the dominant contributor to the electronic transition linewidth and the γ = 0.2 eV linewidth are reasonable.

With respect to the consistent underestimation of the absolute RRS cross sections, it may be possible to adjust the damping factor to make the theoretical cross sections consistent with experimental ones. However, this is not justifiable without additional experimental data that illuminates the contribution from other electronic transition broadening mechanisms.

APPROVED FOR PUBLIC RELEASE

3.2 Measurements and modeling on tyrosine on titania anatase

In order to test our hypothesis, it was critical to capture the changes in the RRS spectrum induced by interaction with a surface, both experimentally and within our theoretical models. To that end, it was necessary to collect RRS spectra from near monolayers of tyrosine and the tyrosine containing peptides on anatase. Formation of crystals of the tyrosine or peptides would mean most of the sample was not in contact with the surface, and that molecules on the surface contributed a small fraction of signal to the measurements. For modeling, it was critical to simulate RRS spectra from tyrosine in contact with the metal oxide surface. These two issues were technical challenges that we did not surmount during this program. A last barrier was the failure of the experimental laser in the last two months of the program which prevented final measurements using differently prepared samples.

To address the first technical barrier, a number of monolayer preparation techniques were attempted using solvent evaporation from the titania nano-particles suspended in an aqueous solution of the tyrosine or peptides. Water was initially evaporated for approximately two weeks from a test tube, and the powdered sample was carefully removed for SEM and spectroscopic measurements. Due to the length of time for evaporation to prepare samples, we attempted to prepare samples by drying the nano-particle/peptide solution onto a glass slide that is compatible with the Raman measurement system. To verify the absence of pure crystalline tyrosine or peptides, we used SEM, UV-fluorescence microscopy, and XRD. For samples prepared on the microscopy slides, UV-fluorescence microscopy showed the tyrosine or peptides crystallized out of solution and preferentially formed pure crystals out of contact with the nano-particles. Based on a feature observed in the RRS spectrum, we believe the signal arose from tyrosine in contact with the titania surface.

Figure 4 shows a comparison of tyrosine in solution, in the solid pure phase, and from tyrosine deposited on titania. For the solution phase RRS, the 8a peak is dominant at 1613 cm^{-1}, and there is a small shoulder to higher frequency that we attribute to intensity sharing with water. For the solid phase tyrosine, the most intense peak is the 8b peak at 1598 cm^{-1} with an absence of the shoulder we attributed to water. For the titania on anatase trace, the 8b peak is dominant, as with the solid tyrosine, but the shoulder is even more intense than occurs fully solvated in solution. We attribute this to intensity sharing with neighboring water molecules adsorbed and immobilized on the titania surface, where the increased signal arises from longer lifetimes for that interaction. For samples measured from the glass slides, spectra were consistently identical to the solid tyrosine spectra.

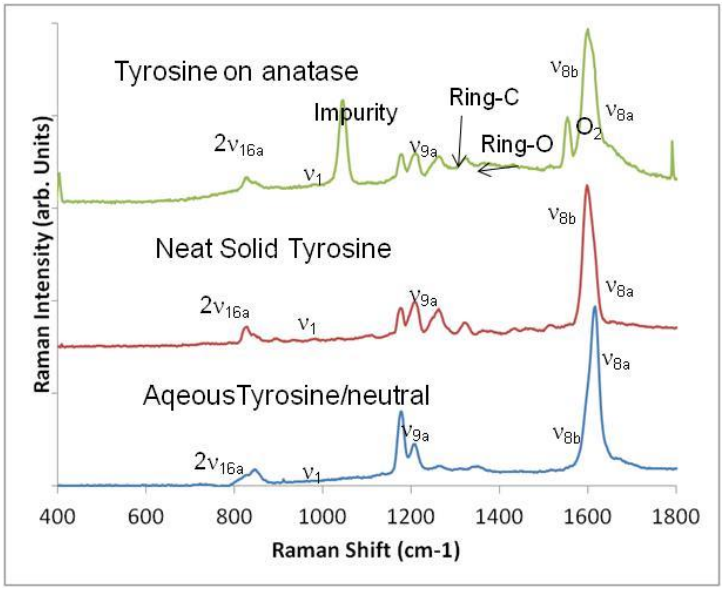

Figure 4. Comparison of RRS spectra from aqueous tyrosine, solid tyrosine, and tyrosine deposited on anatase particles.

Although our data suggests it was possible to obtain signal from tyrosine in contact with the titania surface, due to the preference for tyrosine or peptides to crystallize with itself meant that we could not control the density of tyrosine simply using the concentration of tyrosine or peptides in solution. As a result, it was difficult to draw conclusions from data obtained in this way. We consulted with Dr. John Yates at the University of Virginia, and received a number of recommendations for sample preparation. Titania particles tend to become contaminated with hydrocarbons over time when in contact with the air, and this layer of contaminants may inhibit binding of the peptides to the nanoparticle surface. Dr. Yates recommended baking the particles at high temperature in vacuum to remove the layer of contaminants to form

a closer contact between the surface and the peptides. A second recommendation was to use a surface cleaved from a single crystal for better characterization of the substrate surface. Thus, a correct path forward would be to prepare samples under stricter control within high vacuum systems.

A second technical barrier was encountered for the L-C-propargylglycine containing peptides. Although L-C-propargylglycine had been chosen on the assumption that the symmetric –C-triple bond-C– stretch could experience significant resonance enhancement, even for the shortest distance between it and the tyrosine group, the signal from the reporter molecule was very small for solution and on titania. For titania measurements, the peptides were indistinguishable from the tyrosine alone.

A third technical barrier was encountered when modeling of tyrosine or peptides in contact with the titania surface. In order to use TDDFT methods, the surface had to be treated as a cluster of titanium and oxygen atoms, rather than a true surface with periodic boundary conditions. Initial attempts at the calculations utilized large clusters with up to six titanium atoms using only DFT methods. Calculations using models with a mixture of DFT and classical mechanics and embedded electrostatic charges also failed. The simplest possible models using a single titanium atom with all coordination/bonding sites capped with hydroxyl groups also failed to converge, for both Gaussian and Turbomole codes. We hypothesize that the reason for the failure for the optimization of the electronic structure at a given molecular geometry was an insufficient basis set selection. Atoms capable of hypervalent bonding or coordination, such as S, P, or transition metals, can have significant d orbital structure. Although the basis sets chosen contained d orbital functions (def2-TZVPP in Turbomole, and 6-311+g(2df,2p) in Gaussian), the basis sets may not have been adequate to capture the electronic structure around the titanium ions.

3.3 Investigation of peptide chain length on SERS

The chemical enhancement mechanism of SERS and RRS are related in that a resonance between excitation light and the molecular electronic structure is involved. In the case of SERS, the substrate modifies the electronic structure of the analyte by creating lower energy states that are accessible in the visible range. As such, it appeared that an investigation of the influence of distance between a reporter with distinct vibrational frequencies, such as tyrosine with distinctive ring modes, and an electronic structure modifying substrate, would also help illuminate the connection between RRS and modifications to the electronic structure. We also believed such an approach would permit us to measure the chemical enhancement mechanism of SERS somewhat independently of the electric field enhancement effect, by choice of SERS substrate and excitation wavelength. For the silver colloid substrates used, the plasmon resonance wavelength occurs around ~500 nm. A comparison of the SERS spectra from each peptide chain with 532 nm (on plasmon resonance) and 785 nm (off plasmon resonance) showed some interesting results.

Figure 5 shows a comparison of SERS spectra with 532 nm and 785 nm excitation for the three cysteine containing peptides. For on-plasmon resonance excitation at 532 nm shows much less chain length dependence than the 785 nm excitation, with a wider variety of peaks visible. The 8a and 8b peaks at 1613 cm^{-1} and 1598 cm^{-1}, respectively, from the tyrosine phenyl ring are clearly visible with 532 nm excitation and can be easily assigned. The plasmon resonance mechanism of SERS acts over much longer distance than the chemical enhancement mechanism, and a natural consequence of going off resonance with 785 nm excitation would be to increase the dependence of vibrational modes on the tyrosine on the peptide chain length. Indeed, for the 8a and 8b peaks, there is a marked difference between the Tyr-Cys and the Tyr-Gly-Gly-Cys peptides, where these signals are much weaker with distance. An initial pass with theoretical modeling using Gaussian and a simple model of the peptides joined to a single silver atom showed the 8a and 8a peaks experiencing enhancement more sensitive to peptide length at 785 nm than 532 nm. We attribute the increased enhancement within the model to preresonance with charge transfer states created by the silver atom. More detailed modeling utilizing a larger silver cluster and the sum-over-states approach did not complete in time for this report. Nevertheless, these results demonstrate that additional study of the SERS of these peptides could improve the understanding of the connection between electronic structure the chemical enhancement mechanism of SERS.

APPROVED FOR PUBLIC RELEASE

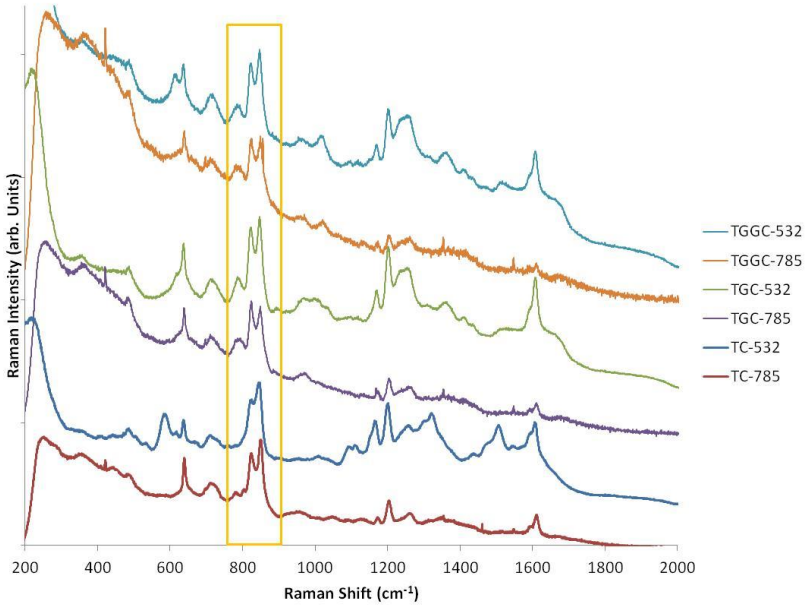

Figure 5. A comparison of SERS spectra for 532 and 785 nm excitation for three peptide chains. In the figure legend, T specifies tyrosine, G specifies glycine, and C specifies cysteine. When the excitation is on the plasmon resonance, the SERS signal is much less sensitive to the distance between the tyrosine and the SERS substrate. For the off plasmon resonance spectra, the 8a ring stretch of the tyrosine intensity drops rapidly with chain length.

4. CONCLUSIONS

A study has been performed to further the understanding of the connection between intermolecular induced changes to the electronic structure and the resulting response in the RRS. To accomplish this task we used a series of tyrosine peptides of varying length between tyrosine and a PG terminus, as well as tyrosine and cysteine containing peptides on silver colloid in SERS measurements.

For the system of tyrosine and tyrosine containing peptides on titania, we encountered four significant technical barriers. The first involved obtaining an understanding of the influence of destructive interference in the sum of states for these systems. The hypothesis used at the beginning of this study had made the assumption that only electronic states in resonance with the optical excitation and that the ground electronic state had significance, and that intermolecular interactions could only significantly affect the RRS through these states. However, our study of destructive interference between states demonstrates intermolecular interactions can affect the RRS through electronic states that are much higher in energy than the excitation. Although there was success in surmounting the first technical barrier, we did not surmount the last three barriers.

For preparation of samples on titania, all methods using aqueous deposition did not produce controlled amounts of peptides evenly distributed on the surfaces. Vacuum techniques are likely necessary to correctly prepare peptides on titania. The third technical barrier not overcome was the correct modeling of the titania surface, where the electronic structure could not be found even for a fixed nuclear geometry. This is likely due to the difficulty in modeling the electronic structure of transition elements such as titanium, and if this is so, simulation with larger basis sets may be necessary. Lastly, PG did not prove to be a suitable “reporter” residue. This is most likely due to the fact that the enhancement coming from the aromatic ring in tyrosine acts over a much shorter distance than anticipated.

In conclusion, although several technical barriers were not overcome, this investigation did shed light on the influence of high energy electronic states through destructive interference. Furthermore, this study revealed the experimental approaches that would be necessary to investigate further the connection between intermolecular interactions, electronic structure, and the RRS spectrum.

ACKNOWLEDGEMENTS

The authors gratefully acknowledge funding provided through the U.S. Army In-House Laboratory Independent Research and Surface Science Initiative program. We also gratefully acknowledge support from the Defense Threat Reduction Agency Joint Science and Technology Office making collaboration with S. Saikin and D. Rappoport possible.

REFERENCES

[1] Farrell, M.E.; Holthoff, E.L.; and Pellegrino, P.M., "Next generation Surface Enhanced Raman Scattering (SERS) substrates for Hazard Detection", in *Proc. SPIE 8358, Chemical, Biological, Radiological, Nuclear, and Explosives (CBRNE) Sensing XIII*. A.W. Fountain, Ed., ed, **2012**.

[2] Christesen, S.D. *et al.*, "Ultraviolet Raman spectra and cross-sections of the G-series nerve agents", *Applied Spectroscopy*. **2008**. 62(10), p1078-1083.

[3] Guicheteau, J., *et al.*, "Bacillus spore classification via surface-enhanced Raman spectroscopy and principal component analysis", *Applied Spectroscopy*. **2008**. 62(3), p267-272.

[4] Rava, R.P. and Spiro, T.G., "Selective enhancement of tyrosine and tryptophan resonance Raman spectra via ultraviolet laser excitation", *Journal of the American Chemical Society*. **1984**. 106(14), p4062-4064.

[5] Albrecht, A.C., "On the theory of Raman intensities", *Journal of Chemical Physics*. **1961**. 34, p1476-1484.

[6] Lombardi, J.R. and Birke, R.L., "A unified approach to surface-enhanced Raman spectroscopy", *Journal of Physical Chemistry C*. **2008**. 112(14), p5605-5617.

[7] He, R., *et al.*, "Franck-Condon processes in pentacene monolayers revealed in resonance Raman scattering", *Physical Review B*. **2011**. 83(11).

[8] Birke, R.L., *et al.*, "A charge-transfer surface enhanced Raman scattering model from time-dependent density functional theory calculations on a Ag10-pyridine complex", *The Journal of Chemical Physics*. **2010**. 132(21), p214707.

[9] Lathrop, E.J.P. and Friesner, R.A., "Vibronic mixing in the strong electronic coupling limit. Spectroscopic effects of forbidden transitions", *The Journal of Physical Chemistry*. **1994**. 98(1), p3050-3055.

[10] Hildebrandt, P.; Tsuboi, M.; and Spiro, T.G., "Ultraviolet resonance Raman spectroscopy of formamide: evidence for n-π* interferences and intermolecular vibronic coupling", *The Journal of Physical Chemistry*. **1990**. 94(6), 2274-2279.

[11] Asher, S.A. and Johnson, C.R., "UV resonance Raman excitation profile through the $1B_{2u}$ state of benzene", *The Journal of Physical Chemistry*. **1985**. 89(8), p1375-1379.

[12] Sweeney, J.A. and Asher, S.A., "Tryptophan UV resonance Raman excitation profiles", *The Journal of Physical Chemistry*. **1990**. 94(12), p4784-4791.

[13] Avila Ferrer, F.J., *et al.*, "Duschinsky, Herzberg-Teller, and multiple electronic resonance interferential effects in resonance Raman spectra and excitation profiles. The Case of pyrene", *Journal of Chemical Theory and Computation*. **2013**. 9(8), p3597-3611.

[14] Ziegler, L. and Albrecht, A.C., "Raman scattering of benzene in the ultraviolet", *Journal of Chemical Physics*. **1977**. 67, p2753-2757.

[15] Dudik, J.M., *et al.*, "Wavelength dependence of the preresonance Raman cross-sections of CH3CN, SO_4^{2-}, ClO_4^-, and NO_3^-", *Journal of Chemical Physics*. **1985**. 82, p1732-1740.

[16] Rappoport, D., *et al.*, "Simplified sum-over-states approach for predicting resonance Raman spectra. Application to nucleic acid bases", *Journal of Physical Chemistry Letters*. **2011**. 2(11), p1254-1260.

[17] Becke, A.D., "Density-functional thermochemistry. III. The role of exact exchange", *Journal of Chemical Physics*. **1993**. 98(7), p5648-5652.

[18] Weigend, F. and Ahlrichs, R., "Balanced basis sets of split valence, triple zeta valence and quadruple zeta valence quality for H to Rn: Design and assessment of accuracy", *Physical Chemistry Chemical Physics*. **2005**. 7, p3297-3305.

[19] Klamt, A. and Schueuermann, G., "COSMO: a new approach to dielectric screening in solvents with explicit expressions for the screening energy and its gradient", *Journal of the Chemical Society, Perkin Transactions 2*. **1993**. 5, p799-805.

[20] Furche, F. and Rappoport, D., "Density functional methods for excited states: Equilibrium structure and electronic spectra", *Theoretical and Computational Chemistry*. **2005**. 16, p93-128.

[21] Bauernschmitt, R. and Ahlrichs, R., "Treatment of electronic excitations within the adiabatic approximation of time dependent density functional theory", *Chemical Physical Letters*. **1996**. 256, p454-464.

[22] Furche, F. and Ahlrichs, R., "Adiabatic time-dependent density functional methods for excited state properties", *Journal of Chemical Physics*. **2002**. 117(16), p7433-7447.

[23] TURBOMOLE V6.5 2013, a development of the University of Karlsruhe and Forschungszentrum Karlsruhe GmbH, **1989-2007**. Available from http://www.turbomole.com.

[24] Furche, F., *et al.*, "Turbomole", *Wiley Interdisciplinary Reviews: Computational Molecular Science*. **2014**. 4(2), p91-100.
[25] Jensen, L., *et al.*, "Theory and method for calculating resonance Raman scattering from resonance polarizability derivatives", *Journal of Chemical Physics.* **2005**. 123(17), p174110.
[26] Perdew, J.P., "Erratum: Density-functional approximation for the correlation energy of the inhomogeneous electron gas", *Physical review B.* **1986**. 34, p7406.
[27] J. P. Perdew, "Density-functional approximation for the correlation energy of the inhomogeneous electron gas", *Physical Review B.* **1986**. 33, 8822(R).
[28] Becke, A.D., "Density-functional exchange-energy approximation with correct asymptotic behavior", *Physical Review A.* **1988**. 38, p3098-3100.
[29] Van Lenthe, E. and Baerends, E.J., "Optimized Slater-type basis sets for the elements 1-118", *Journal of Computational Chemistry*. **2003**. 24(9), p1142-1156.
[30] van Gisbergen, S.J.A., *et al.*, "Application of time-dependent density functional response theory to Raman scattering", *Chemical Physics Letters.* **1996**. 259(5-6), p599-604.
[31] van Gisbergen, S.J.A, *et al.*, "Implementation of time-dependent density functional response", *Computer Physics Communications.* **1999**. 118, p119-138.
[32] Kang, Y., *et al.*, "On the mechanism of protein adsorption onto hydroxylated and nonhydroxylated TiO_2 surfaces", *Journal of Physical Chemistry C.* **2010**. 114(34), p14496-14502.
[33] Pace, C.N., *et al.*, "How to measure and predict the molar absorption coefficient of a protein", *Protein Science.* **1995**. 4(11), p2411-2423.
[34] Fodor. S.P.A, *et al.*, "Deep-ultraviolet Raman excitation profiles and vibronic scattering mechanisms of phenylalanine, tyrosine, and tryptophan", *Journal of the American Chemical Society.* **1989**. 111(15), p5509-5518.
[35] Ludwig, M. and Asher, S.A., "Ultraviolet resonance Raman excitation profiles of tyrosine: dependence of Raman cross sections on excited-state intermediates", *Journal of the American Chemical Society*. **1988**. 110(4), p1005-1011.
[36] Asher, S.A., *et al.*, "UV Resonance Raman excitation profiles of the aromatic amino acids", *Journal of the American Chemical Society*. **1986**. 108(12), p3186-3197.


ECBC
SSI
PROJECTS

Understanding how exosporium hairs affect spore adhesion on surfaces

Jana Kesavan*[a], Craig K. Knox[b], Erica Valdes[a], Vipin Rastogi[a]
[a]U.S. Army Edgewood Chemical Biological Center, Research and Technology Directorate, 5183 Blackhawk Rd, Aberdeen Proving Ground, MD 21010
[b]Leidos, Inc., P.O. Box 68, Gunpowder Branch, Aberdeen Proving Ground, MD 21010

ABSTRACT

Microorganism adhesion plays important roles in numerous processes. Several pathogens of the Gram-positive endospore-forming *Bacillus* genus of bacteria have evolved a thin and highly-deformable outer layer, known as the exosporium or Hirsute hairy nap, which consists of nanometer-scale hair-like glycoprotein filaments and which is believed to play a critical role in spore hydrophobicity and adhesion, both in the environment and *in vivo*. This report summarizes the first year results of a Surface Science Initiative project involving spore-probe atomic force microscopy and air flow experiments to measure the adhesive force between spores and a glass surface. Electron microscopy was used to visually characterize spores. *Bacillus* spores with exosporium hairs (ΔSterne strain of *B. anthracis* and *B. thuringiensis* (Bt)) as well as similar spores without hairs (*B. globigii* (Bg) and ΔcotE/ΔbclA mutants) were studied. Molecular dynamics simulations were performed to probe the interactions of a single exosporium hair on a nanoscale patch of silica (SiO_2) glass. Hydrogen-bonding was observed between hydroxyl protein groups and SiO_2. Hairy Bt spores adhered more strongly to glass than non-hairy Bg spores, demonstrating an enhancement effect. These results may help provide insight into exosporium adhesion effects and guide the development of novel coatings and materials for bio-agent detection, protection, and decontamination.

Keywords: Hirsute nap, filament, bacterium, mutation, aerosol, binding, AFM, molecular modeling

1. INTRODUCTION

1.1 Background

Microorganism adhesion plays an important role in a broad range of processes, including re-aerosolization of particles; surface contamination, fouling, and cleaning; biofilm growth; infection; medical treatment; and microbial colonization, survival, and dispersion. Several pathogenic members of the Gram-positive endospore-forming *Bacillus* genus of bacteria (*B. cereus/anthracis/thuringiensis*) as well as the *Clostridium* genus of bacteria (e.g., *C. botulinum*) possess a thin and highly-deformable outer layer, known as the exosporium[1,2] or Hirsute hairy nap, which consists of a forest of approximately 70 nm hair-like glycoprotein filaments[3] protruding from a crystalline basal layer and which is believed to play a critical role in spore hydrophobicity and adhesion, both in the environment and *in vivo*.[4,5] Studies have suggested that the flexibility of the exosporium helps increase surface contact area,[6,7] thus promoting adhesion, but an in-depth study to understand this behavior has not been previously undertaken.

The exosporium proteins are considered potential sites for immunoresponse and detection. In fact, Dr. Henry Gibbons' Defense Threat Reduction Agency-funded barcoding project is targeting these exosporium proteins for epitope insertion and subsequent spore detection. Most of the exosporium consists of a mixture of proteins and carbohydrates, the principal component of which is believed to be the newly described glycoprotein, BclA.[8] The crystallographic structure of this glycoprotein has recently been resolved.[9] It forms a fibril consisting of a trimer with a collagen-like helical structure, the length of which depends on the number of GXX repeats in the amino acid sequence, which varies among spore species. The C-terminus domain (CTD) is the free end of the fibril, is rich in beta-sheets, and contains several loops; the N-terminus domain (NTD) is the other end and is anchored to the crystalline basal layer. Experimental studies have not probed the molecular mechanisms of exosporium filament-surface interactions. Current knowledge about the structure and function of the exosporium hairs is mostly limited to electron microscopy studies dating back to the 1960s.[3,10]

1.2 Questions

Several questions have not been addressed in the literature and may help elucidate the role of exosporia in spore adhesion. How strongly does the exosporium bind to surfaces, on a per-area basis, and how does this compare to that of the spore coat (layer underneath the exosporium)? Simple spore peel-off surface tests and atomic force microscopy (AFM) experiments have measured *B. cereus*[6] and *B. mycoides*[7] spore binding forces to stainless steel as well as

APPROVED FOR PUBLIC RELEASE

hydrophobic/hydrophilic-coated mica and glass, but these measurements did not include contact area estimations or measurements to directly compare exosporium versus spore coat surface adhesion on a per-area basis to account for the hypothesized increase in contact area due to the exosporium. It may be possible to measure spore-surface contact area using Brunauer–Emmett–Teller (BET) gas adsorption surface experiments[11] or to estimate contact area from AFM and electron microscopy.

Do specific chemical interactions (e.g., electrostatic, hydrogen-bonds) play a strong role in exosporium-surface adhesive forces, or are these forces simply the result of increased contact area? Lequette et al. measured the change in isoelectric point (charge) due to the presence/absence (mutation) of the BclA exosporium glycoprotein of the hairs and attempted to correlate the observed change in spore adhesion to the change in charge and hydrophobicity, but this correlation did not capture the trend. More chemical considerations as well as contact area may need to be included in the correlation.

How much of the exosporium adhesion enhancement originates from hair-surface interactions compared to surface interactions with the basal layer? This question may be difficult to address experimentally, although the BclA mutation study of Lequette et al. suggests that the exosporium hairs are primarily responsible for the observed enhancement in spore adhesion since BclA is the dominant glycoprotein in these fibrils and other proteins, lipids, and carbohydrates make up the basal layer. Molecular modeling may help address this question of contribution to adhesion due to hair vs. basal layer since both structures can be separated and simulated independently.

How deformable and flexible is the exosporium, and how do these mechanical properties affect adhesion? The exosporium has been observed to be loosely-fitting and highly-deformable in AFM and microscopy experiments. Its soft mechanical properties are the basis for the proposed hypothesis in the literature of stronger adhesion due to increased contact area, but quantitative mechanical studies of the exosporium seem to be absent in the literature. Single-molecule AFM force-extension experiments using a single BclA protein attached to a cantilever tip may allow direct measurement of the mechanical properties (e.g., Young's modulus) of the exosporium hairs. Molecular modeling can also calculate exosporium mechanical properties.

How important are the length, surface density, and orientation of hairs? According to the observed spore adhesion enhancement due to the exosporium, these fibril properties should affect spore adhesion if the hairs, rather than the basal layer, primarily contribute to the adhesion enhancement. However, thorough measurements of these properties appear to be lacking in the literature. Electron microscopy studies have reported a wide variation in hair length among different spore species. Variations in the molecular weight of BclA glycoproteins across spore species are directly linked to the number of GXX collagen-like repeats[8] in the protein sequence. Less has been reported about hair surface density and orientation, although electron microscopy visually contains such information. Simulations may help characterize the orientation and structure of the hairs.

How does the hair morphology change in the presence of hydrophobic versus hydrophilic surfaces and environments, and how does this affect spore adhesion? Bowen et al. measured significant differences in spore adhesion on hydrophobic vs. hydrophilic coated glass surfaces. Are the BclA proteins primarily responsible for this change? Do these proteins change structure and orientation near different surfaces and mediate spore-surface forces?

1.3 Hypothesis and objectives

Our primary hypothesis is that the hairs of the exosporium respond to different chemical environments (e.g., hydrophobic versus hydrophilic, aqueous versus dry) to orient and change surface patterning at the nanoscale, affecting the contact area and, thus, spore adhesion. We believe that the observed spore adhesion enhancement from the exosporium is primarily due to the hairs rather than the basal layer. Based on the observed hydrophobicity and charge effects of BclA, we also believe that the exosporium has strong chemical interactions (perhaps electrostatic and hydrogen-bonds) with surfaces, in addition to exposing a larger spore surface area, thus affecting and mediating spore adhesion. Our objective is to scientifically test our hypotheses and attempt to answer as many of the questions above as feasible, given the scope of this project.

2. METHODS

2.1 Spore preparation

Spores of the ΔSterne strain of *B. anthracis* and *B. thuringiensis* (Bt) were prepared in-house. Spores of *B. globigii* (Bg) were procured from Dugway Proving Ground. The ΔcotE mutant (from Prof. Adam Driks, Loyola University) and ΔbclA mutant (from Prof. Alison O'Brien, Uniformed Services University Health Sciences) of the ΔSterne strain of *B. anthracis* were procured from authentic sources. Strains were streaked for single colonies on tryptic soy agar plates and grown overnight at 37 °C. An overnight culture of each strain was grown in tryptic soy broth overnight at 37 °C. For each strain, an aliquot (0.5 mL/plate) was spread over Lab-Lemko plates (15 cm diameter) and incubated at 37 °C for seven days or

until the sporulation level reached > 95% (microscopic assessment). The spore crop over the plates was harvested by dislodging growth on plates using sterile distilled water (25 mL per four plates). The spore crop was filtered through a sterile coffee filter and washed with an additional 25–50 mL of sterile distilled water. The spores were washed by successive resuspension three times in 25 mL of sterile distilled water and heat-treated at 65 °C for 30 minutes. The extent of sporulation was confirmed microscopically and enumerated by dilution plating. Spore hardiness was confirmed by heat-treatment and sensitivity to 2.5 M HCl treatment for 1 minute and 10 minutes, respectively. Spores have been tested in ambient conditions. Humidity controls will be added in year 2 to carefully vary the relative humidity of the air.

To overcome potential challenges in comparing hairy versus non-hairy spores across different spore species, which may exhibit possible differences in surface properties, mutant ΔSterne (hairy) spores with deleted genes (ΔcotE and ΔbclA) were prepared for a more direct exosporium hair versus no exosporium hair comparison within the same species. Since the ΔcotE mutant spores also lack the crystalline basal layer of the exosporium in addition to the exosporium hairs, comparing these spores to the ΔbclA mutant spores should provide direct comparison of hair versus basal layer effects. Although these mutant spores have been prepared and characterized in year 1, they will not be used in adhesion experiments until year 2. Year 1 results compare Bt (hairy) versus Bg (non-hairy) spores, which should provide important insights, especially given the routine use of Bg as a simulant for *B. anthracis*.

2.2 Atomic force microscopy

The experimental portion focused on using AFM to perform spore-probe force spectroscopy[7,12,13] to quantitatively measure the adhesive force between individual spores and a surface. Following the work of Bowen et al., a single spore or a cluster of spores was glued to the apex of an AFM cantilever and scanned over a bare surface to measure the force-displacement profile as the spore-probe approaches, possibly binds, and leaves a surface, as shown in Figure 1. The inverse AFM experiment will also be performed, wherein a bare tipless cantilever will be scanned over a spore-covered surface and the pull-off force will be measured for peeling off individual spores from the surface. If feasible, a third AFM experiment may also be performed involving a single recombinant BclA glycoprotein[8,14] attached to a cantilever tip and scanned over a surface.[15] This would allow direct validation of the molecular dynamics simulations discussed below.

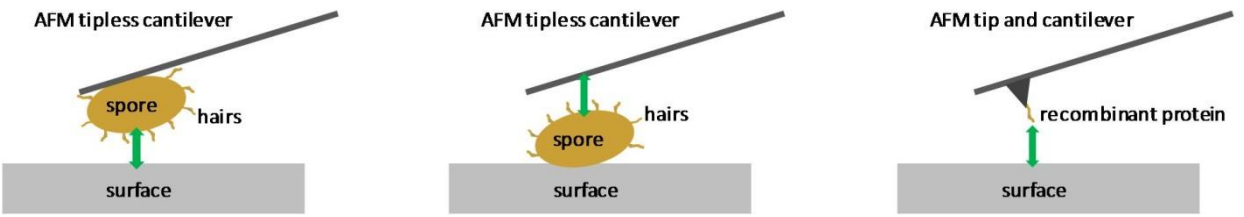

Figure 1. Schematics of AFM methods: (left) spore-probe, (middle) spore peel-off, and (right) single-protein. Green arrows indicate force of interaction to be measured.

2.2.1 Preparation of flat probes and spore-probes

Flat (blunted) probes were prepared by mounting silicon nitride (Si_3N_4) probes in the AFM (Dimension Icon, Bruker Nano Analytics, Ewing, NJ) and scanning a large area (50 µm) at maximum speed on a sheet of abrasive (3M™ aluminum oxide lapping sheets, 1 µm). The probes used were Bruker DNP-10, cantilever B (Bruker AFM Probes, Camarillo, CA) with a nominal spring constant of 0.12 N/m. During lapping the probes were periodically inspected via scanning electron microscopy (SEM) and abrasion was continued until the area of the flattened tip was on the order of 1 μm^2, which is roughly the size of a single spore.

A variety of approaches was explored to make spore-probes, including attaching spores to probes using the AFM as a micromanipulator with various commercial adhesives, using probe tips coated with poly-L-lysine, and performing direct manual attachment. The most effective approach was using a video microscope for viewing and manually manipulating needles to place a spot of Loctite® glass glue on the cantilever tip and to attach spores to the wet glue. Spore-probes used in measurements were spores attached to Bruker DNP-10, cantilever D, Si_3N_4 with measured spring constants between 0.03 N/m and 0.12 N/m after spore attachment. Additional cantilevers containing a single spore glued to the apex were ordered from Novascan Technologies and will be analyzed upon arrival. Spores attached were dried preparations of Bg and Bt.

2.2.2 Morphological characterization of spores and spore-probes

Field emission scanning electron microscopy (FESEM) (JEOL 7001 FLV, JEOL, Tokyo) was used to morphologically characterize spores and to inspect spore-probes and flat probes. Spores were characterized morphologically using FESEM. AFM was also used to characterize the surfaces of the spores.

For FESEM characterization, the spores were suspended in distilled water and deposited on clean aluminum mounts and allowed to dry in air. Imaging of spores was done using the JEOL 7001 FLV in high-vacuum mode, operating at 2 keV with a nominal working distance of 7.5–10.5 mm. Spore-probes were inspected with the FESEM prior to force measurements. Probes were affixed to mounts using conductive carbon tape and imaged at 1 keV at a nominal working distance of 20 mm.

For AFM characterization, the spores were immobilized from water suspension on poly-L-lysine-coated glass microscope slides (Polysciences, Inc., Warrington, PA). The immobilized spores were characterized using Bruker MPP-12200 silicon probes (nominally 5 N/m, 150 kHz, tip radius 8 nm, tip height 17.5 µm; Bruker AFM Probes, Camarillo, CA) operating in tapping mode with amplitude 154.11 mV with a scan rate of 1 Hz. Tips were evaluated prior to use with a TipCheck standard (Aurora NanoDevices Inc., Canada).

2.2.3 Adhesion measurements with flattened probes

Adhesion measurements were performed by collecting the deflection versus position curves as the flattened cantilever approached the spore-covered surface. The deflection or distance the cantilever retracts from the surface without the tip releasing from the surface is related to the adhesion force through the spring constant of the cantilever. AFM measurements were thermally tuned to directly and quantitatively compare the cantilever deflection of the different probes, and these results were converted into force units upon additional calibration to determine the spring constant of each blunted probe. Five measurements were taken on each spore at locations separated by 100 nm in a line across the spore. At each location, adhesion measurements were made after surface delay times, with the probe sitting on the spore for a known time before retracting, of 0 seconds, 20 seconds, 40 seconds, 80 seconds, and 160 seconds. These measurements were done on both Bg and Bt spores immobilized using poly-L-lysine-coated glass microscope slides.

2.2.4 Adhesion measurements with spore-probes

Spore-probe adhesion measurements were made on clean glass microscope slides to best mimic the parallel aerosol measurements. Because there is an apparent dependence on delay time, spore-probe measurements were all done with a delay time of 120 seconds. The probe speed for approaching and retracting from the surface was 100 nm/s. Each tip was used for 25 measurements, with each measurement at a different location in an evenly spaced 5 x 5 array on the surface. Results for each tip were averaged and the standard deviation calculated.

2.3 Air flow experiments

Centrifugation and aerosol experiments were also conducted to help validate the AFM spore-surface force measurements. These experiments involved covering a surface with spores, either spinning or blowing air over the sample, counting the change in the number of spores attached to the surface versus the applied force, and correlating this number to an adhesive force. This allows qualitative validation of the AFM trends. Quantitative validation is more difficult owing to the significant difference in the magnitude and orthogonal nature of the applied forces between the types of experiments. The aerosol experiments may provide the most direct link to estimating stickiness factors of spores for agent fate prediction.

2.3.1 Description and preparation of slides

Hemacytometer glass cover slides (Millennium Sciences, Inc., New York) that contain 3 mm x 3 mm laser-etched grid were used in this experiment. The smallest square size is 0.1 mm x 0.1 mm and the largest square size is 0.5 mm x 0.5 mm. The cover slides were cleaned by washing them with soap and water followed by isopropyl alcohol to remove all particles and oils. The cover slides were air dried before particle deposition.

2.3.2 Particle deposition

A 6 inch diameter by 9 inch long cylinder was used for the fluorescent polystyrene latex (PSL) microsphere deposition. The gridded cover slides were placed on the bottom of the cylinder that was placed vertically on a surface. PSL microspheres of 1 µm, 3 µm, and 5 µm diameter were aerosolized separately using an Aeroneb nebulizer (Aerogen, Galway, Ireland) into the cylinder and allowed to settle onto the cover slides for use in experiments. The 1 µm, 3 µm, and 5 µm PSL microspheres were aerosolized for 1 minute, 3 minutes, 5 minutes, and 6 minutes, respectively, to deposit particles into the cylinder. Bg and Bt were deposited onto cover slides separately using separate Bg and Bt filled metered dose inhalers (puffers). Puffers were placed 12.7 cm (5 in) from the cover slides and puffed twice to deposit organisms by impaction onto slides.

2.3.3 Microscopic counting

The particles in each grid were counted using a microscope (Zeiss axioscope, Carl Zeiss, New York). The UV light of the microscope was employed for easy identifying and counting of the fluorescent PSL microspheres. Visible light was used to identify and count the biological particles based on the size and shape of particles. Bg and Bt have similar size and

shape; therefore, they were deposited on separate cover slides to eliminate misidentification. 1 µm, 3 µm, and 5 µm PSL microspheres were deposited on the same cover slide and they were easily identified and counted using the UV light.

2.3.4 Particle removal by air impingement

Figure 2 shows the experimental setup for removing particles using air impingement. Air flow (85 psi) was controlled through a solenoid to deliver one puff of air through an orifice for each push of a button. A puff duration of 0.56 seconds was employed in this test to remove particles. The separation distance between the orifice and the surface was varied. Distances of 1.5 cm and 2.5 cm were used in this study. Markings on the surface were used to align the cover slide so that the gridded counting region was placed directly under the orifice. Particles on cover slides were counted using a microscope before the particle removal. A puff of air was delivered to each slide and the number of particles remaining on the cover slide was counted via microscopy. Eight replicates were performed of each experiment. Multiple puffs (up to 200) were delivered by pushing the button multiple times to determine the effect of this on particle removal.

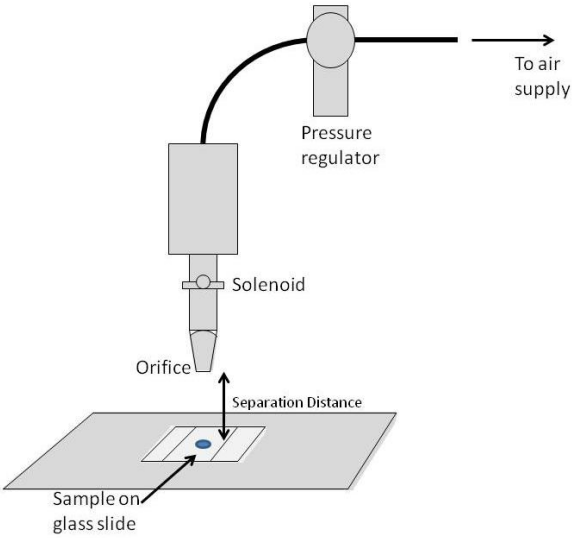

Figure 2. Experimental setup for particle removal by air impingement.

2.3.5 Particle removal by centrifugal force

Centrifugal force at 9250 rpm for 4 hours was used to remove particles from slides. Glass crumbles at high acceleration; therefore, plastic slides were used in this test. As described above, 1 µm, 3 µm, and 5 µm PSL microspheres were deposited onto slides. Grid marks were not on the plastic slides; therefore, an approximate 1 cm circle was drawn to identify the counting region. Pre and post counting of particles were conducted to determine the percent of particles removed by centrifugal force.

2.4 Molecular modeling

The modeling portion focused on using molecular dynamics (MD) simulations with the Chemistry at HARvard Macromolecular Mechanics (CHARMM) force field to probe the molecular-level surface interactions[16,17] of a single exosporium filament hair (CTD of BclA trimer obtained from SWISS-MODEL[18] of the *B. thuringiensis kurstaki* (Bt*k*) strain, using the *Bacillus* collagen-like protein of *anthracis* P159S mutant (3TYJ)[19] from Protein Data Bank Japan (PDBj) as the protein threading template) with various (15 different) orientations on a bare 11.4 nm x 11.4 nm x 1.8 nm patch of an amorphous SiO_2 glass surface (force field parameters from Cruz-Chu et al.[20]), as shown in Figure 3. These simulations focused on probing the dominant chemical or physical interactions (e.g., electrostatic, hydrogen-bonds) and the role of hair orientation. The single-hair results will be converted to spore-surface adhesive forces based on hair surface density and spore-surface contact area estimations, and these results will be compared with experiment. Binding energies, hair orientations and structures, and hydrogen-bonding have been analyzed. The total number of atoms was approximately 20 thousand. Materials Studio and Visual Molecular Dynamics (VMD) were used for building and orienting the system. Each orientation was simulated for 200 picoseconds (ps) after placing the bottom of the hair 0.2 nm above the top of the surface and pushing the hair towards the surface with a gentle (0.1 nm/ps) initial relative velocity (in addition to the atom velocities resulting from the 300 K initial temperature) to accelerate initial binding and thereafter allowing the microcanonical ensemble (NVE) dynamics to progress unaltered. The glass surface atoms were fixed in place. A Large-scale Atomic/Molecular Massively Parallel Simulator (LAMMPS) was used to perform the MD simulations with a 0.8 nm

switching inner cutoff, a 1.0 nm Van der Waals and long-range Coulombic outer cutoff, and a 1.0 femtosecond (fs) timestep. Long-range Coulombic interactions were calculated using the Particle–Particle-Particle–Mesh (P3M) Ewald method (order 6, 1.0×10^{-6} relative accuracy), and periodic boundary conditions extended over the entire glass surface in the xy-plane as well as 20 nm in the z-direction to prevent the hair from interacting with periodic images. Binding energies between hair and surface atoms were efficiently calculated using the LAMMPS group/group compute.

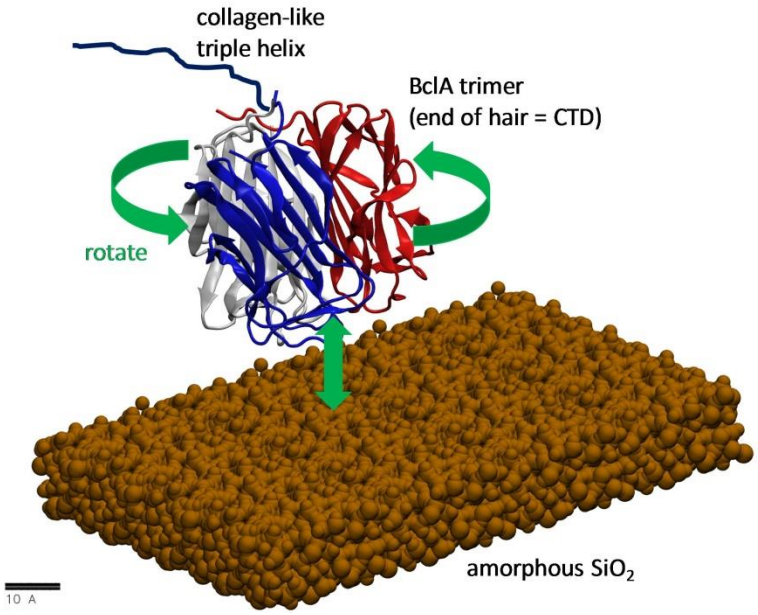

Figure 3. Model setup of single-hair on glass MD system. Glass surface atoms are shown as brown balls. The hair (BclA trimer) is represented as a cartoon, emphasizing the beta-sheet and flexible loop conformations of the CTD, and colored by protein monomer. The collagen-like triple helix of the hair is represented as a wavy blue line for simplicity. Green arrows indicate initial orientation and the hair-surface interaction. Scale bar represents 1 nm.

3. RESULTS AND DISCUSSION

3.1 Morphology of spores and spore-probes

FESEM has been used to visually characterize spores, cantilever tips, and spore-probes, as shown in Figure 4. Transmission electron microscopy and BET gas adsorption surface area studies are planned for year 2 to characterize the exosporia and to estimate contact area and hair density.

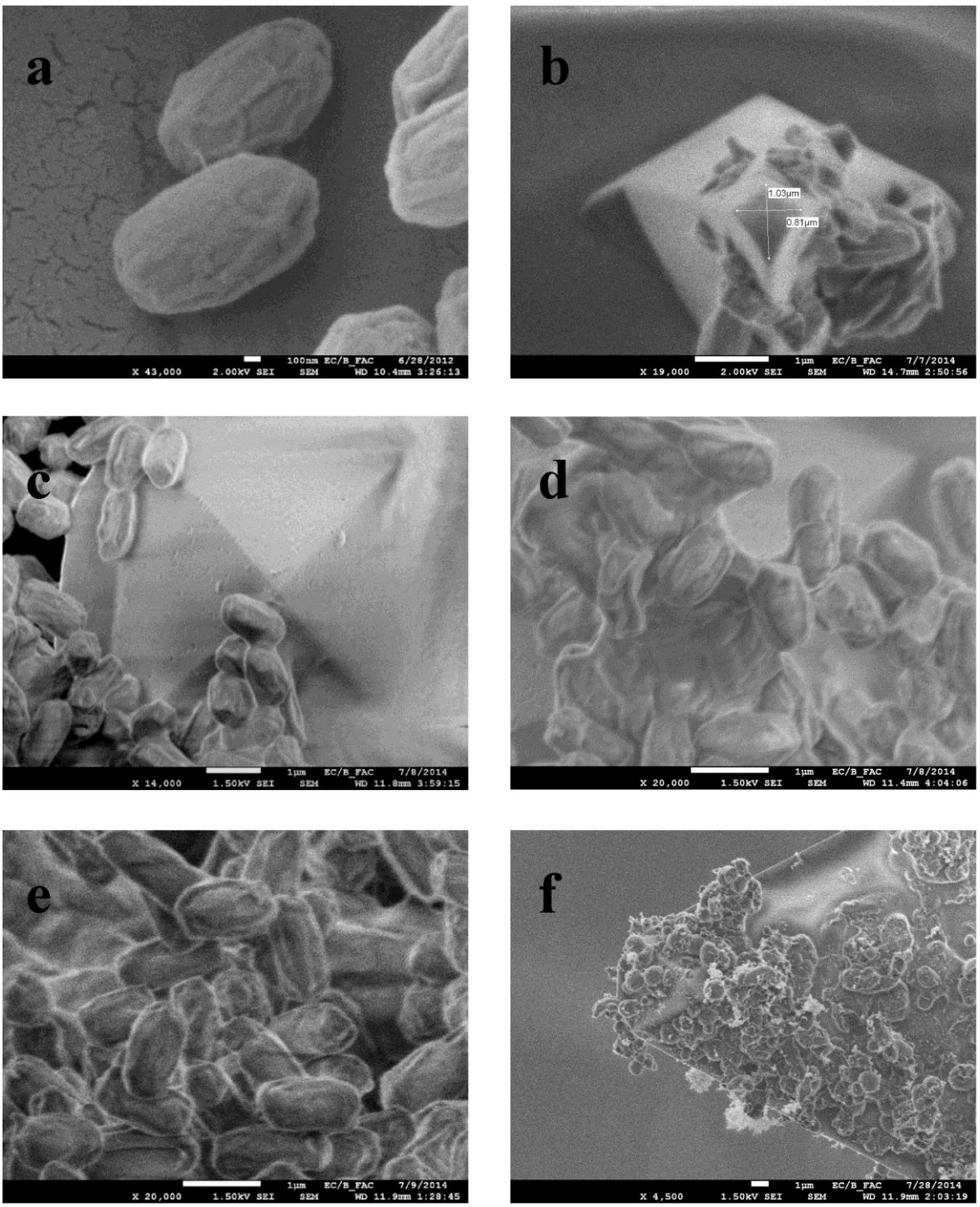

Figure 4. FESEM images of spores and cantilever tips used for AFM adhesion measurements. (a) Bg spores. (b) broadened flat tip after lapping; table dimensions are 1.03 x 0.81 µm. (c-e) Bg spore-probe tips 1-3 with immobilized spores. (f) Bt spore-probe tip 4 with immobilized spores. Scale bar is 100 nm for (a) and 1 µm for (b-f).

3.2 Spore adhesion

Preliminary results of the flattened (blunted) probe pull-off measurements are shown in Figure 5. Measurements were performed at five locations on each spore to provide statistics. The significant differences in adhesion at the different points may be due to a combination of different contact areas resulting from the large probe area combined with the curvature of the spore particle, which would give larger adhesions near the center of the spore. Edge effects may also play a role if the probe tip contacts the vertical side of a spore, resulting in much larger contact areas and thus adhesive forces. In both the Bg and the Bt experiments, the adhesion appears to increase at the edges of the spores and does not occur immediately with initial contact but requires some delay. This effect is more pronounced on the Bg (non-hairy) spores than on the Bt (hairy) spores, suggesting that adhesion occurs more rapidly with exosporium hairs. Bt spores also exhibit a continuing gradual climb in adhesive force with increasing time, while Bg spores exhibit a slight decrease or leveling in adhesion with time after reaching a rapid maximum. This behavior may indicate stronger ordering/patterning of hairs on the surface over time, in agreement with the modeling results below. The cause of the apparent maximum in the Bg adhesive response is not known. Additional spore peel-off experiments and replicates are planned for year 2 to further study these phenomena.

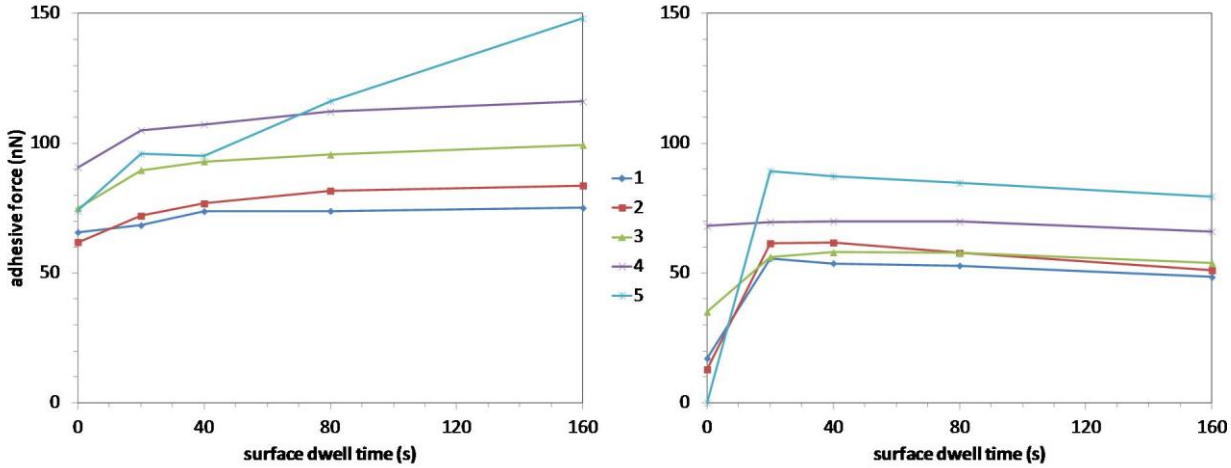

Figure 5. Plot of AFM adhesive force (nN) vs. delay time on surface (s) for blunted tips on Bt (hairy) spore (left) and on Bg (non-hairy) spore (right) at five points across the surface of each spore (1 through 5). Cantilever deflection values were converted to units of force using measured spring constants of 0.15 N/m and 0.12 N/m for the tips on Bt and Bg, respectively. Both plots have same y-axis values and units for comparison.

Results of the AFM spore-probe measurements are summarized in Table 1. These measurements suggest that there is a marked increase in adhesion to silica for the Bt (hairy) spore-probe under ambient conditions compared to that of the Bg spore-probes, in support of the flattened probe results. The number of replicated measurements was 25 for each spore-probe. Since nm deflection of the cantilevers is directly proportional to the adhesive force, these results clearly demonstrate higher adhesion of Bt versus Bg spores, as anticipated, suggesting that exosporium hairs of Bt increase adhesion. These results have successfully completed the year 1 milestone and are included in a manuscript in preparation.

Table 1. Results of spore-probe adhesion experiments.

spore-probe	nm deflection mean	Std dev
Bg tip 1	364	43
Bg tip 2	302	37
Bg tip 3	349	67
Bt tip 4	787	77

The percent removal of 1 µm, 3 µm, and 5 µm PSL particles from glass slides placed 1.5 cm from the orifice using one puff of air is shown in Figure 6. The percent removed was 4.9 ± 5.9, 15.5 ± 6.7, and 84.2 ± 6.5 for 1 µm, 3 µm, and 5 µm PSL microspheres, respectively. As expected, larger particles have less adhesive force and are more easily removed due to their smaller surface area per unit mass.

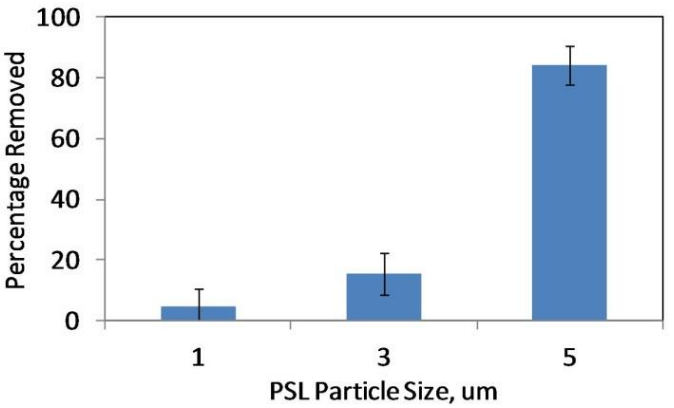

Figure 6. Plot of % of particles removed for 1 µm, 3 µm, and 5 µm PSL microspheres by air impingement. Standard deviation shown as error bars.

The percent removed for 1 µm PSL microspheres and Bg (non-hairy) and Bt (hairy) spores placed at 1.5 cm and 2.5 cm distances from the orifice is shown in Figure 7. The percent removed was 5.7 ± 6, 4.2 ± 4.2, and 4.1 ± 1.1 for 1 µm PSL, Bg, and Bt at 2.5 cm separation distance and 4.9 ± 5.9, 10 ± 4.3, and 8.2 ± 4.9 for the same particles at 1.5 cm, respectively. The PSL microspheres were used as a validation check to compare against the approximate magnitudes of the spore removal data.

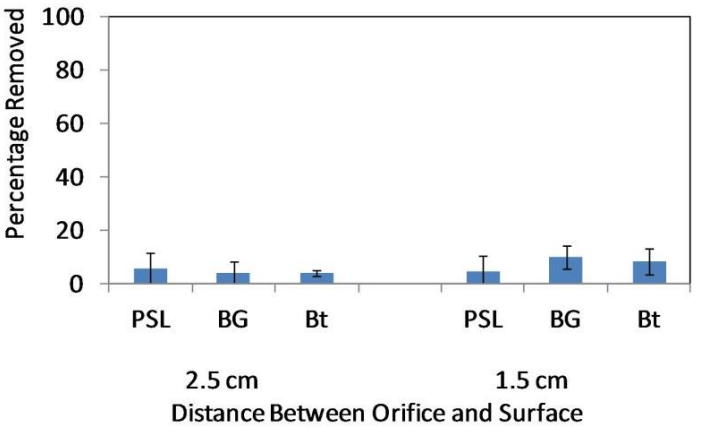

Figure 7. Plot of percent of particles removed for 1 µm PSL microspheres and Bg and Bt spores by air impingement with separation distances of 2.5 and 1.5 cm between glass slide and orifice. Standard deviation is shown as error bars.

The results show that particle removal is similar for 1 µm PSL microspheres as well as for Bg and Bt spores at the same separation distance. Decreasing the separation distance between the glass slide and the orifice seems to slightly increase particle removal. Increasing the number of puffs up to 200 did not significantly increase particle removal of the 1 µm particles placed at 1.5 cm separation (from 3.0% removal for 10 puffs to 7.4% removal for 200 puffs). Centrifugal acceleration at 9250 rpm for 4 hours resulted in smaller percent removed values and relatively larger error bars compared to air impingement (2.3 ± 2.3, 4.1 ± 4.4, and 5.9 ± 7.9 for 1 µm, 3 µm, and 5 µm PSL microspheres respectively). Centrifuge and wind tunnel experiments have not resulted in any spore removal. For the air impingement study, additional nozzle and air flow parameters (air puff duration and orifice size) have been varied to try to optimize particle removal. Results from using closer nozzles, longer puff times, and smaller orifice sizes seem to work best and have yielded the following percent removed values: 53.7 ± 10.6 and 59.4 ± 8.3 for Bt and Bg spores. The lower percent removed for Bt (hairy) spores indicates stronger adhesion and supports the AFM results, but the large error bars prevent statistical certainty. More replicates are planned for year 2 to try to reduce the error bars. Further work is planned in collaboration with Dr. Mark Varady

(Optimetrics, Inc. at Edgewood Chemical Biological Center) and Ryan Keedy (University of Washington) to try to correlate these percent removed values to units of adhesive force using derived fluid mechanics equations and/or computational fluid dynamics.

3.3 Hair adhesion

Calculated single-hair binding energies were ~200 to 400 kcal/mol, depending on orientation, as shown in Figure 8. MD simulation results suggest the formation of several hydroxyl H-bonds between protein and SiO_2 surface (not shown) as well as deformation of protein loops to spread over the surface (see red loop in Figure 8) and increase contact area, possibly supporting the preliminary dwell time flattened tip AFM results on Bt spores.

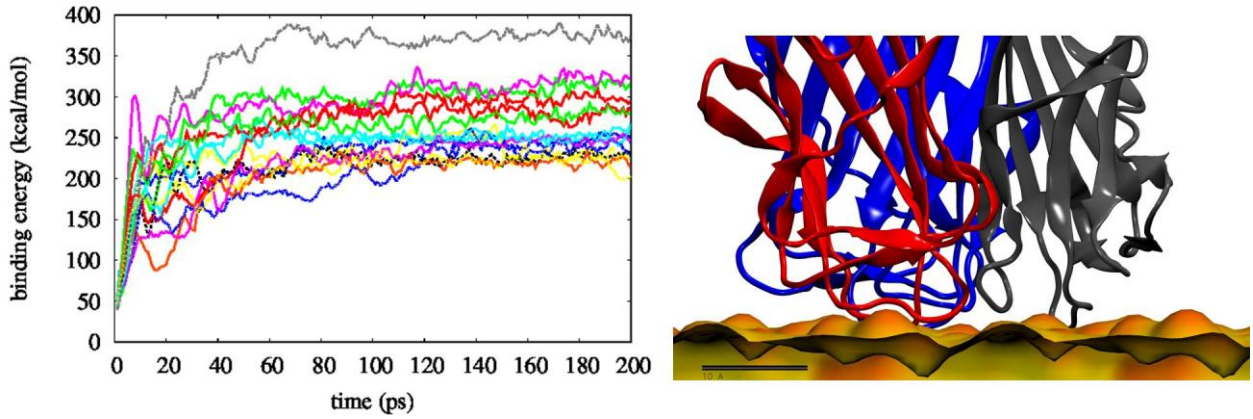

Figure 8. (left) Plot of hair-surface binding energy (kcal/mol) versus simulation time (ps) for each of the 15 different initial hair orientations. (right) Side-view of loops spreading over surface contour; hair represented as cartoon and colored by protein monomer; SiO_2 surface colored yellow/orange; scale bar is 1 nm.

The binding energy values will be converted into force units for comparison with single-protein AFM planned in year 2. Estimated spore surface area, spore-surface contact area, and exosporium hair surface density values will be used to compare these single-hair forces with the whole spore adhesive force AFM measurements as well as to determine the per-area adhesive force. Solvent-accessible surface areas and hydrogen-bond contents will also be calculated. Young's modulus (stiffness) and other mechanical and structural properties may also be calculated from the MD simulations to help understand the dynamic behavior of the exosporium and how it interacts with surfaces.

4. CONCLUSIONS

We have completed our year 1 milestone by measuring stronger Bt (hairy) spore adhesion than that of Bg (non-hairy), demonstrating an adhesion enhancement due to the exosporium hairs, in support of our hypothesis. Both the flattened tip and spore-probe AFM experiments clearly demonstrated this enhancement, and the air impingement study also supported this, although its large error bars prevented statistical confidence. We have developed a methodology to measure spore and 1 μm particle removal from surfaces using air impingement. Recombinant BclA protein will be prepared and purified and used in single-protein AFM and circular dichroism experiments to measure single-hair adhesion and changes in secondary structure (Beta sheet, collagen-like helix, and loop content of protein) upon interaction with surfaces. These studies will facilitate testing the role of hair orientation and allow for more direct comparison with modeling. Future work will focus on humidity-controlled conditions and more spore species (mutant spores already prepared) as well as functionalizing surfaces (e.g., silane, thiol, and amine oligomers; chemical vapor deposition; and polymer brushes) to study how the exosporium hairs respond to different surface and chemical environments and to help aid the design of novel filtration or protective materials.

ACKNOWLEDGEMENTS

The authors would like to acknowledge U.S. Army funding provided through the Edgewood Chemical Biological Center's In-House Laboratory Independent Research and Surface Science Initiative programs.

REFERENCES

[1] Kailas, L., *et al.*, "Surface architecture of endospores of the Bacillus cereus/anthracis/thuringiensis family at the subnanometer scale", *Proceedings of the National Academy of Sciences of the United States of America*. **2011**. 108(38), p16014-16019.

[2] Malkin, A.J. and Plomp, M., "High-resolution architecture and structural dynamics of microbial and cellular systems: insights from in vitro Atomic Force Microscopy", In: *Scanning Probe Microscopy of Functional Materials: Nanoscale Imaging and Spectroscopy*, Kalinin, S.V. and Gruverman, A. (eds.). Springer Science Business Media, New York. **2010**. p39-68.

[3] Hachisuka, Y.; Kojima, K.; and Sato, T., "Fine filaments on the outside of the exosporium of Bacillus anthracis spores", *Journal of Bacteriology*. **1966**. 91(6), p2382-2384.

[4] World Health Organization, *Anthrax in humans and animals*, 4th edition. Geneva: WHO, Switzerland. **2008**. p60.

[5] Faille, C. *et al.*, "Occurrence of Bacillus cereus spores with a damaged exosporium: Consequences on the spore adhesion on surfaces of food processing lines", *Journal of Food Protection*. **2007**. 70(10), p2346-2353.

[6] Lequette, Y. *et al.*, "Role played by exosporium glycoproteins in the surface properties of Bacillus cereus spores and in their adhesion to stainless steel", *Applied and Environmental Microbiology*. **2011**. 77(14), p4905-4911.

[7] Bowen, W.R. *et al.*, "The measurement of Bacillus mycoides spore adhesion using atomic force microscopy, simple counting methods, and a spinning disk technique", *Biotechnology and Bioengineering*. **2002**. 79(2), p170-179.

[8] Sylvestre, P.; Couture-Tosi, E.; and Mock, M., "A collagen-like surface glycoprotein is a structural component of the Bacillus anthracis exosporium", *Molecular Microbiology*. **2002**. 45(1), p169-178.

[9] Rety, S.; *et al.*, "The crystal structure of the Bacillus anthracis spore surface protein BclA shows remarkable similarity to mammalian proteins", *The Journal of Biological Chemistry*. **2005**. 280(52), p43073-43078.

[10] Moberly, B.J.; Shafa, F.; and Gerhardt, P., "Structural details of anthrax spores during stages of transformation into vegetative cells", *Journal of Bacteriology*. **1966**. 92(1), p220-228.

[11] He, L.M. and Tebo, B.M., "Surface charge properties of and Cu(II) adsorption by spores of the marine Bacillus sp. strain SG-1", *Applied and Environmental Microbiology*, **1998**. 64(3), p1123–1129.

[12] Loskill, P. *et al.*, "Reduced adhesion of oral bacteria on hydroxyapatite by fluoride treatment", *Langmuir*, **2013**. 29(18), p5528-5533.

[13] Whisman, N. *et al.* "Probing microplatform for the study of biological adhesion forces", *Review of Scientific Instruments*, **2003**. 74(10), p4491-4494.

[14] Brahmbhatt, T.N. *et al.*, "Recombinant exosporium protein BclA of Bacillus anthracis is effective as a booster for mice primed with suboptimal amounts of protective antigen", *Infection and Immunity*. **2007**. 75(11), p5240-5247.

[15] Fahs, A. and Louarn, G., "Plant protein interactions studied using AFM force spectroscopy: nanomechanical and adhesion properties", *Physical Chemistry Chemical Physics*. **2013**. 15(27), p11339-11348.

[16] Snyder, J.A. *et al.*, "Development of a tuned interfacial force field parameter set for the simulation of protein adsorption to silica glass", *Biointerphases*, **2012**. 7(1-4), p56.

[17] Vellore, N.A. *et al.*, "Assessment of the transferability of a protein force field for the simulation of peptide-surface interactions", *Langmuir*. **2010**. 26(10), p7396-7404.

[18] (a) Arnold, K.. *et al.*, The SWISS-MODEL workspace: a web-based environment for protein structure homology modelling. *Bioinformatics.* **2006**. 22(2), p195-201; (b) Biasini, M. *et al.*, SWISS-MODEL: modelling protein tertiary and quaternary structure using evolutionary information. *Nucleic Acids Research*. **2014**. 42, W252-258; (c) Guex, N.; Peitsch, M.C.; and Schwede, T., Automated comparative protein structure modeling with SWISS-MODEL and Swiss-PdbViewer: a historical perspective. *Electrophoresis*. **2009**. 30(S1), S162-73; (d) Kiefer, F. *et al.*, The SWISS-MODEL Repository and associated resources. *Nucleic Acids Research*. **2009**. 37, D387-392.

[19] Kirchdoerfer, R.N. *et al.*, "Variable lymphocyte receptor recognition of the immunodominant glycoprotein of Bacillus anthracis spores", *Structure*. **2012**. 20(3), p479-486.

[20] Cruz-Chu, E.R.; Aksimentiev, A.; and Schulten, K., "Water−Silica force field for simulating nanodevices", *The Journal of Physical Chemistry B*, **2006**. 110(43), p21497-21508.

Coherent plasmon-exciton coupling in silver platelet-J-aggregate nanocomposites

Brendan G. DeLacy[a*], Owen D. Miller[b], Chia Wei Hsu[c,d], Zach Zander[a], Steven Lacey[a], Raymond Yagloski[a], Augustus W. Fountain[a], Erica Valdes[a], Emma Anquillare[c], Marin Soljačić[c], Steven G. Johnson[b], John D. Joannopoulos[c]
[a]U.S. Army Edgewood Chemical Biological Center, Research and Technology Directorate, 5183 Blackhawk Rd, Aberdeen Proving Ground, MD 21010
[b]Department of Mathematics, Massachusetts Institute of Technology, 77 Massachusetts Ave, Cambridge, MA 02139
[c]Department of Physics, Massachusetts Institute of Technology, 77 Massachusetts Ave, Cambridge, MA 02139
[d]Department of Physics, Harvard University, 17 Oxford St, Cambridge, MA 02138

ABSTRACT

Hybrid nanostructures that couple plasmon and exciton resonances generate hybridized energy states, called plexcitons, which may result in unusual light-matter interactions. We report the observation of a transparency dip in the visible spectra of colloidal suspensions containing silver nanoplatelets and a cyanine dye, 1,1'-diethyl-2,2'-cyanine iodide (PIC). PIC was electrostatically adsorbed onto the surface of silver nanoplatelet core particles, forming an outer J-aggregate shell. This core-shell architecture provided a framework for coupling the plasmon resonance of the silver nanoplatelet core with the exciton resonance of the J-aggregate shell. The sizes and aspect ratios of the silver nanoplatelets were controlled to ensure the overlap of the plasmon and exciton resonances. As a measure of the plasmon-exciton coupling strength in the system, the experimentally-observed transparency dips correspond to a Rabi splitting energy of 221 meV, among the highest reported for colloidal nanoparticles. The optical properties of the silver platelet-J-aggregate nanocomposites were supported numerically and analytically by the boundary-element method and temporal coupled-mode theory, respectively. Our theoretical predictions and experimental results confirm the presence of a transparency dip for the silver nanoplatelet core-J-aggregate shell structures.

Keywords: Plexcitons, plasmons, excitons, nanoshells, J-aggregates, scattering dark state

1. INTRODUCTION

Plasmon-exciton coupling in multilayered nanostructures has garnered much attention in recent years, due to the tunable and unique optical properties that these structures exhibit. These hybrid systems often consist of a core-shell geometry in which the localized surface plasmon resonance (LSPR) of the metallic core couples with the exciton resonance exhibited by a J-aggregate dye or a quantum dot shell.[1-10] This architecture provides a means of studying plasmon-exciton interactions, which have resulted in unique optical phenomena such as induced transparency.[1,2,5,6,11,12] The ability to control the morphology and dimensions of the individual layers at the nanoscale, and the subsequent control of optical properties, are ultimately what drive this field of research. Plexcitonic research, although a relatively new field, has resulted in its use in chemical sensors, light harvesting devices, and optical devices.[13-16]

Metal/cyanine dye hybrid nanostructures are particularly suitable for studying plasmon-exciton interactions in core-shell geometries, due to the relative ease with which the plasmonic nanoparticle morphology and size may be tuned to ensure the overlap of plasmon and exciton resonances. Significant progress in the fabrication and control over the morphology of plasmonic gold and silver nanoparticles has been made in recent years. These efforts have resulted in reliable methods for the fabrication of plasmonic nanorods, nanocubes, nanostars, and nanoplatelets.[17-20]

Cyanine dyes are another class of materials that have been extensively studied due to their use in spectral sensitization and potential applications in novel optoelectronic materials. These dyes have a tendency to aggregate under reduced solubility conditions or when adsorption occurs on particle or substrate surfaces. The J-aggregates that are formed exhibit a narrow lineshape that is red-shifted relative to the monomer absorption band. A Frenkel exciton model is often used to describe this shift as a result of excited states that are formed by the coherent coupling of molecular transition dipoles.[21,22] The tendency of cyanine dyes to aggregate on the surface of nanoparticles makes them ideal candidates as excitonic shells on plasmonic core nanoparticles.

In this report, we explore plasmon-exciton coupling in colloidal suspensions containing silver nanoplatelet-J-aggregate nanocomposites with core-shell structures. The nanostructures were fabricated by electrostatically adsorbing 1,1'-diethyl-2,2'-cyanine iodide (PIC) onto the surface of silver nanoplatelets. The silver nanoplatelet core geometry was chosen for its optical properties and dimensions, which were tuned to ensure the overlap of the plasmonic resonance with the excitonic resonance of the PIC J-aggregate. The overall goal of this study was to ascertain whether or not an induced transparency could be generated using a plasmonic nanoplatelet-J-aggregate core-shell geometry.

Induced transparency is due to the coupling of two or more resonances exhibited by nanostructures with multiple, overlapping plasmonic resonances, plasmonic and excitonic resonances, or dielectric resonances. A plethora of approaches have been taken to model the coupling of resonances in these systems, including perturbative models,[23] a generalization of the Fano formula,[24-26] the electrostatic approximation,[27,28] and coupled-mechanical-oscillator models.[29-33] An analytical treatment of light scattering from a multi-resonant nanostructure was recently developed using temporal-coupled mode theory.[34] In this study, we use both the boundary-element method (BEM) and temporal-coupled mode theory to describe the plasmon-exciton coupling in the silver platelet/J-aggregate nanocomposite.

2. EXPERIMENTAL METHODS

PIC standard and PIC/halloysite clay mixture. A 0.5 mM PIC stock solution was prepared by dissolving 2 mg of PIC (Sigma-Aldrich) in 100 mL phosphate buffer (pH = 6.0). A 0.01 mM PIC standard solution was prepared by diluting 1 mL of the 0.5 mM PIC stock solution with phosphate buffer in a 50 mL volumetric flask. In order to induce the formation of the J-aggregate form of PIC, 2 mL of the 0.01 mM PIC standard solution was mixed with 100 µL of a 1 mg/mL suspension containing halloysite clay (Sigma-Aldrich) in water. (2) To form the silver nanoplatelet/PIC mixtures, 2 mL of a 0.1 mg/mL silver nanoplatelet solution (Nanocomposix Inc.) was mixed with 100 µL 0.5 mM PIC, yielding the spectra provided in Figure 2(c). (3) Silver nanoplatelets were also synthesized in-house using a modified version of Mirkin's approach.[20] Briefly, 25 mL of a 0.11 mM $AgNO_3$ (Sigma-Aldrich) was placed in a 2 oz. Wheaton jar. While magnetically stirring at room temperature, 1.5 mL of a 30 mM sodium citrate (Sigma-Aldrich) solution in water, 1.5 mL of a 10 mg/mL polyvinylpyrollidone (MW = 29,000, Aldrich) solution in water, and a variable amount (ranging from 20 µL to 40 µL) of 30% (w/w) hydrogen peroxide (Sigma-Aldrich) were added. The mixtures were stirred for 15 minutes, after which 100 µL of 100 mM $NaBH_4$ (Sigma-Aldrich) was added to each solution. The solutions were stirred for 24 hours. The variable amount of hydrogen peroxide produced silver platelets with varying size, as measured by dynamic light scattering. Specifically, the addition of the variable amount of 30% hydrogen peroxide solution yielded average platelet sizes from 34.5 nm to 58.2 nm. (4) Synthesized silver nanoplatelets/PIC mixtures were formed by mixing 2 mL of the final silver platelet solutions (~0.01 mg/mL) with 60 µL 0.5 mM PIC.

3. THEORETICAL METHODS

In order to elucidate the optical response of the Ag/PIC nanocomposites, numerical and analytical calculations were performed using the BEM and temporal coupled-mode theory, respectively. Both the numerical and analytical simulations yielded good agreement with the experimental results. Specifically, these simulations predicted the presence of an induced transparency state for multilayered nanoplatelets with the morphology and dimensions of those described in the experiments.

For the numerical computations, a free-software implementation[35] of the BEM[36] was employed. The distribution of experimental sizes was modeled by fixing the thickness of the platelets at 8 nm and varying the diameters of the cross-sections from 30 nm to 50 nm. The size-averaged extinction per unit volume is given by adding the extinction per volume ratios of the individual sizes, weighted by the relative volume fraction (taken to be equal). A thickness of 8 nm was assumed for the PIC coating, which was assumed to have a permittivity described by an oscillator strength of $f = 0.02$ and a linewidth $\gamma = 21$ meV. An induced transparency is clearly visible in the computed volume extinction coefficient, as shown in Figure 1.

APPROVED FOR PUBLIC RELEASE

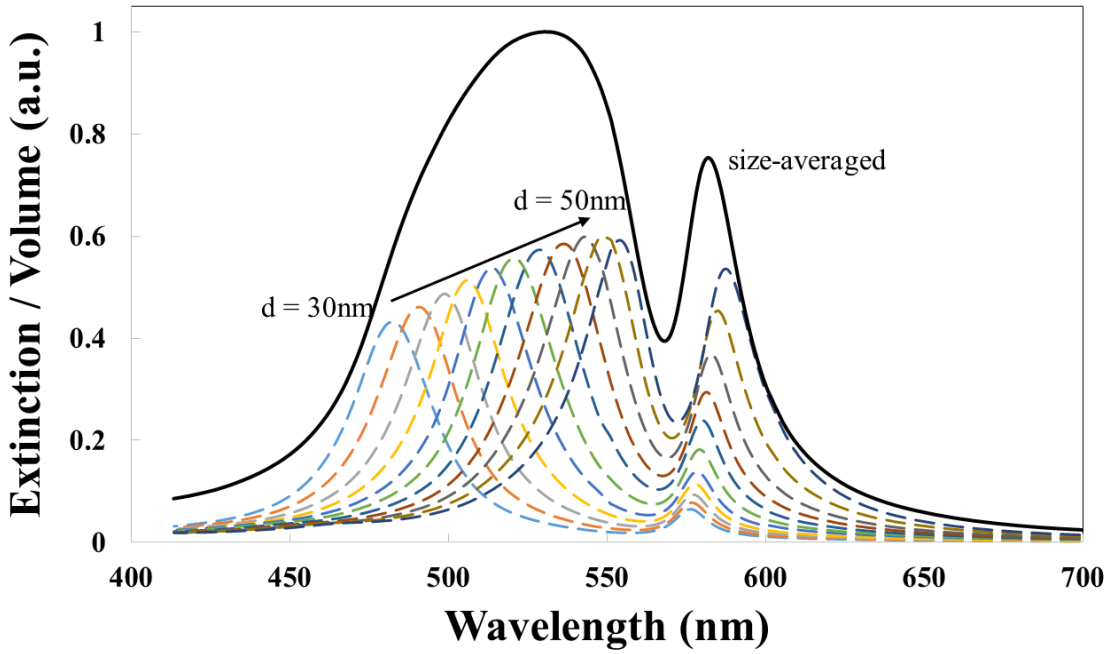

Figure 1. Average extinction cross-section per unit volume of a distribution of PIC-coated silver platelets, computed using the boundary element method. The distribution of experimental sizes was modeled by fixing the thickness of the platelets at 8 nm and varying the diameter (d) from 30 nm to 50 nm. A thickness of 8 nm was assumed for the PIC coating. The PIC permittivity is modeled by an oscillator strength of *f* = 0.02 and a linewidth γ = 21 meV. The single-particle data (dashed lines, scaled up by a factor of three) shows significant transparency dips when the exciton and plasmon resonances are close. In the average extinction over all sizes (solid line), the transparency dip persists, due to the relatively small variation in dark state energies.

The primary limitation to the extent of the transparency dip is the distribution of sizes present in each sample: given a smaller distribution of platelet sizes, an even greater peak to valley ratio is possible.

The suppressed extinction can also be modeled analytically. Since the core-shell structure studied here is much smaller than the wavelength, the scattering and absorption cross sections of the particle are well described by the electric dipole contribution, as

$$\sigma_{sca} = \frac{3\lambda^2}{8\pi}|1 - R|^2, \quad (1)$$

$$\sigma_{abs} = \frac{3\lambda^2}{8\pi}(1 - |R|^2). \quad (2)$$

The extinction cross section is given by $\sigma_{ext} = \sigma_{sca} + \sigma_{abs}$. When loss is small, the reflection coefficient R can be described using temporal coupled-mode theory as[34]

$$R = 1 - 2\frac{[i(\omega_2 - \omega) + \xi_2]\gamma_1 + [i(\omega_1 - \omega) + \xi_1]\gamma_2}{[i(\omega_1 - \omega) + \gamma_1 + \xi_1][i(\omega_2 - \omega) + \gamma_2 + \xi_2] - \gamma_1\gamma_2}, \quad (3)$$

where ω is the frequency of the incident light, $\omega_{1,2}$ are the resonant frequencies, $\gamma_{1,2}$ are the radiative decay rates, and $\xi_{1,2}$ are the absorptive decay rates. Interference between the radiation from the two resonances gives rise to the suppressed scattering and extinction.[34] Figure 2 shows the single-particle cross sections from this analytical model with ω_1 = 1.98 eV, γ_1 = 90 meV, ξ_1 = 66 meV for the plasmonic resonance, and ω_2 = 2.28 eV, γ_2 = 142 meV, ξ_2 = 14 meV for the exciton resonance; it closely reproduces the features seen from the measured data presented in the Results and Discussion section.

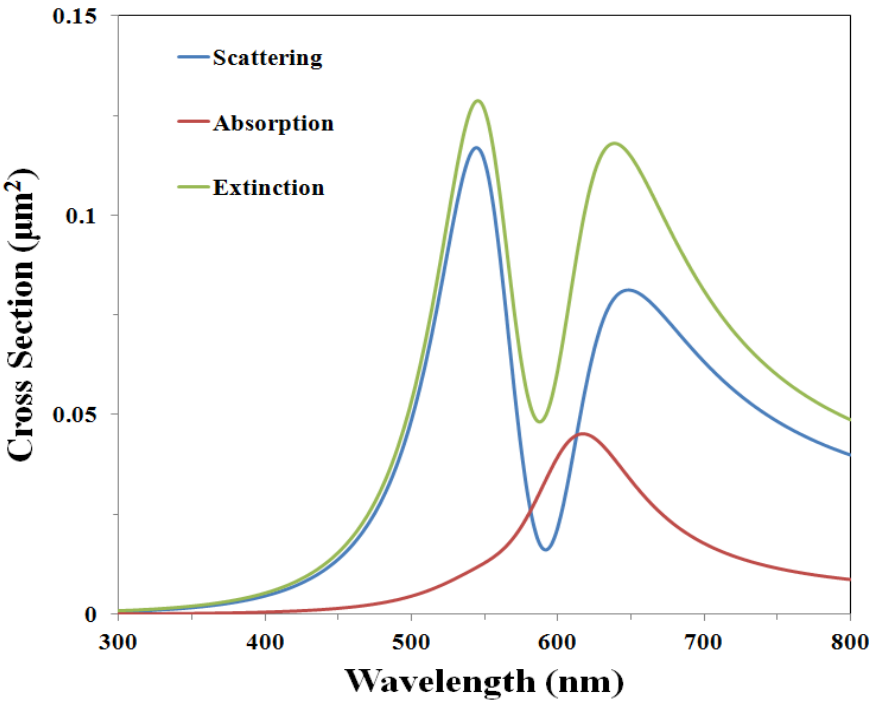

Figure 2. Calculated extinction, scattering, and absorption cross sections of a PIC-coated silver platelet using the temporal coupled-mode theory. For the plasmonic resonance, a resonance frequency of ω_1 = 1.98 eV, a radiative decay rate of γ_1 = 90 meV, and an absorptive decay rate of ξ_1 = 66 meV were used in the calculation. Parameters for the exciton resonance included a resonance frequency of ω_2 = 2.28 eV, a radiative decay rate of γ_2 = 142 meV, and an aborptive decay rate of ξ_2 = 14 meV.

4. RESULTS AND DISCUSSION

The chemical structure of PIC, along with its absorption spectra of the monomeric form (red curve) and J-aggregated form (blue curve) are provided in Figure 3.

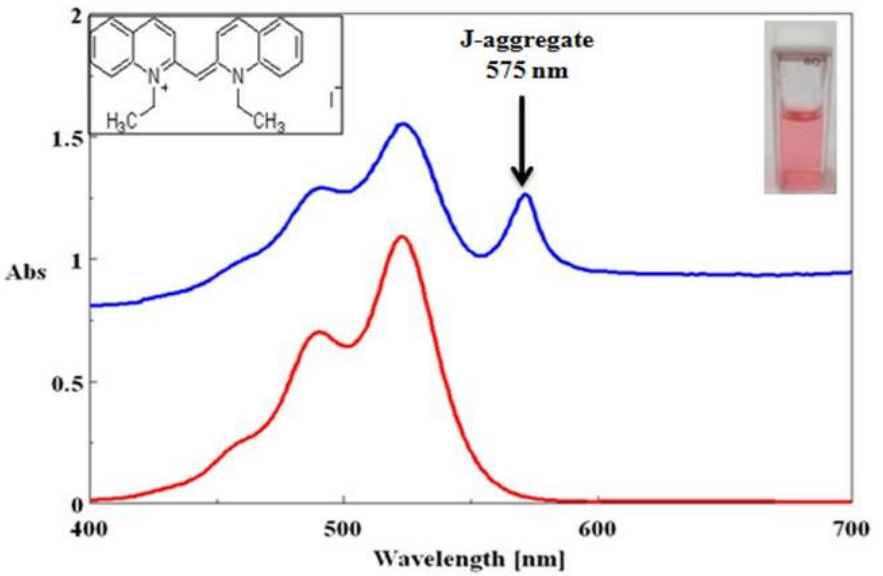

Figure 3. Absorption spectra of 0.02 mM PIC in phosphate buffer, pH = 6 (red curve). Absorption of the monomer is observed. In the presence of halloysite clay (1 mg/mL), the formation of a J-aggregate is induced and a new, red-shifted peak is observed at 575 nm (blue curve). Insets provide the chemical structure of PIC (upper left) and an image of the PIC solution (upper right). The optical path length for all measurements was 10 mm.

APPROVED FOR PUBLIC RELEASE

At low concentrations ($c<<10^{-5}$ M), only the monomer form of PIC is observed, as shown in the red curve. Cyanine dyes, including PIC, have been shown to aggregate in the presence of minerals such as montmillirite clay.[37] It is presumed that the metal-oxide content in the mineral clays produce a negatively charge surface, and promotes the J-aggregation of cationic cyanine dyes onto the surface of the clay. We employed this approach to induce the J-aggregate formation and mixed a small amount (100 µL) of a 0.1 mg/mL suspension of halloysite clay in water with 2 mL of 0.02 mM PIC. A red-shifted J-aggregate peak immediately forms near 575 nm upon addition of the halloysite clay as observed in the blue curve.

In order to explore the interaction between PIC and plasmonic nanoparticles in our study, aliquots of PIC were mixed with solutions containing silver nanoplatelets. Silver nanoplatelets were first fabricated using a common approach in which silver cations are reduced with sodium borohydride, in the presence of polyvinylpyrrolidone (PVP), sodium citrate, and hydrogen peroxide.[20] The PVP and citrate molecules have been shown to adhere to specific crystal faces of the silver as it nucleates and grows, thereby inducing non-spherical nanoparticle geometries.[20,38] In addition to the in-house platelet synthesis efforts, silver nanoplatelets were also obtained from Nanocomposix, Inc. (San Diego, CA). A transmission electron microscopy (TEM) image of silver nanoplatelets synthesized in-house is provided in Figure 4(a). Figure 4(b) provides a schematic of the silver platelet core – J-aggregate shell nanostructure. In Figure 4(c), the absorption spectrum of a 0.1 mg/mL silver nanoplatelet solution (Nanocomposix Inc.) is provided in the blue curve, while the red curve represents a mixture containing 2 mL of a 0.1 mg/mL silver nanoplatelet solution with 100 µL of 0.5 mM PIC.

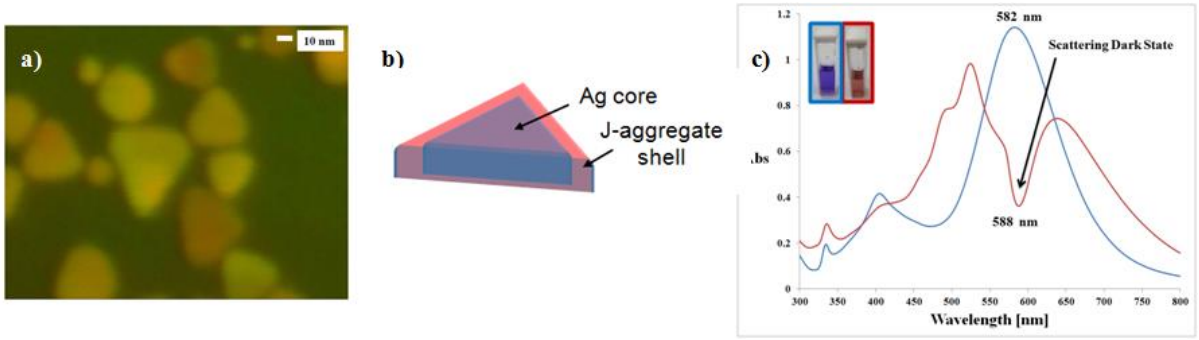

Figure 4. (a) TEM image of silver nanoplatelets (scale bar = 10 nm). (b) Schematic of a bi-layered nanoplatelet, consisting of a silver nanoplatelet core and a PIC J-aggregate shell. (c) Absorption spectra of a solution containing 0.1 mg/mL silver nanoplatelets in water (blue curve), and a solution containing 2 mL of 0.1 mg/mL silver nanoplatelet solution mixed with 100 µL of 0.02 mM PIC (red curve). A scattering dark state is observed. The inset (upper left) provides images of the silver nanoplatelet and silver nanoplatelet/PIC solutions. The optical path length for all spectral measurements was 10 mm.

An attenuation dip at 588 nm emerges when the silver platelets are in the presence of PIC, representing a transparency of >50% (peak to dip). The presence of a transparency dip, a blue-shifted high energy peak (relative to the transparency dip), and a red-shifted low energy peak are all characteristic spectral features of plexcitonic structures that exhibit strong plasmon-exciton coupling.[11,12] The transparency and red-shifted lower energy peak are readily observable for the Ag platelet/PIC spectra shown in Figure 4(c). Further inspection of the red curve in Figure 4(c) reveals the presence of an inflection point at 568 nm, which was hypothesized to be due to the underlying blue-shifted plexcitonic peak that was obscured by the presence of the monomer form of the dye. To reveal more clearly the spectral effects of the J-aggregate, we subtracted out the PIC monomer absorption through the standard least squares background subtraction technique.[38] The background subtraction technique enabled, for example, the conversion of the red curve in Figure 4(c) to the "582 nm" curve of Figure 5; in the latter, the noisy monomer data is removed, the plexcitonic upper branch is clearly visible, and computation of the peak-to-dip ratio is straightforward.

In order to explore the impact of the underlying plasmon resonance energy on the degree of plasmon-exciton coupling in our silver platelet/PIC system, PIC was individually mixed with silver nanoplatelets that varied in aspect ratio. The variation in platelet aspect ratio allowed for the plasmon resonance to be tuned from blue to red, crossing the J-aggregate exciton resonance. Platelet size was controlled by varying the amounts of hydrogen peroxide added during the silver platelet synthetic approach, as described in the experimental section. Upon addition of the PIC to each platelet batch, a transparency dip, a blue-shifted higher energy peak, and a red-shifted lower energy peak were consistently generated, as shown in Figure 5.

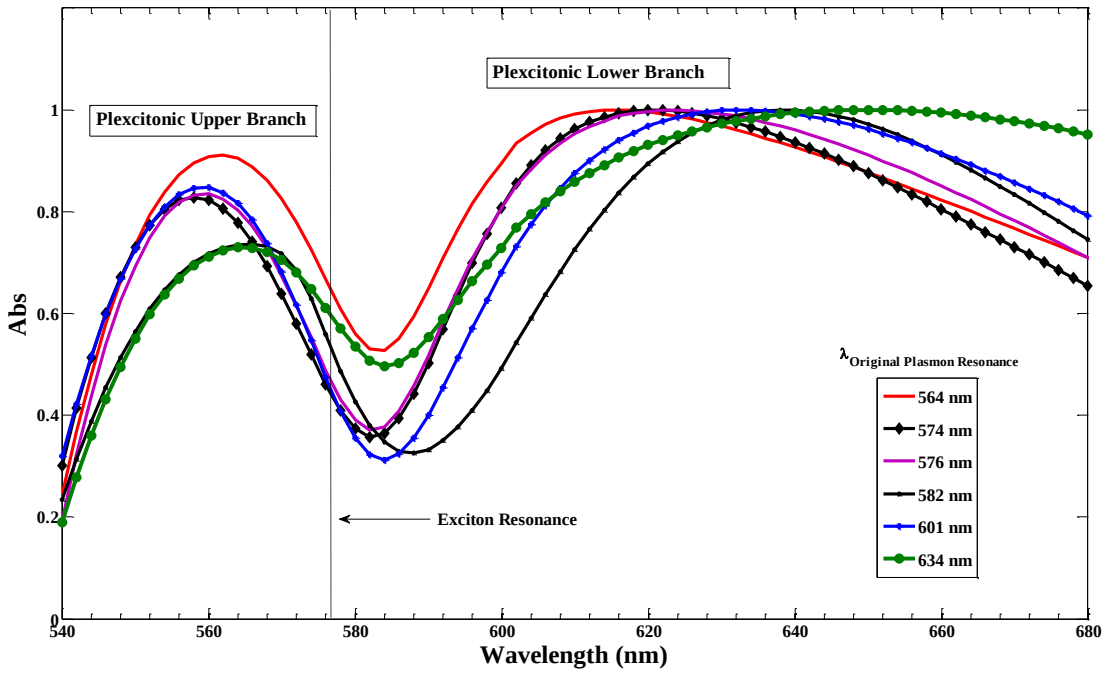

Figure 5. Absorption spectra of silver nanoplatelet/PIC solutions. Each curve represents spectra of Ag platelet/PIC solutions in which 2 mL of a given silver nanoplatelet solution were mixed with 60 µL 0.5 mM PIC. By tuning the aspect ratio of the particles, the original resonant plasmonic wavelength (before adding PIC) was varied from λ_{orig} = 564 nm to λ_{orig} = 634 nm (as indicated in the legend). Adding PIC creates two new peaks, a blue-shifted "upper branch" and a red-shifted "lower branch," that are approximately centered around the resonant wavelength (λ = 575 nm) of the J-aggregate.

Each curve in Figure 5 represents a different original plasmon resonance, within a specific silver platelet batch. The variability in transparency and the degree of spectral shifts clearly demonstrate that the plasmon-exciton coupling is dependent on the plasmon resonance energy, relative to the exciton resonance. The greatest transparencies were observed for those cases in which the plasmon resonance energy most closely matched the exciton resonance (which occurs at 575 nm for aggregated PIC). Specifically, the greatest transparencies were observed for silver nanoplatelets which demonstrated plasmon resonances at 574 nm, 576 nm, 582 nm, and 601 nm (corresponding to silver platelets with diameters of approximately 40 nm, as determined by dynamic light scattering measurements).

In general terms, the formation of both a blue-shifted and a red-shifted lower energy peak may be described as the coherent coupling of the plasmon resonance of the silver platelet with the exciton transition dipole of the J-aggregate hybrid. This coupling produces the formation of two plexcitonic modes, an upper branch (UB) mode (blue-shifted peak) and a lower branch (LB) mode (red-shifted peak).[40] When the plasmon and exciton resonance energies are equal, the energy difference between the upper and lower branches is known as the Rabi splitting energy, $\hbar\omega_R$, or as the coupling energy. Spectral data extracted from the experimental curves shown in Figure 3 were used to calculate the Rabi splitting energy for the plexcitonic silver platelets. This was achieved by plotting the upper branch and lower branch energies as a function of plasmon resonance peak energy, yielding an upper branch curve and a lower branch curve. Parameters from these curves were then used to calculate the Rabi splitting energy as the difference in upper and lower branch energies for the energy at which the plasmon resonance and the exciton resonance were equal, i.e., at 575 nm or 2.156 eV. A Rabi splitting energy of 221 meV was determined, which is among the highest reported for plexcitonic colloids.[12]

Plexcitonic dispersion curves are often useful for visualizing the upper and lower branch energies as a function of plasmon resonance. A coupled harmonic oscillator model may be used to calculate the plexcitonic dispersion curves for the upper and lower plexciton branches,[40]

$$E_{Plexciton}^{UB,LB}(\hbar\omega_p) = \frac{\hbar\omega_p+\hbar\omega_0}{2} \pm \frac{1}{2}\sqrt{(\hbar\Omega_R)^2 + (\hbar\omega_p - \hbar\omega_0)^2} \quad (4)$$

Here $\hbar\omega_0$ and $\hbar\omega_p$ are the uncoupled exciton and silver nanoplatelet energies, respectively. The Rabi splitting energy obtained from the experimental data was used to generate the hybrid dispersion curves for the upper (green curve) and lower branches (purple curve), as shown in Figure 6.

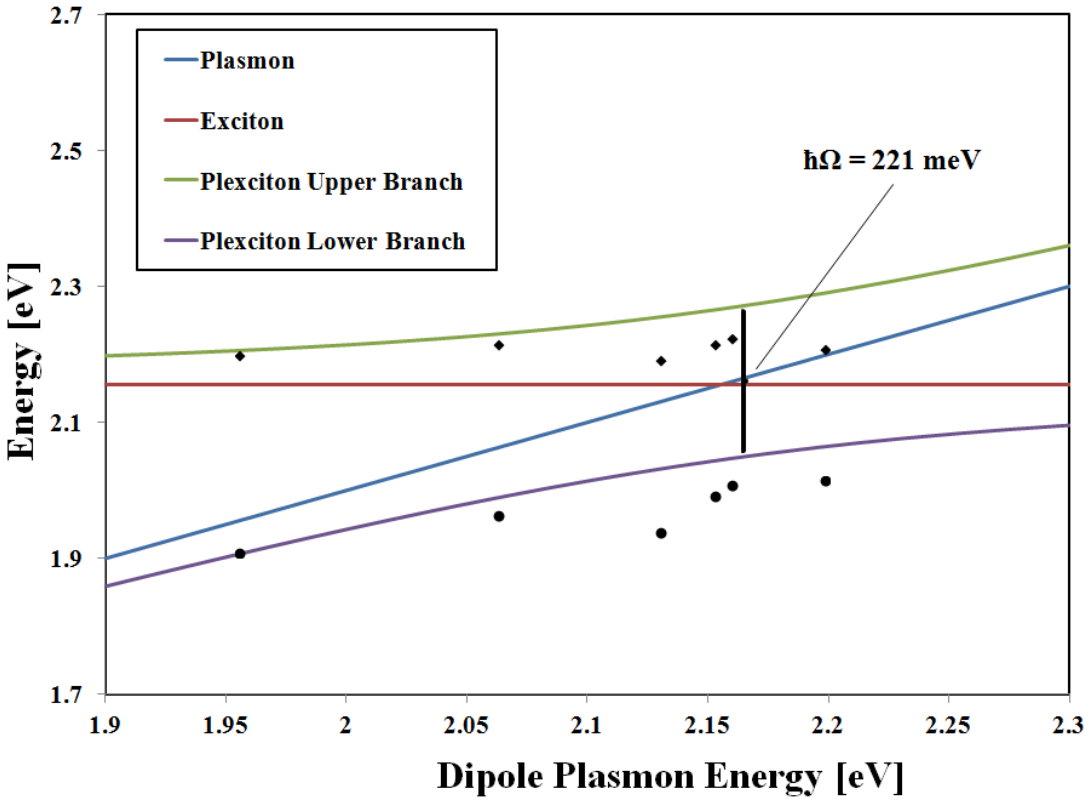

Figure 6. Plexcitonic dispersion curves for the upper (green curve) and lower (purple curve) branches, as calculated using the coupled harmonic oscillator equation provided in the text. The curves are based on a Rabi splitting energy of 221 meV, which was extracted from the upper branch (diamonds) and lower branch (circles) modes that are shown Figure 3. The red and blue curves correspond to the uncoupled exciton and surface plasmon energies, respectively.

The uncoupled exciton and surface plasmon energies are also provided in the figure. Finally, experimental data points for the upper and lower branch energies extracted from Figure 5 are also provided in Figure 6, demonstrating strong correlation between the experimental and theoretical curves.

5. CONCLUSION

We have reported strong plexcitonic coupling between the localized surface plasmon resonance of silver nanoplatelets and J-aggregate excitons. This coupling produced an induced transparency and yielded a Rabi splitting energy that is among the highest reported for colloidal suspensions. The presence of the transparency was also predicted by numerical and analytical calculations. The strongest couplings were observed for those cases in which the plasmon resonance most closely matched the exciton resonance. The large Rabi energy is explained at least in part by our use of small (almost quasistatic) nanoplatelets, which have nearly optimal extinction response and, for the same resonant frequency, yield greater field intensities than coated spheres.[41] We hypothesize that the strong coupling may also be due in part to the orientation of the J-aggregate along the major dimensions of the platelets, i.e. the transition dipoles of the exciton resonance, if aligned with the plasmon resonance of the platelet, produces an enhanced plexcitonic coupling. Future efforts in modeling the dye orientation on the surface silver platelets should provide insight into the impact of dye orientation on plexcitonic coupling.

ACKNOWLEDGEMENTS

This research was funded by the Department of the Army Basic Research Program and sponsored by the Edgewood Chemical Biological Center. Support was also provided by the U.S. Army Research Office under contract W911NF-13-D-0001.

REFERENCES

[1] Kometani, N. *et al.*, "Preparation and optical absorption spectra of dye-coated Au, Ag, and Au/Ag colloidal nanoparticles in aqueous solutions and in alternate assemblies", *Langmuir*. **2001**. 17, p578-580.

[2] Widerrecht, G.P. *et al.*, "Coherent coupling of molecular excitons to electronic polarizations of noble metal nanoparticles", *Nano Letters.* **2004**. 4, p2121-2125.

[3] Yoshida, A. *et al.*, "Silver:dye composite nanoparticles as a building unit of molecular architecture", *Colloids and Surfaces A: Physicochemical and Engineering Aspects.* **2008**. 313-314, p581-584.

[4] Lebedev, W.S. *et al.*, "Absorption properties of the composite silver/dye nanoparticles in colloidal solutions", *Colloids and Surfaces A: Physicochemical and Engineering Aspects*. **2008**. 326, p204-209.

[5] Yoshida, A. *et al.*, "Tuning of the spectroscopic properties of composite nanoparticles by the insertion of a spacer layer: effect of exciton−plasmon coupling", *Langmuir*. **2009**. 25(12), p6683-6689.

[6] Yoshida, A. *et al.*, "Synthesis and spectroscopic studies of composite gold nanorods with a double-shell structure composed of spacer and cyanine dye J-aggregate layers", *Langmuir*. **2009**. 25(19), p11802-11807.

[7] Achermann, M., "Exciton−plasmon interactions in metal−semiconductor nanostructures", *Journal of Physical Chemistry Letters.* **2010**. 1, p2837-2843.

[8] DeLacy, B.G. *et al.*, "Layer-by-layer self-assembly of plexcitonic nanoparticles", *Optics Express*. **2013**. 21(16), p19103-19112.

[9] Lu, Z. and Zhu, K., "Enhancing Kerr nonlinearity of a strongly coupled exciton–plasmon in hybrid nanocrystal molecules", *Journal of Physics B: Atomic, Molecular and Optical Physics*. **2008**. 41(18), p 185503.

[10] Kohlgraf-Owens, D.C. and Kik, P.G., "Numerical study of surface plasmon enhanced nonlinear absorption and refraction", *Optics Express.* **2008**. 16(14), p10823-10834.

[11] Fofang, N.T. *et al.*, "Plexciton dynamics: exciton−plasmon coupling in a J-aggregate−Au nanoshell complex provides a mechanism for nonlinearity", *Nano Letters.* **2011**. 11. p1556-1560.

[12] Zengin, G. *et al.*, "Approaching the strong coupling limit in single plasmonic nanorods interacting with J-aggregates", *Scientific Reports*. **2013**. 3, p3074.

[13] Murphy, C., "Optical sensing with quantum dots", *Journal of Analytical Chemistry*. **2002**. 74(19), p520A-526A.

[14] Govorov, A.O. and Carmeli, I., "Hybrid structures composed of photosynthetic system and metal nanoparticles: plasmon enhancement effect", *Nano Letters.* **2007**. 7(3), p620-625.

[15] Slocik, J.M. *et al.*, "Peptide-assembled optically responsive nanoparticle complexes", *Nano Letters.* **2007**. 7(4), p1054-1058.

[16] Artuso, R.D. and Bryant, G.W., "Optical response of strongly coupled quantum dot−metal nanoparticle systems: double peaked Fano structure and bistability", *Nano Letters.* **2008**. 8(7). p2106-2111.

[17] Orendorff, C.J. *et al.*, "Aspect ratio dependence on surface enhanced Raman scattering using silver and gold nanorod substrates", *Journal of Physical Chemistry Chemical Physics.* **2006**. 8, p165-170.

[18] Au, L. *et al.*, "Synthesis and optical properties of cubic gold nanoframes", *Nano Research*. **2008**. 1, p441-449.

[19] Khoury, C.G. and Vo-Dinh, T., "Gold nanostars for surface-enhanced Raman scattering: synthesis, characterization and optimization", *Journal of Physical Chemistry C*, **2008**. 112(48), p18849-18859.

[20] Metraux, G.S. and Mirkin, C.A., "Rapid thermal synthesis of silver nanoprisms with chemically tailorable thickness", *Advanced Materials.* **2005**. 17(4), p412-415.

[21] Davydov, A.S., *Theory of Molecular Excitons*, 1st edition. Dresner, S.B., Translator. Plenum Press, New York. **1971**.

[22] Van Burgel, M.; Wiersma, D.A.; and Duppen, K., "The dynamics of one-dimensional excitons in liquids", *Journal of Chemical Physics.* **1995**. 102, p20-33.

[23] Artar, A. *et al.*, "Multispectral plasmon induced transparency in coupled meta-atoms", *Nano Letters.* **2011**. 11(4), p1685-1689.

[24] Giannini, V. *et al.*, "Fano resonances in nanoscale plasmonic systems: a parameter-free modeling approach", *Nano Letters.* **2011**. 11(7), p2835-2840.

[25] Gallinet, B. and Martin, O.J.F., "Ab initio theory of Fano resonances in plasmonic nanostructures and metamaterials", *Physical Review B.* **2011**. 83, p235427.

[26] Gallinet, B.; Martin, O.J.F. "Influence of electromagnetic interactions on the lineshape of plasmonic Fano resonances", *ACS Nano* **2011**. 5, p8999-9008.

[27] Davis, T.J.; et al., "Simple Model for the Hybridization of Surface Plasmon Resonances in Metallic Nanoparticles", *Nano Letters.* **2010**. 10(7), p2618-2625.

[28] Forestiere, C. *et al.*, "Theory of coupled plasmon modes and Fano-like resonances in subwavelength metal structures", *Physical Review B.* **2013**. 88, p155411.

[29] Mukherjee, S.; *et al.*, "Fanoshells: Nanoparticles with Built-in Fano Resonances", *Nano Letters.* **2010**. 10(7), p2694-2701.

[30] Artar, A. *et al.,* "Directional double fano resonances in plasmonic hetero-oligomers", *Nano Letters.* **2011**. 11(9), p3694-3700.
[31] Lassiter, J.B. *et al.,* "Designing and deconstructing the Fano lineshape in plasmonic nanoclusters", *Nano Letters*. **2012**. 12, p1058-1062.
[32] Lovera, A. *et al.,* "Mechanisms of Fano resonances in coupled plasmonic systems", *ACS Nano*. **2013**. 7, p4527-4536.
[33] Adato, R. *et al.,* "Engineered absorption enhancement and induced transparency in coupled molecular and plasmonic resonator systems", *Nano Letters*. **2013**. 13, p2584-2591.
[34] Hsu, C.W. *et al.,* "Theoretical criteria for scattering dark states in nanostructured particles", *Nano Letters.* **2014**. 14, p2783-2788.
[35] Reid, M.T.H., SCUFF-EM. http://homerreid.dyndns.org/scuff-EM.
[36] Harrington, R.F., *Field Computation by Moment Methods*. IEEE Press, Piscataway, NJ. **1993**.
[37] Dixon, A. *et al.,* "Self assembly of cyanine dye on clay nanoparticles", *American Journal Undergraduate Research*. **2005**. 3(4), p29-34.
[38] Statham, P.J., "Deconvolution and background subtraction by least-squares fitting with prefiltering of spectra", *Analytical Chemistry*. **1977**. 49(14), p2149-2154.
[39] Zhang, Q. *et al.,* "A systematic study of the synthesis of silver nanoplates: is citrate a "magic", reagent?", *Journal of the American Chemical Society.* **2011**. 133(46), p18931-18939.
[40] Schlather, A.E. *et al.,* "Near-field mediated plexcitonic coupling and giant Rabi splitting in individual metallic dimers", *Nano Letters*. **2013**. 13, p3281-3286.
[41] Miller, O.D. *et al.,* "Fundamental limits to extinction by metallic nanoparticles", *Physical Review Letters*. **2014**. 112, p123903.

Highly ordered nanowire arrays based on polydiacetylene for sensing applications

Liangliang Zhu[a], Helen Tran[a], Frederick L. Beyer[b], Scott D. Walck[b], Kato L. Killops[c], Luis M. Campos[a]

[a]Department of Chemistry, Columbia University, 3000 Broadway, New York, NY 10027
[b]U.S. Army Research Laboratory, 4600 Deer Creek Loop, Aberdeen Proving Ground, MD 21005
[c]U.S. Army Edgewood Chemical Biological Center, Research & Technology Directorate, 5183 Blackhawk Rd, Aberdeen Proving Ground, MD 21010

ABSTRACT

With the aim to achieve rapid and efficient topochemical polymerizations in the solid-state, via solution-based processing of thin-films, we report the integration of a diphenyldiacetylene monomer and a poly(styrene-*block*-acrylic acid) block copolymer template for the generation of supramolecular architectural photopolymerizable materials. This strategy takes advantage of non-covalent interactions to template a topochemical photopolymerization that yields a polydiphenyldiacetylene (PDPDA) derivative. In thin-films, it was found that hierarchical self-assembly of the diacetylene monomers by microphase-segregation of the block copolymer template enhances the topochemical photopolymerization, which is complete within a 20-second exposure to UV light. Moreover, introducing UV-active cross-linkable groups within the block copolymer template can be used to create micropatterns of PDPDA by photolithography, in the same step as the polymerization reaction. The materials design and processing may find potential uses in the microfabrication of sensors and other important areas that benefit from solution-based processing of flexible conjugated materials.

Keywords: Polydiacetylene, block copolymer, self-assembly, thin films

1. INTRODUCTION

The Warfighter in the field is exposed to a diverse range of hazards such as explosives, toxic chemicals, biological pathogens, and fatigue, which can significantly compromise their overall health and cognitive abilities to perform complex operations. This high risk environment places heavy demand on the development of robust abiotic sensing materials that display the *sensitivity*, required for detecting threats at low concentrations, and *selectivity*, in order to distinguish harmful substances from their less toxic analogues. To address this need, recent advances in nanotechnology and self-assembling materials, specifically in the area of conjugated polymers,[1] have lead to miniaturization and signal amplification for sensing applications. Within this area, there has been a wealth of research dedicated to the study of polydiacetylene (PDA) for use as a colorimetric sensing material.[2,3]

With the growing interest for diacetylene (DA) materials to be exploited in excitonic photovoltaic devices (PDA undergoes singlet fission),[4] sensors,[1,5] bioelectronic materials,[6] and other optoelectronic devices,[7] the past decade has witnessed increased interest in controlling the polymerization of DAs. The key strategies have been based on grafting DA monomers on surfaces to form monolayers that are well-aligned[8] and introducing functional groups on the DA monomers to control their aggregation and crystallization, followed by thermal or photochemical polymerization.[9,10] The reactivity of such constructs on a solid surface is usually sluggish, where polymerization proceeds within minutes to hours by heating or ultraviolet (UV) light.[2,11] Recently, Shimizu and co-workers have shown that DA-containing macrocycles can crystallize with the appropriate arrangement for polymerization, though the reaction takes 3 hours with heating.[12,13] Exploiting biomimetic supramolecular interactions, Tovar and co-workers found that the arrangement of diphenyldiacetyltene (DPDA) monomers using oligopeptides can guide the supramolecular assembly, where photopolymerization occurs within 30 minutes.[14] In all cases, the polymerizations are system-specific and not amenable for thin-film processing. Solution-based processing by standard techniques with these systems before and after polymerization is difficult due to the lack of molecular preorganization required for the reaction to proceed, and the insolubility from the resulting polymers. Therefore, the development of processable and modular solid-state templates for topochemical polymerizations of DAs that do not rely on unpredictable crystal engineering strategies, with fast reactivity (within seconds), are highly desired.[15]

To tackle the various challenges associated with obtaining solution-processable thin-films of PDA by conventional techniques, we employ a block copolymer (BCP)[16-19] template-based approach that drastically enhances the topochemical photopolymerization. Additionally, strongly phase segregating BCPs,[20] such as polystyrene-*b*-poly(acrylic acid) (PS-*b*-PAA) templates can be chemically modified in order to access micropatterns by photolithography, which may be

APPROVED FOR PUBLIC RELEASE

beneficial for the fabrication of multiple devices within a single wafer. Figure 1 shows the supramolecular grafting strategy that exploits strong hydrogen-bonding interactions between the imidazolyl diphenyl-diacetylene monomer (IDA)[21-23] and PS-*b*-PAA. The IDA monomer is synthesized in only four steps and PS-*b*-PAA, which is also commercially available, can be prepared by established procedures.[24] The supramolecular complex of these two systems is termed PS-*b*-P(AA-*sg*-IDA), where *sg* stands for supramolecular graft of the IDA monomers to the PAA block. This approach takes advantage of the fact that: 1) the DPDA moiety has a larger molar extinction coefficient relative to a conventional DA; 2) non-covalent interactions provide modularity to tune the monomer loading ratios; 3) the complexes can be processed from solution by spin-coating, and 4) microphase segregation of the side-chain functional BCPs induces local order that enhances the polymerization.[16,24,25]

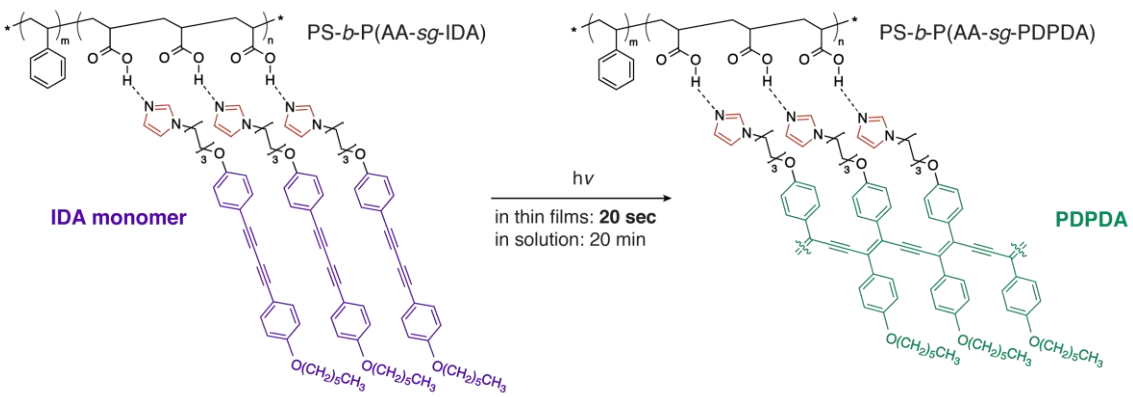

Figure 1. Chemical structures of the BCP PS-*b*-PAA, the monomer IDA, and the corresponding PDA after the BCP-templated photopolymerization of the supramolecular ensemble PS-*b*-(PAA-*sg*-IDA). Solution photopolymerization proceeds in 20 minutes and thin film photopolymerization proceeds in 20 minutes and thin film photopolymerization onloy requires 20 seconds.

2. EXPERIMENTAL

2.1 General

^{1}H nuclear magnetic resonance (NMR) and ^{13}C NMR spectra were measured on a Bruker 400 MHz spectrometer. The fast atom bombardment (FAB) mass spectra and high-resolution mass spectrometry (HR-MS) were recorded on a JMS-HX110 HF mass spectrometer (ionization mode: FAB+). Absorption spectra were recorded on a Shimadzu 1800 spectrophotometer and the photoluminescence emission spectra were collected with a Jobin Yvon Fluorolog-3 spectrofluorometer (Model FL-TAU3). The photoirradiation was carried on PL Series compact UV lamp (4 W) with the irradiation wavelength of 254 nm. The distance between the lamp and the sample was kept within 3-5 cm. Argon bubbling was applied upon the irradiation of those solution samples. Infrared spectra were obtained using a Perkin Elmer Spectrum400 FTIR spectrometer using a PIKE ATR attachment. The atomic force microscopy (AFM) images were collected on a Park System PSI XE100 atomic force microscope. Thermal gravimetric analysis (TGA) was conducted with a TA Instruments Q50. The thickness of thin films was determined by Rudolph EL III Ellipsometer. Transmission electron microscopy (TEM) was performed on a JEOLJEM-2100F field emission TEM at 200 kV. High-angle annular dark field (HAADF) scanning transmission electron microscopy (STEM) images were collected using a Gatan Model 806 HAADF-STEM detector with a 40 µm condenser aperture, 2 cm camera length, and 0.5 nm spot size. Data analysis was performed using Gatan Digital Micrograph 3 software. The fluorescence images were captured by LEICA TCS SP5 confocal microscope.

2.2 Synthesis of compound 1

Compound 1 was prepared according to a similar procedure described in the literature.[26]

2.3 Synthesis of compound 2

A solution of hexyl bromide (1.05 g, 6.36 mmol) in anhydrous acetone (5 mL) was added dropwise into a mixture of compound 1 (1.5 g, 6.41 mmol) and potassium carbonate (0.8 g, 5.8 mmol) in anhydrous acetone (15 mL) at 60 ºC. The mixture was stirred for 12 hours at 60 ºC under Ar. The solvent was removed *in vacuo*, and the residue was purified by silica gel chromatography (hexane : ethyl acetate = 6 1) to afford gray compound 2 (1.02 g, 50.4%). ^{1}H NMR (400 MHz, $CDCl_3$, 298 K): δ = 7.45 (d, J = 9.2 Hz, 2H), 7.42 (d, J = 8.8 Hz, 2H), 6.84 (d, J = 8.8 Hz, 2H), 6.79 (d, J = 8.8 Hz, 2H), 3.97 (t, J = 6.4 Hz, 2H), 1.79 (m, 2H), 1.46 (m, 2H), 1.35 (m, 4H), 0.91 (t, J = 7.2 Hz, 3H). ^{13}C NMR (100 MHz, $CDCl_3$, 298 K): δ = 159.91, 156.32, 134.29, 134.06, 115.66, 114.68, 114.36, 113.62, 81,43, 81.00, 73.01, 72.82, 68.25, 31.57,

29.18, 25.76, 22.60, 14.04. MS (FAB+): calcd. for $[M]^+$ m/z = 318.2, found m/z: 318.3; HR-MS (FAB+): calcd. for $C_{22}H_{22}O_2$ $[M]^+$ m/z = 318.1620, found m/z: 318.1619.

2.4 Synthesis of compound 3

Compound 2 (0.6 g, 1.89 mmol) was added to 1,6-dibromohexane (4.5 g, 18.4 mmol) in acetone (5 mL). Potassium carbonate (520 mg, 3.77 mmol) was added and the mixture refluxed for 6 hours under Ar protection. The solution was filtered and the filtrate was precipitated in a 4-fold volume of hexane. The solid was filtered, washed with petroleum (30 mL) and deionized water (20 mL), and dried under vacuum to obtain gray compound 3 (737 mg, 81.1%). ^{1}H NMR (400 MHz, $CDCl_3$, 298 K): δ = 7.44 (d, J = 8.0 Hz, 4H), 6.83 (d, J = 7.6 Hz, 4H), 3.97 (m, 4H), 3.42 (t, J = 6.8 Hz, 2H), 1.90 (m, 2H), 1.81 (m, 4H), 1.50 (m, 6H), 1.34 (m, 4H), 0.91 (t, J = 6.8 Hz, 3H). ^{13}C NMR (100 MHz, $CDCl_3$, 298 K): δ = 159.89, 159.74, 134.04, 134.04, 114.66, 114.64, 113.85, 113.67, 81,38, 81.27, 72.97, 72.89, 68.17, 67.86, 33.79, 32.66, 31.56, 29.13, 28.99, 27.91, 25.69, 25.28, 22.61, 14.03. MS (FAB+): calcd. for $[M]^+$ m/z = 480.2 (^{79}Br), found m/z 480.2 (^{79}Br); HR-MS (FAB+): calcd. for $C_{28}H_{33}O_2{}^{79}Br$ $[M]^+$ m/z = 480.1664, found m/z: 480.1668.

2.5 Synthesis of IDA

To a mixture of compound 3 (650 mg, 1.35 mmol) and potassium hydroxide (151 mg, 2.78 mmol) in acetonitrile (6 mL), imidazole (645 mg, 9.48 mmol) was added. The reaction mixture was refluxed for 8 hours and then cooled to room temperature. After flash column chromatography (ethyl acetate/methanol = 25 : 2), the crude product was washed with deionized water (15 mL) and dried under vacuum to obtain pure white compound IDA (255 mg, 40.4%).^{1}H NMR (400 MHz, $CDCl_3$, 298 K): δ = 7.46 (s, 1H), 7.44 (d, J = 8.4 Hz, 4H), 7.06 (s, 1H), 6.91 (s, 1H), 6.84 (d, J = 8.8 Hz, 2H), 6.81 (d, J = 8.4 Hz, 2H), 3.96 (m, 6H), 1.78 (m, 6H), 1.47 (m, 4H), 1.34 (m, 6H), 0.91 (t, J = 6.8 Hz, 3H). ^{13}C NMR (100 MHz, $CDCl_3$, 298 K): δ = 159.90, 159.67, 137.10, 134.04, 134.04, 129.50, 118.77, 114.67, 114.62, 113.91, 113.65, 81,42, 81.21, 73.01, 72.87, 68.16, 67.72, 46.94, 31.56, 31.03, 29.12, 28.97, 26.34, 25.69, 25.62, 22.60, 14.03. MS (FAB+): calcd. for $[M + H]^+$ m/z = 469.3, found m/z: 469.4; HR-MS (FAB+): calcd. for $C_{31}H_{37}O_2N_2$ $[M + H]^+$ m/z = 469.2855, found m/z: 469.2860.

2.6 Synthesis of PS-*b*-PAA and P(S-*co*-BrS)-*b*-PAA

PS(7K)-*b*-PAA(8.1K) was synthesized by reversible addition fragmentation chain transfer (RAFT) according to previously reported literature.[24] Likewise, P[S(5.4K)-*co*-BrS(0.7K)]-*b*-PAA(8.1K) was synthesized by RAFT with 10 mol % incorporation of BrS.

2.7 Computational details

Theoretical calculations were carried out using the Gaussian09 program package. The geometries of the monomer model and the DA model were optimized by density functional theory (DFT) calculations, using the hybrid B3LYP functional[27] and the 6-31G* basis set.[28] At the optimized geometries, time-dependent (TD) DFT calculations were performed using the range-separated hybrid CAM-B3LYP functional,[29] with solvent effects of chloroform taken into account by the polarizable continuum model (PCM).[30]

2.8 Thin-film preparation

Solutions of PS-*b*-P(AA-*sg*-IDA)(6mM in dioxane) were spin-coated (2500 rpm, 45 seconds) on silicon chips. The thicknesses of the films were 60-70 nm. The chips were inserted into the cuvette holder with an angle about ~45° to the incident light for the optical tests.

2.9 Solvent annealing

Solvent vapor annealing was optimized by varying the solvent (toluene, benzene, chloroform, acetone, THF, dioxane, and DMF), and annealing time (0.5 hour, 1 hour, 2 hours, 4 hours, 12 hours, 36 hours, and 72 hours). Thin films were analyzed by AFM. We found that the optimal solvent vapor annealing conditions for our system involves annealing in a 200 mL closed jar with DMF vapor for 36 hours.

2.10 Photopatterning

A quartz mask with micron-sized patterns was aligned to the thin films in a nitrogen atmosphere. Irradiation at 254 nm for 20 seconds afforded the cross-linked thin-films and polymerized the IDA monomers. Then, the films were washed with dioxane three times and dried with a nitrogen stream. The micropatterns were imaged with confocal microscopy, using different wavelength channels, where the intensity of each channel was read under the same gain.

APPROVED FOR PUBLIC RELEASE

3. RESULTS AND DISCUSSION

The supramolecular strategy allows for facile tuning of the packing interactions of the IDA monomer by simply varying the molar ratio (R) of the IDA monomer relative to the acrylic acid units along the BCP backbone. In order to evaluate the appropriate loading ratio of the monomer, the hydrogen bonding interaction between PS-*b*-PAA and the imidazole group of IDA at various R values (ranging from 0.1 to 1.5) was investigated by ^{1}H NMR spectroscopy. As expected, the imidazolyl proton signals broaden upon hydrogen bonding, and reach maximal downfield shift at R = 0.2. By increasing R, the imidazolyl proton signals shift upfield. We attribute these changes to weakened hydrogen bonding interactions between the IDA monomer and PAA, which may be due to steric crowding at high loading.[24] Thus, we focused on loading ratios of R = 0.2 and 0.4 for optimal interactions between the IDA monomers and PAA.

To gauge the importance of the BCP template, photopolymerization of the IDA monomer in solution was studied without PS-*b*-PAA. The IDA monomer was dissolved in chloroform and irradiated with a 254 nm UV-lamp for 20 minutes. Linear absorption and photoluminescence spectra were collected for solutions before and after irradiation (Figure 3A,D). The absorption maxima at 321 nm and 344 nm, and emission maxima at 409 nm and 433 nm originate from the DPDA chromophore. Prolonged irradiation to the solutions resulted in minor spectral changes to both the absorption and photoluminescence spectra, which is indicative that the photopolymerization of the free IDA monomer does not proceed appreciably in solution (Figure 2A,D).

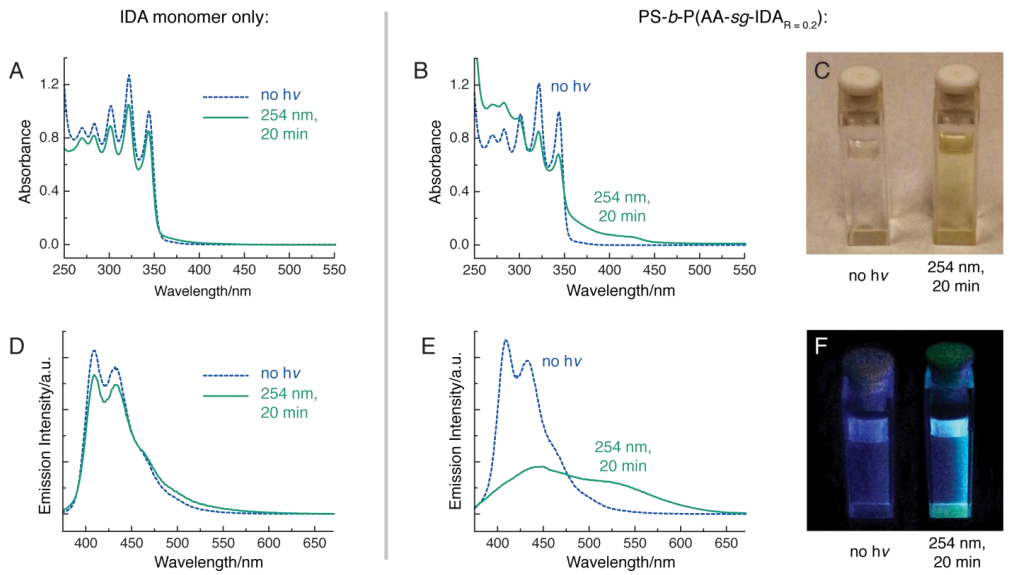

Figure 2. BCP template-based photopolymerization in solution. Absorption spectra of a solution of IDA monomer without irradiation (dashed line) and after irradiation at 254 nm for 20 minutes (solid line) are shown in (A). Absorption spectra of a solution of PS-*b*-P(AA-*sg*-IDA$_{R=0.2}$) without irradiation (dashed line) and after irradiation at 254 nm for 20 minutes (solid line) are shown in (B), and the corresponding image of the solutions under an ambient light is shown in (C). Emission spectra (λ_{ex} = 365 nm) of the IDA monomer without irradiation (dashed line) and after irradiation at 254 nm for 20 minutes (solid line) are shown in (D). Emission spectra (λ_{ex} = 365 nm) of a solution of PS-*b*-P(AA-*sg*-IDA$_{R=0.2}$) without irradiation (dashed line) and after irradiation at 254 nm for 20 minutes (solid line) is shown in (E), and the corresponding image of the solutions under a UV light is shown in (F). Spectra were collected at 40 µM of IDA in chloroform at 298 K.

In contrast to the free IDA monomer studies, the photopolymerization was successful in solution for PS-*b*-P(AA-*sg*-IDA$_{R=0.2}$) to synthesize polydiphenyldiacetylene (PDPDA). This may be analogous to other solution-polymerization studies of DAs, where pre-assembly of liposomes is required for polymerization to occur.[31] In the infrared spectrum of PS-*b*-P(AA-*sg*-PDPDA), the 2208 cm^{-1} vibration appeared due to increased conjugation length along the triple bonds after photopolymerization. The band at 1630 cm^{-1} became broader by overlapping with the band from the double bonds.[38] Also, the absorption bands of the IDA monomer in PS-*b*-P(AA-*sg*-IDA$_{R=0.2}$) showed noticeable changes after 20 minutes of irradiation (Figure 2B)[10,32] with an apparent color change from colorless to pale yellow (Figure 2C). The most notable change was observed in the photoluminescence spectra, where the 420 nm peak corresponding to the IDA monomer diminished after 20 minutes of irradiation, concomitantly with the appearance of an emission peak near 520 nm corresponding to PDPDA (Figure 2E). Similarly, an obvious color change was observed with λ_{ex} = 365 nm (Figure 2F). Both absorption and emission spectral variations saturated after 20 minutes. The low photoluminescence peak intensity of

PDPDA at 520 nm is attributed to low degrees of polymerization, given that this system lacks high degrees of order. Attempts to isolate PDPDA were unsuccessful due to its similar solubility with the BCP and unreacted IDA monomers. Nonetheless, we postulate that the BCP template led to sufficient alignment for the topochemical polymerization of the DA to proceed in solution.

Considering that PS-*b*-P(AA-*sg*-IDA$_{R=0.2}$) is solution-processable, and that microphase segregation of BCPs can enhance molecular alignment through ordered domains,[16,24,25] the photopolymerization was studied in thin films. In addition to organizing the IDA monomers through hydrogen bonding to the PAA backbone, the PS-*b*-PAA template imparts hierarchical order of the IDA monomers through BCP microphase segregation in the solid-state thin films, which is induced with solvent vapor annealing.[33,34] An AFM image of an as-cast film of PS-*b*-P(AA-*sg*-IDA$_{R=0.2}$) displays a featureless surface with roughness circa 15 nm (Figure 3A). The solvent vapor annealing process was optimized and exposure of the films to DMF for 36 hours led to smoother films (roughness ca. 2 nm), with a dot-like nanopattern topography (Figure 3B). Interestingly, a higher loading ratio (R = 0.4) had a subtle enhancement on the packing uniformity of the nanostructure after solvent vapor annealing (Figure 4C,D). High-angle annular dark field scanning transmission electron microscopy (HAADF-STEM) revealed microphase segregation of the supramolecular graft BCP. Figure 3E shows a mixed phase of sphere-like and worm-like structures, in addition to lamellar domains that are attributed to the PDPDA stacks, which are similar to previously reported systems.[24,35-37] The lamellar crystallite features were faintly discernible by bright-field TEM in the as-cast sample, but more pronounced in the annealed film.

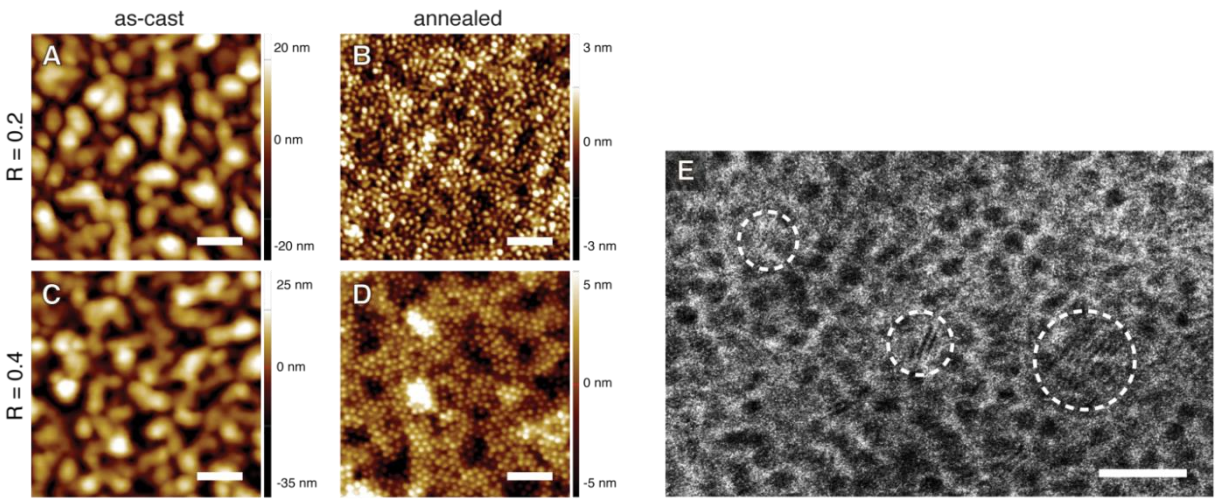

Figure 3. Thin film self-assembly characterization: AFM topography images of PS-*b*-P(AA-*sg*-IDA$_{R=0.2}$) for an (A) as-cast and (B) solvent-annealed film; AFM topography images of PS-*b*-P(AA-*sg*-IDA$_{R=0.4}$) for an (C) as-cast and (D) solvent-annealed film. (E) HAADF-STEM image of a solvent-annealed film of PS-*b*-P(AA-*sg*-IDA$_{R=0.4}$) after irradiation, where the dark spherical regions correspond to the PS domains. Examples of lamellar crystalline domains are circled. Scale bars are (A-D) 200 nm and (E) 60 nm.

Relative to templating in solution, significant enhancement of the topochemical polymerization was expected in thin films, where the hierarchical BCP microphase segregation can serve as a handle to align the IDA monomers. In fact, the photopolymerization of PS-*b*-(PAA-*sg*-IDA) in both the as-cast and solvent-annealed thin films was over an order of magnitude faster than in solution. The reaction proceeded within 20 seconds of UV-irradiation, which is the fastest externally triggered reaction time.[10,11,38,39] Such fast time scales are particularly attractive for high-throughput processing. As compared to the solution reaction, the photoluminescence spectra of both the as-cast and solvent-annealed thin films display a 420 nm peak corresponding to the IDA monomer that diminished concomitantly with the appearance of a pronounced emission peak near 520 nm, corresponding to PDPDA. Notably, the intensity of the 520 nm peak is more intense for the thin films, relative to solution, which suggests that the solid-state topochemical photopolymerization of the IDA monomers proceeded to higher degrees of polymerization.

Given the fast and efficient photopolymerization observed with this BCP-templated system, we sought to investigate photopatterning strategies to generate hierarchical shapes at the micrometer length scale. Thin films of PS-*b*-P(AA-*sg*-IDA) are soluble in common solvents. Hence, 4-bromostyrene (BrS) was incorporated, yielding P(S-*co*-BrS)-*b*-PAA, which simultaneously crosslinks during photopolymerization at 254 nm (Figure 4A,B).[40,41] Solvent-annealed thin films of P(S-*co*-BrS)-*b*-P(AA-*sg*-IDA) exhibit comparable microphase-segregated nanostructures as PS-*b*-P(AA-*sg*-IDA). Through standard shadow-mask photolithography, micropatterns of the hierarchical solvent-annealed thin films of P(S-*co*-BrS)-*b*-(PAA-*sg*-PDPDA) were fabricated and visualized using confocal microscopy in the

510−530 nm channel, which corresponds to emission from PDPDA (Figure 4C). The faint background fluorescence in Figure 4C may be arising from light leakage through the shadow-mask, since this processes was carried out on a bench-top setup without the traditional automated mask aligner. Moreover, confocal microscopy imaging in the 460-480 nm channel shows that the IDA monomer is readily consumed, and the faint signal can be attributed to contributions from the PDPDA and the IDA monomer. In this system, the combination of cross-linkable templates and self-assembly has enabled us to fabricate thin films of micropatterned PDPDA – a strategy that could be useful for the fabrication of microarrays of conjugated photoluminescent materials.

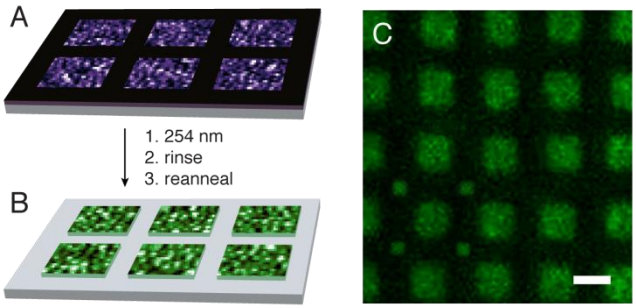

Figure 4. Photopatterning experiments. (A) Solvent-annealed thin films of P(S-*co*-BrS)-*b*-P(AA-sg-IDA) are aligned with a shadow mask and cross-linked with 254 nm. (B) After a rinse and reannealing step, hierarchical patterns are achieved, (C) as observed by confocal microscopy in 510-530 nm channel. Scale bar is 500 µm.

4. CONCLUSION

The BCP-templated strategy described here has enabled us to efficiently drive the topochemical polymerization of a diphenyldiacetylene derivative (IDA) in solution and thin films. It is important to note that common strategies rely on crystal engineering and/or stringent supramolecular recognition design, which can be challenging to control in a predictable fashion. The viability of our approach is not only rooted on processability and modularity, but also on the facile synthesis of the materials. Hydrogen-bonding interactions between imidazole on the IDA monomer and the acrylic acid on the BCP template provided effective molecular alignment that led to rapid photochemical polymerization to synthesize a supramolecularly grafted PDPDA. Moreover, the microphase-segregated structure arising from the BCP further improves the organization of the IDA monomers, which led to a higher degree of polymerization. Notably, the polymerization can be completed within tens of seconds, which is the fastest, controlled, light-triggered polymerization of DAs to date. Exploiting such rapid reactivity, we fabricated micropatterns by photolithography through the simultaneous cross-linking of 4-bromostyrene-functional BCP thin-films during photopolymerization. Future studies will be geared toward exploiting this templated supramolecular grafting strategy, which could be useful in other topochemical reactions that require highly uniform molecular alignment.

ACKNOWLEDGEMENTS

This research was funded by the Department of the Army Basic Research Program and sponsored by the Edgewood Chemical Biological Center. Support was also provided by the U.S. Army Research Office under contract W911NF-12-1-0252. Reprinted with permission from *Journal of the American Chemical Society*, **2014**, *136* (38), 13381-13387. Copyright 2014 American Chemical Society.

REFERENCES

[1] McQuade, D.T. *et al.,* "Conjugated polymer-based chemical sensors", *Chemical Reviews.* **2000**. 100(7), p2537-2574.
[2] Sun, X. *et al.,* "Chromatic polydiacetylene with novel sensitivity", *Chemical Society Reviews.* **2010**. 39(11), p4244.
[3] Reppy, M.A. and Pindzola, B.A., "Biosensing with polydiacetylene materials: structures, optical properties and applications", *Chemical Communications.* **2007**. 42, p4317.
[4] Kraabel, B. *et al.,* "Triplet exciton generation, transport and relaxation in isolated polydiacetylene chains: subpicosecond pump-probe experiments", *Chemical Physics.* **1998**. 227(1–2), p83-98.
[5] Xu, Q. *et al.,* "Polydiacetylene-based colorimetric and fluorescent chemosensor for the detection of carbon dioxide", *Journal of the American Chemical Society.* **2013**. 135(47), p17751-17754.

[6] Diegelmann, S.R. and Tovar, J.D., "Polydiacetylene-peptide 1D nanomaterials", *Macromolecular Rapid Communications.* **2013**. 34(17), p1343-1350.
[7] Pope, M. and Swenberg, C.E., *Electronic Processes in Organic Crystals and Polymers*, 2nd ed. Oxford University Press, New York. **1999**.
[8] Lu, Y. *et al.,* "Self-assembly of mesoscopically ordered chromatic polydiacetylene/silica nanocomposites", *Nature.* **2001**. 410(6831), p913-917.
[9] Sun, A. *et al.,* "Preparation of poly(diiododiacetylene), an ordered conjugated polymer of carbon and iodine", *Science.* **2006**. 312(5776), p1030-1034.
[10] Kim, J-H. *et al.,* "Unique photoluminescence of diacetylene containing dendrimer self-assemblies: application in positive and negative luminescence patterning", *Chemistry of Materials.* **2012**. 24(12), p2356-2363.
[11] Yoon, B. *et al.,* "Recent conceptual and technological advances in polydiacetylene-based supramolecular chemosensors", *Chemical Society Reviews.* **2009**. 38(7), p1958.
[12] Xu, W.L. *et al.,* "Single crystal to single crystal polymerization of a self-assembled diacetylene macrocycle affords columnar polydiacetylenes", *Crystal Growth and Design.* **2014**. 14(3), p993-1002.
[13] Xu, Y. *et al.,* "Thermal reaction of a columnar assembled diacetylene macrocycle", *Journal of the American Chemical Society.* **2010**. 132(15), p5334-5335.
[14] Diegelmann, S.R. *et al.,* "Synthesis and alignment of discrete polydiacetylene-peptide nanostructures", *Journal of the American Chemical Society.* **2012**. 134(4), p2028-2031.
[15] Dou, L. *et al.,* "Single-crystal linear polymers through visible light–triggered topochemical quantitative polymerization", *Science.* **2014**. 343(6168), p272-277.
[16] Bates, F.S. and Fredrickson, G.H., "Block copolymers—designer soft materials", *Physics Today.* **1999**. 52(2), p32.
[17] Eugene, D.M. and Grayson, S.M., "Efficient preparation of cyclic poly(methyl acrylate)-block-poly(styrene) by combination of atom transfer radical polymerization and click cyclization", *Macromolecules.* **2008**. 41(14), p5082-5084.
[18] Sai, H. *et al.,* "Hierarchical porous polymer scaffolds from block copolymers", *Science.* **2013**. 341(6145), p530-534.
[19] Tavakkoli, K.G.A. *et al.,* "Templating three-dimensional self-assembled structures in bilayer block copolymer films", *Science.* **2012**. 336(6086), p1294-1298.
[20] Kempe, K. *et al.,* "Strongly phase-segregating block copolymers with sub-20 nm features", *ACS Macro Letters.* **2013**. 2(8), p677-682.
[21] Arakawa, Y. *et al.,* "Synthesis and evaluation of high-birefringence polymethacrylate having a diphenyl-diacetylene LC moiety in the side chain", *Journal of Materials Chemistry.* **2012**. 22(29), p14346.
[22] Kim, Y. *et al.,* "Switchable nanoporous sheets by the aqueous self-assembly of aromatic macrobicycles", *Angewandte Chemie International Edition.* **2013**. 52(25), p6426-6429.
[23] Wu, S-T. *et al.,* "Room-temperature diphenyl-diacetylene liquid crystals", *Applied Physics Letters.* **1992**. 61(6), p630-632.
[24] Tran, H. *et al.,* "Monoliths of semiconducting block copolymers by magnetic alignment", *ACS Nano.* **2013**. 7(6), p5514-5521.
[25] Gopinadhan, M. *et al.,* "Magnetic field alignment of a diblock copolymer using a supramolecular route", *ACS Macro Letters.* **2012**. 1(1), p184-189.
[26] Park, J. *et al.,* "Pd-catalyzed decarboxylative coupling of propiolic acids: one-pot synthesis of 1,4-disubstituted 1,3-diynes via Sonogashira-homocoupling sequence", *Journal of Organic Chemistry.* **2011**. 76(7), p2214-2219.
[27] Becke, A.D., "Density-functional thermochemistry. III. The role of exact exchange", *Journal of Chemical Physics.* **1993**. 98(7), p5648-5652.
[28] Hehre, W.J., "Self-consistent molecular orbital methods. XII. Further extensions of Gaussian-type basis sets for use in molecular orbital studies of organic molecules", *Journal of Chemical Physics.* **1972**. 56(5), p2257.
[29] Yanai, T. *et al.,* "A new hybrid exchange–correlation functional using the Coulomb-attenuating method (CAM-B3LYP)", *Chemical Physics Letters.* **2004**. 393(1-3), p51-57.
[30] Tomasi, J. *et al.,* "Quantum mechanical continuum solvation models", *Chemical Reviews.* **2005**. 105(8), p2999-3094.
[31] Okada, S. *et al.,* "Color and chromism of polydiacetylene vesicles", *Accounts of Chemical Research.* **1998**. 31(5), p229-239.
[32] Wiley, R.H. and Lee, J.Y., "Thermal polymerization of diphenyldiacetylene", *Journal of Macromolecular Science, Part A: Pure and Applied Chemistry.* **1971**. 5(3), p513-527.
[33] Krishnamoorthy, S. *et al.,* "Nanoscale patterning with block copolymers", *Materials Today.* **2006**. 9(9), p40-47.
[34] Tang, C. *et al.,* "Evolution of block copolymer lithography to highly ordered square arrays", *Science.* **2008**. 322(5900), p429-432.
[35] Deshmukh, P. *et al.,* "Interplay between liquid crystalline order and microphase segregation on the self-assembly of side-chain liquid crystalline brush block copolymers", *Macromolecules.* **2013**. 46(20), p8245-8252.

[36] Majewski, P.W. *et al.,* "Anisotropic ionic conductivity in block copolymer membranes by magnetic field alignment", *Journal of the American Chemical Society.* **2010**. 132(49), p17516-17522.
[37] Mao, G. *et al.,* "Molecular design, synthesis, and characterization of liquid crystal-coil diblock copolymers with azobenzene side groups", *Macromolecules.* **1997**. 30(9), p2556-2567.
[38] Sun, X. *et al.,* "UV-Induced chromatism of polydiacetylenic assemblies", *Journal of Physical Chemistry B.* **2010**. 114(7), p2379-2382.
[39] Sun, X. *et al.,* "Chromatic polydiacetylene with novel sensitivity", *Chemical Society Reviews.* **2010**. 39(11), p4244-4257.
[40] Kern, W. *et al.,* "Photochemical reactions of polystyrenes ring-substituted with thiocyanato groups", *Macromolecular Chemistry and Physics.* **1997**. 198(12), p3987-3999.
[41] Kumar, K. *et al.,* "Formation of self-rolled polymer microtubes studied by combinatorial approach", *European Polymer Journal.* **2008**. 44(12), p4115-4121.

Understanding the role of physical and chemical adsorption on the Raman enhancement from metallic nanoparticles and nanostructured surfaces

Jason Guicheteau[a], Ashish Tripathi[b], Erik Emmons[b], Augustus Fountain, III[a], Martin Moskovits[c], Steven Christesen[a]
[a]U.S. Army Edgewood Chemical Biological Center, Research and Technology Directorate, 5183 Blackhawk Rd, Aberdeen Proving Ground, MD 21010
[b]Leidos, Inc., P.O. Box 68, Gunpowder Branch, Aberdeen Proving Ground, MD 21010
[c]Department of Chemistry and Biochemistry, University of California Santa Barbara, Building 232, Santa Barbara, CA 93106

ABSTRACT

Surface-enhanced Raman spectroscopy (SERS) is a useful technique for probing analyte-noble metal interactions and determining thermodynamic properties such as their surface reaction equilibrium constants and binding energies. In this study, we measure the binding equilibrium constants and Gibbs free energy of binding for a series of nitrogen containing aromatic molecules adsorbed on Klarite® substrates. A dual Langmuir dependence of the SERS intensity on concentration was observed for the six species studied indicating the presence of at least two distinct types of binding sites with different binding energies. We relate the measured binding energies to the previously described SERS Enhancement Value (SEV) and show that the SEV is proportional to the traditional SERS enhancement factor G, with a constant of proportionality that is dependent on the adsorption equilibrium constant determined from the dual Langmuir isotherm. We believe the approach described is generally applicable to many SERS substrates, both as a prescriptive approach to determining their relative performance, and as a probe of the substrate's affinity for a target adsorbate.

Keywords: SERS, equilibrium constant, binding energy, enhancement factor, Langmuir isotherm

1. INTRODUCTION

The strengths of surface-analyte interactions vary greatly. The process of chemisorption is often marked by the formation of strong covalent bonds between the surface and the analyte molecule (e.g., thiol molecules bound to noble metal surfaces), whereas physisorption is usually characterized by weak and transient bonds between the molecule and the surface (e.g., aniline bound to gold). In addition to the nature of the bond between the surface and the adsorbed analyte molecule, the solvent can also play an important role. If the affinity between the solvent and analyte is strong, the analyte-surface reaction may be slowed and the equilibrium may be shifted. Many different experimental techniques have been used to study adsorption of molecules, and surface-enhanced Raman spectroscopy (SERS) has proved valuable for examining the interactions of molecules with noble metals.[1-4]

In 1916, Irving Langmuir devised a model of adsorption reactions on surfaces including a relation called the Langmuir isotherm.[5-6] The Langmuir isotherm remains a common way to describe surface reaction equilibria. The equilibrium describing a molecule-surface reaction is given by:

$$S^* + P \leftrightarrows SP \tag{1}$$

where S^* is an unoccupied surface site, P is an unadsorbed analyte molecule, and SP is a bound analyte/surface-site pair. The equilibrium constant for the reaction, K, can be written as:

$$K = \frac{[SP]}{[S^*][P]} \tag{2}$$

where the brackets indicate concentrations.

Langmuir was able to derive a relation between the fractional coverage of occupied surface sites, θ, and the concentration C of analyte molecules in solution (or, alternatively, in a vapor). This equation is given as follows:

$$\theta = \frac{KC_S}{1+KC_S} \tag{3}$$

APPROVED FOR PUBLIC RELEASE

where K is determined experimentally from the concentration dependence of θ. In general, there are three assumptions that are inherent in establishing the Langmuir isotherm relation:[7]

a) The forward reaction (adsorption) rate is directly proportional to the vapor pressure of analyte in gas phase or molar concentration of analyte in liquid phase, C_S, and to the number of unoccupied adsorption sites. The backward reaction (desorption) rate is directly proportional to the number of occupied adsorption sites.
b) The partial pressure or molar concentration of the analyte is constant during the adsorption process. In other words, at a given analyte concentration the number of adsorbent molecules must be much larger than the number of adsorption sites. In the case where molecules are adsorbed from the liquid phase, one must exercise caution to provide a large enough volume of the analyte solution so that the number of adsorbent molecules present in the solution is much higher than the number of adsorption sites present on the solid surface. This assumption allows for making the rate of forward reaction directly proportional to the number of unoccupied adsorption sites at a given analyte concentration.
c) Enough time must be allowed to reach equilibrium at a given concentration. For a reversible reaction, no amount of time is sufficient for equilibrium to be truly reached. However, a waiting period of seven half-lives is sufficient to bring the reaction to more than 99% completion.

As reported in our earlier work, the rate constant for binding of thiophenol at 5×10^{-7} M (7 mL volume) was estimated at various temperatures and pH values.[8] The rate constant for binding of thiophenol at pH 6 and at 26 °C was determined to be 1.67×10^{-3} s^{-1}. With the half-life of the binding reaction being estimated at 414 seconds, it follows that waiting for about 2900 seconds (or seven half-lives) allows the reaction of thiophenol with Klarite® at 5×10^{-7} M concentration to reach 99% of its equilibrium state. Provided that assumption (b) is satisfied, the rate of the forward reaction will be linearly proportional on the concentration of the adsorbent analyte (in this case thiophenol). Therefore, a concentration of 5×10^{-9} M requires 100 times the waiting period used at 5×10^{-7} M concentration to reach equilibrium. For thiophenol, the waiting time is about 83.3 hours.

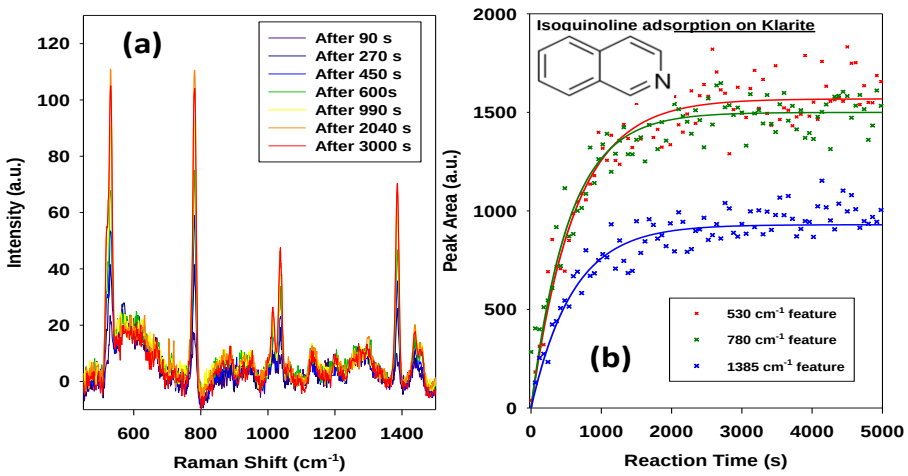

Figure 1. (a) Raman spectra for the reaction of 13.5 mL of 5×10^{-7} M isoquinoline with Klarite® at 23 °C. (b) Temporal response of a few select Raman bands of isoquinoline reacting with Klarite®.

Another analyte considered for estimation of a sufficient immersion time was isoquinoline. The rate constant for binding of isoquinoline with Klarite® at a concentration of 5×10^{-7} M (13.5 mL volume) was estimated at 23 °C. The time-dependent Raman spectral response at various reaction times is shown in Figure 1(a). The temporal profiles of the three most prominent Raman spectral features of isoquinoline at 530 cm^{-1}, 780 cm^{-1}, and 1385 cm^{-1} were evaluated and are shown in Figure 1(b). The half-lives of the reaction, assuming first-order kinetics, were calculated as 429 seconds, 373 seconds, and 409 seconds for the 530 cm^{-1}, 780 cm^{-1}, and 1385 cm^{-1} bands, respectively. About seven half-lives, 3000 seconds for the 530 cm^{-1} band, results in >99% completion of the reaction. As with the thiophenol case, 100 times the waiting period used for 5×10^{-7} M concentration is required for the reaction to reach equilibrium at 5×10^{-9} M concentration. For isoquinoline, this is about 85 hours. Similarly, the waiting period for any concentration can be estimated. Coincidentally, both thiophenol and isoquionoline provide similar half-lives. For each of the analytes studied, we used an immersion time sufficient for the binding reaction to proceed to completion (>99%).

In the present work, the fraction of surface sites occupied by analyte molecules, θ, is calculated from the SERS intensity by the following expression:

$$\theta = \frac{I_{C_S}}{I_{max}} \quad (4)$$

where $I_{C_S}$is the SERS peak area of an analyte specific feature at an analyte molar concentration of C_S, and I_{max} is the SERS peak area of the same Raman feature when a complete self assembled monolayer (SAM) is formed. Combining equations (3) and (4), the following equation is obtained:

$$I_{c_s} = I_{max}\left(\frac{KC_S}{1+KC_S}\right) \quad (5)$$

Equation (5) is used to fit the Raman feature peak area versus analyte concentration data with I_{max} and the equilibrium constant, *K*, as the fitting parameters.

From measurements of the equilibrium constants other thermodynamic properties such as the Gibbs free energy of adsorption (ΔG) can be obtained via the equation:

$$\Delta G = -RT\ ln(K) \quad (6)$$

where *R* is the ideal gas constant and *T* is the temperature.[7] Substituting the equilibrium constant value obtained in fitting the SERS data to equation (5) provides the free energy of adsorption. If ΔG is measured as a function of temperature, the enthalpic and entropic contributions to ΔG can be disentangled via the relation[9-10]

$$\Delta G = \Delta H - T\Delta S \quad (7)$$

This can reveal additional information about the adsorbate binding energy via the enthalpy change and ordering on the surface via the change in entropy.

2. EXPERIMENTAL METHODS

2.1. Materials

Pyridine, aniline, 4-chloroaniline, isoquinoline, pyrazine, and 1,2-di(4-pyridyl)ethylene (BPE) were purchased from Sigma-Aldrich and used without further purification. Solutions were prepared in deionized water in the range of 5×10^{-9} to 0.1 molar concentrations. All the experiments were performed at room temperature (23 °C). Commercially available gold SERS substrates (Klarite®, KLA-312, Renishaw Diagnostics Ltd., UK) were used for this work. The substrates provide adequately strong and reproducible SERS enhancement when 785 nm excitation is used.[8,11]

2.2. Raman microscopy

The Raman measurements were performed with a JASCO NRS-3200 dispersive Raman microscope system operating at 785 nm excitation with approximately 4 mW power incident on the sample. A 10× microscope objective was used both to focus the laser on the substrate and to collect the Raman scattered light. The relatively modest laser power and magnification were used to minimize any laser-induced heating of the substrate. The laser spot size was not measured but is estimated to be in the range of 1−5 μm. The Raman scattered light was dispersed with a 600 grooves/mm diffraction grating (blazed at 750 nm) and a spectrometer entrance slit width of 100 μm was used to obtain a spectral resolution of approximately 8 cm^{-1}. All the Raman spectra were acquired with 25 seconds of integration time and averaged over three co-additions. The Raman scattered light was detected with a thermoelectrically cooled charge coupled device camera (Andor). The strong Rayleigh scattered light was suppressed with a notch filter (Semrock). Raman spectral mapping of the substrate was performed by selecting a 36-location grid, in a rectangular 6×6 format, on the substrate and obtaining a Raman spectrum at each of the locations.

3. RESULTS AND DISCUSSION

To obtain the equilibrium constants for various adsorption reactions, one must satisfy the constraints established in the assumptions listed in the previous section. It is often a limitation that the number of absorbent molecules provided at a given concentration may not be enough to satisfy assumption (b). Especially at low concentrations, this assumption often presents an unreasonable burden on the experimental conditions to establish a true equilibrium. Consider the case of thiophenol binding to a Klarite® substrate. In a previous study,[8] we estimated 1.7×10^{14} molecules of thiophenol are needed to form a SAM on a Klarite® substrate. This implies that about 60 mL of 5×10^{-9} M solution contains a sufficient number of thiophenol molecules to form a SAM. If one needs to maintain the constraint described in assumption (b), then about 1 L of 5×10^{-9} M solution would be sufficient such that after the SAM is formed, the concentration would have dropped to 4.7×10^{-9} M; only a 4% decrease in the concentration.

APPROVED FOR PUBLIC RELEASE

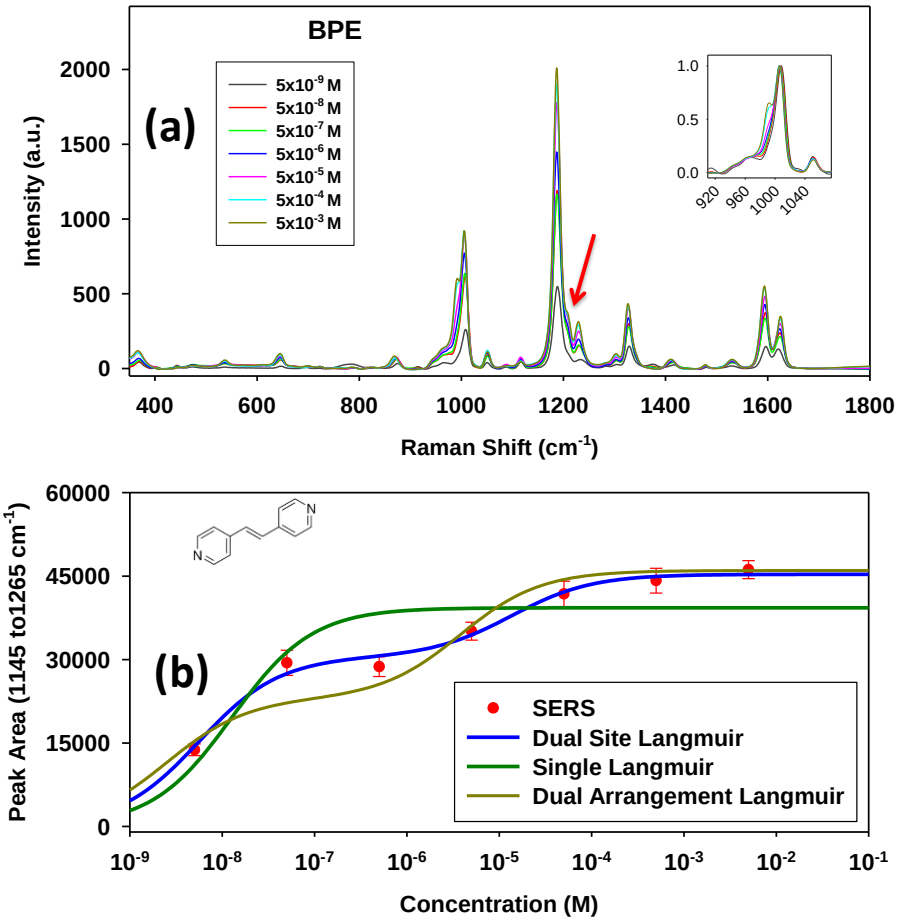

Figure 2. BPE SERS spectra on a Klarite® substrate. (a) Average SERS spectra at various BPE concentrations. (b) Peak area of the 1186 cm^{-1} line as a function of concentration.

We selected six nitrogen based aromatic compounds of varied structure (isoquinoline, BPE, pyridine, pyrazine, 4-chloroaniline, and aniline) to determine how the structure affects their equilibrium constants and free energies of adsorption. The first four of these molecules are azaarenes, with at least one nitrogen atom substituted for a carbon atom in the aromatic ring(s). They differ in the number of rings, the bridging between the rings, and the position and number of nitrogen atoms. The last two are aromatic amines, with NH_2 groups attached to the rings. The Langmuir isotherms were obtained by exposing the Klarite® substrates to more than a sufficient number of analyte molecules for durations of time sufficient to reach 99% of the equilibrium state at each concentration; i.e., the immersion technique described in the previous subsection.

Consider the adsorption of BPE on Klarite®. A 0.1 M BPE stock solution in ethanol was prepared and serially diluted from 5×10^{-2} M to 5×10^{-9} M using ultrapure water (18.3 MΩ·cm) as a diluent. For each concentration used, the Klarite® substrate was immersed in a sufficient volume of solution such that enough molecules were present, that the solution would not be depleted, and for a sufficient length of time in order for the reaction to reach equilibrium. As described above, the volumes and time periods used depended on the analyte concentration. After each immersion period, the Klarite® substrate was transferred to a Petri dish and 7 mL of the solution used during the immersion period was added to the Petri dish to maintain the equilibrium. A Raman spectral map consisting of a 6×6 grid of points was then acquired. This procedure was repeated for each concentration used.

Figure 2(a) shows the average spectra at each concentration. The peak area of the most prominent Raman feature at 1186 cm^{-1} Raman shift was estimated for all the spectra obtained. Figure 2(b) shows the peak area of the 1186 cm^{-1} Raman band as a function of concentration (red circles with 99% confidence error bars). The data was fit to a Langmuir isotherm described by equation (5) with the maximum peak area as a multiplier, as shown by the green curve in Figure 2(b). The equilibrium constant was estimated to be 7.8×10^{7} and this corresponds to a free energy of adsorption of -44.8 kJ/(reaction mole). The coefficient of regression, r^2, was 0.7445, indicating a poor fit. A closer examination of the spectral information offers an explanation for the poor fit to Langmuir isotherm. Consider the Raman spectral feature at 1000 cm^{-1} as shown in

the inset of Figure 2(a). A shoulder (at about 985 cm^{-1}) starts to appear and increases in intensity as the concentration increases. A similar, but relatively smaller, shoulder appears at about 1220 cm^{-1} (shown by a red arrow in Figure 2(a)). These shoulders increase in intensity as concentration increases indicating a dual arrangement of BPE molecules, one at low concentrations and other at higher concentrations. Langmuir (1918)[6] offered two simple models to describe this process.[6]

For the first model, Langmuir assumed that there may be more than one type of "elementary space" making up the substrate. Each of these "elementary spaces" allows the adsorbent to bind in a different orientation and/or density. Let *β1*, *β2*, *β3*, etc., be the fractions representing each of these elementary spaces. In this case, the equivalent of equation (3) becomes:

$$\theta = \frac{\beta_1 K_1 C_S}{1+K_1 C_S} + \frac{\beta_2 K_2 C_S}{1+K_2 C_S} + etc. \tag{8}$$

with the constraint

$$\beta_1 + \beta_2 + \cdots = 1$$

For BPE, the different types of elementary spaces can be viewed as adsorbing BPE in different modes of orientation and/or density.[1,12-17] Based on the spectral data we appear to have two types of elementary spaces. Equation (8) reduces to a dual Langmuir isotherm form:

$$\theta = \frac{\beta_1 K_1 C_S}{1+K_1 C_S} + \frac{\beta_2 K_2 C_S}{1+K_2 C_S} \tag{9}$$

By combining equations (5) and (9), the following equation is obtained:

$$I_{Cs} = I_{max}\left(\frac{\beta_1 K_1 C_S}{1+K_1 C_S} + \frac{\beta_2 K_2 C_S}{1+K_2 C_S}\right) \tag{10}$$

We will refer to the model described by equation (10) as the dual-site Langmuir isotherm. Fitting the dependence of peak area of 1186 cm^{-1} Raman band as a function of concentration (red circles in Figure 2(b)) to equation (7) results in the solid blue line in Figure 2(b). The values of $I_{max}, \beta_1, \beta_2, K_1,$ and K_2 were used as fitting parameters. The coefficient of regression, r^2, was 0.9873, and K_1 and K_2 were estimated to be 1.8×10^8 and 7.3×10^4 respectively. From the equilibrium constants we calculate the free energies of adsorption for the two observed modes of adsorption to be -46.8 kJ/(reaction mole) and -27.6 kJ/(reaction mole).

For the second model, Langmuir assumed that there may be more than one molecule occupying the same "elementary space". This models the rearrangement of molecules that can result in a higher packing density at higher concentrations.[12] Let $\theta_1, \theta_2 \ldots \theta_n$ be the fractions of elemental spaces that are blank, occupied by 1, 2… *n* number of molecules. In this case, equation (3) must be modified to the following form:

$$\theta = \frac{K_1 C_S + 2K_1 K_2 C_S^2 + 3K_1 K_2 K_3 C_S^3 \ldots}{1+K_1 C_S + K_1 K_2 C_S^2 + K_1 K_2 K_3 C_S^3 \ldots} \tag{11}$$

In the case of BPE, up to two molecules can be viewed as adsorbing on the same elementary space. Thus, equation (8) reduces to the following dual-molecule single-site Langmuir isotherm form:

$$\theta = \frac{K_1 C_S + 2K_1 K_2 C_S^2}{1+K_1 C_S + K_1 K_2 C_S^2} \tag{12}$$

By combining equations (4) and (12), the following equation is obtained:

$$I_{Cs} = I_{max}\left(\frac{K_1 C_S + 2K_1 K_2 C_S^2}{1+K_1 C_S + K_1 K_2 C_S^2}\right) \tag{13}$$

We will refer to the model described by equation (13) as the dual-arrangement Langmuir isotherm. Fitting the dependence of peak area of 1186 cm^{-1} Raman band as a function of concentration (red circles in Figure 2(b)) to equation (10) results in the solid yellow line in Figure 2(b). The values of $I_{max}, K_1,$ and K_2 were used as fitting parameters. The coefficient of regression, r^2, was 0.903, indicating a fit that is better than a single Langmuir but not as good as the dual-site Langmuir. The values of $K_1,$ and K_2 were estimated to be 4.0×10^8 and 2.6×10^5, respectively. The free energies of adsorption for the two observed modes of adsorption are calculated as -48.8 kJ/(reaction mole) and -30.7 kJ/(reaction mole). While the dual-site Langmuir and dual-arrangement Langmuir isotherms do offer an explanation for the data, they do not explain the mechanism driving the supposed dual adsorption process. The two processes may be influenced by the geometry of the

Klarite® substrate which is constructed with multiple nano-inverted pyramid structures. The orientation and SERS enhancement of the adsorbed BPE molecules may be different at the edges when compared to adsorption at the faces of the inverted pyramids. It may also be influenced by the rearrangement of adsorbed molecules as the adsorption density increases. It is beyond the scope of the presented work to offer an explanation for the mechanism for this type of adsorption process. Further exploration is required to understand and test the basis of the dual adsorption process.

Table 1. The estimated equilibrium constants of binding (M^{-1}) of the listed analytes to Klarite® substrate and the corresponding free energies of bindings (kJ/reaction mole) at 23 °C.

Chemical	Structure	Single Langmuir		Dual Site Langmuir			Dual Arrangement Langmuir		
		K (ΔG)	R^2	K_1 (ΔG_1)	K_2 (ΔG_2)	R^2	K_1 (ΔG_1)	K_2 (ΔG_2)	R^2
BPE	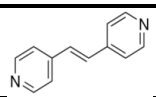	7.8×10^7 (-45)	0.74	1.8×10^8 (-47)	7.3×10^4 (-28)	0.99	4.0×10^8 (-49)	2.6×10^5 (-31)	0.90
Pyridine		$8.8\times10_3$ (-22)	0.91	1.5×10^7 (-41)	3.1×10^3 (-20)	0.98	1.7×10^5 (-30)	1.1×10^3 (-17)	0.95
Isoquinoline		5.5×10^6 (-38)	0.83	2.6×10^7 (-42)	3.5×10^4 (-26)	0.98	4.7×10^7 (-43)	6.2×10^4 (-27)	0.97
Pyrazine		1.4×10^4 (-23)	0.86	2.7×10^5 (-31)	4.0×10^2 (-15)	0.99	1.5×10^5 (-29)	2.8×10^2 (-14)	0.98
Aniline	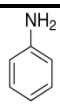	1.9×10^1 (-7.3)	0.96	1.7×10^4 (-24)	1.5×10^1 (-6.6)	0.97	1.0×10^2 (-11)	6.3 (-4.6)	0.93
4-Chloroaniline	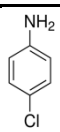	4.1×10^3 (-20)	0.93	4.8×10^6 (-38)	1.7×10^3 (-18)	0.99	2.3×10^4 (-25)	3.7×10^2 (-15)	0.97

The process described above was repeated for pyridine, pyrazine, isoquinoline, aniline, and 4-chloro aniline. For each of these compounds, the dual-site Langmuir model provides the best fits. Table 1 lists the values of fitting parameters obtained from the three Langmuir models for these compounds.

3.1. SERS enhancement and the Langmuir equilibrium constant

It is reasonable to expect that the intra-substrate differences in binding energy for the same analyte and the differences in binding energy for different analytes will have an effect on the SERS enhancement, depending on how we measure that enhancement. The normal definition of SERS enhancement is the SERS enhancement factor, G:

$$G = \frac{I_S N_R}{I_R N_S} \tag{14}$$

where I_S and I_R, are, respectively, the SERS intensity due to N_S "participating" molecules, and the ordinary Raman intensity due to N_R of the same molecules in solution. However, G has proved difficult to calculate reliably as a consequence of the fact that it depends on at least one, and often more than one, hard to determine parameters. Most often it is N_S that cannot be accurately determined because many of the following parameters are not known with confidence: the surface area of the nanostructured surface, the dose, and the cleanliness of the surface, which might already have competing species occupying an indeterminate fraction of the surface. Additionally, as described above, the surface concentration of the analyte will follow an isotherm, which is a function both of the analyte's concentration in solution and on the surface's chemical affinity for that molecule.

For measurements of analytes in solution or in the vapor phase, G is a poor measure of the sensitivity of the SERS substrate because it does not take into account the equilibrium established between the solution (or atmosphere) and the surface; it is simply a measure of the enhancing power of the substrate assuming full coverage. To ameliorate these issues when using G as a measure of substrate efficacy, Guicheteau et al.[11] developed a wholly prescriptive approach resulting in a SERS Figure of Merit, that was called the SERS Enhancement Value (SEV), which gauges the benefit of SERS as an analytical tool over ordinary Raman for a given SERS substrate and a given adsorbate molecule. This measure corrects operationally

for the aforementioned difficulty of determining N_S, and also for the spatial inhomogeneity of the enhancement of many SERS substrates. The spatial inhomogeneity may result in the "sacrifice" of a large fraction of the adsorbed molecules at weakly-enhancing sites. The SEV is also tied to the analyte's Gibbs free energy of binding through the Langmuir isotherm equilibrium constant.

The SEV,[11] which for brevity we will call F, was defined as the ratio of the two analyte concentrations C_R and C_S producing the same Raman and SERS intensities, the former being the concentration of the analyte in solution in the absence of the SERS substrate, the latter being the concentration of the analyte in the solution from which the analyte was adsorbed (at equilibrium) onto the SERS substrate. It is clear that there is an infinite number of pairs of concentrations that would satisfy this condition. Guicheteau et al.[11] used receiver operating characteristic (ROC) curves to identify the SERS intensity that provided a 90% probability of detection (PD) and a 10% probability of false alarm (PFA). That intensity was then used to determine C_R and C_S[11] An alternative approach will be used here inspired by the ROC curves, to determine C_R and C_S by measuring Langmuir isotherms, and replacing the 90% PD with the SERS signal intensity that is 90% of the maximum SERS value. This approach has the benefit that F is defined entirely in terms of measurable and definable factors, such as concentrations, without having to make assumptions regarding the number of molecules that contribute to the SERS or ordinary Raman intensities.

Issues relating to computing the SERS enhancement, and the limitations of its application in chemical analysis have been discussed previously,[3,18,19] most thoroughly by Etchegoin and LeRu.[18] Here we will develop the relationship between F and the SERS enhancement factor, G, and determine the system variables that must be considered when comparing the two measures. We will then show the effect of the equilibrium constant (and, therefore, the binding energy) on the measurement of both F and G.

Restricting our analysis to a SERS substrate that is dosed with a molecular adsorbate out of solution, and comparing the result to what is measured for the same molecule by ordinary Raman spectroscopy in solution, equation (14) may be rewritten as:

$$G = \frac{I_S C_R V}{I_R n_S A} \tag{15}$$

where V is the focal volume which produces the normal Raman signal, A is the focal area, the area that contains the n_S molecules that we associate with the measured SERS signal, C_R is the analyte concentration in the solution from which the ordinary Raman spectrum was measured, and n_S is the number of adsorbed molecules per unit area producing the SERS signal.

Assuming that n_S is the surface concentration when the substrate is in equilibrium with a solution of the adsorbate at solution C_S, we relate n_S and C_S using the Langmuir isotherm described previously in equation (5):

$$n_S = \frac{K C_S n_{max}}{1 + k C_S} \tag{16}$$

where n_{max} is the maximum number of adsorbate molecules that (on average) can occupy a unit area of surface on the SERS substrate. Substituting equation (16) into equation (15) yields:

$$G = \frac{I_S}{I_R} \frac{C_R V (1 + K C_S^0)}{k C_S n_{max} A}. \tag{17}$$

One can define pairs of concentrations C_s^0 and C_R^0 at which $I_S = I_R$. That is, when the SERS substrate is immersed in a solution in which the analyte concentration is C_s^0, and equilibrium is allowed to be established, one obtains a SERS intensity I_S for a given Raman band which is equal to the intensity I_R of the same band measured in the ordinary Raman spectrum of the analyte in a solution in which its concentration is C_R^0. If so, then the quantity $F = C_R^0 / C_s^0$ functions as a measure of the analytical value of SERS over ordinary Raman. For example, if by using SERS one can obtain a Raman signal by exposing a SERS substrate to an analyte with concentration $C_s^0 = 10^{-8} M$ (having achieved adsorption equilibrium); while in solution the same (ordinary) Raman intensity is achieved when $C_R^0 = 10^{-3} M$, then $F = 10^5$. Using these definitions, the $I_S = I_R$ condition, and equation (16), one can relate G to F as follows:

$$G = \frac{F V (1 + K C_S^0)}{k n_{max} A} \tag{18}$$

in which the SERS and the ordinary Raman intensities do not appear.

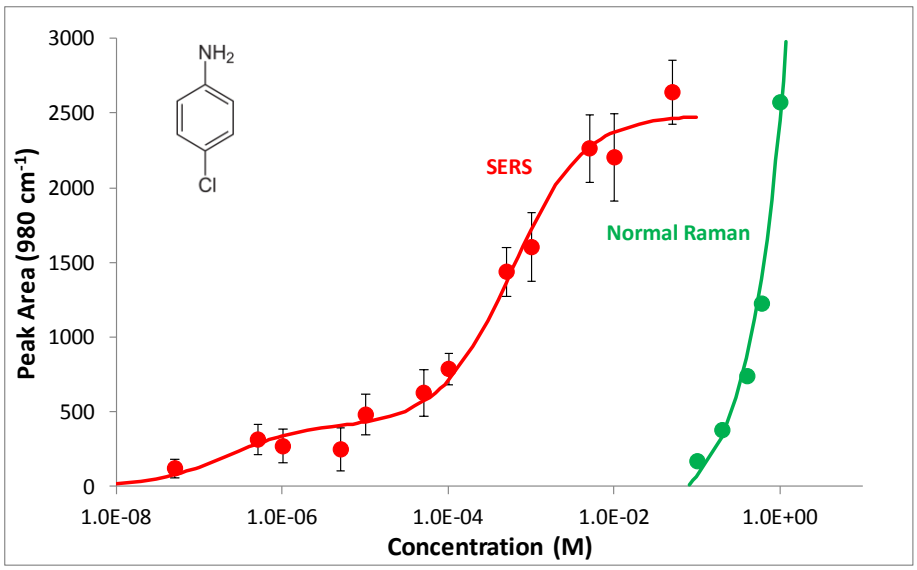

Figure 3. SERS and normal Raman data for 4-chloroaniline.

Following the work of Guicheteau et al.,[11] one can define a more useful and prescriptive version of equation (18) by specifying an appropriate criterion for selecting the value of C_s^0 to use. In doing so we will ignore two potential complications: the first is the possibility that a SERS hot spot also has some special affinity for the adsorbate (either chemical species, or optical field induced), which might result in more intense SERS signals from the first molecules to adsorb on the surface as compared to those that adsorb later on; i.e., we will assume that the adsorbate adsorbs on the SERS substrate's surface in a manner that is independent of that site's SERS enhancement. We will also ignore the decrease in SERS intensity per molecule on approaching monolayer coverage due to the depolarizing effect of neighboring adsorbate on a given molecule. This depolarizing effect results in a SERS intensity at full monolayer coverage that is actually a little less than for partial (but near full) monolayer coverages, as first pointed out by Murray and Bodoff,[20] and reported by other groups.[21] Ignoring these effects, we assume that the SERS intensity will be proportional to n_S; so that when the SERS intensity is a factor $\alpha \leq 1$ of its maximum value then $n_S = \alpha n_{max.}$ Defining F_α as the value of F measured according to equation (18) and evaluating the value of C_s^0 by substituting $n_S = \alpha n_{max}$ in equation (16), one obtains the following equation relating F_α to G:

$$F_\alpha = G\frac{(1-\alpha)Kn_{max}A}{V} \tag{19}$$

Several properties of F_α are obvious from equation (19). First, F_α is proportional to the Raman enhancement factor, G, however, it is, in general, numerically different from it. F_α depends critically on several molecular and instrumental parameters, and (trivially) on the choice of α. Chief among these parameters are the focal volume, V, and the focal area, A, which depend both on the magnifying power of the lens used to focus the excitation laser and on the numerical aperture used to collect the laser light (which in some instruments is accomplished using the same lens), and also on both the longitudinal and lateral sizes of the aperture. A large focal volume, for example, will result in a smaller value of F_α, and a molecule that has a greater affinity for the SERS substrate (i.e., a greater value of K) will produce a larger value of F_α than one with a lower affinity. Finally, molecules characterized by small values of n_{max} will produce lesser values of F_α, all else being equal.

Values of F_{90} (i.e., F values evaluated at $\alpha = 90\%$) were derived for five adsorbate molecules (aniline, 4-chloranaline, isoquinoline, pyrazine, and pyridine) by measuring their SERS intensities at various concentration, thereby determining the adsorption isotherm of each as described above. The normal Raman spectrum of each of the species was also measured as a function of the concentration in aqueous solution. As an example, the measured SERS isotherm and ordinary Raman peak intensity dependence on concentration for 4-chloroaninline are shown in Figure 3. The Raman intensities are for a single peak and the values at each concentration are the average of 16 spectra measured at different locations on the Klarite® substrate. Similar to the other analytes measured, the SERS intensity for 4-chloroaniline as a function of concentration produced a function that fit to the dual site Langmuir isotherm described by equation (10) (red curve in Figure 3). As discussed previously for BPE, this implies that there are two distinct sites for that molecule with differing chemical affinities. While the dual arrangement isotherm fit is not as good as the dual site fit, we cannot completely rule out that the

molecule changes orientation as a function of coverage resulting in two saturation regimes as a function of concentration.[1,12-17]

Assuming the dual-site explanation for the observed Langmuir fit, the calculated values of the free-energy of adsorption indicate that the surface possesses at least two classes of adsorption sites with site 1 forming a more stable surface bond than site 2. The ΔG values vary between -47 kJ mol-1 and -24 kJ mol-1 for site 1, and between -28 kJ mol-1 and -7 kJ mol-1 in site 2. The relative occupation probability in sites 1 and 2 at equilibrium as indicated by the β_1/β_2 ratio (Table 1) does not always favor the site with the lower value of the adsorption free energy, reflecting the complex nature of the equilibrium which includes dynamical processes involving molecules in the two adsorption sites and their counterparts in solution, as well as molecular exchanges between the two adsorption sites, to which both entropic and enthalpic effects contribute. Nevertheless, the larger values of β_1 roughly correspond to the more negative values of ΔG_1 with a few outliers.

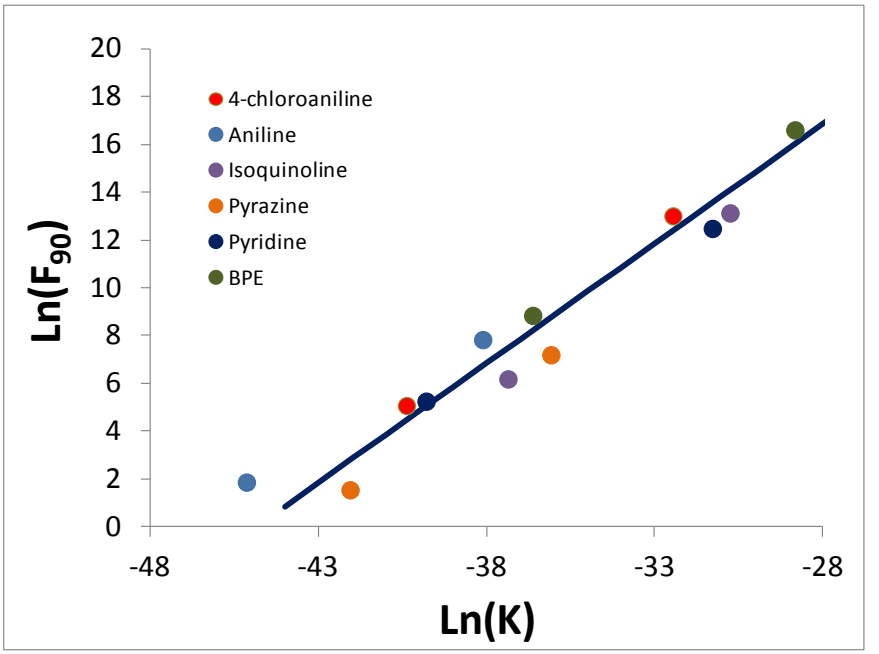

Figure 4. A ln-ln plot of the measured values of F_{90} vs. K illustrating their proportionality as predicted for these two quantities (equation (5)). There are two points for each chemical corresponding to the dual Langmuir fits to the data. The blue line corresponds to a best fit, forcing a slope of unity. The intercept corresponds to the quantity defined by equation (20).

Table 2. Measured values F_{90} and calculated Gn for the six species studied.

Molecule	$F1_{90}$	*Calculated Gn	$F2_{90}$	*Calculated Gn	**Calculated Gn
4-Chloroaniline	450000	6.3×10^{16}	160	3.3×10^{17}	3.9×10^{17}
Aniline	2500	1.3×10^{17}	6	1.2×10^{18}	1.3×10^{18}
Isoquinoline	510000	8.1×10^{16}	480	5.7×10^{16}	1.4×10^{17}
Pyrazine	1300	4.4×10^{16}	5	6.0×10^{16}	1.0×10^{17}
Pyridine	260000	7.1×10^{16}	190	2.6×10^{17}	3.3×10^{17}
BPE	16000000	3.8×10^{17}	6900	1.8×10^{17}	5.6×10^{17}
	Average	**1.3×10^{17} (1.3×10^{17})**		**3.5×10^{17} (4.5×10^{17})**	**4.8×10^{17} (4.6×10^{17})**

Calculated using equation (18) (*), and equation (15) (**) where $I_s = I_{max}$ and $n_s = n_{max}$ and expressed to two significant digits. The following values were assumed: $V = 5.46\times10^{-11}$ cm^3; $A = 7.93\times10^{-8}$ cm^2. The numbers in parentheses are the standard deviations of the calculated Gn values.

The measured SEV (F_{90}) values, extracted from the measured isotherms (Table 2) range from ~5 for pyrazine and aniline to ~ 1.6×10^7 for BPE; and the respective K (L mol^{-1}) values (Table 1) ranged from 15 (aniline) to 1.8×10^8 (BPE). The four azaarenes were found to have the largest values of K, implying a high affinity for the gold surface, likely due to the fact

APPROVED FOR PUBLIC RELEASE

that these molecules can pi-bond by lying flat on the surface. The higher values of K for BPE, isoquinoline, and pyrazine, which can bond through both rings, is consistent with this conjecture (although we recognize that several other factors may also be at play here). The molecules with lowest affinity are the anilines, whose amine group may prevent them from lying flat on the surface thereby hindering the establishment of a good pi-bond.

The values of F_{90} are plotted in Figure 4 as a function of K (a ln-ln plot is used to accommodate the wide range of K values). The good fit between the fitted line (with a forced slope of unity) and the measured points suggests that the above analysis has considerable validity. It also shows that F_{90} is a good proportional measure of G for a given molecule when comparing the relative merits of various SERS substrates. Referring to equation (19), a ln-ln plot of F_α versus K (Figure 4) yields an intercept of:

$$ln\left(\frac{G(1-\alpha)n_{max}A}{V}\right) \tag{20}$$

A least squares fit to the data listed in Table 1 (Ks for dual site Langmuir) and Table 2 (Fs) yields an intercept value of 44.7 which corresponds to a value for the quantity in parentheses in equation (20) of 4.1×10^{19} molecules/cm^3. G is generally presumed to be a characteristic property of the Klarite® substrate and if robust values of V, A, and n_{max} are available, the SERS enhancement can be determined from F via equation (19). The quantity A might be estimated from the diffraction-limited size of the illuminating laser beam and V from the numerical aperture of the microscope objective. The estimated values of V and A used are listed in Table 2. The value of n_{max} is the least straightforward quantity to estimate, largely on account of the heterogeneity of many SERS substrates both in terms of their SERS enhancement, and with respect to their adsorption affinity towards a target analyte. For example, the value of n_{max} would be reduced if the analyte is reluctant to adsorb on a significant portion of the substrate's surface either intrinsically or because some sites on the surface are already occupied by other species. Conversely, its value would be increased if the surface's roughness factor is greater than unity, thereby permitting a larger number of molecules to occupy a unit projected area.

The fit in Figure 4 would indicate that the quantity $G \times n_{max}$ (hereafter denoted as Gn), and not G, is a fundamental property of the substrate alone and is independent of the analyte. If G is the enhancement per molecule, then Gn can be considered the average enhancement per unit area of the substrate. From equation (20), we calculate a value of 1.8×10^{17} for Gn. This value is very close to those calculated for each analyte using equation (15) with $I_s = I_{max}$ and $n_s = n_{max}$ (last column in Table 2).

Equation (19) also provides a method of calculating Gn for individual analytes. In this case, we get two values for each analyte; one for each F_α/K pair obtained from the dual Langmuir isotherm fit (third and fifth column in Table 2. All of the Gn values agree to within about a factor of 30 even though two different methods were used for their calculation. The Gn values averaged over all analytes is also close to that obtained from the intercept of the $\log_e(F)$ vs. $\log_e(K)$ plot described above. In addition, although the values for the K vary from 6.3 to 4.0×10^8 (Table 1), the Gn values calculated using equation (19) differ by less than a factor of 30.

If we assume an average value of 1.9×10^{14} molecules/cm^2 used in previous estimates[8] of G for Klarite® one obtains a value of G = 925 from the intercept in Figure 4. This is much smaller than what is claimed for Klarite® by the manufacturer, possibly implying that those reported values were measured under especially favorable circumstances, and illustrate starkly the difficulty of estimating meaningful SERS enhancement values.

4. CONCLUSIONS

SERS continues to hold great promise as a flexible sensor platform due in part to its large per molecule sensitivity and the plasmon resonance of a nanostructured metallic substrate can be tuned over a wide range of laser excitation wavelengths, allowing the development of a SERS sensor to capitalize on the vast diversity of spectroscopic systems with respect to lasers, spectrographs, and detectors. However, the SERS effect has not been universally demonstrated for many classes of potential chemical analytes, and as the literature suggests, the relative enhancement for a given molecule is often acutely substrate dependent. A key consideration often neglected in SERS measurements is the affinity of a molecule to adsorb or even covalently bond to the substrate surface. Since, out of necessity, SERS substrates are nanostructured and therefore often surface-structurally complex, they would also often be surface-chemically heterogeneous. The mechanism(s) driving these equilibrium reactions require further study in order to determine *a priori* which molecules can be analytically detected using a given SERS substrate. It is also important to establish experimental conditions that allow for a realistic calculation of the enhancement factor and/or understand the limitations of that estimate when ideal conditions are not met.

Although the SERS Enhancement Factor, G, has gained near universal acceptance as a substrate's figure-of-merit, we believe that our development of the SEV accomplishes two important goals. First, by measuring the equilibrium constant for a series of molecules, the SERS substrate's response can be quantified with fewer assumptions and arguably less error.

Also from knowledge of the equilibrium constant, the sensor's performance could be estimated prescriptively. This could lead to greater predictability of SERS activity of molecules, which is a critical factor when developing sensors or sensing strategies for a wide range of analytes. Second, the SEV produces an unbiased analysis of substrate performance permitting direct comparison of the relative merits of various substrates, produced by disparate substrate manufacturing techniques and often with parameters that are nearly impossible to correctly estimate. The analysis we present provides a simple formula for deriving the SERS enhancement from the SEV and indicates clearly what parameters need to be known accurately in order to calculate a meaningful SERS enhancement value (and if unknown, what quantitative assumptions are being made). While the SEV is fundamentally tied to the analyte's equilibrium constant, our analysis indicates that the product of the normally defined SERS Enhancement Factor times the maximum number of molecules per unit area that can bind to the surface ($G \times n_{max}$) is a fundamental property of the substrate alone.

ACKNOWLEDGEMENTS

The authors would like to acknowledge U.S. Army funding provided through the Edgewood Chemical Biological Center's In-House Laboratory Independent Research and Surface Science Initiative programs.

REFERENCES

[1] Biggs, K.B. *et al*., "Surface-enhanced Raman spectroscopy of benzenethiol adsorbed from the gas phase onto silver film over nanosphere surfaces: determination of the sticking probability and detection limit time", *The Journal of Physical Chemistry A*. **2009**. 113(16), p4581-4586.

[2] Wang, H. *et al*., "Nanosphere arrays with controlled sub-10-nm gaps as surface-enhanced Raman spectroscopy substrates", *Journal of the American Chemical Society*. **2005**. 127(43), p14992-14993.

[3] Le Ru, E.C. and Etchegoin, P.G., *Principles of Surface-Enhanced Raman Spectroscopy: and related plasmonic effects*, 1st edition. Elsevier, Amsterdam, **2009**.

[4] Stiles, P.L.; *et al*., "Surface-enhanced Raman spectroscopy", *Annual Review of Analytical Chemistry*. **2008**. 1(1), p601-626.

[5] Langmuir, I., "The constitution and fundamental properties of solids and liquids. Part I. Solids", *Journal of the American Chemical Society*. **1916**. 38(11), p2221-2295.

[6] Langmuir, I., "The adsorption of gases on plane surfaces of glass, mica and platinum", *Journal of the American Chemical Society*. **1918**. 40(9), p1361-1403.

[7] Atkins, P.W., *Physical Chemistry*, 6th edition. W.H. Freeman and Company, New York, **1999**.

[8] Tripathi, A. *et al*., "Kinetics and reaction mechanisms of thiophenol adsorption on gold studied by surface-enhanced Raman spectroscopy", *The Journal of Physical Chemistry C*. **2013**. 117(44), p22834-22842.

[9] Karpovich, D.S. and Blanchard, G.J., "Direct measurement of the adsorption-kinetics of alkanethiolate self-assembled monolayers on a microcrystalline gold surface", *Langmuir*. **1994**. 10(9), p3315-3322.

[10] Schessler, H.M. *et al.,* "Quantitating the balance between enthalpic and entropic forces in alkanethiol/gold monolayer self assembly", *Journal of the American Chemical Society*. **1996**. 118(40), p9645-9651.

[11] Guicheteau, J.A. *et al*., "Surface-enhanced Raman scattering (SERS) evaluation protocol for nanometallic surfaces", *Applied Spectroscopy*. **2013**. 67(4), p396-403.

[12] Carron, K.T. and Hurley, L.G., "Axial and azimuthal angle determination with surface-enhanced Raman-spectroscopy - thiophenol on copper, silver, and gold metal-surfaces", *Journal of Physical Chemistry*. **1991**. 95(24), p9979-9984.

[13] Haehner, G. *et al*., "Investigation of intermediate steps in the self-assembly of n-alkanethiols on gold surfaces by soft x-ray spectroscopy", *Langmuir*. **1993**. 9(8), p1955-1958.

[14] Schreiber, F., "Structure and growth of self-assembling monolayers", *Progress in Surface Science*. **2000**. 65(5-8), p151-256.

[15] Schreiber, F. *et al*., "Adsorption mechanisms, structures, and growth regimes of an archetypal self-assembling system: decanethiol on Au(111)", *Physical Review B*. **1998**. 57(19), p12476-12481.

[16] Schwartz, D.K., "Mechanisms and kinetics of self-assembled monolayer formation", *Annual Review of Physical Chemistry*. **2001**. 52, p107-137.

[17] Whelan, C.M.; Smyth, M.R.; and Barnes, C.J., "HREELS, XPS, and electrochemical study of benzenethiol adsorption on Au(111)", *Langmuir*. **1999**. 15(1), p116-126.

[18] Le Ru, E.C.; *et al*., "Surface enhanced Raman scattering enhancement factors: a comprehensive study", *The Journal of Physical Chemistry C*. **2007**. 111(37), p13794-13803.

[19] Moskovits, M., "Persistent misconceptions regarding SERS", *Physical Chemistry Chemical Physics*. **2013**. 15(15), p5301-5311.

[20] Murray, C.A. and Bodoff, S., "Depolarization effects in Raman scattering from cyanide on silver-island films", *Physical Review B*. **1985**. 32(2), p671-688.
[21] Blue, D. *et al*., "Diffusion of ethylene and xenon in thin pyrazine layers", *The Journal of Physical Chemistry*. **1989**. 93(24), p8080-8089.

Electronspun nanofibers for the exploration of chemical interactions with materials

Thomas P. Pearl*[a], Richard H. Hoff[b], Jill L. Ruth[c], Matthew P. Willis[d], Matthew J. Shue[d]
[a]OptiMetrics, a DCS company, 100 Walter Ward Blvd, Abingdon, MD 21009
[b]United States Military Academy, Dept. of Chemistry and Life Science, West Point, NY 10996
[c]Leidos, Inc., P.O. Box 68, Gunpowder Branch, Aberdeen Proving Ground, MD 21010
[d]U.S. Army Edgewood Chemical Biological Center, Research & Technology Directorate, 5183 Blackhawk Rd, Aberdeen Proving Ground, MD 21010

ABSTRACT

This project investigated routes for studying surface properties of polymeric solid-phase materials to better understand the nature of the interaction between the material surface and vapor-phase chemical species. Recent work at the U.S. Army Edgewood Chemical Biological Center used a finite element method and inverse analysis to quantify the physical parameters of transport in solids, specifically coatings like paint. This work identified difficulties in the modeling process because of the number of simultaneous transport mechanisms. In order to address these challenges for polymer based materials such as paint, we hypothesized that a solid phase extraction approach for measuring vapor phase species could be used to differentiate between absorption and adsorption processes in a model contaminant-material transport system. We chose to fabricate electrospun polymer nanofibers (high specific surface area) with tunable dimensions and of variable polymer blends for coupling to solid phase micro extraction (SPME) tips to allow for selective sampling of vapor headspace of high volatility liquid analytes. This report describes efforts to establish an electrospinning method for polymer nanofibers and the attachment of nanofiber mats to bare SPME tips. We also show data that illustrates the development of SPME methods with commercially available, bulk polymer coated SPME tips, for use with our analytical chromatography platforms.

Keywords: Mass transport, coatings, diffusion, nanofibers, SPME

1. INTRODUCTION

There is a strong interest in the field of decontamination sciences to better understand mass transfer processes in bulk phases of materials. Contaminants in solids present a significant threat and challenge with respect to removal and neutralization since there is a significant lack of accessibility to subsurface concentration fields for different decontamination approaches. When considering mass transport in solids, the range of relevant interactions and processes associated with transport under various mechanisms is very broad and is driven by a number of molecule- and substrate-specific attributes. The problem becomes even more entangled when treating absorption and reemission phenomena into and out of engineered polymeric coatings like paint systems. Work at the U.S. Army Edgewood Chemical Biological Center (ECBC) has demonstrated that the efforts to model sorption and desorption of chemical warfare agents in combination with the current Chemical Agent Resistant Coating system involve processes that cannot be described by Fickian diffusion alone.[1,2] Additionally, results from scanning electron microscopy (SEM) and energy dispersive spectroscopy (EDS) used for measuring concentration profiles in the cross section of contaminated military paint systems show a strong influence of specific coatings components on subsurface mass transport rates as a function of paint and contaminant types.[3] Figure 1 illustrates the morphology of surface and bulk regions of uncontaminated military paint systems resolved by SEM and Figure 2 highlights an example of varying transport rates or contaminant affinity as a function of coating component using EDS.

APPROVED FOR PUBLIC RELEASE

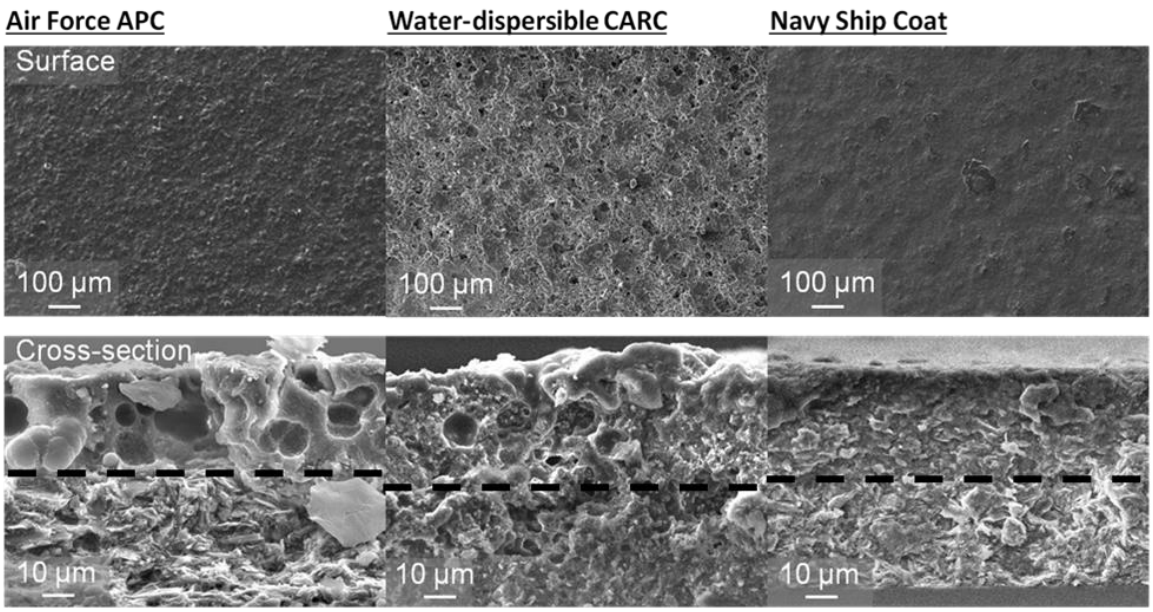

Figure 1. SEM images for surfaces (top row) and cross sections (bottom row) for three different military paint systems. The dashed line through the images in the bottom row is an identification of the topcoat/primer boundary for the paints. Texture and morphology variation on the µm length scale is evident for these materials systems both at the surface and in the bulk (adapted from Cooley et al.[3]).

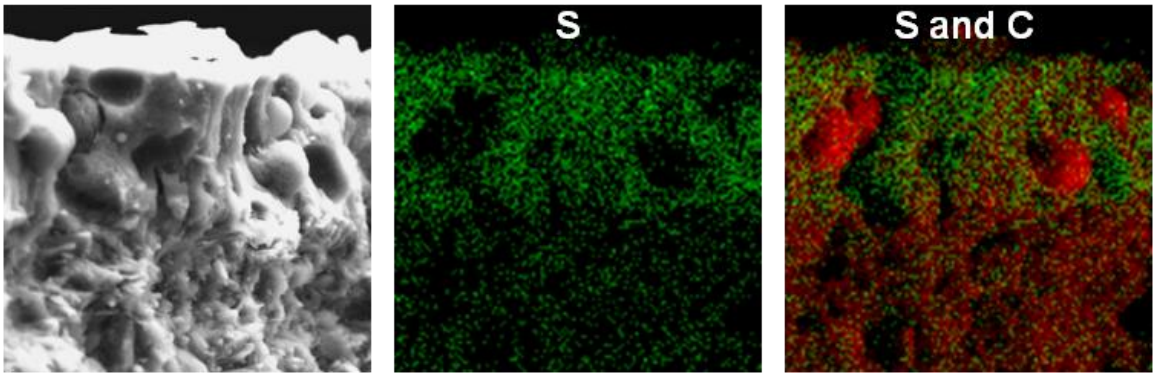

Figure 2. SEM (left) and select element EDS (middle, right) mapping of 2-chloroethylethyl sulfide (CEES, distilled mustard simulant) contaminated Air Force APC after a 30 minute residence time (images: 100 µm x 100 µm). The EDS maps quantify the spatial distribution of sulfur (S) (indicative of CEES concentration) or S and carbon (C) in the matching SEM image in the left panel. Notice the voids in the middle image for S that can then be attributed to the presence of C-rich polymeric beads as shown by the right image (adapted from Cooley et al.[3]).

In order to elucidate fundamental mechanisms associated with mass transport in solid phase matrices, it is necessary to employ experimental approaches that are sensitive to the spectrum of contaminant-material interactions occurring at the material surface and in the bulk material. Overall, the challenge with studying these types of systems is the significant convolution of materials properties, from chemistry to morphology, which can dictate the routes and rate limiting factors for mass uptake into the subsurface and bulk layers. For the case of trying to better understand behavior in a complex material like paint, two different challenges need to be overcome, which in principle can be accomplished through the judicious choice of a model contaminant-material system. First, the model system will only consider a single component from a full coating system so that effects of key constituents of the material can be understood separately instead of in concert. In the case of a polyurethane based paint, isolation of the polymer base for the paint formulation is a logical starting point. Second, creation of a distinction or disparity between surface and bulk regimes by virtue of material aspect ratio would allow for absorption processes to be discerned in contrast to adsorption specific, surface related events. An important aspect of this second criterion is that the rate of permeation and uptake into the bulk of polymer solids has slow kinetics relative to adsorption and furthermore, the choice of interaction between contaminant and material will be limited to vapor phase exposure of the chemical species that will absorb into the material. This is the basis for the use of polymeric

nanofibers for the study of bulk mass transport. We describe in this technical summary the initial work towards creating a detection scheme that utilizes a nanofiber functionalized solid phase micro extraction (SPME) approach for time-resolved chromatography-based measurements of mass uptake rates that can then be used for determining bulk mass transport parameters.

Electrospinning is a technique that can generate nanoscale polymer fibers from polymer solutions or polymer melts. A large direct current electric field (~10 kV) is set up between a source of fine droplets and a collector. The electric field generates electrostatic forces in the droplets that overcome surface tension and cause the droplets to elongate, and then expel a fine spray of material out of both ends. With the large surface to volume ratio of these jets, solvent evaporates and polymer fibers at micro to nanoscale are formed.[4] The nanofibers can be created from a wide variety of polymer formulas and the geometry of the collector can be varied to collect the fibers as a random mat or highly oriented. Much has been learned about control of electrospinning so that fiber surface characteristics can be modified for a variety of purposes. Applications of electrospun fibers have included tissue scaffolds,[5] sensors,[6-9] and electronics.[10-11]

In the study of adsorption and transport on solid surfaces, nanoparticles and nanofibers have the advantage of providing enormous surface area with very little solid material required. In addition to the small diameter of the fibers obtained by electrospinning, often on the order of 100 nm in diameter, it is also possible to generate porous nanofibers with control over the pore size. For instance, it was shown that silica nanoparticles could be introduced into a nylon 6,6 electrospinning experiment. After removal of the silica with hydrofluoric acid, the specific surface area and pore size increased from 4.68 m^2g^{-1} to 8.31 m^2g^{-1} and 0.0133 cm^3g^{-1} to 0.0250 cm^3g^{-1}.[12]

Recently the electrospinning method was employed to deposit nylon 6,6 fibers directly onto a stainless steel wire with no binder or other substance involved. This combination was robust enough to be employed as a SPME extractor, and in combination with a gas chromatography–mass spectrometer (GC-MS), chlorophenols were quantized with detection limits in the ng/L range.[13] However, the kinetics of the equilibrium between the concentration of analyte in the headspace and concentration on the fibers were very slow. Exposure times of 40-60 minutes were required to achieve optimum extraction. In another study, better extraction efficiencies were obtained, but the kinetics were still slow.[14]

SPME techniques, coupled with gas chromatography (GC) and mass selective detectors (MSD), have been in use long enough to have gained wide acceptance and extensive commercial development. The variety of sorbents on SPME extractors has been documented and characterized elsewhere.[15] The SPME technique was used in conjunction with detection of bis(2-chloroethyl) sulfide on soil and was effective at concentrations as low as 237 ng/g of soil.[16] Even though the absolute quantity of analyte absorbed by the SPME method is lower than that absorbed by other solid phase extraction methods, the sensitivity of the SPME method is higher because the extracts collected are cleaner. One goal of this research is to find the optimum selectivity and sorption characteristics to enhance this sensitivity.

This technical summary will highlight the work that was performed as a result of a research collaboration between the Decontamination Sciences Branch at ECBC and the United States Military Academy (USMA). The content herein outlines the steps taken at ECBC to establish conventional SPME methods in existing analytical chromatography platforms using commercially available SPME tips. These methods would then be ready for use with electrospun nanofiber coated SPME tip assemblies. Details on the work performed at USMA involving polymer electrospinning are highlighted with respect to method development for controlled fabrication of mats and bundles of polymer specific nanofibers. Details on the development efforts for both parts of the collaboration will be shown in the subsequent section as well as comments on the prospect of utilizing this approach for mass transport measurements.

2. METHODS

2.1 Methods development approach

A key premise in the project hypothesis is that differentiation between adsorption (fast kinetics) and absorption (slow kinetics) of chemical species on a polymer could be achieved by measuring the mass uptake on to a polymer-coated SPME tip for both short and long exposure times. This was proposed to be most tractable in the limit of high specific surface area fibers that would ultimately comprise the outer coating of the SPME tip and organic solvents were chosen as the class of analytes to target for detection. With a significant disparity between available surface sites and bulk free volume, along with assuming that the adsorption process would be very fast relative to absorption, it would be possible to track the rate of absorbed mass increase as a function of time after accounting for the mass uptake associated with adsorption alone. The absorption process could then be modeled to determine mass transport parameters for diffusivity and saturation concentration in the material. In order to accomplish this, we needed to develop SPME chromatography methods as well as optimize the procedures on a recently constructed apparatus for electrospinning polymer nanofibers.

APPROVED FOR PUBLIC RELEASE

2.2 SPME method development

In SPME, a polymer-coated fused silica fiber is used for the extraction of an analyte from the headspace of a liquid sample, which in-turn is desorbed to allow for detection of the analyte. There are several distinct steps involved in the process, extraction, adsorption, desorption, and detection, and all steps need to be optimized for the compound of interest.

The first step in this method development process was to demonstrate that we could measure adsorbed mass for a solvent onto a stock, bulk polymer-coated SPME fiber coating (not functionalized by polymer nanofibers). This involved choosing a short exposure time to the solvent vapor phase headspace and finding an asymptotic limit for analyte response for different analyte concentrations as a function of volatilization temperature. The measured mass could then be approximated as the adsorbed mass and any mass uptake for much longer exposure would be associated with absorption processes.

A simple, common solvent compound was to be used for the purpose of this research. Several solvents, such as methanol, 2-propanol (IPA), hexane, 1,1,1,2-tetrachloroethane, and 1,2-dichloromethane, were tested as possible candidates. Potential solvent incompatibility with the electrospun nanofibers and SPME polymers was considered in making the choice. Ultimately, hexane was chosen as the analyte of interest in order to minimize any possible solvent-induced dissolution or degradation of the nanofiber polymers. Various concentrations of hexane were prepared for use in calibration. The hexane standards were made in IPA due to hexane's immiscibility with water and the fact that hexane and IPA are chromatographically separated.

Using an existing Agilent 6890 gas chromatograph with a 5973 mass selective detector (GC/MSD), a dedicated instrument for performing manual SPME injections was set up. An appropriate inlet liner (Supelco, Cat. #26375), time, temperature, and fiber depth were chosen for efficient transfer and sample desorption. A DB-624 analytical column (Agilent, Part #121-1324), 20 m x 0.18 mm x 1.0 μm, was installed in the instrument for resolution of hexane. Appropriate oven parameters and a selected ion monitoring method were used for the analysis and selective detection of hexane. After adsorption of the sample onto the SPME fiber, the fiber was desorbed directly into the hot inlet of the GC/MSD. The fiber desorption time was 5 minutes with an inlet temperature of 250 °C at a depth of three on the manual SPME holder.

There are several variables in the analyte extraction process. With SPME, neither complete extraction of the analyte nor full equilibrium is necessary, but consistent sampling time and temperature are critical. It also is important to keep vial size and sample volume constant; hence, the ratio of liquid to headspace is consistent. A sample consisted of a 7 mL vial with a polytetrafluoroethylene/silicone septum cap (Supelco, Cat. #27341) containing 4 mL of a standard solution. Samples were heated in a heating block at 50 °C for 20 minutes. These conditions produced a headspace with a sufficient concentration of hexane for adsorption and ultimately detection, independent of the fiber type, while allowing for a dynamic calibration range over several orders of magnitude ranging from 5 ppm to 7500 ppm.

2.3 Custom built electrospinning apparatus

Electrospinning of polymer fibers from solutions of volatile solvents is a well-documented process.[17] Since the process itself is no longer novel, authors tend to be less than meticulous in describing their experimental parameters. Information that is critical to the reproduction of earlier work is often missing, and methodical trial and error must be applied to account for this. The variables that can be critical are: identity of the polymer, volatility of the solvent used, dielectric coefficient of the solvent, length (M_W) of the polymer molecules, surface tension of the polymer solution, viscosity of the polymer solution, electric field strength (V), distance between the polymer source and the collector, flow rate of the polymer solution, and the geometry of the needle through which the polymer solution is delivered. A photograph and schematic of the apparatus constructed recently at USMA, which allows for control over these variables is shown in Figure 3. The results will highlight optimization procedures for a variety of polymer blends and deposition configurations.

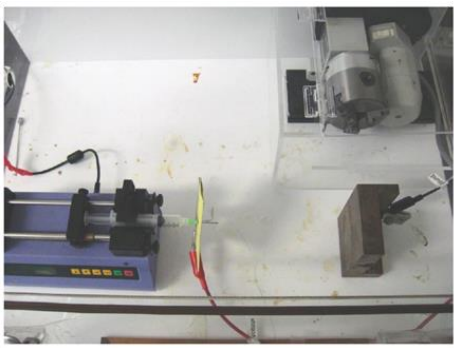

Syringe pump, motor and collecting plate

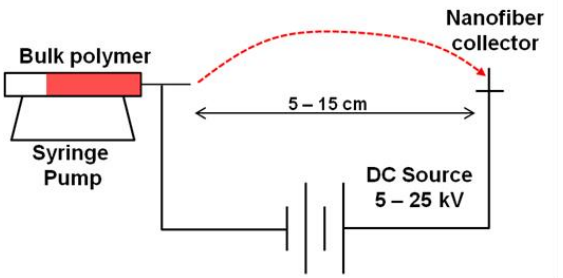

Figure 3. Illustration of electrospinning apparatus constructed at USMA and a schematic diagram for the deposition setup. Polymer solution would be injected at a fixed rate by a syringe pump into a high electric field established between the tip of the syringe and a collector.

3. RESULTS AND DISCUSSION

3.1 SPME method development results

For SPME, an appropriate fiber type must be chosen to absorb the compound of interest. This selection is based upon the molecular weight and polarity of the compound. Several commercial fiber types, polydimethylsiloxane (PDMS), polyacrylate and carboxen/PDMS, along with various film thicknesses, 7 µm, 85 µm, and 100 µm, were tested with hexane. The fiber was fitted into a manual SPME fiber holder (Supleco, Cat. #57330-U). After the sample solution was heated at 50 °C for 20 minutes, the fiber was exposed to the headspace of the sample for a set time. The final fiber choice, based upon peak shape and response, was an 85 µm polyacrylate SPME fiber (Supelco, Cat. #57304). After testing at various exposure times, a time of 2 minutes was chosen (a sufficiently short time in order to only sample the adsorption processes). Figure 4 shows two concentrations of hexane/IPA solutions detected as a function of volatilization temperatures and exposure times with the commercially available 85 µm polyacrylate SPME fiber. The left panel illustrates the proportional scaling of the hexane response for the same volatilization temperature across the two concentrations probed (250 and 2500 ppm hexane/IPA). It is also apparent that at a temperature of 50 °C, for 2 minutes of vapor exposure time, the hexane response has begun to reach an asymptotic limit indicating that higher volatilization temperatures (for a 2 minute exposure time) would not result in more uptake for adsorption. The right panel shows the vapor exposure time sensitivity at a fixed volatilization temperature where 2 minutes is shown to be sufficient for measuring short time uptake for adsorption. No increase in signal past 2 minutes at 50 °C for either concentration indicates saturation of the surface sites of the SPME fiber. These steps in setting up a SPME method, including demonstration of solvent volatilization temperature and vapor exposure time, were necessary for moving toward detection of the same analyte with nanofiber-coated SPME tips.

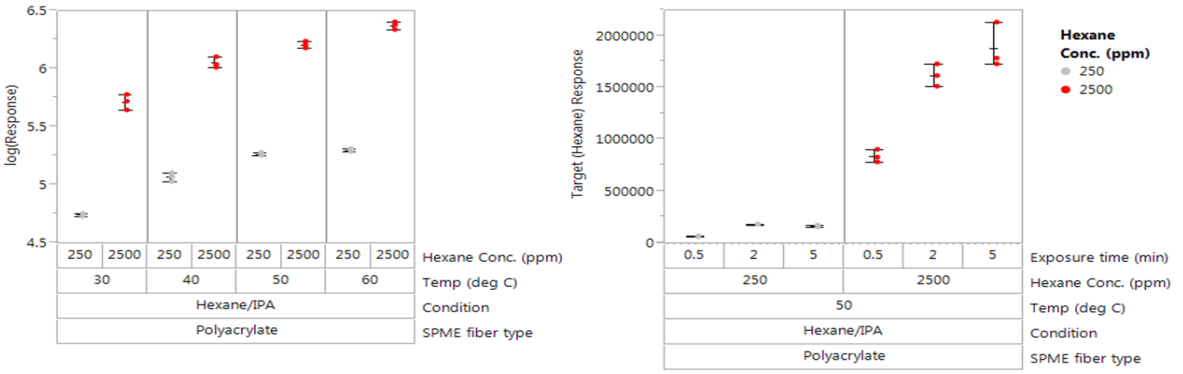

Figure 4. Results for measurement of hexane vapor from dilute (250 ppm and 2500 ppm) hexane/IPA solutions with SPME using commercially available, bulk polyacrylate-coated SPME tips.

3.2 Electrospinning of polymer nanofibers

Polystyrene was chosen as the first polymer to work with partly because published parameters are available.[18] Its non-polar structure is also a good mimic for the non-polar sorbents used as stationary phases in chromatographic separations. The citation above on electrospinning of polystyrene used a 300 kDa M_W polymer, but we had a range of M_W samples available. A series of experiments were performed with solutions of polymer samples ranging from 25 kDa to 2.0 MDa to find the most likely M_W with which to go forward. The spun samples were examined for extent of fiber formation, evidence of incomplete solvent evaporation, and percentage of polymer material that impacted on the collector. Both samples at 75 kDa and 100 kDa provided the most abundant fibers, but with a significant (10 to 50%) percentage of polymer mass present as beads. Further optimization of flow rate, voltage, and distance to collector resulted in consistent production of fibers with no beading and an average diameter of 500 nm to 1000 nm. The optimization process can be observed in Figure 5, with panel D representing the final product.

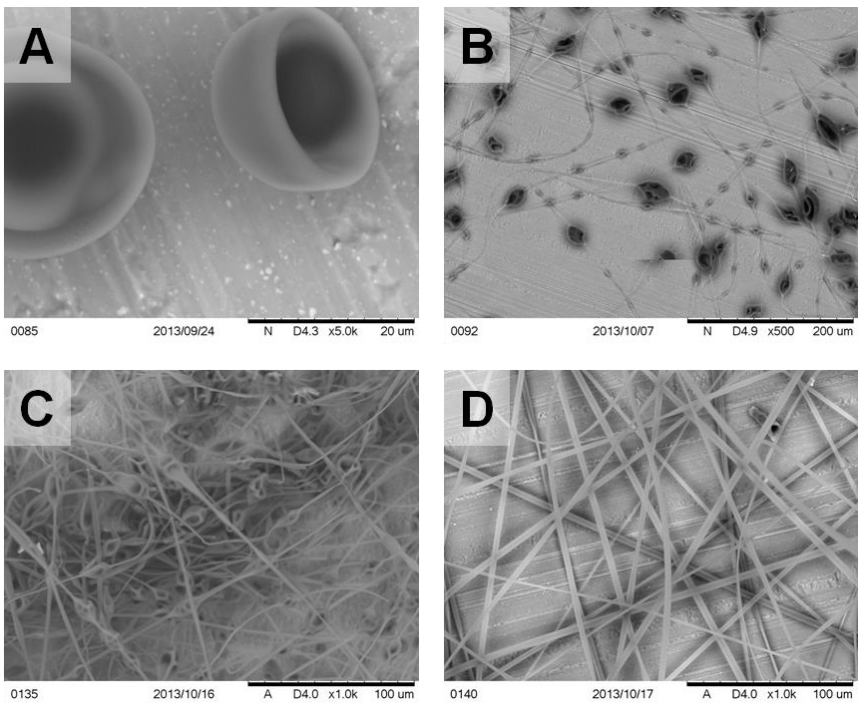

Figure 5. SEM images illustrating the optimization of process control variables for the deposition of polystyrene nanofibers from electrospinning including control over polymer blend viscosity, applied voltage, distance between syringe pump and collector, and flow rate for syringe pump. Pre-processing parameters included solvent composition, polymer molecular weight, and blending. Preliminary deposition as 10-40 µm droplets (A); Initial formation of polymer fibers, dfiber~100-300 nm (B) with the majority of the mass expressed as droplets; Transition of electrospun polymers to mostly fibers (C); Optimized deposition conditions to favor fiber formation (D). Bead formation resulted if the viscosity of the polymer blend was too low and the flow rate too high along with deposition at higher applied voltages and shorter distances between syringe pump and collector.

Other polymers were investigated for electrospinning potential. The first of these, poly(acrylic acid) (PAA), was cited in a significant number of published works.[19] However, when we attempted to duplicate the spinning conditions in our lab, the solutions turned out to be completely unsuitable for spinning due to very high viscosity. This problem was consistent over several solvent and concentration changes. While the syringe pump system had sufficient force to pump the solution, the viscosity and surface tension were too high to be overcome by the electrostatics of the DC field. Some work was done with poly(methyl methacrylic acid) (PMMA), using parameters from literature.[20] These proved to be more reliable and nanofibers were produced, though over the course of ten runs there were issues with beading in about half of them.

The majority of our further work was conducted using a polyurethane: (poly[4,4'-methylene bis(phenyl isocyanate)-alt-1,4-butanediol/di(propylene glycol)/polycaprolactone]). This material, the only polyurethane readily available commercially, was purchased in the form of pellets and was used as received. The monomers that compose the polymer are known, but the exact order of attachment, extent of cross-linking, and M_W are not. Spinning parameters from literature[21] got us close to a solution, while systematic modification of solution concentration, flow rate, pump to collector distance, and field strength optimized our system for fiber production.

In parallel to the effort on optimizing control over nanofiber geometry and composition, work was done to fashion a means of attaching nanofibers to a shaft or needle for integration into a SPME fiber assembly. Deposition of nanofibers by electrospinning is not suitable for precise placement of the fibers. When the droplet of polymer solution leaving a syringe first bursts into a fibrous structure, the flow is stable and the orientation is linear in the direction of electric field density. This linear flow is very short lived and the fiber enters a zone of chaotic flow before reaching the collector. This disperses the fibers over a relatively large area at the collector. For example, with a 15 cm gap between the syringe tip and collector, the impact area of the fiber exceeds a 6 cm square area. This is difficult to control, requiring more field generators to focus the flow. However, it is possible by simply modifying the shape of the collector or putting the collector into motion to affect some control over the orientation of fibers. While there is ample information available on a variety of collector geometries, there is almost no information on deposition onto a needle. We tried both axial (pointing toward source) and perpendicular orientations for the needle, and found little symmetry in the deposition of fibers. Axially, the fibers built up as a knob on the end of the needle. In perpendicular mode the fibers were better distributed along the needle, but did not cover its circumference. The solution that we found was to hold the needle perpendicular to the source and spin the needle as fibers were deposited. A mini lathe was adapted to this purpose. See Figure 6 for the influence of collector shape on the orientation of deposited fibers.

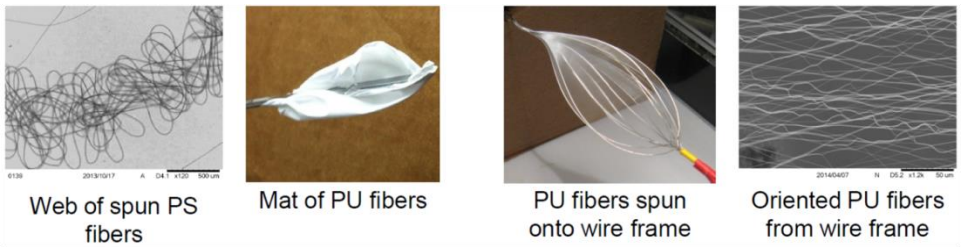

Figure 6. Examples of polyurethane nanofibers grown or deposited in a variety of configurations using electrospinning.

Initial efforts were based on the strategy of spinning the fiber onto a shaft of very small diameter (approximately 0.08 mm). With a rotational speed of 600 rpm, the fibers were deposited very evenly around the shaft. The distribution was random, not oriented, which is preferred as it forms a mat with plenty of pore space. However, handling and assembly of this fiber coated shaft into a workable SPME was problematic. The Supelco company, the provider of the complete SPME assemblies, did offer a “blank” tip, which was simply the fused silica rod which supports the sorbent in many of their complete assemblies. Attempts to spin directly onto these “blank” tips was frustrating, because the very fine (0.10-0.12 mm) silica tip is so fragile. Supelco manufactures SPME assemblies with steel or flexible polymer in place of the silica rod, but will not sell these as blanks.

Further work with the fused silica tip revealed that the shaft holding the silica tip was hollow and that we could remove the silica tip ourselves and replace it with another material. We purchased stainless steel wire with a 0.1016 mm diameter and were able to epoxy this into place and spin polyurethane mats onto the SPME tips. The SPME assembly outer wall is a 24-gauge syringe needle with an inner diameter of 0.33 mm. Inside, this is a moveable shaft, with an outer diameter of 0.30 mm. This shaft is hollow, with a 0.14 mm round annulus. Into this annulus, a rod of diameter range from 0.08-0.12 mm is epoxied. The SPME assembly is then put together, and the final step is spinning fiber onto the tip. As of the date of this report, a SPME assembly had been constructed, but not extensively tested. An example of the attachment of a mat of polymer nanofibers to a 0.08 mm wire is shown in Figure 7.

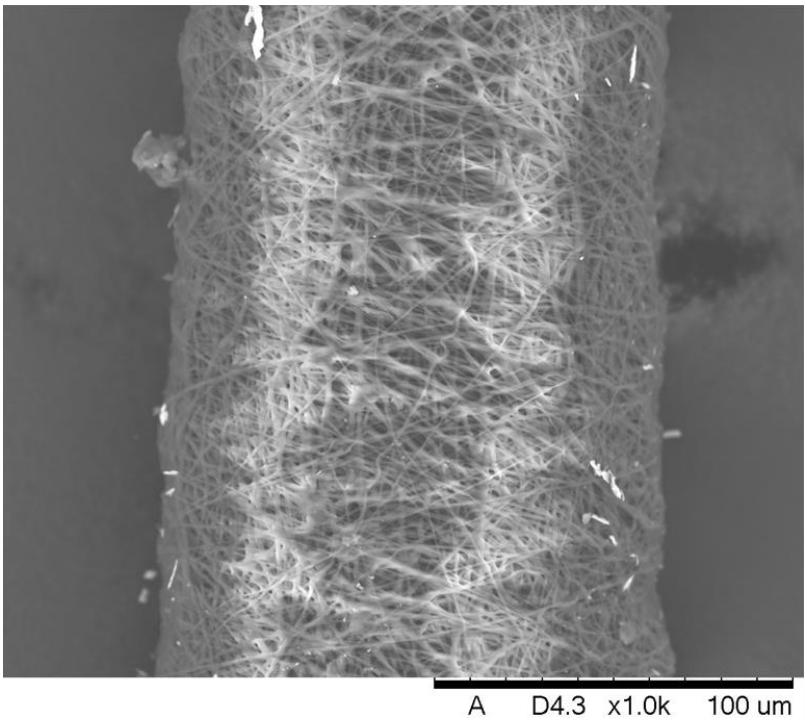

Figure 7. Example of polyurethane nanofibers attached to a tungsten wire in preparation for integration with a SPME tip.

4. CONCLUSIONS

While progress was made on the development of an electrospinning capability for polymer nanofibers that could be used in conjunction with SPME methods for measuring contaminant-material interactions, there is still some question as to whether the morphology introduced by the polymer mat would create an unnecessarily difficult system to model with respect to absorption into the fiber bulk. Bringing this direction to fruition would require greater material control than what has been achieved to date, which is difficult but not impossible, both in terms of the specific surface area of the fibers and their spatial orientation. Additionally, there would need to be further assessments of the robustness of the nanofiber mats with respect to temperature cycling, necessary for a chromatography measurement, and exposure to solvent molecules. There are other complementary experimental methods for the measurement of time-resolved mass uptake that would be necessary to invoke including utilization of a quartz crystal microbalance in conjunction with thermal desorption spectroscopy in order to establish full confidence in the nanofiber/SPME route for measurement of mass transport.

ACKNOWLEDGEMENTS

The authors acknowledge support from the ECBC Surface Science Initiative program, the ECBC Decontamination Sciences Branch, and the USMA Department of Chemistry and Life Science.

REFERENCES

[1] Willis, M.P. *et al.*, "Characterization of chemical agent transport in paints", *Journal of Hazardous Materials*. **2013**. 260, p907-913.
[2] Willis, M.P.; Mantooth, B.A.; and Lalain, T.A., "Novel methodology for the estimation of chemical warfare agent mass transport dynamics, part II: absorption", *Journal of Physical Chemistry C*. **2012**. 116(1), p546-554.
[3] Cooley, K.A. *et al.*, "Direct measurement of chemical distributions in heterogeneous coatings", *ACS Applied Materials & Interfaces*. **2014**. 6(18), p16289-16296.
[4] Ramakrishna, S. *et al., An Introduction to Electrospinning and Nanofibers*. World Scientific Publishing, New Jersey. **2005**.
[5] Boudriot, U. *et al.*, "Electrospinning approaches toward scaffold engineering - a brief overview", *Artificial Organs*. **2006**. 30(10), p785-792.

[6] Aussawasathien, D.; Dong, J-H.; Dai, L., "Electrospun polymer nanofiber sensors", *Synthetic Metals*. **2005**. 154(1-3), p37-40.
[7] Shim, W.G. *et al.,* "Adsorption characteristics of benzene on electrospun-derived porous carbon nanofibers", *Journal of Applied Polymer Science*. **2006**. 102(3), p2454-2462.
[8] Luoh, R. and Hahn, H.T. "Electrospun nanocomposite fiber mats as gas sensors", *Composites Science and Technology*. **2006**. 66(14), p2436-2441.
[9] Ding, B. *et al.,* "Electrospun nanofibrous membranes coated quartz crystal microbalance as gas sensor for NH_3 detection", *Sensors and Actuators B: Chemical*. **2004**. 101(3), p373-380.
[10] Moran-Mirabal, J.M. *et al.,* "Electrospun light-emitting nanofibers", *Nano Letters*. **2007**. 7(2), p458-463.
[11] Pinto, N.J. *et al.,* "Electrospun hybrid organic/inorganic semiconductor Schottky nanodiode", *Applied Physics Letters*. **2006**. 89(3), p033505.
[12] Shi, Q. *et al.,* "A facile approach to fabricate porous nylon 6 nanofibers using silica nanotemplate", *Journal of Applied Polymer Science*. **2011**. 120(1), p425-433.
[13] Bagheri, H. *et al.,* "Novel polyamide-based nanofibers prepared by electrospinning technique for headspace solid-phase microextraction of phenol and chlorophenols from environmental samples", *Analytica Chimica Acta*. **2012**. 716, p34-39.
[14] Zewe, J.W.; Steach, J.K.; and Olesik, S.V., "Electrospun fibers for solid-phase microextraction", *Analytical Chemistry*. **2010**. 82(12), p5341-5348.
[15] Zewe, J.W. "Electrospun fibers for solid-phase microextraction", Electronic Thesis or Dissertation. Ohio State University, **2010**.
[16] Kimm, G.L.; Hook, G.L.; and Smith, P.A., "Application of headspace solid-phase microextraction and gas chromatography-mass spectrometry for detection of the chemical warfare agent bis(2-chloroethyl) sulfide in soil", *Journal of Chromatography A.* **2002**. 971(1-2), p185-191.
[17] Huanga, Z.M. *et al.,* "A review on polymer nanofibers by electrospinning and their applications in nanocomposites", *Composites Science and Technology*. **2003**. 63, p2223-2253.
[18] Lee, M.W. *et al.,* "Electrospun polystyrene nanofiber membrane with superhydrophobicity and superoleophilicity for selective separation of water and low viscous oil", *ACS Applied Materials & Interfaces*. **2013**. 5(21), p10597-10604.
[19] Lee, S.H. *et al.,* "Poly(acrylic acid) nanofibers by electrospinning", *Materials Letters*. **2005**. 59(7), p829–832.
[20] Wang, H. *et al.,* "Electrospun poly(methyl methacrylate) nanofibers and microparticles", *Journal of Materials Science*. **2010**. 45, p1032-1038.
[21] Zhuo, H. *et al.,* "Preparation of polyurethane nanofibers by electrospinning", *Journal of Applied Polymer Science*. **2008**. 109(1), p406-411.